

CARBON NANOTUBES AS VERTICAL INTERCONNECTS
IN 3D INTEGRATED CIRCUITS

MASTERS THESIS

BY

STEN VOLLEBREGT

BORN ON THE 15TH OF MAY 1984 IN DELFT

SEPTEMBER 5, 2009

SUPERVISORS:

PROF. DR. C.I.M. BEENAKKER

DR. R. ISHIHARA

DR. J. DERAKHSHANDEH

DELFT UNIVERSITY OF TECHNOLOGY
FACULTY OF ELECTRICAL ENGINEERING, MATHEMATICS AND
COMPUTER SCIENCE
DELFT INSTITUTE OF MICROSYSTEMS AND NANOELECTRONICS
LABORATORY OF ELECTRONIC COMPONENTS, TECHNOLOGY
AND MATERIALS

Preface

This report is the result of almost a year of reading, writing, discussing and experimenting as part of my MSc thesis. While only my name on it as author such a work could not have been made possible without the help of many others. First I would like to thank my direct supervisors, dr. Ryoichi Ishihare and dr. Jaber Derakhshandeh for introducing me into the wonderful field of 3D integration and carbon nanotubes. I would especially want to thank Jaber for all his support on cleanroom processing, measurements, reviewing and all the nice discussion about the obtained results.

For this work it was necessary to visit external facilities in order to grow the required nanotubes. I would like to thank dr. Ken Teo and dr. Nalin Rupesinghe from AIXTRON, Cambridge UK, for letting me do two full days of growth experiments at their facility, even though snow was trying to prevent it all from happening.

The second external facility was NanoLab Inc. in Newton, MA (USA) at which I was able to perform experiments for eight weeks. I want to thank the owner of the company, David Carnahan, for allowing me to perform many experiments on their systems. I want to thank my former colleagues at NanoLab for the support, especially Dan Esposito, for performing all the SEM analysis together with me, the interesting discussions about the field of carbon nanotubes and continuing the growth experiments for me after I left.

Finally I want to thank the DIMES ICP engineers, but especially Charles de Boer, for the training and support in the DIMES cleanroom facilities. Furthermore many thanks to dr. Meng-Yue Wu for performing the TEM analysis, dr. Fredrik Creemer for the advice on thermal modelling and finally, prof. C.I.M. Beenakker and prof. G.Q. Zhang for participating in my thesis committee.

The final report should give the reader a complete introduction into the field of carbon nanotubes and the results we obtained in it. The report is written with the goal that someone with a BSc in Electrical Engineering, or a similar degree, should be able to understand most of it. Although some background in micro-electronics and the fabrication thereof is highly recommended.

Chapter one gives an introduction why carbon nanotubes (CNTs) should be used for 3D integrated circuits, and why we should try to create 3D integrated circuits at all. The next two chapters introduce the reader to the field of carbon nanotubes. Chapter two gives a quick, and hopefully thorough, introduction into the structural, electrical and thermal properties of CNTs currently found in literature. Chapter three quickly discusses the history of CNT fabrication followed by a more in-depth investigation on the growth of CNTs using chemical vapour deposition and how we can control it.

After this the results of my research are being discussed. In chapter four we derive electrical models for our structures and compare these with metals. In chapter five the designed fabrication processes and measurement structures are discussed. Chapter six discusses all the growth results investigated using SEM, TEM and Raman spectroscopy. Finally a conclusion is drawn, and recommendations for future work are given.

There are two appendixes I want to bring to the readers attention. First of all appendix A which gives a brief introduction in the concept of phonons, which is a subject that is almost completely ignored in the BSc and MSc of Electrical Engineering at our university. Second, appendix C specifies the measurement equipment used in this report. It also gives an introduction into the field of Raman spectroscopy on CNTs for readers unfamiliar to this subject.

Delft, August 2009
Sten Vollebregt

Abstract

In integrated circuits the delay caused by interconnects, their power consumption, production and reliability are challenges to be solved. Using the third dimension for additional layers of transistor has been proposed as a solution to this problem by reducing the length of the interconnects. A problem in 3D integration is the creation of reliable, low resistance and high aspect ratio vertical interconnects. We propose the use of carbon nanotubes (CNT) for this purpose.

There exist single-walled (SWNT) and multi-walled nanotubes (MWNT), the latter consisting of multiple tubes inside each other. Carbon nanofibres (CNF) are tube-like structures without graphite walls parallel to the tube axis. Diameters are between 0.5-100 nm, while lengths can be up to several mm. CNTs can behave semiconducting or metallic depending on the diameter and chirality.

A metallic SWNT with two conductive bands has a quantum resistance of 6.45 k Ω , and can have ballistic conduction up to several microns. Each wall in a MWNT can contribute in conduction, the amount of conductive bands depends on the amount of walls and diameter. Beside a quantum resistance CNTs have a large quantum capacitance and kinetic inductance, and an electrostatic capacitance. Lastly, CNTs can carry current densities up to 10⁹ J/cm².

Beside being good electrical conductors CNTs have a high thermal conductivity, with values between 1000-6600 W/m·K being reported. They oxidise at temperatures between 600-800 °C and deform in a vacuum above 2000 °C.

CNTs can be grown on top of substrates using (plasma enhanced) chemical vapour deposition ((PE)CVD) using a catalyst and carbon feedstock. Vertical alignment can either be achieved by Van der Waals interaction between tubes or by a strong electric field during growth. The geometry of CNTs can be controlled by the activation of the catalyst layer and the growth parameters (table 3.1).

We derived electrical models for SWNT and MWNT bundles. The quantum capacitance and kinetic inductance can be neglected when a bundle is formed. The resistance against the MFP, diameter and density was calculated. It was found that only SWNT can perform better than bulk Cu or Al when very high density bundles are formed, otherwise it rapidly increases. MWNT have a resistance that is one order of magnitude higher than Cu or Al, which hardly increases for low densities.

We designed electrical measurement structures using two and four-point measurement which can be created using four masks. Two cleanroom compatible processes, one with interlayer oxide deposited before and the other after CNT growth, were made. As photo resist patterning was found to have a negative influence on the CNT growth quality an additional lift-off process was created. The four-point structure can also be used for electrical reliability and thermal conductivity measurements.

Vertical aligned growth was possible when using a BlackMagic (HF-)PECVD at 500 °C, in combination with Ni and Pd as catalyst. The same system in APCVD mode resulted in aligned CNFs with Pd at 450-640 °C, and random CNTs using Co and Fe at 640 °C. Scanning electron microscopy (SEM), transmission electron microscopy (TEM) and Raman spectroscopy were used to investigate the grown CNTs.

Using the custom equipment at NanoLab vertical CNTs were observed using DC-PECVD at ~ 800 °C, with both Ni and Fe as catalyst. A recipe was developed for a tube furnace which gave vertical growth at 600 °C in combination with 1 nm of Fe, and random growth with thicker layers of Fe and Ni. High quality random CNTs were grown using the same recipe at 500 and 600 °C on Fe patterned with the lift-off process. In all experiments there was 10 nm Ti underneath the catalyst, except for the lift-off which used 1 μ m Ti.

The different Raman spectroscopy quality indicators were investigated vs. temperature and the results obtained with SEM and TEM. It was found that the product between I_D/I_G and FWHM(D) or the I_D/I_G' ratio are good indicators of quality, while only the I_D/I_G is not sufficient. Thermal CVD samples were of higher quality than the PECVD samples.

No growth, due to a too low substrate temperature, was obtained when using the Novellus Concept One PECVD or novel RF assisted CVD at NanoLab. The combination of a 1 μ m Ti layer and Ni also resulted in no growth, due to Ni diffusion into the Ti.

Contents

Preface	iii
Abstract	v
1 Introduction	1
1.1 The interconnect era	1
1.2 Improving interconnect performance	3
1.3 Carbon nanotubes in 3D ICs	3
1.4 Goals	5
2 Properties of carbon nanotubes	7
2.1 Structural properties	7
2.1.1 Carbon nanotubes	7
2.1.2 Carbon nanofibres	9
2.2 Electrical properties	10
2.2.1 Electrical resistance	11
2.2.1.1 Resistance of single-walled nanotubes	12
2.2.1.2 Resistance of multi-walled nanotubes	15
2.2.1.3 Carbon nanofibres	16
2.2.1.4 Contact resistance	16
2.2.2 Capacitance and inductance	16
2.2.3 Electrical reliability	18
2.3 Thermal properties	18
2.3.1 Specific heat	19
2.3.2 Thermal conductivity	20
2.3.3 Thermal stability	22
2.4 Conclusion	23
3 Growth of carbon nanotubes	25
3.1 Arc-discharge & laser ablation	25
3.2 Chemical vapour deposition (CVD)	26
3.2.1 Requirements	26
3.2.2 Growth models	27
3.2.3 CVD methods	29
3.2.3.1 Thermal CVD	29
3.2.3.2 Plasma-enhanced CVD (PECVD)	30
3.2.4 Geometry control	32
3.2.5 CVD for vertical interconnects	35
3.3 Conclusion	36
4 Electrical model and simulations	39
4.1 Single-walled nanotubes	39
4.1.1 Electric model	39

4.1.2	Resistance simulations	42
4.2	Multi-walled nanotubes	44
4.2.1	Electric model	44
4.2.2	Resistance simulations	46
4.3	Conclusion	48
5	Process design	51
5.1	Resistance measurement structures	51
5.2	Fabrication process	52
5.2.1	Oxide after growth (P2748)	53
5.2.2	Oxide before growth (P2752)	55
5.2.3	Lift-off	56
5.3	Masks layout	57
5.4	Other possible uses of the designed structures	60
5.4.1	Reliability testing	60
5.4.2	Thermal conductivity	61
5.5	Conclusion	63
6	Carbon nanotube growth results	65
6.1	Experiments using Novellus Concept One PECVD	65
6.2	Experiments using BlackMagic II 2" R&D CVD	67
6.2.1	DC-PECVD	68
6.2.2	Atmospheric pressure CVD	72
6.2.3	Hot filament PECVD	75
6.3	Experiments performed at NanoLab	76
6.3.1	RF assisted CVD	77
6.3.2	HF-PECVD	79
6.3.3	Thermal CVD	83
6.3.4	Experiments with lift-off wafers	89
6.3.4.1	PECVD	89
6.3.4.2	Thermal CVD	91
6.3.4.3	Possible cause for the absence of growth on Ni	93
6.4	Conclusion	95
	Conclusion and future work	97
	Publications	101
	Appendices	103
	A Phonons	105
	B Process flowcharts	107
B.1	P2700	107
B.1.1	Starting material	107
B.1.2	Process steps	107
B.1.3	Growth conditions	108
B.2	P2748	111
B.2.1	Starting material	111

B.2.2	Process steps	111
B.3	P2752	114
B.3.1	Starting material	114
B.3.2	Process steps	114
B.4	Lift-off	118
C	Experimental methods & Raman spectra	121
C.1	SEM and TEM	121
C.2	EDX spectrum of lift-off Ni sample	122
C.3	Introduction to Raman spectroscopy on CNTs	122
C.4	Raman spectra of growth experiments	124
C.4.1	BlackMagic II	125
C.4.1.1	DC-PECVD	126
C.4.1.2	APCVD	128
C.4.1.3	HF-PECVD	130
C.4.2	NanoLab	131
C.4.2.1	HF-PECVD	133
C.4.2.2	Thermal CVD	138
D	Matlab files	143
D.1	SWNT simulations	143
D.2	MWNT simulations	143
D.3	Raman analysis	144
	References	146
	List of Figures	157
	List of Tables	159
	List of Abbreviations	161

Chapter 1

Introduction

1.1 The interconnect era

Since the discovery of the transistor (1947) and a decade later the integrated circuit (IC, also called die or chip) the microelectronic industry evolved rapidly. Nowadays a world without integrated electronics would be unthinkable. Almost every electrical device contains multiple ICs. Mobile phones, high speed computers and the internet wouldn't have existed if it wasn't for cheap ICs. ICs become more powerful, smaller, energy efficient and cheaper every year, which is a direct effect of Moore's Law.

In 1965 Gordon E. Moore (co-founder of Intel) first observed a trend in the microelectronics industry which is now known as Moore's law. The law states that every two year the amount of transistors on an integrated circuit will double (see figure 1.1). Even after forty years this law still holds. It changed, however, from an observation to a goal of the industry and became a self-fulfilling prophecy [1]. High end microprocessors now contain over one billion (10^9) of transistors (figure 1.1). A truly staggering number, especially if one takes into account that these ICs are only several square centimetres big.

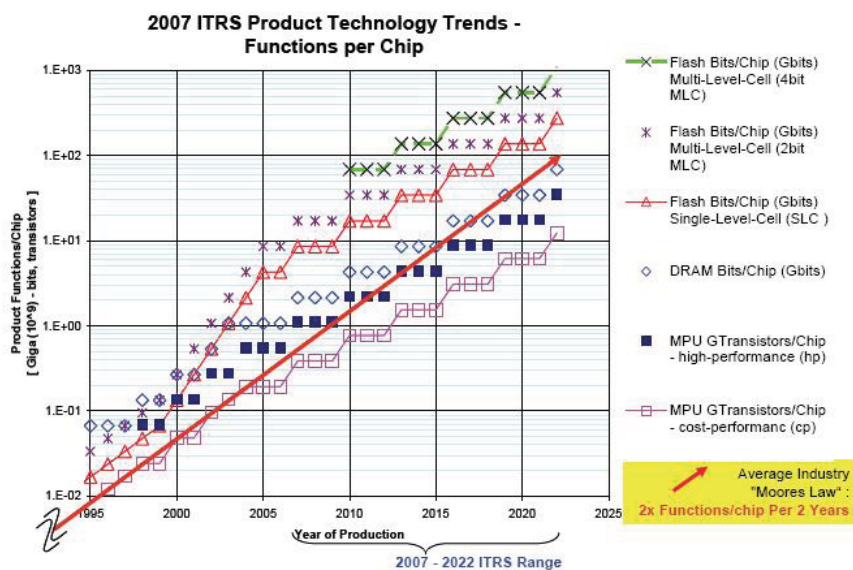


Figure 1.1: Moore's Law, from [2]

But not only the amount of transistors increased, also the speed increased, while the power consumption for an individual transistor decreased. The main driving force for this is the reduction of the size of the transistors, which makes them cheaper to produce. The fact that the speed actually increases is a convenient side effect. At the moment of writing the 45 nm technology node is in industrial production and the first 32 nm experimental chips are being processed. This means that the smallest features on a chip are about a thousand times smaller than a human hair.

However, the decrease in feature size and increase in the amount of transistors creates several difficulties. For instance the small size demands very expensive and sophisticated lithography processing. Beside that the energy density of the chip increased due to a larger amount of transistors. The amount of interconnects to connect all the transistors also increased dramatically. For instance, the ITRS roadmap update of 2008 [2] predicts an high-end IC interconnect length of 2000 m/cm² for 2009, against a length of 1712 m/cm² in 2008! The amount of metal levels is estimated to be 12. In the future these numbers will only get larger.

In the past the delay in transistors (logic delay) was much bigger than the delay in the interconnects caused by charging the parasitic capacitances (RC-delay, R being the line resistance and C the capacitance). However, while the delay in transistors decreased due to channel size reduction, the delay per unit length of interconnects increased quadratically. The cause of this is the simultaneous reduction of both the interconnect height and width for smaller technology nodes [3, 4].

Beside scaling issues, scattering and grain boundaries effects will dramatically increase the resistivity of the, often copper, wires for small interconnects with dimensions of several tens of nm [5, 6]. Power consumption in the interconnects will rise for decreasing feature sizes [4], which will also have an impact on the lifetime of these interconnects due to electromigration [5].

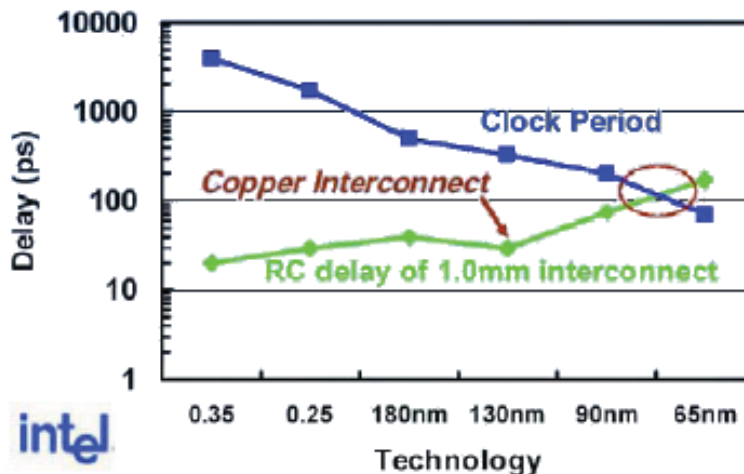


Figure 1.2: Interconnect RC delay vs. clock cycle (logic delay), source: Intel

Thus interconnects are becoming more important in realizing smaller circuits. Already the interconnect delay dominates over the logic delay, especially for the long global interconnects [5], see also figure 1.2. Even if we had a superconducting interconnect material the delay would be larger than that of a 10 nm transistor, due to the long time of flight [4]. Furthermore, they are the major source of power consumption, and contribute up to 70% of the total capacitance [7].

1.2 Improving interconnect performance

Different solutions have been suggested to improve interconnect performance. One solution suggest changing to optical lines (especially for clock distribution which is the biggest power consumer and most critical to be evenly distributed over the die [4]). Although losses over the optical line would be minimal, conversion of the electrical signal to an optical one imposes major delay problems (with delays equal to many hundreds of μm of Cu line). Beside the large conversion delay incorporating the III-V semiconductors needed for the optics into the Si process will pose to be a big challenge. [3, 8]

Another solution is the use of RF interconnects (antennas) in digital electronics, again primarily for clock distribution. However, the minimum distance required for those antennas would be the same as the actual die size, making them unattractive for use on a single die. RF distribution might be interesting for die to die communication, though [8].

A different technology from the field of RF analog electronics to solve interconnect issues would be the use of transmission lines. The use of wide flat lines would reduce the influence of the resistance and make propagation time flight dependent (LC-lines). However, due the large size of the transmission lines this would result in a low bandwidth density, increasing the die footprint or number of interconnect layers [3]. The same is true when for interconnects with dimensions from previous nodes are used in future ones. While for some global interconnects this might be beneficial, for the intermediate interconnects the loss in bandwidth density will make them unattractive [3].

Carbon nanotubes based interconnects have also been proposed. They have the potential to outperform current materials in future nodes where the resistance of metals rises rapidly due to the small dimensions [3, 8]. However, the biggest challenge so far remains the horizontal growth of CNTs, which still poses a major yield problem [9].

The most promising solution to lower the delay of interconnects which receives much attention is 3D integration [3]. With this the usage of the third dimension for device layers is denoted, instead of using only the direct surface of a wafer. One of the major research goals mentioned in the ITRS 2008 roadmap update is 3D integration [2]. This 3D integration also introduces another dimension in which the interconnects can be routed, resulting in shorter lines and hence lower delays [4, 5, 10], and a reduction of power consumption [10, 11].

But not only a reduction of power consumption and increase in speed is a feature of 3D ICs, of course 3D integration also allows more transistors in the same chip area. Even more interesting: it also allows the integration of different processes into one single die. For instance combining memory and micro controllers or pixels and read-out electronics. This can lead to fully integrated Systems on Chip (SoC) and System in Package (SiP) [12]. In other words 3D ICs fit nicely in both the “More Moore” and “Moore than Moore” concepts introduced in the 2005 roadmap from ITRS, see also figure 1.3.

1.3 Carbon nanotubes in 3D ICs

Before 3D ICs can be fully exploited some challenges have to be solved [8, 10]. Current challenges are the creation of device layers on top of each other (in case of production of 3D ICs on a single wafer) or stacking of multiple wafers (which need wafer thinning, good alignment and bonding). A big problem is heat transfer. This is because the surface area of the chip decreases while the transistor density increases. Another challenge is

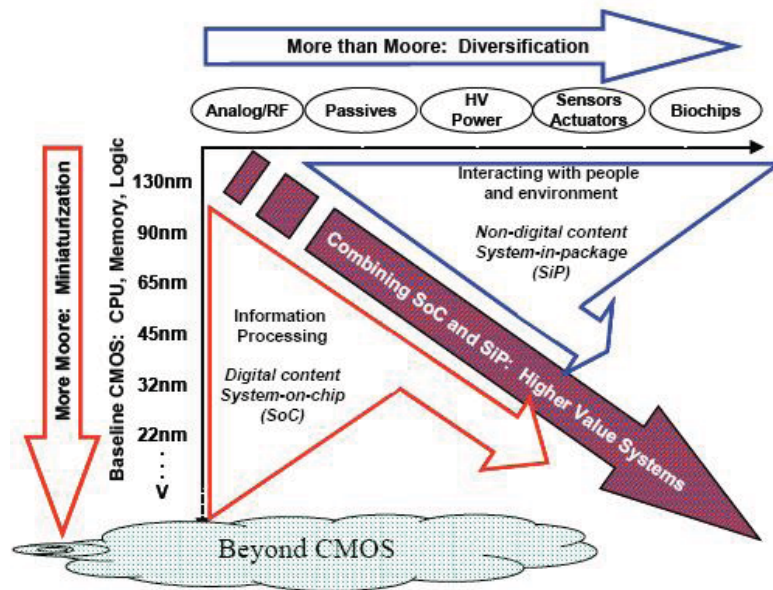


Figure 1.3: Trends in chip design, from [2]

the creation of high aspect ratio (HAR) low resistance vertical interconnects (vias), even between multiple transistor levels, without consuming too much area.

For the creation of HAR vias and thermal management, carbon nanotubes (CNTs) could be an excellent option [13]. As will be explained in chapter 2, CNTs have extraordinary properties that make them very interesting for future electronic devices. First of all a single nanotube can have a diameter of just a few nanometres, but a length of micro- or even millimetres (thus giving an aspect ratio of thousands to millions). They exhibit ballistic electron transport at μm scale, which implies that the resistance ideally doesn't depend on the length of the nanotube. They further have high current carrying capabilities (up to three orders of magnitude higher than metals).

Besides interesting electrical properties, CNTs also have interesting thermal and mechanical properties. In theory they can conduct heat parallel to their tube axis better than copper. This property could be very useful for thermal management. Finally, they are the strongest and stiffest material presently known in terms of elastic modulus (Young's modulus) and tensile strength [14].

Especially the ballistic conduction and current carrying properties have created much interest in CNTs for interconnect applications in current 2D ICs, especially to replace copper vias [5, 15–18] but also for local [7, 19, 20] and global interconnects [7, 21, 22]. As can be seen especially vias have much attention. The main reasons often stated in the mentioned papers is the fact that vias are most prone for electro migration at high current densities. But another, probably even more important, reason is that so far only vertical growth on substrates has been successful in achieving the required yield [9]. In theory the resistance of a densely packed bundle of CNTs could be lower than traditional metals especially for small feature sizes where grain boundaries increase the resistance of metals [21, 23].

However, there has been less interest in CNT vias for 3D IC's, although the long ballistic transport and high aspect ratio could be really promising for those vias as their length tends to be quite long (from many hundreds of nanometres up to tens of micrometres (or even hundreds for through wafer interconnects)). Only minor research

on through-wafer interconnects has so far been published [24,25]. Another argument for CNTs in 3D IC's would be thermal management. As 3D ICs have less surface area and transistor are packed more close together the need for good thermal management inside the chip is mandatory.

1.4 Goals

In this thesis the application of CNTs as vertical interconnects for 3D ICs is investigated. To be compatible with 3D IC's a restraint has to be placed on the growth temperature of the CNTs. To prevent further distribution of doping atoms implanted in the device layers the temperature should be below 500-600 °C. As we use Al for the metallisation in our cleanroom, which has an eutectic melting point with Si at 577 °C, we can set the upper limit to be 550 °C.

The *goal* of this research is to realize CNT deposition below 550 °C and investigate the structural and electrical properties. All with the purpose to in the end use these CNTs as vertical interconnects in 3D integrated circuits. The main questions to be answered during the research are the following:

1. *Can carbon nanotubes be an effective replacement of metal vertical interconnects for 3D ICs?*
2. *What kind of process should be used to create vertical interconnects with carbon nanotubes?*
3. *How should low temperature, high density, carbon nanotubes be grown?*
4. *How can we investigate the structural and electrical properties?*

The structure of this report is as follows. In chapter two an introduction to carbon nanotubes will be given, discussing the structural, electrical and thermal properties. Chapter three is about the different techniques to grow nanotubes, the techniques most suitable for our application will be selected and further described. We will discuss the current growth models and investigate how the properties of CNTs can be influenced with the process parameters.

In chapter four an electric model is derived for both single as multi-walled CNT bundles and used in simulations to compare these CNT bundles with bulk Cu and Al. Chapter five is about which processes can be used to create the interconnect measurement structures in the DIMES cleanroom. Chapter six discusses the results of various growth experiments performed on different equipment. The results are investigated using scanning electron microscope (SEM), transmission electron microscopy (TEM) and Raman spectroscopy. After this a conclusion will be drawn and recommendations for future research will be given.

Chapter 2

Properties of carbon nanotubes

In this chapter first a short introduction into carbon nanotubes and their structure will be given (section 2.1). After this the electrical (2.2) and thermal (2.3) properties of CNTs will be investigated and compared with those of metals.

2.1 Structural properties

Since their discovery in 1991 by Sumio Iijima [26] (although there is evidence that he was actually not the first to discover them [27]) there has been a lot of research on the properties and growth of CNTs. However, even to date not all mechanisms are yet fully understood, mainly due to the fact that observing the properties of CNTs on nanometre scale is quite complicated and theories for this scale are not yet fully developed. In this section the basic properties and structure of carbon nanotubes will be discussed. The section is mainly based on information from the first chapter of the book ‘Carbon Nanotubes: Science and Applications’ edited by M. Meyyappan [28] and appendix I of the book ‘Electrical Properties of Materials, 7nd Edition’ by L. Solymar and D. Walsh [29].

2.1.1 Carbon nanotubes

As their name suggests CNTs are extremely thin tubes made from carbon. The element carbon (C) has an atom number of 6, and thus six electrons orbit the nucleus. Two of these electrons fill the 1s electron orbital, while the other four are in the outer 2s and 2p orbitals, and function as valence electrons.

Carbon has the ability to form different types of covalent bonds, depending on how the 2s and 2p orbitals are arranged. In case of sp^3 hybridisation one of the 2s electrons is ‘promoted’ to an 2p electron. The remaining 2s electron and the three 2p electrons (hence the name sp^3) form four equally spaced orbits, which can form strong so-called σ -bonds. Carbon in this configuration can form diamond when bonding with other carbon atoms. Combined with hydrogen this type of bonding also leads to alkane hydrocarbons as methane and ethane. In this type of bonding all electrons are tightly bonded, and the material will be an electrical insulator.

Another possibility is sp^2 hybridisation, in which one 2s and two 2p orbitals form three sp^2 orbitals, which are able to form in-plane σ -bonds, while the remaining valence electron can form a weak out-of-plane (still covalent) π -bond. When bonding with other carbon atoms this will result in graphene, which is a single-atom thick sheet and has a honeycomb or hexagonal lattice. Multiple layers of graphene stacked on top of each other

will form the well known graphite. When bonding with hydrogen this will lead to alkenes (for instance ethylene). The in-plane σ -bond strength in sp^2 hybridisation is stronger than that of sp^3 , thus graphene is in-plane stronger than diamond. The out-of-plane π -bond is weak, making materials with this type of bonding electrical conductors.

To complete the picture the last, not surprisingly called sp hybridisation, arrangement will be treated. In this case, one $2s$ and one $2p$ orbital form two sp orbitals. This enables thus two σ -bonds and two π -bonds. This can form carbyne and together with hydrogen alkynes like acetylene. Again the π -bonds can be used for electrical conduction.

A CNT can be thought of as a seamless rolled up sheet of graphene. The crystal lattice of a nanotube is thus also a hexagonal (or honeycomb) lattice with on each corner a carbon atom. The bonding is almost the same as the sp^2 hybridisation. However, due to the curvature of the tube shell the hybridization is slightly altered, especially for tubes with a small diameter. The three σ -bonds are slightly out-of-plane and the π -bond is more delocalized to compensate this. Due to this the σ -bonds are stronger than those in graphite and the π -bonds are more loose, allowing better electric conduction.

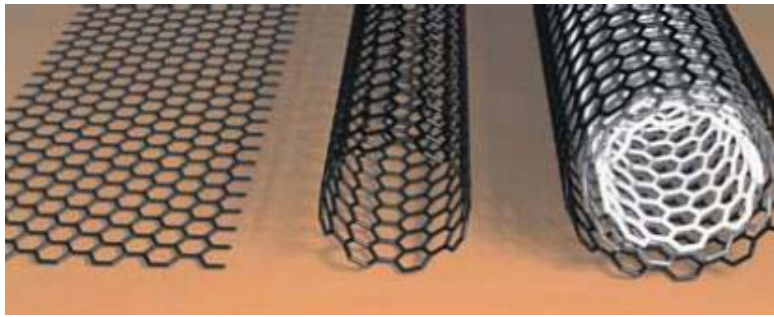


Figure 2.1: Graphene sheet, SWNT and MWNT

It is possible to create a nanotube with multiple walls, such a tube is called a multi-walled nanotube (MWNT). The spacing between the tube layers is normally around 0.34 nanometre, which is close to the spacing between graphite planes (0.334 nm). A tube with only one wall is called a single-walled nanotube (SWNT), see also figure 2.1 for an overview. MWNT with only 2 walls are often called double-walled nanotubes (DWNT).

Diameters of SWNT are often somewhere between 0.6 and 3 nanometre, the smallest tube reported being 3 Å [30]. Small diameter (< 0.6 nm) tubes are unstable due to the high curvature of the graphene sheet. Because of their small diameter and, often large length, SWNT can be seen as 1D materials. Multi-walled nanotubes are typically between 3-50 nanometre in diameter, but also tubes larger than 100 nanometre have been grown [31]. MWNT are normally not regarded as 1D materials, and also behave less like 1D materials and more like in-plane graphite due to their larger diameter. As will be shown in section 2.2 the diameter of the carbon nanotube will have influence on their electrical properties, so good diameter control is important.

Beside the diameter also the chirality of the nanotube influences its properties. The chirality can be seen as the way the graphene plane is folded to create the tube and is represented by a pair of indices (n, m) which is called the chiral vector (figure 2.2). By definition $n > m \geq 0$. The chiral vector is defined as $\vec{C}_h = n\vec{a}_1 + m\vec{a}_2$ where \vec{a}_1 and \vec{a}_2 are the unit vectors of the hexagonal crystal lattice of the graphene sheet. A chiral angle can be defined between the $(n, 0)$ and (n, m) vectors as:

$$\theta = \arctan(\sqrt{3}n/(m + 2n)) [^\circ] \quad (2.1)$$

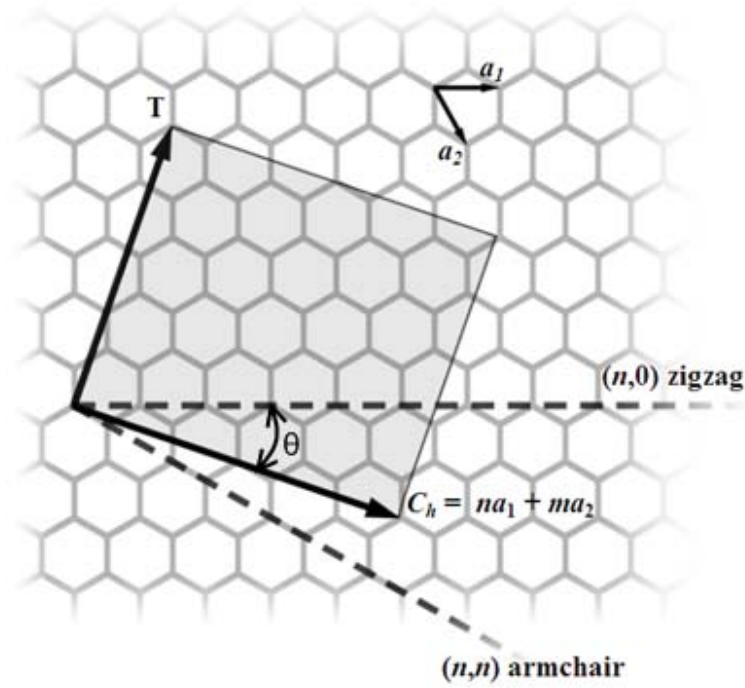


Figure 2.2: Chiral vector and chiral type naming

The chiral indexes also have a relation with the diameter of the nanotube, which is given by the following equation:

$$d = |\vec{C}_h|/\pi = a\sqrt{n^2 + nm + m^2}/\pi \text{ [nm]} \quad (2.2)$$

In which $a = |\vec{a}_1| = |\vec{a}_2| = 2.46 \text{ \AA}$ is the lattice constant (and $a_{cc} = a/\sqrt{3} = 1.42 \text{ \AA}$ is the C-C bond length). Tubes with a chiral index in which $m = 0$ ($\theta = 0^\circ$) are called zigzag, while tubes with $n = m$ ($\theta = 30^\circ$) are called armchair. All other tubes are simply called chiral ($0^\circ < \theta < 30^\circ$). MWNT normally consist of walls with different chirality.

When created CNTs can stick together forming bundles of SWNT and/or MWNT with different diameter and chirality. The driving force behind this are the Van der Waals interactions between the tubes [32,33]. These bundles can contain tens to hundreds of separate tubes ideally forming a triangular tight packing lattice.

2.1.2 Carbon nanofibres

Beside CNTs an other, often encountered structure, are carbon nanofibres (CNFs). The difference between a CNT and CNF is that in the first case the graphite planes are parallel to the tube axes, while in case of the latter they're not (see figure 2.3). The angle between the graphite planes and tube axis can be as large as 90° , forming a graphite filament (carbon nanofilament, confusingly often abbreviated as CNF). However, normally the angle is somewhere between a few and tens of degrees and there still exist a hollow core. In case of a smaller angle often some graphite planes cross the entire tube diameter, giving the tube a bamboo-like, herringbone or arrowhead structure, which still can be regarded as a CNT when it has complete graphite planes parallel to the axes.

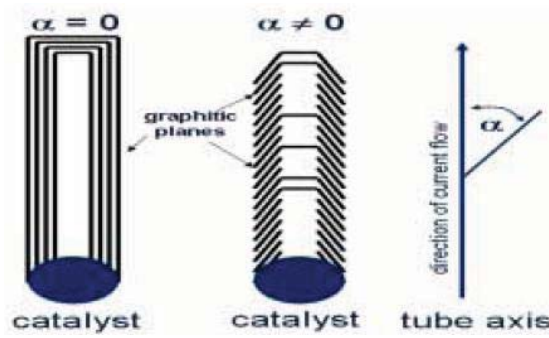


Figure 2.3: The definition of carbon nanotubes (left) and nanofibres (centre), from [34]

2.2 Electrical properties

In this section the electrical properties of CNTs are discussed. First some physical background on the band structure of CNTs will be given. This is followed by the resistance of CNTs where a model of the resistance vs. tube geometry will be presented. After this the capacitance and inductance of CNTs will be treated shortly. Lastly the electrical stability of CNTs will be discussed. For the first part of this section and the following subsection the fourth chapter of the book ‘Carbon Nanotubes: Properties and Applications’ edited by Michael J. O’Connell has been used as reference [35].

The electrical properties of CNTs depend on their chirality and diameter, and in case of MWNT on the amount of walls. First of all, nanotubes can exhibit metallic or semiconducting behaviour depending on their chirality and diameter. That metallic behaviour can be observed in tubes with a diameter of just a few nanometre is quite unusual. Most one-dimensional configurations of materials that normally (in 3D) exhibit metallic behaviour re-arrange their atoms in a 1D configuration in such a way that makes them semiconducting [36]. This effect is called Peierls distortion or instability. In the case of CNTs, however, such an atomic re-arrangement is not favourable as the energy needed to do this is quite high (due to the strong σ -bonds) while the energy gained is small.

The band structure of a carbon nanotube depends on its chirality. All armchair (n, n) are metallic, and have a band structure where two bands cross the Fermi level (E_F), see also figure 2.4a. A (n, m) SWNT is metallic if $n - m = 3i$ in which i is a non-zero integer. Although a very tiny bandgap of several meV exists in these tubes, it can be neglected at room temperature. In all other cases the CNT is semiconducting, with no bands crossing the Fermi level, as can be seen in figure 2.4b. For an uniform distribution of the indexes (n, m) this would imply that one-third of the SWNT will be metallic and therefore two-third semiconducting.

In case the nanotube is semiconducting the bandgap (E_g) is given by equation 2.3 [28], in which a_{cc} is the C-C bond length (0.142 nm) d is the diameter of the tube in nm and γ_0 the so-called C-C hopping constant which is 2.5-3.2 eV. As can be seen the bandgap is inversely proportional to the diameter. Wide tubes will thus exhibit (semi-)metallic behaviour at room temperature due to a very small bandgap which can be overcome by the thermal energy of the electrons [7].

$$E_g = \frac{2a_{cc}\gamma_0}{d} \approx \frac{0.84}{d [\text{nm}]} [\text{eV}] \quad (2.3)$$

Multi-walled nanotubes, due to their larger diameter, almost always show metallic

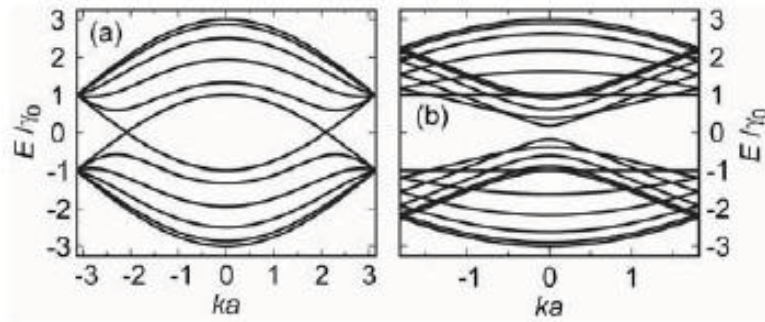


Figure 2.4: Band structure of a) (5,5) metallic CNT and b) (10,0) semiconducting CNT. In this figure ‘a’ is the lattice constant and ‘ γ_0 ’ the so-called C-C lattice hopping constant in graphene, from [35]

behaviour [28]. Theoretical work done by Saito et al. [37] already predicted that a MWNT with only one metallic wall will behave metallic, which is confirmed by Tison et al. [38]. However, they, and other groups, found that small diameter double walled nanotubes consisting of semiconducting walls can also behave metallic. The mechanism behind this is the interaction between the walls of the tubes, which can alter the bandgap. Thus, it is generally more difficult to accurately predict the behaviour of a MWNT, especially when the diameter is small and they consist of only a few walls. It must be noted that although the entire tube might show metallic behaviour, this doesn’t imply that all walls are in fact metallic.

2.2.1 Electrical resistance

As mentioned in chapter 1 metallic CNTs exhibited so-called ballistic transport. In metals electrons travelling through the material are slowed down due to collision with the crystal lattice and other electrons (a process called scattering). The average distance which can be travelled by the electron before scattering occurs is called the mean free path (MFP). This mechanism leads in the end to Ohm’s law, $J = \sigma E$ (where J is the current density, σ the electrical conductivity and E the electric field) or $I = U/R$ (where I is the current, U the potential and R the resistance), and a resistance that depends on the length and cross sectional area of the conductor ($R = l\rho/A$, l being the length, $\rho = 1/\sigma$ the resistivity and A the area). For a derivation of Ohm’s law the reader is referred to the book of L. Solymar and D. Walsh [29].

In case of ballistic transport the travelling electron does not scatter with the lattice as the MFP is larger than the length of the conductor. This can happen in any conductor when its length is short enough (e.g. for copper the length should be less than 40 nm). In case of ballistic transport the resistance is only a function of the number of available conduction channels and the transmission quality of the contacts (which is ideally equal to 1, for no reflection at the contacts).

While metals often have a very short MFP, CNTs have been shown to have a MFP of several hundreds nm up to a couple of micron at room temperature, depending on the tube quality (i.e. the amount of defects) [35, 39, 40]. Due to the 1D nature of CNTs the direction in which electrons can scatter is very limited, ideally only backwards scattering can occur. For high quality CNTs the probability for such a scatter event will be low. A ballistic length of a staggering 25 μm has even been reported [41].

Although there might be ballistic transport the nanotube will still have a non-zero

resistance. This is due to the limited number of available conduction channels, and the less than ideal contact to the tube endings.

A single conduction channel accepting only electrons with one type of spin has an universal quantum (or contact) resistance of $R_Q = h/e^2 \approx 25.9 \text{ k}\Omega$ ($G_Q = 1/R_Q \approx 38.6 \text{ }\mu\text{S}$) if there is no scattering in the material and at the contacts. Here $h = 6.626 \cdot 10^{-34} \text{ J s}$ is the Planck constant and $e = 1.602 \cdot 10^{-19} \text{ C}$ the electron charge. This resistance originates from the mismatch which exist between the large number of modes available in the macroscopic contacts and the few modes available in a 1D conductor. If one adds the amount of available channels (M) and the reflection probability, which is a function of the Fermi energy, ($T_i(E_F)$) a simple form of the Landauer Formula is obtained (equation 2.4).

$$G = \frac{e^2}{h} M T_i(E_F) \quad (2.4)$$

2.2.1.1 Resistance of single-walled nanotubes

As can be seen in figure 2.4a a metallic SWNT has four bands that cross the Fermi level ($E = 0$ in the figure). Two of these bands are carrying right moving electrons, the other two left movers. Each band is so-called spin-degenerate which mean it can transport a spin-up and spin-down electron. Thus there are in total four channels available in each direction ($M = 4$). This gives a resistance for a SWNT with ideal contacts of $R_Q/4$ as given in equation 2.5. This resistance will exists at the contacts, instead of the full length [42]. Hence the name contact resistance is also used for the quantum resistance. This also means that Joule heating occurs at the contacts and not across the length in case of fully ballistic tubes [42].

$$R_{Metallic,SWNT} = \frac{R_Q}{4} = \frac{h}{4e^2} = 6.45 \text{ k}\Omega \quad (2.5)$$

It must be noted that ballistic transport doesn't imply that there is no scattering at all. Scattering is a probabilistic phenomena, which still occurs if the length of the conductor is less than the MFP. However, the chance that a scattering event occurs is quite low, thus the majority of the electrons being transported will not be scattered and as such it can be called ballistic transport on a macroscopic scale.

Semiconducting SWNT don't have any conduction channels available as no bands cross the Fermi level and thus a bandgap exists with a width given by equation 2.3. This bandgap is inversely proportional to the diameter, which means that thick tubes will conduct at room temperature.

While semiconducting tubes become metallic when the diameter increases, for metallic tubes more and more bands will cross the Fermi level, increasing M . Beside chirality the resistance is thus also dependent on the diameter and temperature. The latter because at higher temperature electrons are able to cross a larger bandgap and the MFP depends on temperature.

To model the dependency of the resistance on diameter Naeemi derived a model for the number of conductive shells available vs. diameter, taking into account that only 1/3 of the tubes are metallic [7, 43]. The number of conductive channels vs. the diameter is plotted in figure 2.5. The simplified model for the average number of conductive channels per wall against diameter (d) and temperature (T) is given by equation 2.6, where $a = 2.04 \cdot 10^4 \text{ nm}^{-1}\text{K}^{-1}$, $b = 0.425$ and $d_T = 1300 \text{ nmK}$.

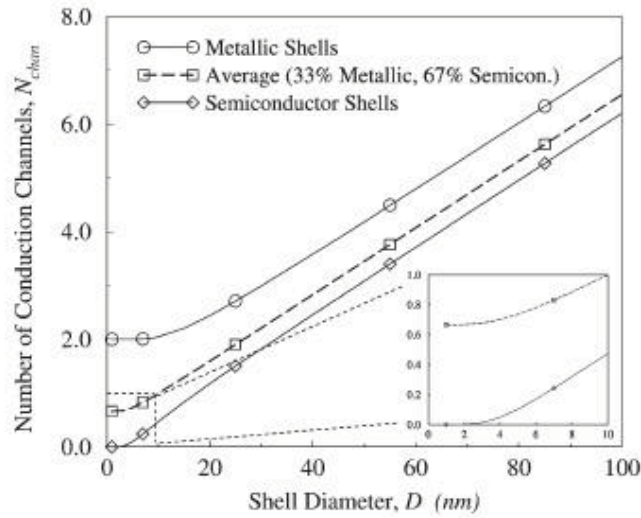


Figure 2.5: Number of conductive channels per wall vs. diameter ($T = 300$ K), from [43]

$$\begin{aligned}
 N_{chan}(d, T) &\approx aTd + b, & d > d_T/T \\
 &\approx 2/3, & d < d_T/T
 \end{aligned}
 \tag{2.6}$$

Beside for a single SWNT this model can also be used for bundles of SWNT. Generally the interaction between different tubes seems to be weak. Although tunnelling between tubes is possible, intra-tube transport dominates the electric conductance [39]. In case of weak interaction the ideal total SWNT bundle resistance will be the resistance for each spin-degenerate channel ($R_0 \approx 12.9$ k Ω) divided by amount of conductive channels in the entire bundle. Which for an uniform diameter for all the tubes in the bundle is the number of tubes times the number of conductive channels N_{chan} .

Unfortunately the reality is more complex. In realistic tubes there will be defect and phonon scattering. At higher temperature or under high bias these effects can become quite important [7, 44, 45]. Of course interconnects using CNTs can also be longer than their MFP. There are various models to incorporate these effects (see previous references). Here the model from Pop et al. [44] will be discussed as it maintains simplicity while taking into account all important scattering effects.

Ideally scattering will mainly be due to phonon scattering as the mean free path of defect scattering is larger than that of the phonon scattering mechanisms for high quality tubes [7]. The two important scattering principles are acoustic phonon (AP) and optical phonon (OP) scattering (for more information about phonons, see appendix A). The latter can be both due to emission or absorption of an OP.

For a metallic SWNT the resistance taking into account scattering is given by equation 2.7. This resistance multiplied by two is the resistance per conductive channel, assuming that the MFP of the scattering mechanisms is the same for each channel.

$$R(U, T) = \frac{h}{4e^2} \left(\frac{l + \lambda_{eff}(U, T)}{\lambda_{eff}(U, T)} \right)
 \tag{2.7}$$

Here l is the length of the tube and λ_{eff} the effective mean free path given by equation 2.8. In this λ_{AC} is the MFP due to acoustic phonons, $\lambda_{OP,ems}$ the MFP by optical

phonon emission and $\lambda_{OP,abs}$ by optical phonon absorption.

$$\lambda_{eff}(U, T) = \frac{1}{\lambda_{AC}^{-1}(T) + \lambda_{OP,ems}^{-1}(U, T) + \lambda_{OP,abs}^{-1}(T)} \quad (2.8)$$

The individual mean free paths of the phonon scattering are dependent on temperature (T) and in case of OP emission also on the electrical field and therefore potential (U). The derivation of their lengths is beyond the scope of this text (the interested reader is referred to [44] and its references). Only the results will be shown, which for low bias are shown in figure 2.6. Although these results are for low bias it has been shown that for long nanotubes or bundles with enough parallel tubes the resistance will not increase significantly under high bias [46], enabling us to use the same model in those situations.

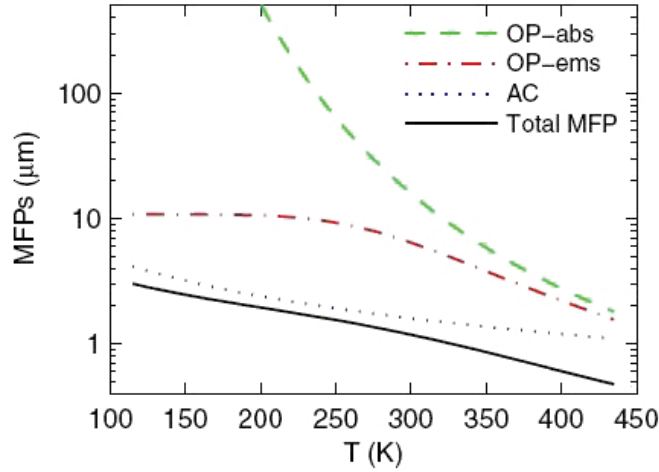


Figure 2.6: Different MFP vs. temperature for low bias, from [44]

As can be seen in figure 2.6 at higher temperatures the OP MFP starts to dominate the total MFP. This means that according to this model the total resistance will increase for higher temperatures. However, the model doesn't take into account that at higher temperature more conductive bands become available, decreasing the resistance. From experiments it appears that the latter dominates [47–49].

As mentioned before scattering caused by defects has also an influence on the MFP. Simulations have shown that vacancies can reduce the conductance of small CNTs with 50%, while bigger diameter tubes are less influenced (e.g. 25% for a 25 nm wide tube) [50]. If the defects locally change the structure from four hexagons to two pentagons and two heptagons (a so called Stone-Wales defect) simulations show that the conductance is hardly affected [51].

Beside defects, tube bending can also influence the resistance. While slight bending hardly changes the conductance, kinks induce strong backscattering. Twisting a tube can even introduce a large bandgap in metallic tubes [51]. Unfortunately measuring the effect of defects and structural deformations on tubes is difficult, as control over defect densities and deformations is not established. It is, however, safe to conclude that it is best to avoid defects and structural deformations as much as possible to get an optimum conductance.

2.2.1.2 Resistance of multi-walled nanotubes

For MWNTs the situation is more complex as they consist of multiple walls, which may influence each other due to the close spacing. Early results by Frank et al. reported that only the outer wall will contribute to conduction [42] but with only one G_0 (which is the conductance of a single channel, thus $G_Q/2$), and that even a conduction of $0.5G_0$ is possible. Other results stated that only metallic walls may conduct [52], but possibly again only with one conductive channel per wall instead of the two for SWNT [53].

More recent experiments show that the resistance of single [53,54] or bundled [55–57] MWNTs can be lower than that of an ideal metallic SWNT (bundle), indicating that more than one wall contributes to conduction. The results of Frank et al. can be explained by considering that only one wall made contact with the gold electrode, while interwall interaction can block conductive channels [58]. Li et al. [41] reported a MWNT with a conductance of 460 times G_0 at zero bias, which means a resistance of 34.4Ω , for a single large diameter MWNT. This shows that for a well contacted tube many shells can contribute to the electrical conductance. These findings are supported by simulations by Yan et al. [59].

Naeemi et al. derived a physical model for the conduction of MWNT [43]. This model is basically the same as equation 2.6 in which the amount of conductive channels is taken over all the walls of the MWNT with their respective diameters. The total number of conducting channels is then multiplied with the resistance of each channel (for which Naeemi et al. uses a slightly more complex model than that from Pop et al. discussed before, in which the MFP is also proportional to the diameter). The total model will again not be treated and can be found in the reference, however, in figure 2.7 the results are shown. For small MWNT length the conductivity decreases for increasing diameter, whereas for long length it increases with diameter according to the model of Naeemi et al.

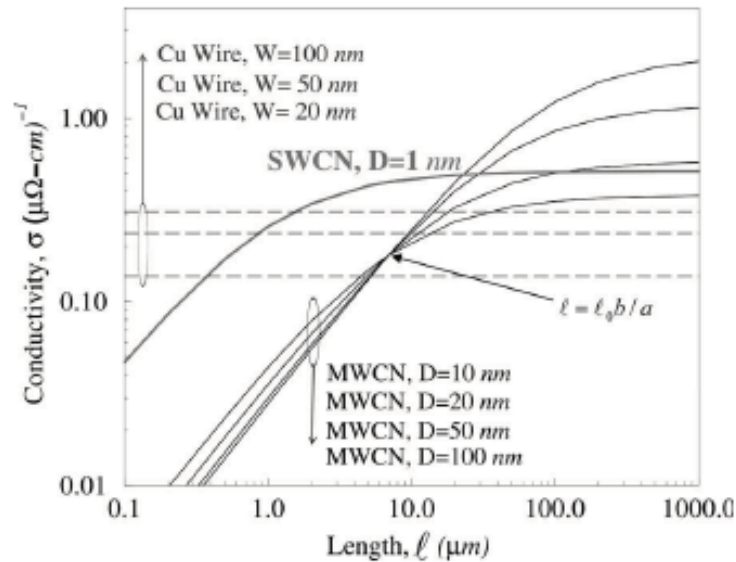


Figure 2.7: Conductivity of various diameter MWNT compared with SWNT and copper with different dimensions (including small size scattering effects), from [43]

2.2.1.3 Carbon nanofibres

In case of a CNF, with no complete tube walls, there will be no ballistic transport over the length of the nanotube, due to the high disorder in graphite planes [60]. Zhang et al. [61] report measurement of the I-V characteristics of CNF, which appear to be linear like normal metal conductors. Thus CNFs appear to behave metallic. The resistance of such fibres depends on the angle α mentioned in figure 2.3, and is between the resistance of graphite parallel to the plane and perpendicular to the plane. Zhang et al. presented an equation for the resistivity of a CNF, which is repeated here in equation 2.9, where $\rho_a = 4 \cdot 10^{-5} \Omega\text{cm}$ is the resistivity parallel to the graphite plane and $\rho_c = 4 \cdot 10^{-2} \Omega\text{cm}$ is the resistivity perpendicular to the graphite plane.

$$\rho(\alpha) = \rho_a \cos^2 \alpha + \rho_c \sin^2 \alpha \text{ } [\Omega\text{cm}] \quad (2.9)$$

2.2.1.4 Contact resistance

In the previous sections it was assumed that the interface between the nanotube and the environment was ideal with a transmission of 1. In reality this is, however, not the case, and the transmission will be (much) lower than one. This can be modelled as a contact resistance between the metal and the CNT (not to be confused with the other name of the quantum resistance).

In early reports this resistance was quite high (up to several $\text{M}\Omega$). However recently the resistance was reduced [56,62] to values below $\text{k}\Omega$ s. For this reduction often titanium is used, which forms titanium carbide (TiC) which aids in the formation of a good contact [55,63,64]. It is also suggested that other metals that can form carbides (e.g. tungsten, molybdenum and tantalum) are useful as contact material for nanotubes [65].

Javey et al. state that the work function of the metal and the contact area have influence on the contact resistance by influencing the Schottky Barrier (SB) [66]. They found that palladium, which has a high work function can be used to obtain a good contact to the valence band of a semiconducting SWNT. Other high work function metals (i.e. Pt or Au) failed in achieving a low contact resistance, presumably because Pd forms a better contact with the CNT [66,67]. Numerous other publications found that Pd can also be used to lower the contact resistance of metallic CNTs [34,68,69].

Some manufacturing techniques have been shown to improve the contact resistance to CNTs. Rapid Thermal Annealing (RTA) has been shown to aid in the formation of a good contact, probably by aiding TiC formation [64]. Second, Chemical Mechanical Polishing (CMP) has been used to remove the caps of the CNTs which aids in enhancing the conduction [57].

2.2.2 Capacitance and inductance

A nanotube not only has a quantum resistance, but also a quantum capacitance and kinetic inductance caused by the low dimensionality of the system and the limited charge carriers and states. Burke [70,71] gives a straightforward derivation for both, which will be shortly treated here.

A SWNT can be seen as a 1 dimensional quantized electron gas consisting of four non spin-degenerate parallel channels. The Pauli exclusion principle states that two electrons cannot occupy the same quantum state simultaneously. All quantum states till the Fermi energy (E_F) are already occupied (at low temperature), thus the electron should be added above E_F . As electrons travel at E_F through metals energy should

be added to the electron to put it in the available quantum state above E_F . For a 1D quantum wire of length L the energy difference (δ) between quantum levels is given by equation 2.10, where k is the wave number, E the energy, $v_F = 8 \cdot 10^5$ m/s, [52] the Fermi velocity, and $\hbar = h/2\pi$.

$$\delta = \frac{dE}{dk} \delta k = \hbar v_F \frac{2\pi}{L} \quad (2.10)$$

The quantum capacitance per unit length can now be calculated using equation 2.12, which is the relation between the quantum capacitance and the required energy. As the CNT consists of four parallel channels the total quantum capacitance should be four times the quantum capacitance of a single 1D wire (hence the factor four in equation 2.12).

$$\frac{e^2}{C_Q} = \delta \quad (2.11)$$

$$C_{Q,CNT} = 4 \frac{2e^2}{\hbar v_F} \quad (2.12)$$

$$C_{Q,CNT} = 400 \text{ aF}/\mu\text{m}$$

Besides a quantum capacitance a CNT also has an electrostatic capacitance. This capacitance can be calculated by setting the capacitive energy equal to the stored electrostatic energy for a wire over a ground plane, and can be found in typical textbooks about electromagnetic fields. Only the solution given in [70] will be cited, in which the distance between the nanotube and the ground plate is replaced with the length of the tube.

The electrostatic capacitance couples the four channels in a CNT. As it works on all four channels together it must not be multiplied by four. The equation for the electrostatic capacitance is given by 2.13 together with an approximation in case $l > 2d$, where l is the length of the tube, d the diameter and ϵ the permittivity. The value of this capacitance for a tube with an aspect ratio of 100 in air (e.g. 10 nm diameter and 1 μm long, $\epsilon_r = 1$) is 12 aF/ μm . Which is relative close to the quantum capacitance and can thus not be neglected.

$$C_{E,CNT} = \frac{2\pi\epsilon}{\cosh^{-1}(2l/d)} \approx \frac{2\pi\epsilon}{\ln(l/d)} \quad (2.13)$$

Due to the low density of current carriers in nanotubes there is a large kinetic energy stored in the current flow, therefore a CNT has a dominant kinetic inductance, the magnetic inductance can even be neglected as it is many order smaller [52, 70]. Again we follow the derivation of Burke [70, 71]. The kinetic energy per unit length in a 1D wire is the sum of the kinetic energies of the particles moving left and right. In case of a net current one of the particles streams dominates. If for instance the particles moving to the left dominate and their Fermi energy is raised by $e\Delta\mu/2$ (where $\Delta\mu$ is the change in mobility, which depends on the effective mass, which in turn depends on k), and the E_F of the particles moving to the right is decreased by the same amount, the net current in the 1D wire will be:

$$I = (e^2/h)\Delta\mu \quad (2.14)$$

The increase in kinetic energy is the amount of excess electrons times their added energy and is given by (δ is the same as in equation 2.10):

$$N_{exec} \Delta E_{elec} = \left(\frac{e\Delta\mu}{2\delta} \right) \left(\frac{e\Delta\mu}{2} \right) = \frac{(e\Delta\mu)^2}{4\delta} \quad (2.15)$$

Combining equation 2.14 and 2.15 and taken into account that the kinetic (or inductive) energy equals $\frac{1}{2}LI^2$ an expression for the kinetic inductance per unit length can be derived (equation 2.16). Again care has to be taken that the CNT consists of four parallel channels, and the total inductance should be divided by a factor four.

$$\begin{aligned} L_{K,CNT} &= \frac{1}{4} \frac{h}{2e^2 v_F} \\ L_{K,CNT} &= 4 \text{ nH}/\mu\text{m} \end{aligned} \quad (2.16)$$

For MWNT with perfect contacts each conducting wall simply contributes $L_{K,CNT}$ and $C_{Q,CNT}$ in parallel, therefore reducing the kinetic inductance and increasing the quantum capacitance [72, 73]. According to Rossi et al. [73] only the electrostatic of the outer wall has to be considered. This is because metallic CNTs effectively shield electrostatic fields. They also introduce a coupling capacitance between adjacent walls (the capacitance between non adjacent walls is again shielded by the walls in-between). This capacitance, C_{CM} , is derived from the coupling between two cylinders in a traditional coaxial cable (equation 2.17) with d_1 and d_2 being the diameter of the outer and inner wall under consideration. If the walls carry the same signal this capacitance can be neglected.

$$C_{CM} = \frac{2\pi\epsilon}{\ln(\frac{d_1}{d_2})} \quad (2.17)$$

2.2.3 Electrical reliability

An astonishing property of carbon nanotubes is that they can carry a very high current density without degradation or failure. The mechanism behind this are the very strong σ -bonds of the sp^2 hybridization. While metals often suffer from electromigration at current densities above $10^6 - 10^7$ A/cm², carbon nanotubes have shown no failure after long term exposure to current densities of $5 \cdot 10^8$ A/cm² at room temperature [34] and densities between $10^9 - 10^{10}$ A/cm² at elevated temperature [54].

In case of carbon nanofibres maximum current densities between $10^6 - 10^7$ A/cm² have been reported [74–76]. This indicates that the quality of the tubes has an impact on their electrical reliability. Suzuki et al. [76] also found that the resistance of the CNF has influence on the maximum allowed current density, the lower the resistance, and thus higher quality, the higher the maximum current density. They state that local heating is the driving force behind CNF breakdown.

2.3 Thermal properties

Beside being a good and reliable electrical conductor CNTs are also good thermal conductors. There has been a lot of research on the thermal properties. It is, however, quite difficult to measure these properties at such a small scale, which results in values that differ much between different measurements. Beside measurements a lot of theoretical calculations have been done on CNTs to determine their thermal properties. In these simulations there is again quite some difference between results, as different models are being used as there is yet no conclusive way to model thermal properties on the nano scale.

The result of this is that there is no consensus on the thermal transport properties of CNTs, unlike the theory for electric transport which is quite matured (at least, when compared to other fields in CNT theory). Still there is enough information available to

discuss the thermal properties (specific heat, thermal conductivity and stability) in this section. Phonons, the carriers of heat, are a less treated topic in Electrical Engineering, readers looking for some background information are invited to read appendix A.

2.3.1 Specific heat

The specific heat (symbol c) indicates the heat energy needed to increase the temperature of a unit quantity (either in gram or mol, we use the first) of a material by a certain temperature. Its unit is joule per gram-kelvin ($\text{J/g}\cdot\text{K}$). The higher the number the more energy is required to heat up the sample. Metals often have a specific heat between 0.1 and 1 $\text{J/g}\cdot\text{K}$, for instance copper has a specific heat of 0.385 $\text{J/g}\cdot\text{K}$.

The specific heat can have both an electron and phonon contribution. However, even in a metallic CNT the phonon contribution is two orders of magnitudes higher, thus phonons dominate the specific heat in CNTs [77, 78]. As the phonon contribution depends on the available phonon states, which in turn depends on the temperature of the material, the specific heat is temperature dependent.

For our application the specific heat and temperature dependent behaviour around room temperature are the most interesting. However, to get an idea how complex phonon heat transfer in CNTs actually is, very shortly the low temperature behaviour will be discussed using figure 2.8 [77].

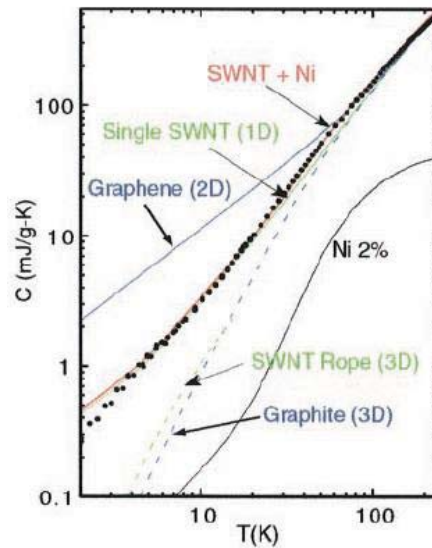


Figure 2.8: Temperature dependency of the specific heat for various systems, from [77]

First of all it can be seen from figure 2.8 that at room temperature the specific heat of CNTs (but also graphene) will be similar to that of graphite. However, at lower temperature the dependency deviates from that of graphite. This is due to the fact that the OP phonon modes start to freeze. At a temperature of ~ 5 K only the AP modes remain and SWNT show a 1D temperature behaviour with a linear temperature dependency. For MWNT or bundles of CNTs the low temperature behaviour is different due to the larger size and coupling between walls and tubes [78]. Although this 1D behaviour is extremely interesting for a physicist, we will focus on the room temperature behaviour.

As mentioned before at room temperature SWNT (and also MWNT and bundles of CNTs) act as graphite [77, 78]. The specific heat is around 0.7 J/g·K which is in the same range as that of metals. The temperature dependence is linear as more OP modes contribute when temperature increases.

The chirality appears to have no influence on the specific heat of CNT, however according to Cao et al. [79] the diameter does have an influence, even in our temperature region of interest. Very small tubes show a drop in specific heat, while large tubes saturate to a value of approximate 0.687 J/g·K. They derived the following equation for the diameter (d) dependency of the specific heat: $c = 0.687 - 0.009/d^2$ J/g·K.

2.3.2 Thermal conductivity

The thermal conductivity (symbol λ , but often also k is used) states how good a material is in conducting heat and has units of Watt per meter-Kelvin (W/m·K). The thermal conductivity of metals is typically hundreds of W/m·K. Copper, which is nowadays the mainstream interconnection material, has the second highest thermal conductance of metals (380 W/m·K, only silver conducts better).

However, carbon based materials are known to be able to conduct heat much better than metals, with diamond having a thermal conductivity of 2000-3000 W/m·K. It was expected for carbon nanotubes to have very good thermal properties. Simulations have indeed shown a thermal conductivity for a (10,10) tube of 6600 W/m·K [80]. This is roughly 2 times higher than diamond and about 17 times higher than copper! The mechanism behind this high conductivity are the strong sp^2 bonds which have good acoustic properties (high speed of sound) combined with few crystal defects, enabling long phonon diffusion lengths.

It must be noted that other publications of calculated thermal conductivities predict different values, for instance Che et al. predicted a conductivity of 2980 W/m·K [81]. Although much smaller, this value is still much higher than that of metals. These high values for the thermal conductivity are parallel to the tube axis, the thermal conductivity perpendicular to the tube is much smaller [82].

As with specific heat the thermal conductivity has both a contribution from electrons and phonons. Again the phonon contribution dominates over the electron one [83]. Therefore, only the phonon contribution will be discussed.

The phonon thermal conductivity is related to the specific heat, phonon velocity and phonon MFP by $\lambda \propto cvl$, where c is the specific heat, v the sound (or group) velocity in the material and l the phonon MFP [80, 84, 85]. At low temperature the MFP tends to be constant due to defects dominating the MFP or the fact that at very low temperatures only the AP modes remain, which have a long MFP. Thus at very low temperature the thermal conductivity follows the specific heat and has a linear thermal dependency. At higher temperature this dependency will increase to a quadratic one as OP modes start contributing [86]. At a certain point Umklapp scattering starts to dominate over the other scattering mechanism and the thermal conductivity will reach a maximum and decrease for increasing temperature (as now the phonon MFP is dominating λ).

Although there has been much research on thermal conductivity at low temperature, there are few publications about the higher temperature behaviour. Pop et al. [87] investigated a single SWNT from 300 K to 800 K and found a temperature dependency close to $1/T$, which corresponds to Umklapp scattering, see figure 2.9. The small deviation from the $1/T$ behaviour was due to the second order three-phonon scattering which give an additional $1/T^2$ dependency. The thermal conductivity at room temperature is 3500

W/m·K and 1000 W/m·K at 800 K. It must be noted that the results are based on some assumptions, but the results give a nice first impression on the high temperature behaviour. Simulations done by Grujicic et al. showed a similar behaviour, although in their case the maximum conductivity occurs at 100 K instead of 300 K [85].

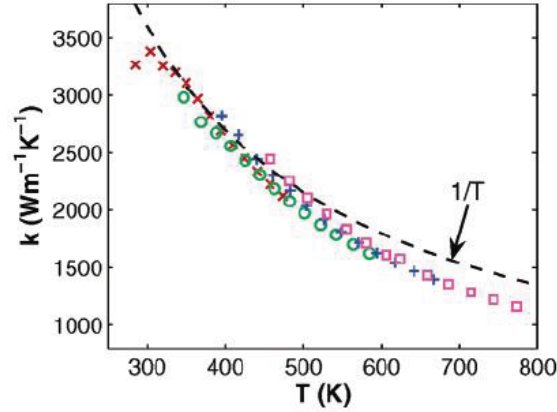


Figure 2.9: Thermal conductivity at high temperature, from [87]

Next we will look at the influence of geometric and structure effects on the thermal conductivity. In [14,86] it is stated that chirality has no influence on the low temperature thermal conductivity. For the higher temperature regime Grujicic et al. calculated that chirality may influence the thermal conductivity by 20%, however this isn't verified by experiments yet [85]. The diameter also influences the thermal conductivity, but only on low temperature [14].

The dependency of the conductivity on the amount of defects in a tube is also an important parameter, as manufactured tubes often contain them. Che et al [81] calculated the influence of vacancies and so called (5,7,7,5) or Stone-Wall defects where four hexagons are changed into two pentagons and two heptagons, which is a common defect in nanotubes. A vacancy concentration of 0.5% already changed the thermal conductivity from 2980 W/m·K to 700 W/m·K. The effect of (5,7,7,5) is less severe as it doesn't change the basic bonding mechanism. For a similar concentration of 0.5% the thermal conductivity becomes 800 W/m·K. Yamamoto et al. also mention the influence of defects and state that a vacancy concentration of 1% decreases the conductivity by 25%.

It can be concluded that defects have quite a large influence on the thermal conductivity. Therefore, CNFs have a very poor thermal conductivity, like the value of only 12 W/m·K at 300 K observed by Yu et al. [88]. Zhang et al. found that Rapid Thermal Annealing (RTA) improves the thermal conductance of CNFs by improving the quality of the tubes and the thermal contact [89]. The total improvement is up to 30%.

Last, but certainly not least, we look at the thermal conductivity of bundles of CNT. Already in the first thermal simulations it was predicted that when forming a bundle of nanotubes the conductivity would drop due to interactions between the tubes, just like in graphite which is made from stacked graphene [80].

This was also predicted for a single MWNT, although the results of Kim et al. [84] show that this is not the case, probably due to weak interactions between the walls. They also measured the conductivity of bundles with different diameter and found that it decreases when the diameter of the bundle increases, approaching a value of 250 W/m·K.

Che et al. [81] calculated the conductivity of closely packed (10,10) SWNT and found that it was 950 W/m·K along the tube axis and 5.6 W/m·K perpendicular to the axis. Both values closely correspond to that of respectively in and out-plane graphite. Xie et al. [90] calculated a much smaller room temperature thermal conductivity of 60 W/m·K for an aligned MWNT array.

As it can be seen the values differ between results, but are clearly smaller than the values for isolated tubes. The large differences between the measured and calculated values are due to different methods of measurement and assumptions used when calculating the values. But also the used samples and their quality vary greatly. As said before determining thermal properties at nano scale is quite difficult as there are no default measurement tools available and the mechanisms are not yet fully understood. More research in this area is definitely required.

2.3.3 Thermal stability

Because of their strong sp^2 bonds and the corresponding high electrical stability it was expected that CNTs would exhibit a high thermal stability. Again measuring this stability is very challenging. Measurement at high temperature are already quite challenging, and the nano scale only makes this more difficult [91]. However there have been numerous experiments and simulations regarding the thermal stability of all kinds of CNTs.

Two types of stability can be distinguished: against thermal oxidation and against thermal failure (the latter is the temperature at which a CNTs start to break up due to bond weakening). The first type is often investigated in air or oxygen atmosphere, while the second is performed in an inert gas atmosphere (like argon) or in vacuum.

In case of thermal oxidation DWNT have been shown to be resistant against oxidation up to 800 °C, while MWNT are able to withstand slightly higher temperatures [92]. SWNT have been observed to start oxidizing between 550-750 °C in a pure oxygen environment, while oxidation starts at 950 °C in an environment where water is bubbled into the chamber with pure nitrogen [93]. If the samples have a better quality (i.e. are more crystalline) the resistance against oxidation becomes higher, as shown by Liu et al. [92].

Nanotubes bundles have been found to coalesce at high temperatures by both simulations [94] and experiments [14], forming large SWNT or MWNT. At temperatures of 2000-2200 °C SWNT start to coalesce into bigger SWNT, at even higher temperatures MWNT are formed [95]. The onset of the coalescence is the formation (or presence) of vacancies. The resulting tubes are highly defective, especially when the chirality of the tubes differs a lot [94].

In case of single tube the temperature for complete failure of a MWNT has been indirectly calculated to be 2900 °C [91]. A thermal stability simulation by Dereli et al. on a single (10,10) SWNT predicted a temperature of 2227 °C [96]. A simulation done by Liew et al. predicted a value above 3000 °C for very short tubes (12 nm), while longer tubes (24 nm) failed at temperatures around 2500 °C [97]. Their results predict that longer tubes fail at lower temperatures. Larger diameter tubes are more stable than smaller, because the lower curvature induces less stress. Therefore it is foreseen that MWNT are more thermal stable than SWNT. Beside this, interactions between the walls can aid in the thermal stability for MWNT [14].

2.4 Conclusion

A carbon nanotube (CNT) is formed by rolling up a sheet of graphene and has a hexagonal lattice consisting of carbon atoms. A CNT with one wall is called single-walled (SWNT) and with multiple walls multi-walled (MWNT). The way the walls are rolled up is called the chirality and influences the properties of the tube. Nanofibres (CNF) are nanostructures without complete graphite walls along the tube length. The diameter of a CNT can range from 0.5 to over 100 nm, while the length of a single CNT can be up to several mm.

While for a piece of metal the resistance depends, beside temperature, on the cross sectional area and the length (and for small sizes also on effects like grain boundary scattering) the ideal resistance of a CNT has a value of $6.45 \text{ k}\Omega$ for a SWNT or MWNT wall. For a SWNT or MWNT wall the resistance depends on the chirality, diameter, length, quality and temperature:

- *Chirality*: determines if a tube/shell is in principle semiconducting or metallic, for an uniform distribution 1/3 will be metallic
- *Diameter*: the band gap of a semiconducting tube is inversely proportional to the diameter. Larger diameter tubes will have more conductive bands available lowering the resistance
- *Length*: the MFP of CNTs can be very long, enabling ballistic (length independent) transport of electrons, When the length is longer than the MFP scattering will start to increase the resistance
- *Quality*: low quality or deformed tubes have a shorter MFP. CNFs act more like graphite due to the absence of complete walls over the tube length
- *Temperature*: at higher temperature more conductive bands become available, however also the MFP will be reduced

Beside a quantum resistance a CNT will also have a contact resistance between the CNT and metal. Publications have shown that this resistance can be lowered, and thus should not pose to be a fundamental limit. A single CNT will generally not show a lower resistance than metals, unless a wire is required which is only a nanometre wide as in that case metals will become semiconductors. For larger dimensions only a bundle of CNT can potentially outperform the resistance of metals.

Other electrical properties of CNTs are, beside the traditional electrostatic capacitance, a quantum capacitance of $400 \text{ aF}/\mu\text{m}$ for a SWNT. The magnetic inductance can be neglected, however a so-called kinetic inductance of $4 \text{ nH}/\mu\text{m}$ exists. Both are caused by the limited amount of states and charge carriers in the system. Finally CNTs have been shown to be able to carry a current density as large as $10^9 \text{ A}/\text{cm}^2$.

The specific heat of a CNT is with $0.7 \text{ J}/\text{g}\cdot\text{K}$ comparable to that of metals. The thermal conductivity, however, can be one order higher than that of metals. The exact value for the thermal conductivity for a single tube or bundle is still unclear due to many different values being reported. For single tubes values are often between $2000\text{-}6000 \text{ W}/\text{m}\cdot\text{K}$, while for bundles values between 60 and $1000 \text{ W}/\text{m}\cdot\text{K}$ have been reported.

The thermal stability of CNTs before failing or coalesce in a oxygen depleted environment is $2000 \text{ }^\circ\text{C}$ or higher. This is higher than the melting temperature of most metals. SWNT start oxidizing around $550\text{-}750 \text{ }^\circ\text{C}$, while MWNT can withstand temperatures up to $800 \text{ }^\circ\text{C}$.

Chapter 3

Growth of carbon nanotubes

In order to become mainstream materials carbon nanotubes have to be manufactured reproducibly in large quantities for a low price. However, at the moment nanotubes still cost a staggering hundred to a thousand euros per gram, depending on the purity, quality and production method. Beside that reproducibility is still low. Although diameter control is possible it is not yet possible to directly produce CNTs of the same electrical type let alone with the same chirality without sorting. In other words there are still quite some challenges in the production of CNTs [98]. In the next sections we will look how CNTs can be fabricated with different techniques. The technique useful for our experiments will be further elaborated and geometry control will be treated (section 3.2).

3.1 Arc-discharge & laser ablation

There are currently three main production methods for carbon nanotubes, namely arc-discharge, laser ablation and Chemical Vapour Deposition (CVD). Of these methods arc-discharge was the first used for CNTs production (it was also the method used by Iijima in 1991 [26] when he discovered CNTs). It uses two carbon electrodes inside a helium atmosphere with an arc ignited between them. This evaporates the carbon based electrodes, which can condensate into MWNT under the right conditions. Already in 1992 high quality MWNT production at the gram level was possible. For the synthesis of SWNT a metal catalyst is needed, for which often nickel or cobalt are used. Substantial production of SWNT by this method was reached in 1993. [33, 98]

The first method to produce SWNT on the gram scale used laser ablation and was discovered in 1996. In this method a powerful laser is used to heat up a carbon target, which contains half a percent of catalyst, to evaporate both. The target is placed in a furnace, heated up to 1200 °C, through which a gas flow passes which transports the evaporated carbon and metal catalyst to a cold surface where they condensate into CNTs. [33]

Both arc-discharge and laser ablation produce high quality CNTs which are randomly orientated into bundles forming a powder. However, the machinery required are quite expensive and the energy requirements are high, resulting in high costs per gram of material. Controlled growth on substrates is currently not possible. [98]

In our case we want to produce nanotubes on top of a silicon substrate, with metal layers for the horizontal interconnects. Production temperature should be moderate to low in order to prevent diffusion of dopants in previous device layers and to prevent

aluminium metal layers from melting. This means the maximum temperature is about 550 °C as mentioned before in section 1.4.

The high temperatures required, lack of controlled growth on substrates and high costs make both arc-discharge and laser ablation unattractive methods for our purpose. However the third method of producing CNTs, CVD, doesn't have these downsides and will be discussed in depth in the next section.

3.2 Chemical vapour deposition (CVD)

Chemical vapour deposition (CVD) is a technique used in semiconductor industry to deposit thin films of highly pure material on a substrate. This is done by thermal decomposition of gases in a reactor chamber at a certain pressure and temperature. The product of the reaction will be deposited on the substrate. Popular materials produced by CVD are silicon, silicondioxide, siliconnitride, siliconcarbide, certain metals (like molybdenum, tungsten or titanium) and synthetic diamond.

Pressures at which CVD can take place range from atmospheric to the mbar range and temperatures can range from several hundreds degree Celsius to over a thousand degree. A plasma can be used to assist the decomposition of the gas, in order to lower the required temperature. This method is called Plasma Enhanced CVD, or PECVD, and is used extensively in the semiconductor industry as it enables deposition of materials at low enough temperatures to prevent diffusion of dopants and the melting of aluminium.

CVD has become quite popular for the creation of carbon nanotubes the last decade [33, 98]. Both thermal CVD as PECVD have been investigated extensively and are used to produce gram quantities of relative cheap CNTs. Often production is done at temperatures between 400-900 °C with pressures between several mbar and atmospheric, depending on the CVD method. Controlled vertical growth on substrates is possible and also horizontal growth has been investigated [33, 98–100]. The process is often partly or completely compatible with standard semiconductor processes, making CVD a very attractive method for CNT growth.

In the next section the requirements for CVD growth will be discussed (section 3.2.1) followed by the growth models (section 3.2.2). After that thermal CVD (section 3.2.3.1) and PECVD (section 3.2.3.2) will be discussed, both are often used methods to synthesize CNTs. The control of the CNT geometry by the process parameters will be discussed in section 3.2.4. Finally, we will discuss which CVD processes fit our needs 3.2.5.

3.2.1 Requirements

In case of carbon nanotube growth using chemical vapour deposition a catalyst is always required (contrary to arc-discharge and laser ablation in which MWNT can be grown without catalyst). For the catalyst transition metals are used, among which nickel (Ni), iron (Fe) and cobalt (Co) are the most popular. The choose of catalyst has influence on the CNT growth. However, the optimum catalyst depends on the environment in which CNTs are grown and no general conclusions can be made to which catalyst performs best [101]. CNT growth cannot take place on an layer of catalyst material, but needs catalyst nano-particles instead. More information about the creation of these catalyst nano-particles will be given in section 3.2.4.

Beside a catalyst also a carbon feedstock is required, for which methane (CH₄) and acetylene (C₂H₂) are the most popular choices. However, also ethylene (C₂H₄), alcohols and carbon monoxide (CO) are sometimes used. The choice of gas has influence on the

growth, as they don't have equal thermal stability. Acetylene is the least stable of the three hydrocarbon gases, followed by ethylene and methane [102]. Thus acetylene should be easier to decompose and more suitable for growth at low temperature.

The last requirement is enough energy for nucleation (growth) to occur. This energy can either be supplied in the form of thermal energy (thermal CVD) or as a combination of plasma and thermal energy (PECVD). The later often requires less thermal energy for nucleation, enabling growth of CNFs at temperatures as low as 120 °C [103] and CNT growth below 400 °C [16, 104].

3.2.2 Growth models

Before it was possible to observe the actual growth of carbon nanotubes by high resolution transmission electron microscopy (HRTEM) already a model [105] was postulated stating that the growth of CNTs occurred similar to that of carbon filaments observed in the 70's (e.g. Baker et al. [106]). In 2004 Helveg et al. were the first to observe in situ growth of carbon nanotubes using HRTEM [107]. Their findings combined with other observations [108–110] and simulations [111–113] can be used to extract the following two models (or mechanisms) which are indeed quite similar to the growth of carbon filaments.

The models are named after the position where the catalyst particle is located and where the tube is extended by the addition of more carbon. In the root (or base) growth model the catalyst particle remains at the substrate due to strong surface-catalyst interaction and additional carbon atoms are added at the root of the tube. In case of the tip growth model the catalyst particle is at the tip of the nanotube and moves forwards when the tube grows. Carbon is added at the tip of the tube. Figure 3.1 illustrates both growth models. There are also results published suggesting that a catalyst particle can sustain both tip and root growth at the same time, however this seems to be uncommon [114, 115].

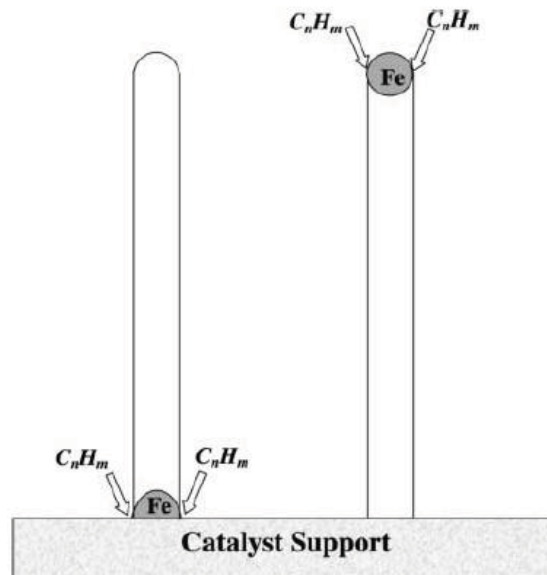


Figure 3.1: CNT growth models. Left: root growth, right: tip growth (from [33])

Both growth methods have similarities. In both the catalyst particle absorbs and dissociate the hydrocarbon molecules, which then diffuse over the surface and subsequently

nucleate into a carbon nanotube. The reason that a tube is formed and not amorphous carbon (a-C) or graphite is that tube formation is energetically favoured [111]. HRTEM analyses of the catalyst particle has shown that the particle can deform in both growth methods, however, it remains crystalline [110]. Before in-situ observation it was thought that a carbon supersaturated catalyst particle (or metal carbide formation) was required for growth. However, this has not been observed [113], carbon atoms seem to remain on the surface of the particle.

There are also some differences between the growth models. In case of root growth the carbon atoms on the catalyst surface start to form a cap [110,112]. In this process the catalyst particle can resize until the cap formation is completed, after which the tube will extend while the catalyst remains fixed at the substrate. Growth will stop when the catalyst is isolated from the hydrocarbon gas, either by blocking it by a-C or when the process gases are turned off.

The tip growth mechanism involves no cap formation. At the bottom of the catalyst a rolled up graphene sheet (or in case of CNFs loose graphene sheets) will form, elongating the particle while it is moving up. At a certain point the increase in surface energy of the catalyst due to elongation can no longer be compensated by the energy gain provided by binding with the carbon atoms, resulting in a rapid upwards contraction of the catalyst particle. If this elongation/contraction mechanism occurs binary a CNF will be formed, if the mechanism is more smote a nanotube will be produced [110]. It is suggested that when the particle is completely covered by a-C growth will terminate. It can occur that the catalyst particle breaks during growth and along the tube catalyst remnants are found, as was observed by Abdi et al. [116].

Hofmann et al. [113] investigated the rate limiting step in CNT growth. They divided the growth in four phases:

1. Adsorption of the precursor gas molecule on the catalyst surface
2. Dissociation of the absorbed molecule
3. Diffusion of the carbon atoms on or through the catalyst particle
4. The final nucleation or incorporation of the atoms in the CNT structure

They measured activation energies for PECVD in the range of 0.2-0.4 eV for the popular three catalysts. In case of thermal CVD, however, an activation energy of 1.21 eV was found, which is considerably higher. By analysing the mentioned growth steps they deduced the rate limiting steps in the two CVD processes.

Step four is the same for both thermal CVD and PECVD. The energy barrier should be small as no covalent bonds are being broken and the formation of tubes is energetically favoured. This conclusion is supported by simulations [117]. Step three should also be the same for both processes. Carbon is transport by surface diffusion, and not by bulk diffusion and saturation of the particle (as has also been proposed as a mechanism for CNT growth [33]). This conclusion is supported by simulations done by other researchers [112,117] and by x-ray spectroscopy performed by Hofmann et al. [110].

The difference should thus be in the first or second step. Simulations on the absorption and dissociation of hydrocarbon molecules on the catalyst surface show that this energy barrier is between 0.9 and 1.3 eV. In case of PECVD the gas is dissociated by the plasma, which makes direct absorption on the surface possible, with no significant energy barrier. As the last step has no significant energy barrier the rate limiting step will be the surface diffusion in case of PECVD. The energy barrier of this step is estimated to be 0.4-0.5 eV [113].

These conclusions fit well in the result on the activation energy of thermal and plasma CVD growth of nanotubes. The activation energy found for PECVD (0.23-0.35 eV) is close to the surface diffusion energy of the used catalysts, whereas the energy needed for bulk diffusion is much higher. The activation energy of thermal CVD (1.21 eV) is close to the combination of adsorption and dissociation energy barrier (0.9-1.3 eV).

3.2.3 CVD methods

3.2.3.1 Thermal CVD

In its simplest form a thermal CVD apparatus is nothing more than a (often quartz) tube surrounded by heaters in which a gas flow is present (figure 3.2). Besides a carbon feedstock often an inert gas (like argon or nitrogen) or etching gas (hydrogen or ammonia) is added to reduce the amount of carbon supplied to the catalyst for optimum growth. Growth temperatures are generally high (600-900 °C) and pressures can be anywhere between a couple of mbar to atmospheric pressure.

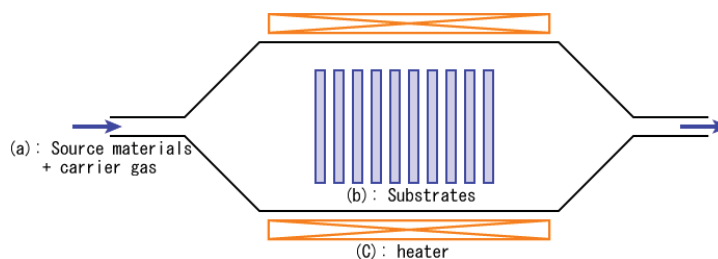


Figure 3.2: Typical hot-wall thermal CVD lay-out

The high temperature processes tend to be at atmospheric pressure with hot-wall reactor chamber (e.g. [13, 100, 118, 119]). The low temperature systems on the other hand (400-600 °C) tend to be at pressures of a ones or tens of mbar [56, 120]. In these machines typically only the wafer holder is heated, making it a cold-wall reactor.

To enable growth at lower temperature often special catalyst pretreatments are done by using hydrogen or ammonia to optimize the catalyst size and remove oxidation [121] or by using an optimum catalyst and substrate combination [122]. Another trick is using a two zone heating hot-wall furnace in which one zone is at high temperature to dissociate the gas and the growth area is at a lower temperature [122].

Heating the substrate is also possible with a heated filament (often close to 1000 °C [123]) positioned in the gas flow above the sample. As the filament is away from the substrate it can be at higher temperature, thus aiding in dissociating the gases. This method is called hot-filament (HF) CVD. Although not an often used method it has been shown that good quality MWNT can be grown by HF-CVD [124, 125]. A combination of plasma and HF-CVD (often dubbed plasma-assisted HF-CVD) has also been demonstrated for the growth of vertically aligned MWNT [126].

One advantage of the thermal growth of CNTs is that the system is relative simple. Furthermore, all kind on nanotubes can be grown, from SWNT to MWNT and CNFs. The deposition of amorphous carbon beside nanotubes (especially the areas without catalyst) is less of a problem as the self-pyrolysis of the carbon feedstock is negligible at the lower growth temperatures. When two-zone or HF heating is used the formation of a-C is, however, more likely.

Vertical alignment is possible by the Van der Waals forces between the tubes [127]. However in case of low density growth the nanotubes will not be aligned and will form

a random layer of tubes [98, 121]. The quality of the tubes is temperature dependent and can be very good. Growth at low temperature is often more defective [128, 129]. In some systems an optimal temperature for growth is observed [119, 130], this is related to the catalyst activation which will be treated in section 3.2.4.

3.2.3.2 Plasma-enhanced CVD (PECVD)

In case of plasma-enhanced CVD a plasma is generated inside the reactor by an electric field. This plasma dissociates the feedstock gases, enabling growth on lower temperatures. The plasma is a glow discharge plasma, which means that the electrons in the plasma are more accelerated (at higher energy) than the ionized atoms. Further the density of ions and electrons is moderate ($10^8 - 10^{13} \text{ cm}^{-2}$), and last: the plasma is relative cold. The plasma consists of electrons, ions/radicals and neutral species generated from the feedstock gases.

The pressure in a PECVD chamber is relative low, ranging between tenths to tens of mbar. This pressure ranges makes it possible to couple the electric power supply to the plasma. As with thermal CVD a gas flow is present in the reactor, often the gas is injected into the chamber at the same place the plasma is generated (e.g. through a shower head which is used as one of the electrodes for the electric field). Almost always hydrocarbon gases are used (CO introduces harmful oxide species, but has been used by Lee et al. with iron as catalyst [131]), often combined with an etching gas like hydrogen or ammonia or a dilution gas like nitrogen or argon. Finally, the substrate is often heated to temperatures between 400-700 °C to enable growth. For an example of a typical PECVD reactor lay-out see figure 3.3.

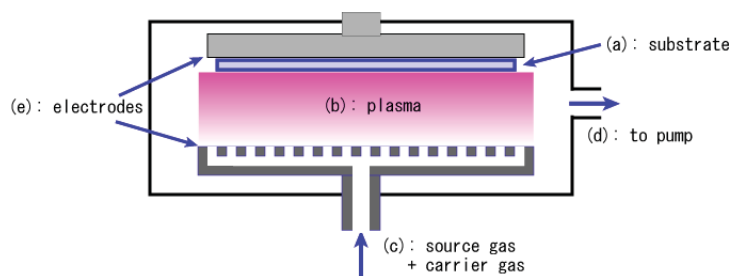


Figure 3.3: Typical RF or DC PECVD lay-out

For the growth of CNTs, PECVD has been researched extensively. There are many different PECVD methods, based on the way the plasma is generated. Semiconductor industry often used capacitively coupled plasma (CCP) RF-PECVD, in which RF stands for radio-frequency. This frequency normally is 13.56 MHz and the electrodes are often two parallel plates of which one is grounded and used to hold the substrate and the other is a gas shower head to which the RF source is connected (see also figure 3.3). The inverse configuration is also possible, reversing the direction to which the ions and electrons are directed.

An RF plasma is uniform over large areas enabling large area deposition with good reproducibility. Ion damage by accelerated ions is moderate, due to the often low bias between plasma and substrate. This also reduces the substrate heating. For these reasons the method is popular in semiconductor industry [132]. The growth of CNTs by RF-PECVD is however more difficult, and often results in CNFs with a small length and amorphous carbon deposited on the tips and sides of the tubes [133].

The first results using RF-PECVD used special devices using non-standard reactors, employing for instance two RF sources [134] or magnetic fields to create a so-called high density magnetron plasma [135]. More recent results employ normal RF-PECVD systems [136–138]. Sometimes a grid or metal plate is used to shield the substrate from the plasma as ion or electron bombardment can damage the tubes (or prevent growth at all) [133, 137, 139].

Mainly vertically aligned (VA) CNFs and MWNT were grown in the first experiments. However, in 2004 VASWNT growth was reported using the magnetron RF-PECVD [140]. Recently VASWNT growth using standard RF-PECVD was reported [137]. It seems that SWNT are much more susceptible to ion damage due to the plasma, thus the environment in the reactor should be such to minimize this damage by ions [137]. MWNT are less susceptible to ion damage and therefore grow more easily.

Beside CCP RF-PECVD (RF-PECVD for short in this work) it is also possible to have an inductively coupled plasma (ICP), which will be called ICP-PECVD. The RF is applied to a coil outside the reaction chamber and is supplied to the inside through a dielectric window (often made from quartz). This technique was also investigated to grow VACNTs but the quality seems to be poor resulting in CNF growth, probably due to the higher plasma density [141–144].

Another problem with ICP-PECVD is that coupling the power to the plasma is more difficult, as a hydrocarbon plasma has a large capacitive component [132]. An ICP device has also been used to create a plasma in a more thermal CVD like furnace which resulted in high quality SWNT [145]. In this device the plasma is generated far away (40 cm) from the substrate and the dissociated gas is carried toward it by the gas flow.

Because RF-PECVD of CNTs appears to be rather difficult a lot of other methods are used that are less frequently used in standard semiconductor industry. A popular method for CNT growth uses a DC (Direct Current) plasma, with a similar configuration as RF-PECVD devices. It was one of the first methods used for extensive research on nanotubes grown by PECVD, with the first results being published in the beginning of 2000 [146].

The first results were mainly bamboo-like multi-walled VACNFs [31, 103, 146], however more recently better quality MWNT have been grown using DC-PECVD [147, 148]. There is a large bias between the plasma and the substrate, making it prone to ion damage and substrate heating [149]. To the authors knowledge no (VA)SWNT have been grown by DC-PECVD.

Another PECVD method that has been used for the deposition of diamond films and is now frequently used for the growth of CNTs is microwave (MW) PECVD using a frequency of 2.45 GHz. As with ICP-PECVD the electric energy is introduced into the chamber by a dielectric windows and again the plasma density is high compared with RF or DC plasmas.

High quality VAMWNT have been reported using this method [114, 150], sometimes with the aid of substrate shielding [151]. Researchers of Waseda university in Japan reported high quality VASWNT [152] and MWNT [57] growth using a so-called point-arc MW-PECVD system consisting of a MW antenna protruding into a large reaction chamber. The plasma is only a couple of cm in diameter and exists at the tip of the antenna.

Between the plasma and the substrate often an electric field is present. In case of DC-PECVD this field always exist and is quite large. For RF-PECVD such a field will be generated by self-bias. When using ICP and MW-PECVD an external bias can be applied, enabling control of the magnitude and direction of the field. Because the field

only exists in the, often small, region between the plasma and the substrate the field strength can be quite high [153].

This field is the driving force behind the VA of the nanotubes [154]. When thermal CVD was performed in the PECVD chamber without a plasma, but otherwise equal parameters, randomly orientated CNTs instead of VA were observed [31, 116, 153–155]. In case of growth outside the electric field (i.e. at the other side of the electrode) also random orientated nanotubes were observed [156]. It is believed that tip growth is required for aligned growth in an electric field [157]. Indeed, all low density aligned growth experiments published seem to be with tip growth (at high density Van der Waals forces can also align the tubes, thus allowing both tip and base growth).

Because the plasma dissociates the gas, the formation of amorphous carbon is a problem in all forms of PECVD. A solution often used is adding an etching gas like NH_3 or H_2 to the gas mixture. There exists an optimum ratio between the carbon source and the etching gas [144, 158]. In case of too little etching gas there will still be a-C. However, when there is too much etchant it will start to attack the carbon nanotubes. Beside removing a-C an etchant can also suppress the decomposition of the carbon feedstock [153].

Another method used to prevent or minimize the formation of a-C is adding inert gases like helium, argon and nitrogen to the mixture [134, 141, 155]. This way the amount of carbon atoms can be reduced in the systems. If most (or all) carbon that is available is absorbed by the catalyst for CNT growth hardly any is left for a-C formation. Combinations of etchant and inert gases together with hydrocarbons have also been used [136, 142]. Finally, some papers report the usage of pure methane [134, 143]. The hydrogen dissociated from the CH_4 is thought to aid in the removal of a-C.

From the discussed methods for PECVD growth of CNTs it can be concluded that PECVD has some advantages over thermal CVD. The biggest advantage is the growth at lower temperature, enabling the growth of CNTs compatible with VLSI processes or on substrates that cannot withstand high temperatures (like plastic and glass). Another major advantage is the vertical alignment of the grown CNTs as long as a strong electric field is present between the substrate and the plasma.

There are some disadvantages when using PECVD for the growth of CNTs, though. First of all the device will be more complex. Another is the formation of amorphous carbon alongside the tubes if the reaction environment has a too large supply of carbon or too little etching. Lastly ion bombardment damages the tubes, making the growth of SWNT more difficult and reducing the quality of MWNT. However, good quality growth of both MWNT and SWNT have been demonstrated by PECVD, sometimes with the aid of substrate shielding.

3.2.4 Geometry control

In this section the control on five nanotube parameters, namely its diameter, density, length, quality and chirality will be discussed. The diameter and type of the tube is mainly controlled by the catalyst particle size [31, 98, 123, 147]. Small particles of only a few nanometre will result in SWNT with a similar diameter. If the particles becomes larger MWNT with more and more shells will start to form [152, 159]. Very large particles will result in multiple MWNT per particle, in CNFs instead of CNTs or in no growth at all but instead the formation of a-C or graphite [146, 160].

To create catalyst nano-particles there are several possibilities. Most often a catalyst layer is deposited (by evaporation or sputtering) on top of a buffer layer (often SiO_2 or

a metal) which is there to prevent the formation of silicides. The thickness of the catalyst layer can be used to select the average particle diameter, but also the substrate and deposition method have influence on the average diameter [118, 147]. An increased surface roughness of the buffer layer seems to aid in the formation of CNTs with smaller diameter [118], and higher density [147]. It is also proposed that a titanium buffer layer can prevent the deposition of amorphous carbon and aids in the formation of smaller particles [124].

The transformation from a thin film to nano-particles is called activation, see also figure 3.4. To activate the catalyst film it is heated to a certain temperature under a certain pressure in a certain gas environment (like argon, hydrogen or ammonia), sometimes with a plasma in case of PECVD. Particles are formed from the film in order to reduce the surface energy of the metal film [161]. The etching of the plasma or gas environment when using gases like H_2 and NH_3 can remove metal oxidation (which reduces the activity of the catalyst [110, 136]) and aid in the activation of the catalyst layer by etching the layer and ion bombardment [121, 148, 162].

Sometimes an additional very thin (< 1 nm) non-catalyst is deposited on top of the catalyst layer, which aid in the formation of small particles with a high density and uniform distribution [136, 152, 159]. Besides thermal heating of the catalyst film also laser heating has been used, which results in smaller and more spherical particles due to the fast heating [155].

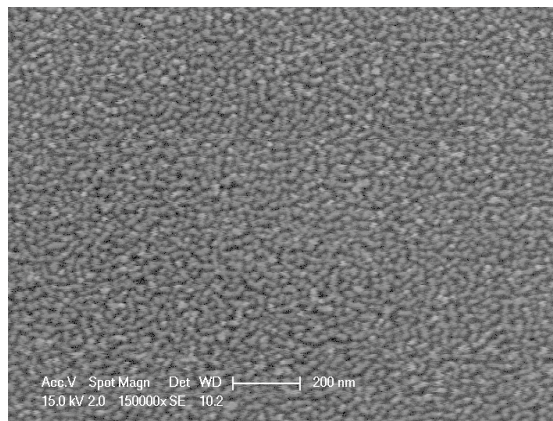


Figure 3.4: Close-up of nickel nano-particles on titanium buffer layer

Other methods to create catalyst particles involve the deposition of pre-sized particles by direct deposition onto the substrate, a technique exploited by Fujitsu Limited [123]. Another deposition technique uses chemical solutions to form small particles. This method is, however, time consuming and cumbersome [132]. Lastly a direct CVD process using ferrocene (an organic metal) as metal source and xylene as a carbon source has been demonstrated [13].

Determining where the CNTs should grow is not complicated when using metal films as they can be patterned using optical lithography followed by (dry) etching or lift-off, or by using e-beam lithography. In case of solution based deposition of nano-particles it is more difficult to create a pattern as the deposition is more or less uniform over the entire area and are more difficult if not impossible to pattern by, for example, lithography [13].

As mentioned before the process to activate the catalyst layer influences the particle diameter an density, and thus the CNT morphology. From results by Pisana et al. it can be concluded that a thinner catalyst film results in a higher density (and smaller

diameter) [161]. Also the layer underneath the the catalyst influences the final density of the growth [118,152].

Not surprisingly also the parameters used to activate the film play a role. For instance, Abdi et al. and Jönsson et al. both observed that for a higher plasma power the density decreases [116,163]. Pressure, gases and their ratios used to activate the layer were found to influence both the density and the diameter [140,161,164]. Also temperature plays a role as it influences the mobility of the catalyst atoms and thus their size [130], often an optimum temperature exists [165,166]. Finally time can be important in activating the film, a too short time will result in low density due to an incomplete film break-up with larger diameter tubes [167], but a long time might allow the particles to agglomerate together [165].

The nanotube length (or growth rate) can be determined by the deposition time, the temperature, gas chemistry and plasma power. The growth rate is also influenced by the tube diameter, larger tubes tend to grow slower [31,147]. The relation between time and length is quite logical, it must however be noted that growth can terminate (or slow down) when the catalyst becomes covered by a-C over time [24,119].

Generally higher temperatures or plasma power will result in faster growth [168]. Although sometimes an optimum growth temperature has been observed which is again related to the size of the nano-particles [130,165]. At low temperature the catalyst particles are not mobile enough to generate nano-particles and there might be not enough energy for effective growth. At high temperature particles will fuse together forming large islands, slowing down the growth or preventing it at all.

In case of a plasma higher power can result in decreased growth rates due to the etching of nanotubes by the plasma [31,104], while also an increased growth rate for higher power has been reported [137].

As for the ratio of different gases (that is, between the carbon feedstock and the etching and diluting gases), often there exist an optimum gas ratio which results in the fastest growth [31,130]. This is due to a balance in etching and carbon supply between the gas mixture.

Bronikowski found that even the geometry of the patterned catalyst has influence on the growth rate. For smaller CNT bundles or bundles placed further from each other growth decreases [130]. It is thought that by-products created during the growth of CNTs can aid the growth of nearby tubes.

Quality is a difficult parameter to assess as no real quantitative number exist for it. Different measures have been used, ranging from qualitative assessment by looking at the SEM and TEM pictures and judging from the (crystal) structure and the amount of a-C the overall quality. More quantitative numbers can be obtained when using a measurement technique like Raman spectroscopy (for more information on this method the reader is invited to read appendix C.3) by comparing different Raman active band widths and ratio's between the samples.

Quality can be influenced by about every parameter available in the (PE)CVD system. A higher temperature generally results in an improvement in quality [31,169], but in some cases an optimal temperature has been found [165]. Higher plasma power seems to induce more defects and hence decrease quality [133,137]. A higher plasma bias enables more aligned growth [31]. However as discussed before in section 3.2.3.2 ion and electron bombardment has been shown to negatively influence the growth. This means that a higher plasma bias can also be disadvantageous as it accelerates more charged particles towards the substrate [137].

Xu et al. [25] found that in their experiments a lower C_2H_2 flow rate improved quality, while an optimum pressure existed. Antunes et al. found that a thicker catalyst layer results in lower quality growth [170]. Normally time doesn't influence the quality. However, when the CNT growth stops due to catalyst poisoning still a-C can be deposited reducing the overall sample quality [165].

Chirality control is considered the holy grail of CNT research. For application to electronic devices it would be a very useful property, for interconnects only metallic tubes are wanted and for transistor made from CNTs only semiconducting. However, exceptions from the normal distribution of semiconducting and metallic nanotubes are rare, and no good mechanism to control chirality has been found to date.

Simulations suggest that the geometry of the catalyst nano-particle can have influence on the chirality as certain caps of the root growth mechanism are more stable on top of the nano-particle surface than others [171]. Li et al. [145] managed to grow SWNT with a much higher percentage of semiconducting SWNT than normally expected (85-90% vs. 66%). It was later explained that this is due the higher stability and energetical favourability of semiconducting SWNT vs. metallic ones in case of small diameters [172].

A qualitative summary of the CNT growth properties discussed in this section that can be controlled and the influence of the growth parameters on them is displayed in table 3.1. The 'ratio' column shows the influence of the etching (or diluting) gases and the carbon feedstock. A '+' indicates that the properties are proportional, a '-' indicates the inverse. The 'O' stands for optimum, 'X' for no influence, and an 'I' for inconclusive.

Table 3.1: Qualitative overview of growth properties vs. parameters, for an explanation of the symbols see the text

	Temperature	Pressure	Time	Ratio	Plasma power	Cat. thickness
Growth rate	+ [168] or O [130, 164]	+ [31]	+ [130]	O [130]	I [31, 104, 137, 153]	- [130]
Diameter	O [130, 165]	- [161]	O [165, 167]	- [164]	+ [163]	+ [31]
Quality	+ [169] or O [165]	O [25]	X or - [165]	+ [25] or O [31]	- [133, 137]	- [170]
Density	O [165, 166]	+ [161]	O [165, 167]	+ [164]	- [116, 163]	- [164]

3.2.5 CVD for vertical interconnects

As discussed in section 3.1 CNT growth using chemical vapour deposition is the only method that has the potential to give growth on a low enough temperature and directly on substrates. In chapter 2 it was found that the electrical resistance depends on the length, diameter, density and quality of the tubes. With this information we can determine which CVD growth techniques would be most suitable for us.

To reach a length sufficient for our needs we will need vertical alignment, as with random growth it is difficult to control the height of the structure. Another argument for aligned growth is that it minimizes the total tube length, and thus the resistance of the tube if the MFP is shorter than the total length.

Both thermal CVD and PECVD can produce a so-called forest of vertically aligned CNT (VACNT). In case of thermal CVD an area of VACNT will always be of high density, otherwise the Van der Waals forces are not strong enough to self-align the tubes. This is very suitable for our situation as a higher density means a lower resistance for the same area. PECVD will almost always result in VACNT, even with low densities.

We can control the diameter by changing the catalyst thickness, a technique that works for both plasma as thermal CVD. However, the growth of SWNT is more difficult in a plasma system. The catalyst layer is also the primary method to control density,

together with the activation process. It appears, however, that PECVD samples tend to be less dense than thermal CVD grown CNTs.

Quality depends on temperature, which is a downside for us as we're limited to an upper bound of 550 °C. In case of PECVD the plasma can be used to add additional power, however a plasma also can have a negative influence on the CNT quality. Careful control will be necessary over all parameters to optimize the growth.

We can thus conclude that both PECVD as thermal CVD can suite our needs. The first has the advantage that alignment is no challenge, however the process is more complex. Thermal CVD can only grow high density aligned tubes, which requires that the catalyst is activated in such a way that it supports self-alignment.

To achieve good quality the temperature limit might prove to be a problem, though. Recipe optimization will be required in order to obtain low temperature high density growth of sufficient quality. Considering the choice of PECVD method, RF-PECVD and DC-PECVD seem to be more established and generally produce better results. They're also the only two methods available in commercial CNT equipment.

3.3 Conclusion

There exist three methods to produce, or grow, carbon nanotubes: arc-discharge, laser ablation and chemical vapour deposition. The first two require expensive equipment, high temperatures and don't support direct growth on top of substrates. Chemical vapour deposition doesn't have these downfalls and was further investigated.

For growth using CVD there are three requirements: a catalyst, carbon feedstock and energy. As catalyst mainly Co, Fe and Ni are used. For the carbon feedstock C_2H_2 and CH_4 are the most popular, often diluted with inert or etching gases to improve growth. Energy is normally added by heating the sample (thermal CVD) or a combination between a plasma and substrate heating (plasma enhanced CVD).

There are two main types of growth: root (or base) growth and tip growth. The methods are named after the place where the catalyst particle is located and the tube is extended. The catalyst particle absorbs the carbon gas and dissociates it, followed by transportation over the catalyst by surface diffusion and in the end nucleation into the CNT. In thermal CVD the absorption and dissociation is said to be the rate limiting step, while it is surface diffusion for PECVD as the gases are already dissociated by the plasma.

Thermal CVD is performed in either a hot or cold wall furnace, sometimes with hot-filament heating. Pressure ranges from several mbar to atmospheric and temperature is generally high (> 600 °C) to achieve growth. Advantages of thermal CVD are the simplicity of the system, the fact that it can grow any type of CNT, and the general high quality due to the higher deposition temperature. Vertical alignment is only possible by Van der Waals interaction between the tubes, requiring high density growth.

For PECVD CNT growth all different methods to generate a plasma have been used (CCP RF-PECVD, DC-PECVD, ICP-PECVD and MW-PECVD). The latter two techniques are less popular and often produce lower quality CNTs due the high plasma intensity. SWNT growth has been demonstrated using remote ICP and MW-PECVD, and RF-PECVD, while MWNT can be grown by all methods. Substrate shielding by a grid or metal plate has been used to protect the CNTs from ion bombardment by the plasma, which has a negative influence on the growth.

The big advantage of PECVD that it can easily produce aligned CNTs due to the electric field between the substrate and plasma. The plasma also allows for lower growth temperatures. Disadvantages are the more complex system and the formation of a-C due to the gas dissociation by the plasma. Mixing the carbon feedstock with an etching or inert gas can reduce the a-C formation.

Table 3.1 displays a qualitative overview between the CNT properties and several growth parameters. The geometry can both be influenced by the activation of the catalyst layer (which is the breaking up of the catalyst film into nano-islands) and the growth parameters. Generally the diameter and density are determined by the activation and used layers, while the growth rate and quality are determined by the growth parameters. Chirality control has yet to be established.

For our purpose, the growth of low temperature high density CNTs, both thermal CVD as PECVD can be used. In case of PECVD, DC-PECVD and RF-PECVD seems to be the most frequently used and well established techniques. Recipe optimization will be required in order to achieve high density, good quality growth at low enough temperatures.

Chapter 4

Electrical model and simulations

In this chapter we will derive an electrical model for single and multi-wall nanotubes, and bundles consisting of these tubes. After model derivation parameters like tube density and diameter will be changed and the influence on the electrical properties will be investigated. The first part of this chapter start with the derivation and simulation of a SWNT electric model, followed by extending this model to MWNT. The m-files used for the simulations can be found in appendix D.

Already quite some research has been done on the field of CNT modelling. A recent book chapter by Naeemi et al. [173] threads the subject of CNT modelling extensively. We will use their work, together with that of Burke [70, 71] as a starting point for our models and simulations.

We will assume that we can consider the via to be under low bias condition, which should hold as long as there are sufficient parallel tubes [46]. As we want an as low as possible resistance, which as shown in chapter 2 can be obtained with a large amount of parallel tubes, this requirement follows our goal.

4.1 Single-walled nanotubes

4.1.1 Electric model

In section 2.2.1.1 it was already discussed that metallic SWNT have a fundamental minimal resistance, called the quantum resistance (R_Q), which is 6.45 k Ω per tube. This resistance will increase when the tube is longer than it's MFP, which in turn is related to scattering by phonons or defects. Beside a quantum resistance an nanotube also has a quantum capacitance and kinetic inductance, beside the regular electrostatic capacitance and neglectable magnetic (or self-) inductance. Again these components pose a fundamental limit to the electrical properties of the SWNT.

As vertical interconnects are generally short we will not model the metallic SWNT as a transmission line as done by Naeemi et al. [173], but we will use a model with lumped elements. We use a model which contains the inductance and capacitance of the nanotubes in order to judge their qualitative influence on the circuit.

As we assumed low bias conditions the electron scattering will be mainly due to defect or acoustic phonon scattering. The MFP of acoustic phonon (AP) scattering has been found to be as long as 1.6 μm at room temperature for SWNT [44, 173]. The quantum resistance can be modelled using equation 4.1, in which $R_Q = 6.45 \text{ k}\Omega$ the quantum resistance of a nanotube, l is the nanotube length and l_0 is the MFP of the defect or AP scattering. As the diameter of a SWNT is generally between 0.6-3 nm

the diameter is too small to effectively add conductive channels for the larger diameter SWNT, fixing the quantum resistance.

$$\begin{aligned}
 R_{SWNT,metallic} &= R_{NT} = R_Q \Theta\left(\frac{l}{l_0}\right) \\
 \Theta(x) &= 1 \quad \text{If } x < 1 \\
 &= x \quad \text{Otherwise}
 \end{aligned}
 \tag{4.1}$$

Beside the tube resistance the contact resistance of a SWNT often can not be neglected, as it can be two orders of magnitude higher than the SWNT resistance in case of a bad quality contact. We incorporate the total contact resistance in our model by adding a resistor R_c . As mentioned in section 2.2.2 we can neglect the self-inductance of the CNT, however the electrostatic capacitance (C_E) should be included. Finally we add the kinetic inductance, $L_K = 4 \text{ nH}/\mu\text{m}$, and quantum capacitance, $C_Q = 400 \text{ aF}/\mu\text{m}$. The simplified model for a single CNT is displayed in figure 4.1.

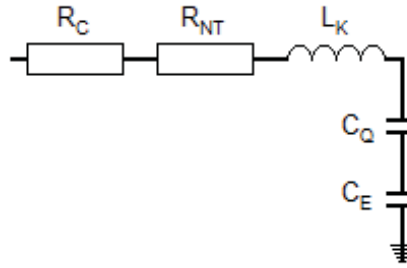


Figure 4.1: Simplified circuit model for a single metallic SWNT

Again, we're interested in the performance of CNT bundles. To model a bundle of CNTs we use a hexagonal tight packing model. As in reality tubes are not tightly packed, but have quite some distance in-between, we need to add a way to separate the tubes in the model. This can be done by varying the horizontal separation between tubes, while keeping the vertical tightly packed, as done by Srivastatva and Banerjee [22]. However, in case of a large separation the vertical tight packing distance becomes a bit unrealistic compared to the large horizontal separation. The model they use to calculate the number of tubes also seems to severely underestimate the actual number of tubes, even in case of complete tight packing, due to an error in the equations.

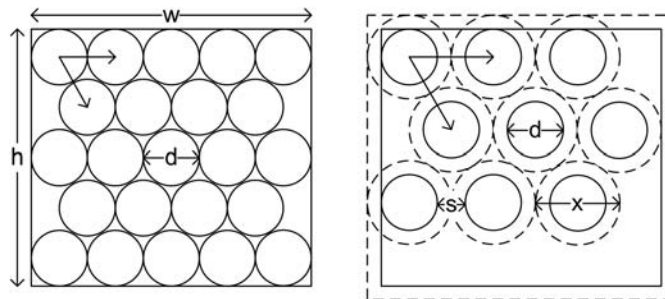


Figure 4.2: Ideal tight packed (left) and sparse packed (right) bundle

Instead we will use a model where we increase the diameter virtually and remain tightly packed with this virtual diameter (x). This ensures a tube spacing which scales

equally in the directions of the vectors in our triangular lattice. We assume that the virtual diameter has no-influence on the edges. That is, if the virtual diameter is too big to fit another tube to a row or column, but the real diameter (d) is small enough, the tube will be added. In figure 4.2 both an ideal tight packing and packing using the virtual diameter has been illustrated.

To determine the amount of tubes (N_{CNT}) that fit in an area with a width w and height h , consisting of tubes with a diameter d , and optional with a separation s the following equations can be used:

$$N_W = \left\lfloor \frac{w + s}{x} \right\rfloor \quad (4.2)$$

$$N_H = \left\lfloor \frac{h - d}{\sqrt{3}/2x} \right\rfloor + 1 \quad (4.3)$$

$$x = d + s$$

$$N_{CNT} = N_W N_H \quad \text{if } w + s - N_W x \geq \frac{x}{2} \quad (4.4)$$

$$= N_W N_H - \left\lfloor \frac{N_H}{2} \right\rfloor \quad \text{otherwise} \quad (4.5)$$

In figure 4.3 the CNT density as predicted by the model is displayed against diameter (ranging from 0.3 to 100 nm) and separation (1–10 nm). As expected for zero separation the density decreases quadratic for increasing diameter, while for tubes with a large separation and small diameter the influence of the diameter is only small. For small diameter tubes the density decreases sharply when the separation is increased, as many tubes are being removed from the bundle. For large diameter tubes increasing the separation removes only a few tubes, resulting in a weak dependency on separation.

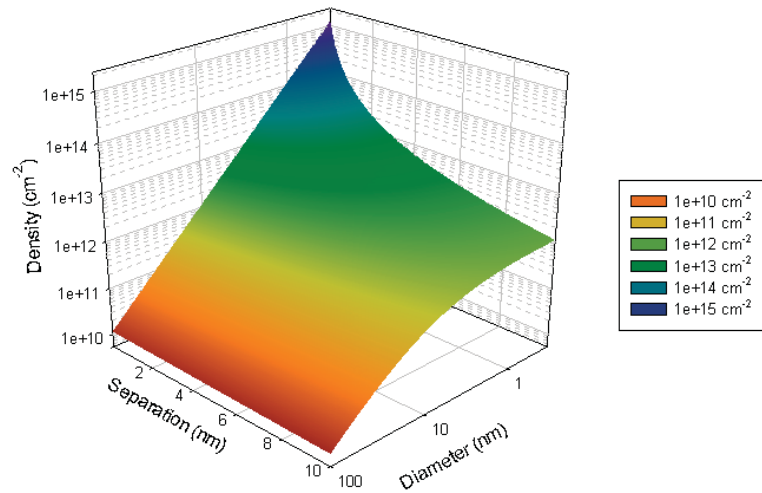


Figure 4.3: CNT density as predicted by the model against diameter and separation

Next we have to investigate what happens to our SWNT model if more tubes are packed together. We will assume that all tubes have the same potential as they're connected in parallel and are coupled. This means that we can neglect the electrostatic capacitance and mutual inductance between the individual tubes [173].

As all tubes are parallel, so are the quantum capacitances. The total quantum capacitance equals $N_{SWNT,metallic} \cdot C_Q$ and can become quite a large value. However, the electrostatic capacitance of the bundle remains relative low, in the order of tens of

aF/ μm [70]. According to simulations done by Naeemi et al. even for a bundle with low packing density it still follows the electrostatic capacitance for a solid piece of metal quite well [173]. As both capacitances are in series the electrostatic capacitance will conveniently dominate (and equals that of a metal piece with the same dimensions), and the quantum capacitance can be neglected.

The kinetic inductance is again in parallel, and thus decreases for every tube added ($L_K/N_{SWNT,metallic}$). Although the kinetic inductance has a large value it can be neglected for reasonable bundle sizes. The magnetic inductance will not change for a bundle, as it depends on the geometric properties. Naeemi et al. investigated the influence of the magnetic inductance on the performance and concluded that for normal applications CNT interconnects should operate in the RC regime where inductances can be neglected [173].

It should be of no surprise that the resistance of a bundle decreases when more tubes are added. Every contacted metallic tube fully participates in the conduction. However, the same isn't true for semiconducting tubes. On average only 1/3 of the tubes in a bundle is metallic. Some authors like Srivastava and Banerjee adjust the density of the bundle to incorporate this [22]. However, we would like a model where the density equals that of all tubes, in order to compare densities with observed growth samples (as you cannot tell apart metallic and semiconducting tubes in a SEM). The resistance of a SWNT bundle in our model is given in equation 4.6, and that of the contact resistance in equation 4.7.

$$R_{NT,SWNT-bundle} = \frac{3R_{NT}}{N_{CNT}} \quad (4.6)$$

$$R_{c,SWNT-bundle} = \frac{3R_c}{N_{CNT}} \quad (4.7)$$

In conclusion: when a bundle of SWNT is used the kinetic inductance and quantum capacitance rapidly decrease and the bundle acts for the outside similar to a piece of metal with equal dimensions for the reactances. The resistance also decreases for additional tubes. In the end the circuit can be modelled by only a contact and quantum resistance, combined with a electrostatic capacitance to nearby vias carrying another signal or to the ground plane.

As the electrostatic capacitance is as good as equal to that of metallic interconnects the only parameter that differs between a CNT bundle and a metal via is the quantum resistance. Our focus will thus primarily be on the resistance of a CNT bundle, as this will most likely be the limiting factor.

4.1.2 Resistance simulations

In this section the electrical model developed in the previous section will be used to simulate the influence of different parameters (length, contact resistance, diameter and separation (density)) on the total resistance and compare the values to bulk Al and Cu. As we're interested in the resistance the electrostatic capacitance will be treated as an open connection. Unless otherwise specified we will assume that the total bundle length is smaller than the MFP of the SWNT (assumed to be 1.6 μm).

Naeemi et al. [173] calculated the conductivity of a bundle to investigate the dependency on, for instance, length. There is a downfall to this approach, however. The resistivity (or conductivity) of a ballistic wire is poorly defined as the resistivity due to scattering is neglectable. The resistance of a ballistic wire is independent of length.

For a ballistic bundle the resistivity would be proportional to $1/l$ when our model from equation 4.1 is used. This would imply that the resistivity would decrease for a longer wire (till $l > l_0$, after which it becomes invariant to l) implying a longer bundle would perform better than a short one. This is, however, not true as the actual resistance of a short or long bundle, both within the ballistic regime, is exactly the same. Instead of the resistivity we will use the resistance per square cm as a measure to evaluate the bundle performance to circumvent this issue.

First we will investigate the influence of the length and the MFP of the SWNT on the total resistance per unit area by equation 4.1. For the SWNT in the bundle we will assume a diameter of 1 nm, assuming ideal tight packing this gives a density of $1.15 \cdot 10^{14} \text{ cm}^{-2}$. The total (quantum) resistance in that configuration will be $1.68 \cdot 10^{-10} \text{ } \Omega/\text{cm}^2$, assuming an ideal contact resistance, and a length shorter than the MFP.

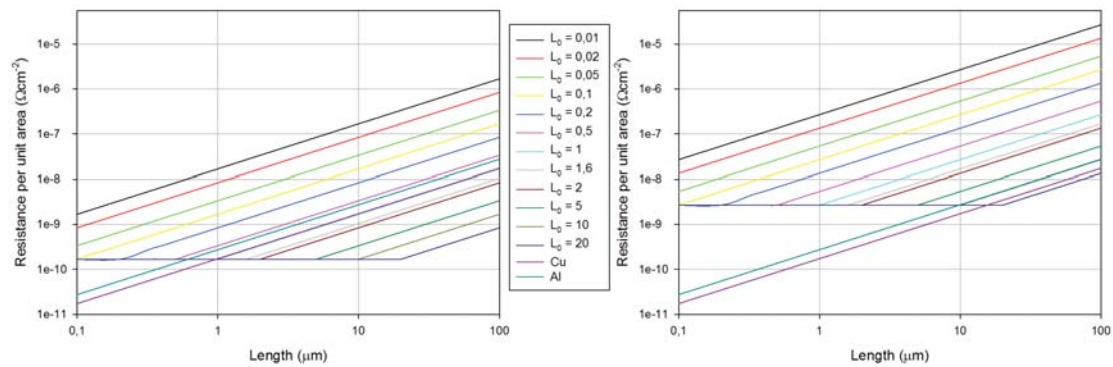


Figure 4.4: SWNT bundle resistance per unit area vs. length for different l_0 , a) ideal tight packing ($1.15 \cdot 10^{14} \text{ cm}^{-2}$), b) realistic packing ($7.22 \cdot 10^{12} \text{ cm}^{-2}$)

In figure 4.4a the resistances per unit area for the ideal bundle are plotted against bundle length, while varying the MFP (l_0) of the SWNT. Together with the different SWNT bundles the bulk resistance per unit area of Al and Cu are plotted. As was to be expected for SWNT bundles with a short MFP (below $1 \text{ } \mu\text{m}$), even with ideal tight packing, will have a bundle resistance that is always higher than that of bulk Al and Cu. For longer MFP, however, our ideal bundle outperforms both Cu and Al. It is thus important that the SWNT quality is high enough to allow the MFP to be limited by acoustic phonons only which should give a MFP of at least $1.6 \text{ } \mu\text{m}$ [44, 173].

In reality bundle density will be lower than tight packing. Current reported bundle densities are in the upper 10^{12} cm^{-2} . We can simulate such a bundle by setting the separation to 3 nm , while keeping the diameter fixed at 1 nm , which gives us a density of $7.22 \cdot 10^{12} \text{ cm}^{-2}$. The same length dependence for different MFP has been calculated and is displayed in figure 4.4b. As can be seen a MFP of $10 \text{ } \mu\text{m}$ has the same resistance per unit area as Al, while for a resistance per unit area lower than Cu the MFP should be close to $20 \text{ } \mu\text{m}$. Such high MFP values have not been reported for SWNT, and theoretical simulations only predict values between $1\text{-}10 \text{ } \mu\text{m}$ [174].

Next we investigate the influence of the diameter and the separation (which combined determines the density) on the bundle resistance per unit area. We again assume zero contact resistance. The results, together with the bulk resistance per unit area of a Cu and Al via with a length equal to $l_0 = 1.6 \text{ } \mu\text{m}$ are plotted in figure 4.5. Not surprisingly the resistance increases for lower density. What can clearly be seen is that only the smallest diameters combined with tight packing are able to deliver a resistance smaller

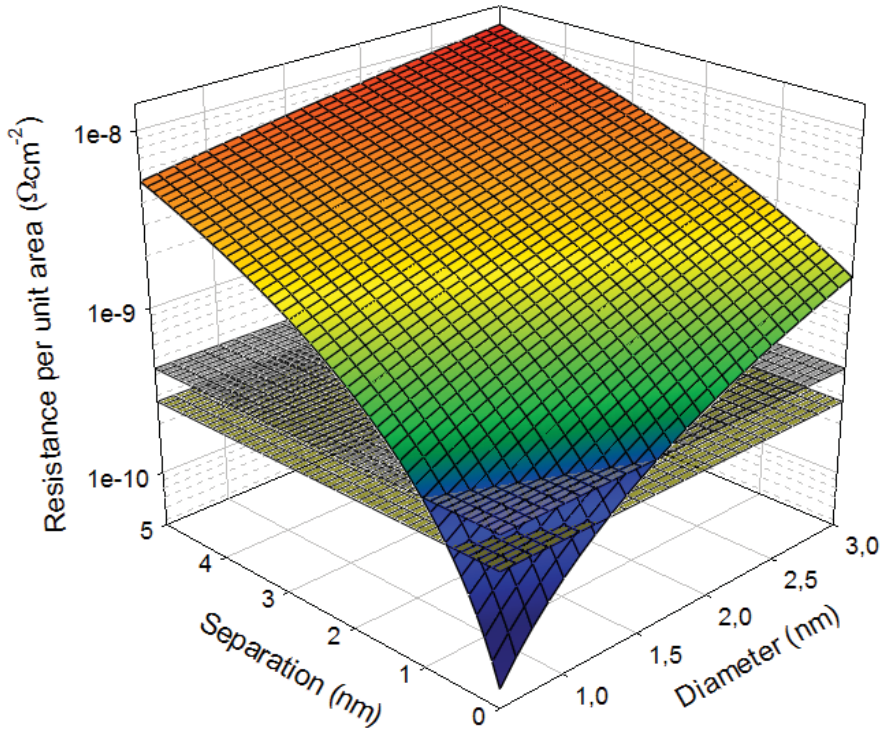


Figure 4.5: SWNT bundle resistance per unit area vs. tube diameter and separation, together with bulk resistance of Cu (brown) and Al (grey) with a length equal to l_0

or similar to that of bulk Cu and Al. Large diameter SWNT or bundles with a more realistic density ($10^{12} - 10^{13}$) will always result in a higher resistance.

In the previous two simulations we assumed a zero contact resistance. However as already discussed in section 2.2.1.4 forming a good Ohmic contact to a CNT is still a challenge. As the contact resistance is in series with the quantum resistance and has the same density dependency it can be treated as an up-shift in the total resistance. For values of R_c smaller than R_Q the influence of the contact resistance is relatively small. In case the value is comparable to the quantum resistance it effectively doubles the total resistance. However, in case of a bad contact ($100 \text{ k}\Omega$ and higher) the contact resistance will dominate the total bundle resistance.

From the simulations we can conclude that only small ($< 1.25 \text{ nm}$) and very dense ($> 5 \cdot 10^{13}$) tubes with a MFP above $1 \mu\text{m}$ and a contact resistance at least one order of magnitude smaller than R_Q have the potential to outperform bulk Cu and Al. In other cases the resistance of the SWNT bundle will increase towards values one or even two orders of magnitude higher than those of bulk Cu and Al.

4.2 Multi-walled nanotubes

4.2.1 Electric model

Multi-walled nanotubes have some interesting properties that were already discussed in chapter 2. As the inner shells in MWNT are packed close together (separated by only 0.34 nm), and the bigger diameter of the tubes allow more conduction bands to

participate, they look like the ideal candidate for interconnects purposes. In this section our SWNT model will be extended to incorporate the features of MWNT.

Every metallic shell of a MWNT adds another two conductive channels to the tube. If we take the diameter dependence out of the equation a bundle of 10 metallic SWNT would have the same resistance as a single MWNT with 10 metallic shells. In section 2.2.1 it was discussed that the diameter of a CNT has influence on the number of conduction channels, and a model published by Naeemi was presented (equation 2.6 and figure 2.5).

In the same paper where Naeemi et al. presented the model for the amount of conductive channels [43, 173] he also discusses the diameter dependency of the MFP. However, the papers he references state that their analysis on the diameter dependency of the MFP is derived for ‘small diameter, weakly disordered metallic nanotubes’ [174, 175]. It is unclear if this model is still valid for nanotubes between, say, 10-100 nm, as no theoretical data for those diameters is available. There is one publication reporting a MFP of 25 μm for a 100 nm tube, however no TEM images of the tube structure are shown, and there are no other publications of MFP this long [41].

It is thus unclear if the MFP increases for large diameter tubes, or instead levels of to some constant. Even if the MFP increases, at some point it is likely that defect scattering start to dominate. We therefore assume that the MFP can be regarded independent of diameter. Our model will thus give a more pessimistic view of the CNT resistance than that of Naeemi et al.

In the publication of Naeemi and Meindl where the model to calculate the number of available channels for a certain diameter is presented they also give an excellent model to calculate the amount of channels for a MWNT specified by its outer and inner diameter [43]. We will use this model, displayed in equations 4.8 and 4.9, to calculate the number of conductive channels. In the equations D_{max} is the maximum and D_{min} the minimum diameter of the MWNT. The parameter δ is the spacing between the shells of the MWNT, which is normally 0.34 nm, while a and b are constants with values of 0.0612 nm^{-1} and 0.425, respectively. For the ratio D_{min}/D_{max} values between 0.35 and 0.8 have been reported, with an average of 0.5 which we will use for our simulations [43].

$$N_{chan} = \frac{2}{3} \left(1 + \left\lfloor \frac{(D_{max} - D_{min})}{2\delta} \right\rfloor \right), \text{ for } D_{max} < 6 \text{ nm} \quad (4.8)$$

$$= \left(1 + \left\lfloor \frac{(D_{max} - D_{min})}{2\delta} \right\rfloor \right) \left(\frac{1}{2} a (D_{max} + D_{min}) + b \right), \text{ otherwise} \quad (4.9)$$

For every channel another parallel quantum resistance is added with a value of 12.9 k Ω . Besides a reduction in resistance every channel adds a parallel kinetic inductance and quantum capacitance. If we assume that all walls have the same potential and carry the same signal electrostatic capacitance between the walls of a MWNT can be ignored. As the walls of a nanotube form an electromagnetic shield only the outer shell has to be taken into account to calculate the electrostatic capacitance [173]. We can thus use the same model as displayed before in figure 4.1 in combination with equations 4.10-4.12.

$$R_{NT,MWNT} = \frac{2R_0}{N_{chan}} \Theta \left(\frac{l}{l_0} \right) \quad (4.10)$$

$$C_{Q,MWNT} = N_{chan} \cdot 200 \text{ aF}/\mu\text{m} \quad (4.11)$$

$$L_{K,MWNT} = \frac{8}{N_{chan}} \text{ nH}/\mu\text{m} \quad (4.12)$$

$$R_{c,MWNT} = \frac{2R_{c,swnt}}{N_{chan}} \quad (4.13)$$

The question remains how the contact resistance scales. Can it be treated as a resistance per tube, per wall or per conductive channel? From the work of Philip Wong et al. on SWNT FET modelling it can be concluded that the contact resistance exists between the metal and each channel as a Schottky barrier [176]. Thus even if a MWNT wall has multiple channels they must be treated as each having their own contact resistance. Equation 4.13 gives the contact resistance of a MWNT, when using the contact resistance of a SWNT as a reference (the factor two is due to the two channels of a SWNT).

Extending the MWNT model to bundles follows exactly the same reasoning as with a bundle of SWNT. Again the kinetic inductance and quantum capacitance can be neglected, while the electrostatic capacitance remains. As the model by Naeemi and Meindl already takes into account that 2/3 of the chiralities results in semiconducting tubes the final resistance of the MWNT bundle in our model is just that of a single MWNT divided by the number of tubes from our tight packing model, as displayed in equations 4.14 and 4.15.

$$R_{NT,MWNT-bundle} = \frac{R_{NT,MWNT}}{N_{CNT}} \quad (4.14)$$

$$R_{c,MWNT-bundle} = \frac{R_{c,MWNT}}{N_{CNT}} \quad (4.15)$$

4.2.2 Resistance simulations

As the MFP dependency for MWNT is assumed to be equal to that of SWNT the dependency of the resistance vs. length for different MFP is similar to that of SWNT. However, the resistance per unit area vs. density (diameter and separation) of MWNT should show a different behaviour. Although for bigger diameter tubes the density decreases they also gain additional channels. Thus two processes with opposite diameter dependence influence the resistance.

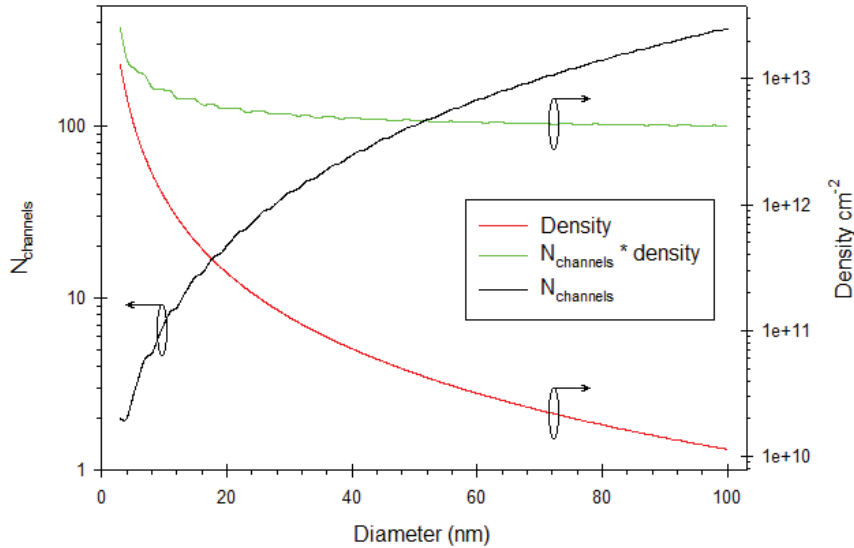


Figure 4.6: $N_{channels}$, density and product of channels and density vs. diameter

In figure 4.6 the number of channels per tube and the density are plotted against the tube diameter for $s = 0$. As can be seen the functions behave opposite from each other.

The product of the number of channels and the density is also plotted. While for small diameter the product is dominated by the decreasing density, for large diameter tubes the product of both flattens and becomes much less dependent on diameter. The results of this will be a resistance which is more or less constant for large diameter tubes.

Figure 4.7 confirms this behaviour, above a diameter of 40 nm the influence of the tube diameter on the resistance becomes small. As expected from figure 4.3 large diameter tubes also have a weak influence on the separation parameter. MWNT are not able to outperform the popular metals in the semiconductor industry, due to the low density caused by the larger diameter. Only very small diameter MWNT come close to the resistance per unit area of Al, but their resistance increases rapidly once the separation (and thus density) decreases.

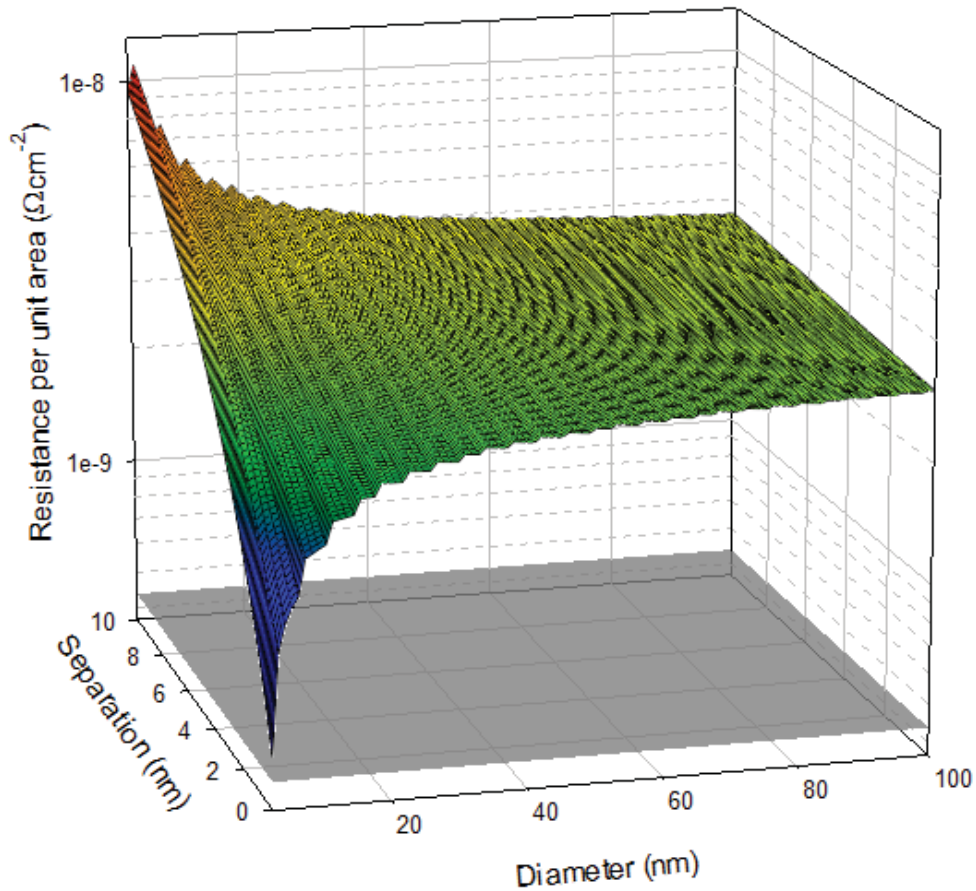


Figure 4.7: MWNT bundle resistance per unit area vs. tube diameter and separation, together with bulk resistance of Al (grey)

There is another parameter of interest for MWNT. This is the ratio D_{min}/D_{max} which determines how large the hollow core of the MWNT is, with lower ratios resulting in a smaller hollow core. As mentioned before ratio's between 0.35 – 0.8 have been reported, and in the previous calculations we assumed a ratio of 0.5. In figure 4.8 the resistance per unit area for different ratio's has been plotted. As expected the resistance increases rapidly if a bundle with a more hollow core is used, especially once the ratio gets higher than 0.5. The fluctuations in the plot are due to the floor function in the model from Naeemi (equations 4.8 & 4.9) which is used to calculate the number of walls that fit in the MWNT.

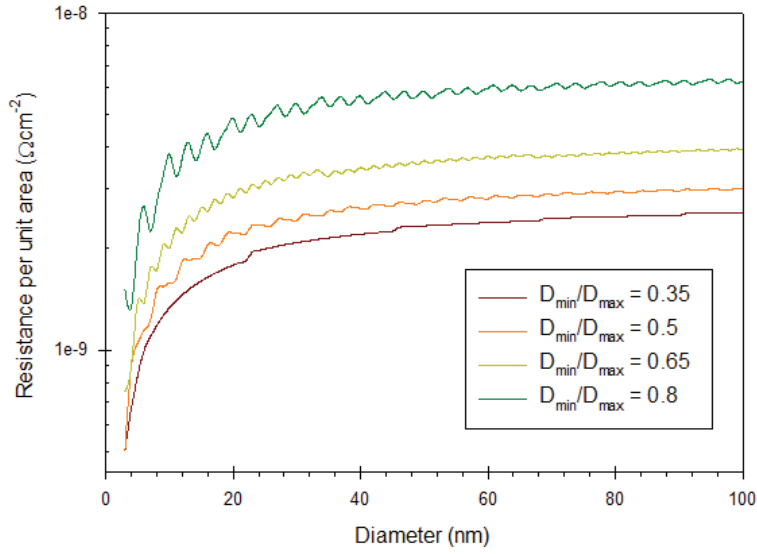


Figure 4.8: MWNT bundle resistance per unit area against tube diameter for different D_{min}/D_{max} ratio's

As the contact resistance of MWNT scales the same way as the quantum resistance again it causes an up-shift of the total resistance, as was the case for SWNT. All calculations done in this section were performed assuming an ideal contact, in reality the bundle resistance may thus be multiples or factors higher if the contact resistance is high compared to the channel resistance.

We can thus conclude that a MWNT bundle has a higher resistance than a SWNT model according to our models. For large diameter tubes the resistance starts to become relative independent on tube diameter. This can be advantages to minimize the influence of process variations on the bundle resistance, as diameters always show some spread even within the same bundle. For optimal resistance the hollow core of the MWNT should be as small as possible and the contact resistance small compared to the channel resistance.

4.3 Conclusion

After deriving the electrical models for SWNT and MWNT we can conclude that for bundles the quantum capacitance and kinetic inductance can be neglected and only the contact resistance, quantum resistance and electrostatic capacitance remain. Of these the electrostatic capacitance should be equal to that of a metal with the same size. We created a model to simulate the packing of the tubes for different diameters and separation distances between tubes.

From the resistance per unit area calculations we can conclude that the MFP of the, in this case 1 nm, tubes should be at least 1 μm to have the same resistance as bulk Cu. Still, very high density ($> 5 \cdot 10^{13} \text{ cm}^{-2}$) and small diameter tubes (below 1.25 nm) are required in order to outperform bulk Cu. For densities currently reported in literature the bundle resistance will be at least 1 order of magnitude higher. The contact resistance should be lower than the quantum resistance, otherwise it will dominate the overall bundle resistance.

In case of a MWNT bundle even for the smallest tubes with ideal packing the resistance per unit area only comes near to that of bulk Al. For tubes above 40 nm the resistance becomes diameter independent, as the lowering of the density for larger diameter and the generation of additional channels cancel each other. This can be advantageous to minimize process variation. The minimum diameter of the inner wall of a MWNT should be as small as possible to have an optimum resistance, above a ratio of D_{min}/D_{max} of 0.5 the bundle resistance increases rapidly. Again a long MFP and small R_c will ensure the lowest resistance.

CNTs are thus not very likely to outperform metals for the larger via sizes. However, their bundle resistance has the potential to stay within one order of magnitude from that of metals. SWNT have the advantage that they have the potential to be close or even outperform metals when the density is high, however for realistic densities the resistance increases fast. MWNT have the advantage that they are less sensitive to diameter and density variations, having a resistance one order of magnitude higher even at very low densities. If the increase in resistance is acceptable then the other properties of CNT, high thermal conductivity, reliability and high aspect ratio, can be interesting enough to select CNTs over metals.

It must be noted that the comparison with metals was performed using their bulk resistivity. In the processes we're interested in the dimensions are large enough that the metal resistivity approximately equals that of bulk materials. However, when the dimensions are reduced surface boundary and grain scattering will increase the resistance of the metals rapidly [6, 173]. At these dimensions a CNT bundle with a much lower density will be able to outperform metals, making CNTs an interesting candidate for future small dimension nodes [15].

Chapter 5

Process design

In this chapter the structures to measure the electric properties of carbon nanotube vertical interconnects and the processes available to create those structures are discussed. Our primary goal is to determine the resistance of a vertical interconnect (via) consisting of a bundle of CNT, as in chapter 4 it was determined that this parameter differs most from that of a metal via.

Before designing the structures the measurement goals will be listed, such that the final structures can be optimized for that purpose. Our primary goal is to measure the resistance of a CNT via versus:

- Average tube diameter
- Via length
- Different via configurations

The first two goals follow directly from the dependency of the resistance on CNT diameter and length, as discussed in chapters 2 and 4. Bronikowski [130] reported a growth rate dependency on bundle configuration (bundle size and separation between bundles). It will be interesting to investigate if a similar effect exists in our process and if it influences the resistance.

First the measurement structures will be selected and discussed in section 5.1, after which the fabrication process (section 5.2) and the mask lay-out (section 5.3) will be discussed. Finally some other possible measurement which are compatible with the resistance measurement structure are discussed in section 5.4.

5.1 Resistance measurement structures

To measure resistance several methods can be used [177]. The simplest one is a 2-point method, which uses two probes to the device one wants to measure. This method is the most simple, however, a measurement error is introduced as also the resistance of the wires is measured. In most cases this error is relative small, though.

In case of the 4-point method the amount of probes is doubled. Through one set of probes a known current is driven, while the other set measures the potential over the device the current flows through. As a good voltmeter has a high impedance a negligible current flows through the measurement wires and the resistance of these wires can be ignored, improving accuracy.

We decided to implement both measurement methods on a single die; the 4-point for its accuracy and the 2-point for its simplicity. In figure 5.1 a 3D sketch of the 4-point

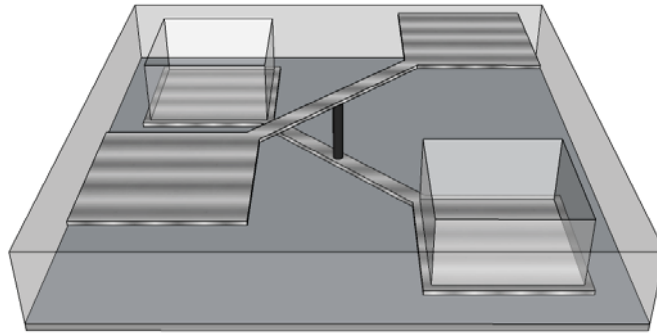


Figure 5.1: 3D image of 4-point probe structure

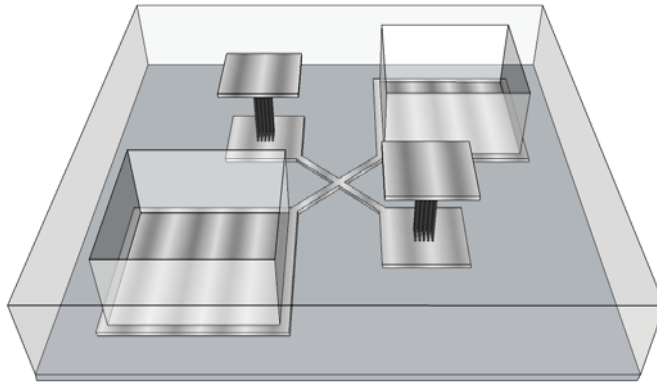


Figure 5.2: 3D image of 2-point probe structure

probe structured is shown. As we want to measure a vertical structure we need to contact both the contacts at the bottom and top of the structure. The structure is completely symmetrical, with the nanotube via in the centre. By using the left contacts for the applied current and the right contact for the potential measurement the resistance can be measured accurately.

Figure 5.2 shows the 3D sketch of a 2-point probe structure. This structure can either be used to measure the resistance of a single via or two vias in series connection. The resistance of the metal interconnect between the vias can be subtracted by measuring the resistance between the two bottom probes (assuming the resistance of the contact pads is negligible compared to the much smaller connection wire).

Two structures similar to the one in figure 5.2 are also placed on the same die. One in which no bottom contact pads exist, instead two metal vias are formed with the same size as the top contact pad to interface the bottom contacts. Another one has no bottom contact at all and can only be used to measure two vias in series. On the top metal level a wire resistance measurement structure with the same dimensions as the bottom layer is placed. Of course the thickness of the first and second metal layer should be the same to give a reasonable approximation if this top structure is used to correct the resistance.

5.2 Fabrication process

Now the measurement structures have been selected the next step is to create a suitable process, or processes, to create such a structure on a silicon substrate. Before we do that, however, we need to select the materials we want to use.

As a substrate we will use simple test wafers. In our case we use p-type, but choosing n-type wafers should not influence any measurements. There is perhaps one small advantage when using p-type wafers, which is a lower sensitivity to alignment errors on the EVG-120 coater/developer, according to the responsible process engineer.

For the 1st and 2nd metallisation the default interconnect material used in the DIMES cleanroom will be used, which is aluminium with 1% Si to prevent spiking. For the catalyst our first choice is Ni, as it is available in the Trikon Sigma sputter coater and there is experience using this material. The other known catalysts (Fe, Co and Pd) are only available in the class 10000 e-beam evaporator, but might in the future be used in the new class 100 e-beam evaporator.

It is important to form a good ohmic contact between the CNTs and the metal layers to reduce the influence of the contact resistance on the measurements and reduce the overall resistance. As mentioned in section 2.2.1.4 two popular materials in literature to form a good contact are titanium and palladium. As Pd is at the moment an exotic material in the semiconductor industry our choice goes out to Ti, which is again available in the Trikon Sigma sputter coater. As Ti has a higher resistivity than Al we don't want this layer to be too thick. According to research by Nihei et al. the layer should be at least 6 nm thick [55], we decided to increase the thickness slightly towards 10 nm. In a later stage the thickness of the contact layer can be optimized.

Finally as isolation material between the metal layers SiO₂ deposited by PECVD will be used. To isolate the subsequent structures from each other the first step will be the deposition of a thin high quality oxide layer using thermal oxidation. Although this is at higher temperature than our restraint of 550 °C this will be the very first step before any metallisation and therefore doesn't give any problems. Such a thermal oxidation step is also not required for the production of CNT vias.

There are two orders in which the structures can be made. It is possible to first grow the CNTs followed by oxide deposition to isolate the metal levels. The second possibility is to deposit the oxide first, make holes where the vias should be and then grow CNTs. As the choice of the method influences the environment in which the CNTs are grown we decided to create a process for both of them, with the goal to determine which performs better.

5.2.1 Oxide after growth (P2748)

In this process first the CNTs will be grown, after which the oxide isolation between the metal layers will be deposited. In appendix B.2 the P2748 flowchart for this process can be found.

In figure 5.3 a cross-sectional overview of the P2748 (oxide after growth) process can be found. The starting material is a p-type wafer which has been covered by oxide using thermal oxidation (figure 5.3a). The purpose of this first step is to electrically isolate the structures from each other. The second step (figure 5.3b) is the formation of a thick oxide layer at the backside of the wafer. This step is to remove back side contamination once the Ni has been deposited.

The next step is the deposition of all the three metals in one step without breaking the vacuum of the sputter coater in-between depositions (figure 5.3c). This will make sure no native oxide layer will form between the metals, which can increase the resistance between layers and the contact resistance of the CNTs [125]. After the metal deposition the backside oxide will be removed in the MEMS lab to prevent contamination of the class 100 equipment (figure 5.3d).

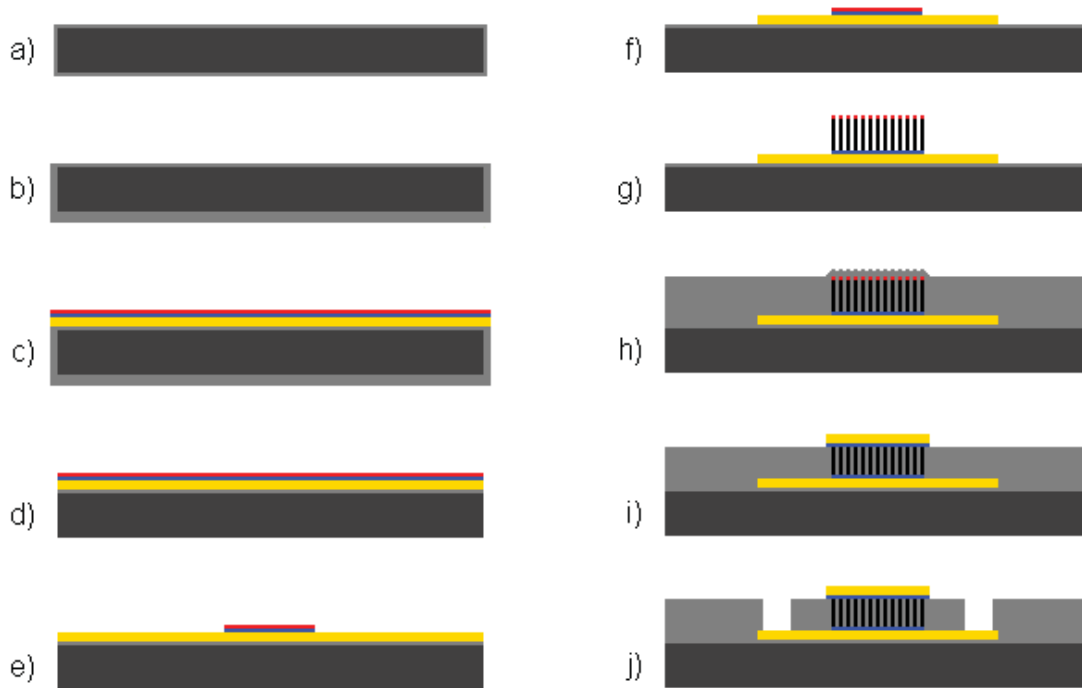


Figure 5.3: Overview of the P2748 process. Dark grey: Si, light grey: SiO₂, yellow: Al, blue: Ti, red: Ni, black: CNTs. Figure is not to scale.

Back in the class 100 cleanroom the wafer will be coated, exposed and developed using the first mask to pattern the catalyst. The short wet etching of the Ni and Ti layer will be performed in the MEMS lab to prevent contamination, the result is shown in figure 5.3e. The etching should be as short as possible, as the etchant will also remove the (much thicker) Al layer. The next step is the patterning of the 1st Al layer, again in the class 100 using a second mask. The wet etching will again be performed in the MEMS lab to prevent contamination, the result is shown in figure 5.3f.

After this the CNT growth can be performed which should result in a forest of aligned CNTs with a length longer than the required length of the via (figure 5.3g). This step is followed by the deposition of oxide to isolate the two metal layers (figure 5.3h). The oxide will also cover the tips of the CNTs as demonstrated by Li et al. [18]. To open up the tips of the CNTs chemical mechanical polishing (CMP) or etching can be used. The advantage of CMP is that it will planarize the surface.

In both cases also part of the bulk oxide will be removed, thus this layer should be thicker than the final required thickness. After this the top Ti contact layer and the 2nd Al layer can be deposited and patterned using a third mask, the result is shown in figure 5.3i.

To improve the contact resistance the entire wafer can be annealed to a temperature of 400-500 °C. As mentioned in section 2.2.1.4 this can aid in the formation of TiC. The final step shown in figure 5.3 is the opening of access holes to the first metal layer using the fourth and final mask.

This process has the advantage that the CNTs are not obstructed during growth and the process gases can easily reach the catalyst, even with a base growth mechanism. Another advantage is that the metal layers can be deposited in one step, which optimizes the contact between the different layers.

However, the process also has some disadvantages. Etching the Ni and Ti will also etch the Al as the solutions needed to remove the Ni and Ti attack the soft Al. Therefore the etching should be short to prevent too much over etching of the Al layer. A second disadvantage is that when oxide is deposited after the CNT growth the tips of the tubes will be covered. A complex CMP or etching step is needed to remove the unwanted oxide, which will also decrease the total oxide thickness. Currently no CMP recipes are available for this purpose, these should be developed in the future.

The main disadvantage, though, is that during the first growth experiments (section 6.2.1) it was found that covering the catalyst layer with photo-resists negatively influences the growth. To circumvent this problem a lift-off procedure was designed, which will be discussed in section 5.2.3.

5.2.2 Oxide before growth (P2752)

In this process the CNTs are grown in holes which are etched in the oxide layer separating the metal layers. In appendix B.3 the complete process flow of this process can be found.

Figure 5.4 shows a cross-sectional overview of the P2752 (oxide before growth) process. The first two steps (figure 5.4a, b) are the same as in process P2748 and are the deposition of thermal oxide for isolation and a layer of backside oxide against contamination. The next step is the deposition and patterning of the 1st Al layer, which can be done with the same mask as the P2748 process (figure 5.4c).

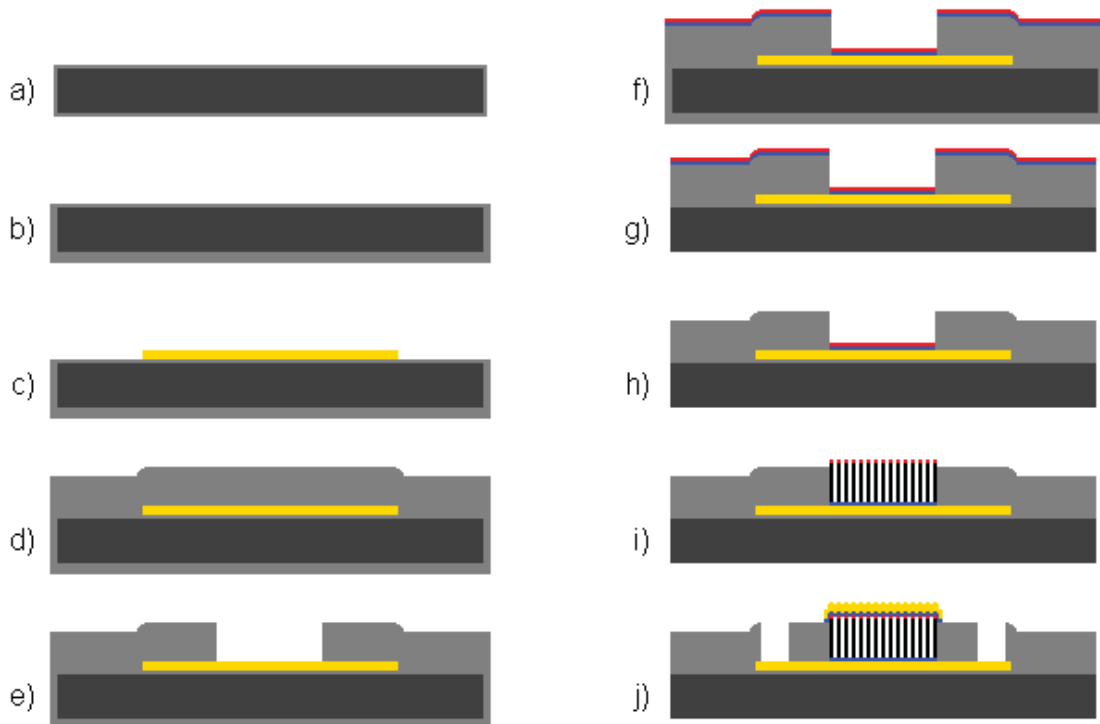


Figure 5.4: Overview of the P2752 process. Dark grey: Si, light grey: SiO₂, yellow: Al, blue: Ti, red: Ni, black: CNTs. Figure is not to scale.

After this the metal layer isolation oxide will be deposited (figure 5.4d) and patterned (figure 5.4e). The patterning of the oxide can be done with the same mask from P2748 if negative resist is being used. Next the contact metal and catalyst are sputtered, to remove the native oxide the sample is first treated with a plasma in the sputter coater

before depositing the metals. After this the backside oxide is removed with the same purpose as P2748: to prevent contamination of class 100 equipment.

The next step is the removal of the Ni and Ti at the spots no CNTs should be grown, resulting in the structure of figure 5.4h. Again the catalyst mask can be used, this time with positive resist. After this the sample is ready for CNT growth (figure 5.4i).

If the density of the growth is high enough it is possible to directly deposit the Ti contact layer and the second Al layer (assuming the length of the tubes is only slightly longer than the oxide thickness). For low density growth it might be required to first deposit oxide to fill the via in order to keep the second metal layers relative uniform. In this case CMP or etching would be required to expose the CNT tips. For patterning the same mask can be used as in P2748.

Again it is possible to perform thermal annealing to improve the contact between the metal layers and the CNTs. The last step is the opening of the contact holes to the first Al layer, which can again be done with the same mask as in P2748 (figure 5.4j).

This process has the advantage that with high density growth a CMP step can be avoided. Again the contact between the Al and Ti layer should be good due to the native oxide etching performed in the sputter coater before the Ti deposition. It is also possible to realize this process using the exact same masks of the P2748 process if negative resist is used. It must be noted that this resist is not frequently used in our cleanroom, so it is likely this part has to be optimized for our purpose.

The disadvantage is that the catalyst has to be deposited in the via holes, which might give difficulties when the aspect ratio is high (especially with sputtering). If the catalyst would be deposited before the oxide it cannot be partially removed after the oxide has been deposited. As all known catalyst for CNTs are easy diffusers in silicon which negatively affect the performance of transistors we want to minimize the amount of catalyst remaining. Patterning the catalyst first as was in P2748 and depositing the oxide afterwards will give difficulties when the oxide has to be etched away. Making a hole without removing the extremely thin catalyst layer will require very accurate control over the etching process.

5.2.3 Lift-off

As will be discussed in section 6.2.1 during the first growth experiments it was discovered that coating the catalyst with photo-resist and/or the cleaning with EKC505 have a negative influence on the CNT growth, preventing good activation of the catalyst layer.

By using a lift-off process it is possible to prevent photo-resist from being deposited on top of the catalyst layer. The required process steps with the latest optimized values can be found in appendix B.4. In figure 5.5 a schematic overview of a lift-off process on a wafer which already has a first Al layer is shown. Such a patterned layer of Al can be obtained by following the P2752 process and stopping before the interlayer isolation oxide is deposited (step 12 in appendix B.3 and figure 5.4c).

It is also possible to use the lift-off process after oxide deposition and patterning has been performed. In this case it is best to keep the resist layer used to pattern the oxide. If a new layer resist is used instead, the alignment with the previous layer should be almost perfect as the smallest features are just one or a few micron. After this the metal can be deposited in the e-beam evaporator. Wet instead of dry etching can be used when lift-off is found to be difficult after dry etching (due to, for instance, resist thinning).

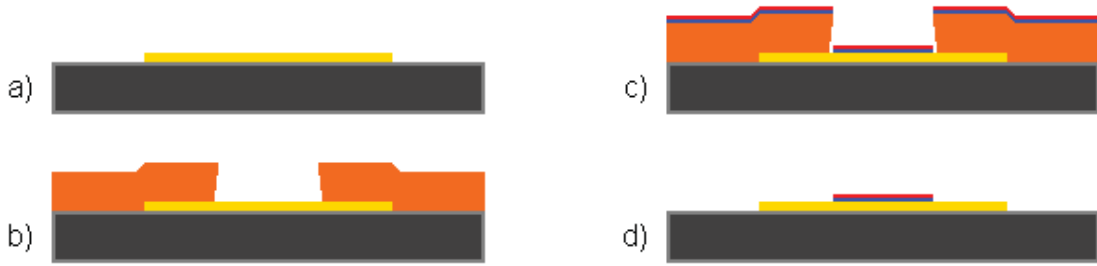


Figure 5.5: Overview of the lift-off process to obtain ‘oxide after growth’ wafer. Dark grey: Si, light grey: SiO₂, yellow: Al, blue: Ti, red: Ni, orange: resist. Figure is not to scale.

When an oxide after growth sample is required the next step is to coat the wafers with negative resist and to expose it using the catalyst mask. After development the unexposed areas will have no resist remaining (image 5.5b). For optimal lift-off usually a slight negative slope is created by optimizing the exposure time. The reason for this becomes clear in figure 5.5c when the contact metal and catalyst layer are deposited using e-beam evaporation. For a slightly positive slope metal could have been deposited on the side of the photo-resist, making successful lift-off more difficult as the acetone cannot reach the photo-resist and the unwanted and wanted metal layers are physically connected. A negative slope prevents this.

The final step is the removal of the remaining resist using an acetone bath (figure 5.5d). This dissolves the photo-resist and will strip (or lift-off) the metal layer on top of it. After this the wafer is ready for CNT growth.

As mentioned before at the start of this section an advantage of this process is that no photo-resist is deposited on the catalyst. Another advantage is that no etching is required to pattern the contact metal (Ti) and catalyst layer (Ni). The etchant normally used for this (BHF:HNO₃(%65):H₂O=1:1:50) will also etch Al due to the HF which is part of it.

The disadvantage of the lift-off process is that the metal deposition has to be done in the e-beam evaporator as wafers with photo-resist are not allowed in the sputter coater. In this case no plasma etching step can be done before metal deposition which implies that native aluminium oxide will exist between the Al and Ti layer, which can increase the resistance of the via.

5.3 Masks layout

As became clear from the previous section in which the process flows were discussed all of them can be made using four masks in combination with negative and positive resist. Masks are expensive to fabricate, thus minimizing the amount of masks required is a good habit.

The four masks required are:

1. *Metal1*: for patterning the first metallisation layer
2. *Catalyst*: for patterning the catalyst with positive resist using etching or with negative resist using lift-off and for patterning the oxide using, again, negative resist
3. *Metal2*: for patterning the second metallisation layer

4. *Contact*: for opening up the oxide layer between the metallisation layers or creation of metal vias

The measurement structures will be placed in 10x10 mm dies, which can be put multiple times on the wafer. This enables the collection of sufficient measurement points from a single wafer to average values under certain growth conditions and also allows the measurement of resistance spread across the wafer. The lay-out of the measurement structures die can be found in figure 5.6.

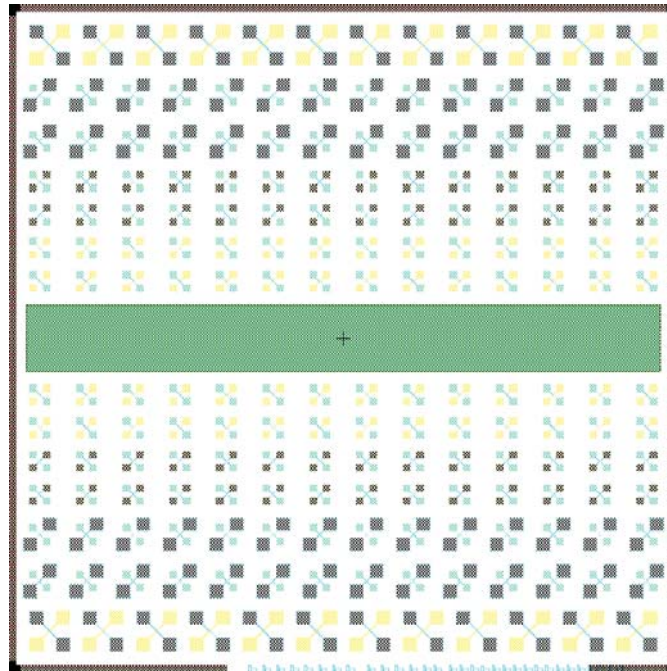


Figure 5.6: Overview of the die lay-out. Mask levels: blue: metal 1, green: catalyst, yellow: metal 2, black: contact.

The bar in the centre of the die enables quick visual inspection if growth has taken place (carbon nanotubes appear black). Beside of being a visual check it can also be used for Raman and TEM analysis of the sample. The actual via bundles are too small for easy Raman or TEM analysis, but can be easily investigated by SEM. The structures above and below the bar are the same, except for the fact that the catalyst will be square above the bar and a circle below the bar, in order to check if one of these geometries performs better.

On the top and bottom of each die the four point measurement structures can be found, see also figure 5.7(a). The next two rows are the two point structures with a measurement hole to the first metal layer, enabling measurement of a single CNT bundle (figure 5.7(b)). The following two rows are the same structure without the large bottom contact pad (figure 5.7(c)). In this case the hole can be filled with Al, although this can be not done independently of the other structures. The last two rows are structures which can only be used to measure two CNT bundles in series connection (figure 5.7(d)).

As can be seen in figure 5.7 the contact areas are 100x100 μm , to allow the use of contact needles. For the metal 1 layer contacts the area is four times bigger, to make sure the needle can also touch these pads for thicker oxides. The contact openings are slightly smaller than the actual contact pad in order to prevent damage to the wires between the pads due to over-etching. The design is made in such a way that the maximum

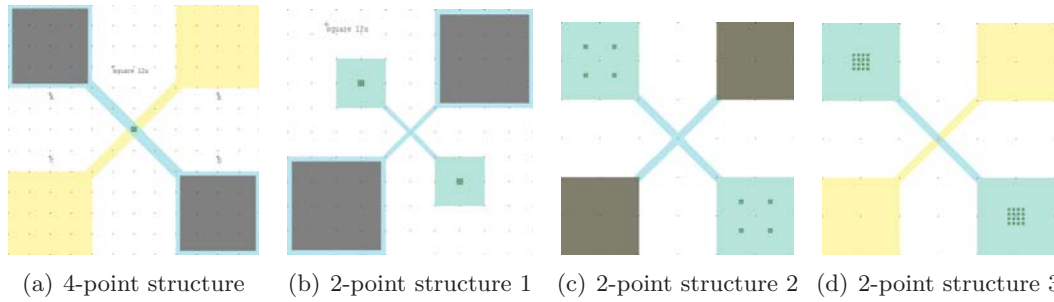


Figure 5.7: Overview of measurement structures. Scales between figures are not equal; distance between small dots equals $50\ \mu\text{m}$.

alignment error between two mask levels may be up to $5\ \mu\text{m}$.

To measure the influence of the bundle configuration on the resistance, different configurations have been applied, as can also be seen from figures 5.7(c) and 5.7(d). These structures are meant to investigate the influence of via geometry on the resistance, as mentioned in the start of this chapter. An overview of the included configurations can be found in table 5.1. Configurations with the same total area are placed within the same column. The spacing between individual vias in configurations consisting of multiple bundles is $3\ \mu\text{m}$, unless otherwise specified.

Table 5.1: Via configurations

	Edge length / diameter (μm)							
4-point	1	2	3	4	6	8	10	12
				4x 2	4x 3	4x 4	4x 5	
2-point	1	2	3	4	6	8	10	12
						4x 4	4x 5 ^a	4x 6
						16x 2	25x 2 ^b	16x 3
							100x 1 ^c	

^a3, 4, 8, 16 or $32\ \mu\text{m}$ spacing

^b3, 4, 8 or $16\ \mu\text{m}$ spacing

^c2, 4 or $8\ \mu\text{m}$ spacing

As could already be seen in the flowcharts of P2748 and P2752 (appendixes B.2 and B.3) growth will be performed in an external facility, as the cleanroom has no CNT growth capabilities at the moment. Contamination is more difficult to prevent in external systems, therefore processing after growth will be performed in the MEMS lab. Besides contamination issues the external systems don't support 4" wafers, such that wafers have to be cut into smaller pieces. As the waferstepper cannot be used for contaminated wafers, and doesn't support pieces of wafers, exposure will be done on the contact aligner in the class 100 before growth and the MEMS lab after growth.

To make the mask design compatible with the contact aligner the die design has been copied into a $10\ \text{mm}$ die size contact aligner mask template (FWAMv351g10a-1). Additional alignment markers have been added to allow for accurate alignment when the wafers is cut into 4 equal pieces along the (100) crystal plane in the centre of the primary and secondary flat. The complete mask design can be found in figure 5.8.

Finally, at a certain point it became clear that low temperature processing in the equipment available in NanoLab was not possible (see section 6.3.1). It was decided to

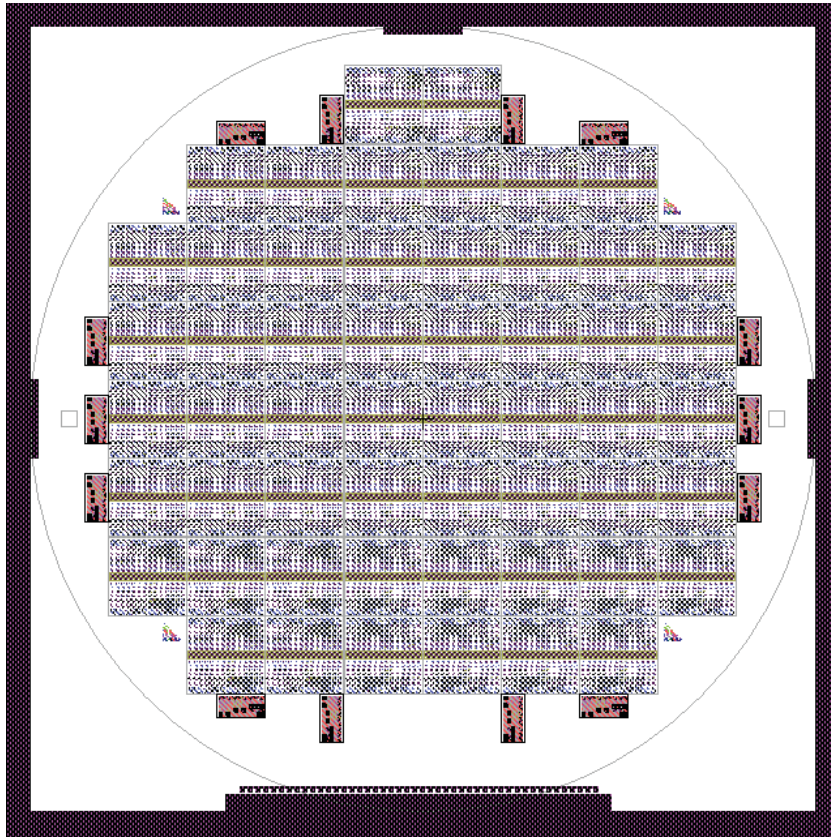


Figure 5.8: Lay-out of the contact aligner masks

replace the Al layer with $1\ \mu\text{m}$ Ti, which is resistant to temperatures over $1000\ ^\circ\text{C}$ and available in the sputter coater. Etching of the Ti was done using the Trikon Omega 201 ICP dry etcher using the available recipe for $1\ \mu\text{m}$ Ti.

5.4 Other possible uses of the designed structures

Although the process and wafers have been primarily designed for the measurement of the resistance it is possible to use the created structures for other purposes. In this section these functions will be shortly discussed.

5.4.1 Reliability testing

One possibility is the usage of the four-point probe to evaluate the electrical reliability of the structures by passing a large current through the via as described, for instance, by Wei et al. [54]. The four-point structures are better suited for this as the cross-sectional area of the Al lines is much bigger than the two-point structures, allowing for a higher current density to be passed through the vias.

If we assume that the Al lines can maximally carry a current density of $10^5\ \text{cm}^{-2}$ the default four-point structure using two contacts on both levels (to maximize the area) should survive a current of 70 mA. If a thicker layer of Al is deposited instead of the default $1.4\ \mu\text{m}$ this maximum current can be increased (for instance $2\ \mu\text{m}$ allows a current of 100 mA and $5\ \mu\text{m}$ 250 mA).

The current density through a tube is normally calculated by using the cross-sectional area of the tube determined by its diameter [54]. As an example we will calculate the maximum current through a 1x1 μm bundle of 1 nm CNTs with a density of 10^{13} cm^{-2} . This results in a total of 100,000 tubes in the bundle, each with an area of $7.85 \cdot 10^{-15} \text{ cm}^2$, the total area is thus $7.85 \cdot 10^{-10} \text{ cm}^2$. If we assume a maximum current of 100 mA allowed by the Al lines this would allow testing of a current density of $1.27 \cdot 10^8 \text{ cm}^{-2}$ through the CNTs, which is already considerable higher than that of metals. Equation 5.1 can be used to calculate the maximum CNT current density allowed, here $I_{Metal,max}$ is the maximum allowed current by the structure, d is the average diameter of the tubes, A is the via area and D the tube density.

$$J_{CNT,max} = \frac{I_{Metal,max}}{\pi(d/2)^2 AD} \quad (5.1)$$

5.4.2 Thermal conductivity

Measuring thermal properties at small scale is difficult. For instance if normal thermocouples are used the thermal mass of these sensors is often large compared to the object one wants to measure, which introduces a large error. To measure the thermal conductivity of CNT (bundles) many different methods have been used, one of them being the so-called 3ω -method [47–49].

In this method a CNT (bundle) is often suspended above a gap between two electrodes. After this a harmonic signal of frequency ω is passed through the CNT. This in turn will result in a power dissipation with a 2ω component. This power dissipation in the sample will introduce a temperature increase which is proportional to the electric power and thus also has a 2ω component. As the electrical resistance depends on temperature this will induce a resistance change, again with a 2ω component.

This changing resistance will induce a third harmonic voltage drop across the sample (hence the name 3ω -method). By measuring this 3ω component the AC fluctuation of temperature can be determined when the temperature dependence of the CNT resistance is known. This can be measured by simply heating up or cooling the sample and measuring the resistance by a 4-point probe method.

Often a lock-in amplifier is used to supply an accurate harmonic signal and measure the third harmonic component, more details can be found in the publications mentioned before. After the AC temperature is known the thermal conductance can be determined, and combined with the geometric information of the CNT (bundle) the thermal conductivity.

The question which arises is if our 4-point measurement structure could be used together with the shortly described 3ω -method to measure the thermal conductivity of our bundle. There are a couple of difficulties involved. One of them is that only the resistance change due to the heating should generate higher harmonics. Beside that only the CNT bundle should be heated, not the Al lines otherwise the measured conductance will be a combination of both. Finally the heat of the CNT bundle should ideally be removed from the ends of the bundle (to approach a ‘suspended’ bundle), which means heat loss into the oxide should be minimal. If the loss to the substrate is not neglectable it should be included as was done by Wang et al. [49].

Non-linear parasitic components like Schottky barrier diodes may introduce a third harmonic voltage component and should thus be avoided. This means that the contacts between the different electrical conductive materials should be Ohmic. Verifying if this is indeed the case can be done by measuring the I-V characteristics and investigate if

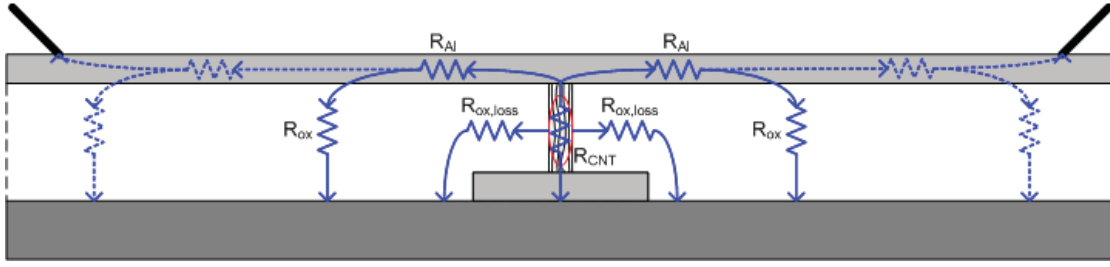


Figure 5.9: Cross-section along diagonal of 4-point structure including zeroth order thermal model

the plot is a straight line through the origin. Measuring the resistance vs. temperature can also be used, as Schottky diodes have an exponential temperature dependency, while that of CNTs should be linear. Finally, the harmonic frequency should be selected in such a way that resonance points are avoided [48, 49].

Next we investigate the thermal properties of our structure using zeroth order modelling. Heat generated in the CNT bundle will move towards the two Al contacts. The bottom contact is directly placed on the substrate, which is at ambient temperature. As the contact area is large the bottom contact will remain at ambient. Another flow of heat will go into the top Al contact. This heat energy will be spread out by the Al layer and move towards the substrate through the oxide.

The top Al layer should remain at ambient in order to not introduce an error in the measurements. For the dimensions we assume that the layer is $25\ \mu\text{m}$ wide and $2\ \mu\text{m}$ thick. The length from the CNT bundle to the contact pads is $140\ \mu\text{m}$, these big pads are assumed to be at ambient temperature. For the CNT bundle length and oxide thickness we take a length of $2\ \mu\text{m}$. As the oxide area underneath the Al layer is large most of the heat energy will flow towards the substrate through this oxide.

After a length of $30\ \mu\text{m}$ the thermal resistance of the Al lines equals the thermal resistance of the oxide underneath this line area (assuming a thermal conductivity of $237\ \text{W/m}\cdot\text{K}$ for Al and $1\ \text{W/m}\cdot\text{K}$ for SiO_2). The thermal energy will thus be carried away towards the substrate rather fast. The thermal resistance of the oxide and the Al line piece at this length equals: $R_{Al} = R_{ox} = 2600\ \text{K/W}$. As this mechanism works both ways of the line (parallel connection) we take this value as the thermal resistance from the top of the CNT bundle towards the substrate.

The thermal resistance (R_{CNT}) of a $1\times 1\ \mu\text{m}$ CNT bundle with a length of $2\ \mu\text{m}$, a theoretical thermal conductivity of $3000\ \text{W/m}\cdot\text{K}$ and a fill factor which is 10% of the bundle dimensions (this is approximate a density of $10^{13}\ \text{cm}^{-2}$ with a tube diameter of $1\ \text{nm}$) is approximately $6700\ \text{K/W}$.

If we assume the centre of the CNT to be at the highest temperature the heat flowing to ambient ideally ‘sees’ half R_{CNT} in a parallel configuration, which is a total thermal resistance of $1675\ \text{K/W}$. However, in our case the top contact is not directly connected to ambient, but with a thermal resistance of $2600\ \text{K/W}$. Now the heat flow ‘sees’ a resistance of $2140\ \text{K/W}$, which is 30% higher than the ideal case.

The fact that the top contact is not directly connected with the ambient will thus introduce an error in the measurement, but this error should be small enough to measure the order of magnitude of the thermal conductivity of the CNT bundle. This can be sufficient to evaluate if the CNT bundle performs better than metals.

The error can even be reduced by using a higher signal frequency. The thermal mass of the oxide and Al layer, corresponding to a length of $30\ \mu\text{m}$, is in the order of

$5 \cdot 10^{-9}$ J/K. This means that heat with a frequency around 25 kHz equals the RC cut-off frequency of the thermal structure, reducing the thermal impedance. As the heating frequency is double the signal frequency only half of this frequency has to be generated by the lock-in amplifier.

Determining the thermal conductance of the CNT bundle will be easier if it can be assumed no heat is lost towards the oxide. We approximate the thermal resistance of the oxide surrounding the CNT bundle by a cylinder, which has a thermal resistance that equals $R_{cyl} = \ln r_2/r_1(2\pi\lambda L)^{-1}$. For the internal radius (r_1) we take a value of 0.5 μm . If the heat is generated in the centre of the bundle with length 2 μm and the heat energy spreads out uniform through the oxide it will reach the substrate (ambient) after 1 μm , for r_2 we thus take 1.5 μm . This gives a thermal resistance of 87 kK/W, which is much higher than the thermal resistance of the CNT bundle.

Thus heat loss towards the oxide should be minimal. If it is possible to deposit the second metal layer without depositing oxide in the CNT cavity first, this value will even become much higher. In that case the bundle will be in vacuum as the deposition is done under vacuum conditions.

In conclusion, from these zeroth order calculations it follows that the structure can be used in combination with the 3ω -method described in this section. There should exist no non-linear components in the electrical path (for instance Schottky diodes) to make sure the third harmonic is created solely by the heating of the CNT bundle. An error will be introduced by the top contact to the bundle, which is not directly connected to ambient. Still the order of magnitude of the thermal conductivity should be measurable, and this error can be reduced by using an electric signal in the order of 10 kHz.

5.5 Conclusion

We will use two and four-point measurement structures to measure the resistance of the grown CNT bundles against average diameter, length and for different via configuration. To create these structures several different processes, which are compatible with the contamination requirements in our cleanroom, have been created.

The ‘oxide after growth’ (P2748) process deposits interlayer oxide after growth, which means the CNT growth is not obstructed by oxide. Another advantage is that the contact between the metal layers is optimal. Disadvantages are a difficult catalyst etching step and the need for CMP or etching to remove the oxide from the CNT tips.

Another process, dubbed ‘oxide before growth’ (P2752), grows CNTs in holes created in the oxide between the metals. This eliminates the need for CMP. Disadvantages are that negative resists is required, the CNTs grow inside holes, and that metal deposition inside high aspect ratio holes can be difficult.

A variant to these processes was designed using lift-off to prevent the catalyst layer from being covered by photo-resist, which was demonstrated to reduce growth quality in section 6.2.1. The disadvantage of this process is that a native oxide layer will exist between the Al and the subsequent contact and catalyst layer, which will likely increase resistance.

Beside being able to measure resistance it was also explained that the structures can be used to measure electrical reliability and thermal conductivity with the 3ω -method. No special requirements are required. However, in both cases the measurement would benefit from slightly thicker (2 μm) metal layers.

Chapter 6

Carbon nanotube growth results

In this chapter the results from different growth experiments will be presented and evaluated. The growth is mainly analysed by Scanning Electron Microscopy (SEM) and Raman spectroscopy. On some samples Transmission Electron Microscopy (TEM) was performed. Readers unfamiliar to Raman spectroscopy on carbon nanotubes are invited to read the short introduction to this subject in appendix C.3.

The first section (6.1) of this chapters is about the growth experiments in the Novellus Concept One PECVD in the DIMES class 100 clean room. The second section (6.2) treats the experiments done on a 2" BlackMagic II R&D (PE)CVD machine at AIX-TRON in Cambridge, UK. The third section (6.3) discusses the experiments performed at NanoLab Inc. in Newton, MA using the custom made equipment available.

6.1 Experiments using Novellus Concept One PECVD

In this section the attempts to grow nanotubes in the Novellus Concept One PECVD (Novellus) in the DIMES class 100 clean room are described. The Novellus is an industrial, recipe driven PECVD which is used for the deposition of several different types of silicon dioxides (doped or undoped and TEOS), silicon nitride and silicon carbide. It has a RF-PECVD power supply combined with a low frequency power supply and shower head electrodes. The substrate heater can reach a maximum temperature of 400 °C. Available gases controlled by mass flow controllers are N₂, Ar, NH₃, CH₄, CH₄ and H₂ (1:3) mixture, SiH₄, N₂O, O₂, PH₃, B₂H₆ and C₂F₆.

The reactor has eight wafer holders and in normal depositions the wafers are transported from stage to stage till the required thickness is achieved on the last stage. Power and gases are divided equally over the eight stages. For our experiments switching of the plasma followed by transporting the wafer and switching it on again is not favoured for growth. Therefore we operate the Novellus in uniformity mode with a wafer on the 4th stage.

In previous experiments performed by dr. J. Derakhshandeh the growth at powers between 400 and 1600 W was attempted (this is the total power, the stage power is approximately 1/8 of this). The substrate holder temperature was set to the maximum of the Novellus, which was 420 °C in early experiments and the current 400 °C later on. The gases used were pure NH₃ for the activation and CH₄ for growth, with flow rates of 3000 sccm (Standard Cubic Centimetres per Minute) when 1.6 kW power was used and 300 sccm for lower power. The pressure was set to roughly 2.67 mbar with a plasma power of 1.6 kW and to roughly 0.8 mbar for the lower powers. Under these conditions

no growth was observed. In most cases the catalyst layer was activated and sometimes a-C was observed.

For the new experiments silicon wafers with 10 nm Ti as contact layer and 3 nm Ni as catalyst were prepared using the P2700 process, which can be found in appendix B.1. Shortly, the Ti and Ni were deposited using sputtering and a pattern was transferred into the Ni using photo lithography and wet etching. The etchant was unable to significantly etch the Ti layer. Although this was not required it would've increased the contrast between the areas covered with catalyst and the uncovered areas. This can aid in analysing the samples with the SEM by making focusing more easy. The samples were analysed on a Philips FEI XL50 SEM which supports full 4" wafers.

The experiments described here mainly focus on higher power growth. The plasma was stable at powers of 1.8 and 2 kW, however no complete run could be done when using a power of 2.2 kW. The other parameters were set as following: 400 °C substrate and pressure of 2.67 mbar. The flow rate was 3000 sccm both for the activation using NH₃ and the CH₄ used for the growth experiment, see for all the different conditions table B.1. On both power levels no growth was observed, however activation appeared better when using 2 kW.

Only the outer rim of the wafer seemed activated after 1 minute of activation followed by 19 minutes of growth. Therefore the growth time was altered to either 9 minutes or 39 minutes. In the latter case the activated rim increased by a couple of mm's.

The difficulty with the first experiments was that due to the lack of visible structures focusing on the sample was extremely difficult. The effect of this is that it is hard to observe the catalyst nano-particles. Furthermore the 3 nm Ni layer was deposited by sputtering. The uniformity of such small layers deposited by equipment designed for relative thick layer deposition is most likely poor. Therefore it could be that only at the edge of the wafer a layer of Ni was deposited.

To overcome both possible problems a new batch of wafers was prepared using the same flow chart. However, instead of depositing 3 nm a layer of 6 nm was deposited (recipe '6nmNi'). Another change is the etching solution used at step 12. In this case a combination of 65 % HNO₃ and BHF (1:1) was used. This time the patterns could be observed under a microscope or with the naked eye because the uncovered Ti was completely removed.

All the experimental conditions for the second batch can be found in table B.2. Wafer nr. 1 was covered with a thick layer of a-C (figure 6.1a, bottom left), therefore we reduced the flowrate of the gases to introduce less carbon inside the reactor, while maintaining the same pressure. If the pressure is changed the coupling of the electric power to the plasma changes, which gave problems as can be seen with wafer nr. 9. Wafer nr. 3 was still covered with a thick layer of a-C, therefore we changed the activation time from 1 to 5 minutes to give the Ni layer more time to break up before introducing the carbon.

As can be seen from figure 6.1b the increase in activation time aided in improving the activation of the Ni catalyst. Three layers can be distinguished on the picture, the bottom left is the Si, the top right the Ni catalyst and the layer in-between the Ti layer which broke up. Due to the wet etching the layer was not uniformly etched which explains the Ti layer which isn't covered by Ni. As can be seen the Ni particles are clotted together by a-C.

It was not possible to decrease the pressure or increase the power without the system aborting due to errors. Therefore we investigated the effect of adding LF power on the activation and possible growth of CNTs. Unfortunately in order to add LF power the RF power had to be decreased, a stable configuration we found used 1 kW of RF combined

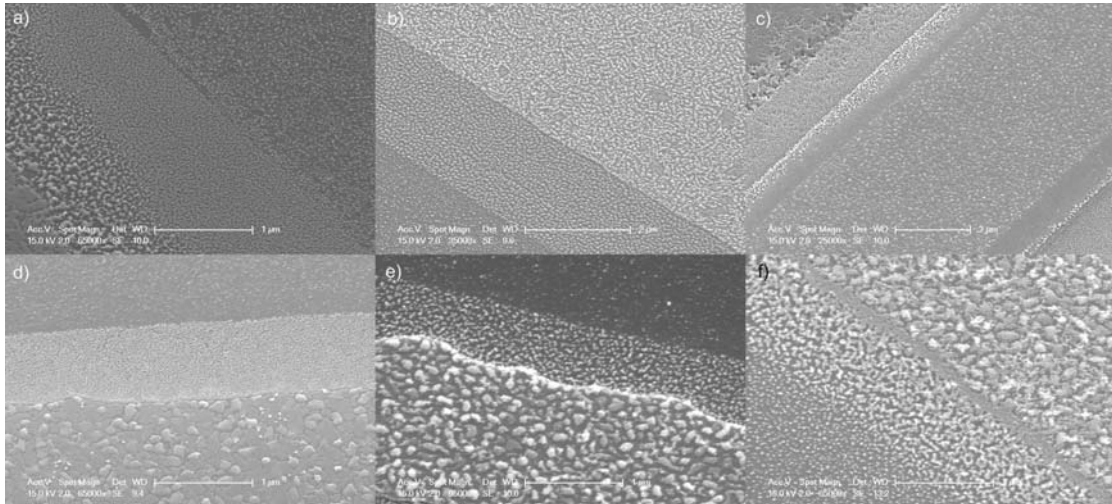


Figure 6.1: SEM images of batch 2: a) wafer 1, b) 4, c) 5.2, d) 6, e) 6.2, f) 8

with 250 W LF power. The results with these settings for different growth times can be seen in figures 6.1c-f. It seems that longer growth time give more separated particles (figures 6.1e,f, total time 1 hour) than with shorter time (figures 6.1c (30 minutes) and d (10 minutes)).

At none of the conditions we tested growth was observed, although the Ni layer could be activated. This is the same result as found before with lower power conditions. It can therefore be concluded that it is not possible to grow CNTs or CNFs in the Novellus Concept One PECVD. It is very likely that the main reason for this limitation is the low substrate temperature, as different power levels and configurations, different pressure, activation and growth times and different flow rates didn't aid in the growth of nanotubes.

6.2 Experiments using BlackMagic II 2" R&D CVD

This section discusses the results of experiments performed on an AIXTRON Black-Magic II 2" R&D (PE)CVD. This machine is one of the first (and few) commercial growth reactors available for CNT growth. It can operate under both (pulsed) DC-PECVD, HF-PECVD and thermal CVD mode (either with substrate or hot filament (HF) heating) with substrate temperatures up to 1000 °C. The temperature is monitored by a thermocouple placed on top of the substrate surface. These experiments were performed in the assembly hall of AIXTRON Ltd. in Cambridge, UK.

The system was operated in four different set-ups with four different catalysts (i.e. Ni, Fe, Co and Pd) all on top of 10 nm Ti. Pd and Co had a thickness of 1 nm, while Ni was tested on 6 and 9 nm and Fe on 1, 5 and 10 nm. These layers were all deposited in the LH 560 e-beam evaporator in the class 10,000 cleanroom on top of p-type test wafers, except for the Ni samples which were created using sputtering (for both the Ti and Ni layer). There were also patterned 6 nm samples from the second batch of process P2700 (see appendix B.1) available.

The following experiments were performed:

1. Pulsed DC-PECVD between 350-500 °C
2. Atmospheric Pressure (AP) CVD between 450-640 °C

3. HF-APCVD at 400 °C
4. HF-PECVD at 500 °C

HF-CVD gave only the formation of a-C and no growth for all the different catalysts, these results will not be discussed further. It is likely that the growth temperature was too low. The a-C formation was due to the dissociation of the C_2H_2 by the much warmer HF. In table 6.1 the process conditions for the other three set-ups can be found. In the next sections the results of these three growth set-ups will be discussed. To investigate the grown CNTs SEM (Philips FEI XL30), TEM (FEI Tecnai G²) and Raman spectroscopy (Renishaw inVia) are used.

Table 6.1: Process conditions BlackMagic II

Process	Temp. (°C)	Pres. (mbar)	Step	Time (min)	Plasma	Gases	Flow (sccm)
PECVD	350-500	6	Acivation	3	70 W, pure-DC	NH ₃	250
			Growth	30	80 W, 15 kHz	NH ₃ /C ₂ H ₂	250/50
APCVD	450-640	>720	Acivation				
			Growth	5		H ₂ /N ₂ /C ₂ H ₂	691/505/20
HF-PECVD	500	6	Acivation	2	75 W, 15 kHz	NH ₃	250
			Growth	30	75 W, 15 kHz	NH ₃ /C ₂ H ₂	250/60

6.2.1 DC-PECVD

As can be seen in table 6.1 the growth experiments using DC-PECVD were performed on temperatures between 350-500 °C, with steps of 50 °C. All four catalysts mentioned before were tested on these temperatures. However, Fe and Co only gave some minor growth on 500 °C and not on lower temperature (the catalyst layer was still activated on lower temperature, except for the 10 nm Fe sample). The results for Co and Fe can be found in figure 6.2. As can be seen the growth was not very good, especially in case of the Fe samples. Because there was no growth at lower temperature, these catalyst will not be further discussed. On the other hand both Ni and Pd gave growth on lower temperatures, in the case of Pd even minor growth at 350 °C was observed.

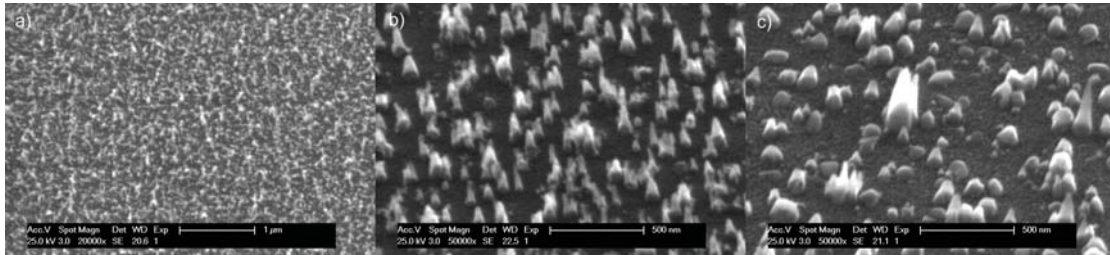


Figure 6.2: SEM images of DC-PECVD growth at 500 °C: a) 1 nm Co, b) 5 nm Fe, c) 10 nm Fe

Palladium is not often used as a catalyst, to date only a few papers have been published about this material as catalyst [115, 178–184]. As discussed in section 2.2.1.4, Pd has been demonstrated to be an excellent contact material. It has been suggested that when using it as a catalyst the Pd might aid in the formation of a good electrical contact [115].

A downside of Pd is that the diffusion constant (D_0) of Pd in Si is quite high ($D_0 = 2.95 \cdot 10^{-4} \text{ cm}^2/\text{s}$, with E_d , the activation energy, being 0.22 eV) [185], and the lifetime of charge carriers is reduced by Pd [186]. The same is true for Ni, Co and Fe (and many

other metals), and unfortunately Pd is no exclusion. Therefore just as with Ni care should be taken to prevent contamination of equipment when Pd is used.

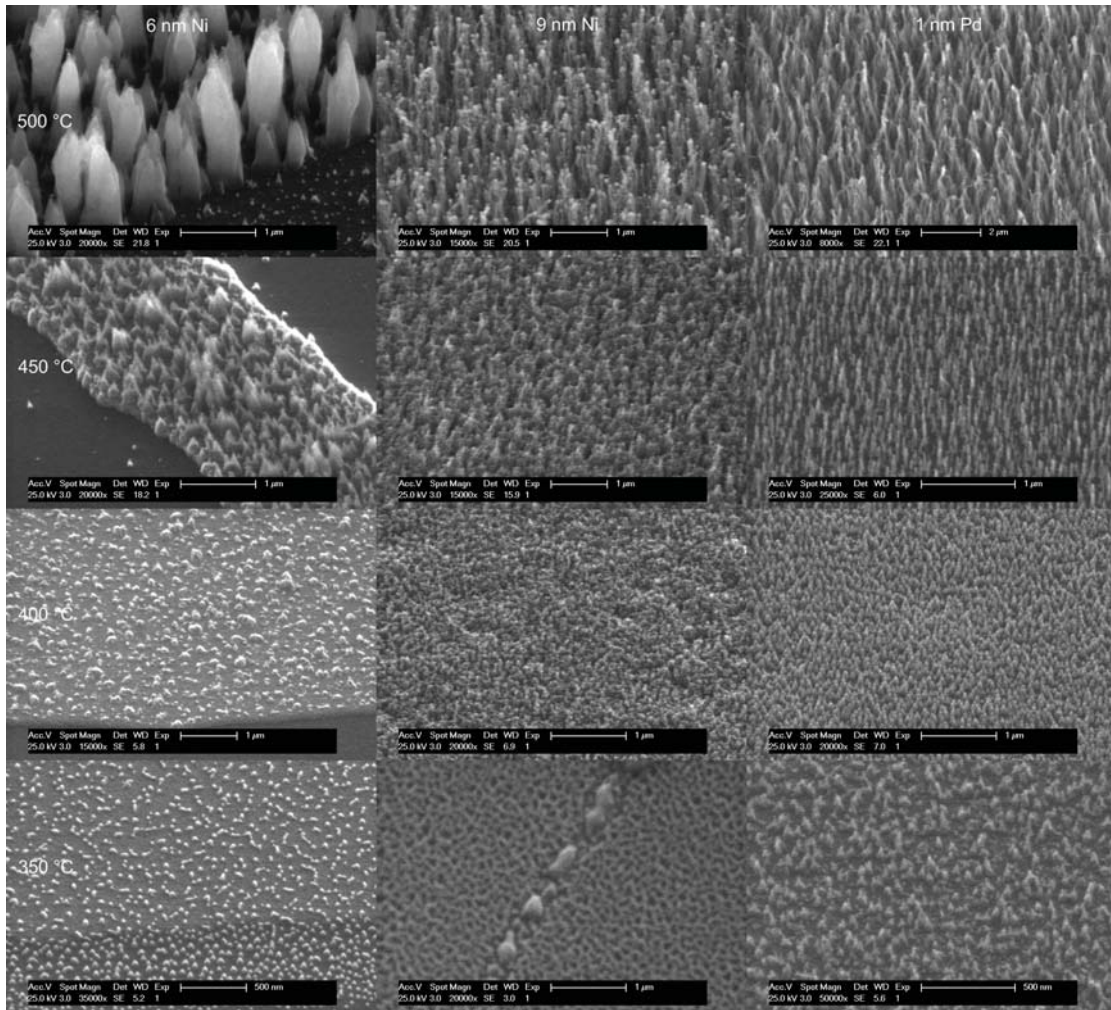


Figure 6.3: PECVD results for 6 and 9 nm Ni and 1 nm Pd between 350-500 °C

In figure 6.3 an overview of the growth results of 6 nm of patterned Ni (by the P2700 process), 9 nm of sputtered Ni and 1 nm of e-beam evaporated Pd, all on top of 10 nm of Ti, using PECVD (table 6.1, row 1) between 350-500 °C can be found. The first thing that can be observed for all samples is that the quality and length of the growth rapidly decreases when the temperature goes down. At 350 °C no growth and on 400 °C hardly any growth is observed on the samples with Ni, however Pd still shows some nano structures on these temperatures (albeit very short).

When we look at the properties of the samples on 500 °C the 6 nm patterned Ni gives large diameter aligned growth (100-200 nm). Most likely they are CNFs, judging from odd shape and big diameter. The diameter and length are non-uniform, especially the length varies a lot (from hundreds of nm up to 1.5 μm). Density is approximately 10^9 cm^{-2} .

The 9 nm Ni samples show a clear tip growth mechanism (the tip is bright due to the Ni catalyst). Again the diameter (50-100 nm) and length (1-2 μm) are quite non-uniform. The structures seem to bend, especially at the tip, and diameter varies over length. They are very probably again CNFs, but seem of higher quality than the

CNFs grown on the 6 nm patterned Ni. Also the density increased (due to the smaller diameter) and is now in the order of 10^{10} cm^{-2} .

In case of the Pd sample the growth seems to be more uniform, but again with some bending. Some nanostructures show a bright tip, suggesting a tip growth mechanism. The, again most likely, CNFs appear to become thinner at the tip, having a diameter around 100 nm. The density is similar to that of 9 nm of Ni and is around 10^{10} cm^{-2} . Length is again 1-2 μm .

Raman spectra were obtained for the 6 and 9 nm of Ni and 1 nm of Pd samples at 500 °C and the 9 nm of Ni and 1 nm of Pd at 450 °C PECVD growth. They can be found in appendix C.4.1.1 and the obtained ratio's and widths in table C.1. A strong baseline was observed in case of the 6 nm patterned Ni sample, making it difficult to extract reliable information from the spectrum. No clear second order peaks were observed in the spectra, which implies low graphite quality [164].

In figure 6.4 the Raman spectrum of the 9 nm Ni sample grown at 500 °C is shown to illustrate how a typical PECVD sample looks like. Often a Si peak can be observed around 500 cm^{-1} and sometimes 1000 cm^{-1} , indicating low density as the laser was able to reach the Si substrate. Next we find the graphite peaks, which are the defect related D peak and the C-C bond related G peak around, respectively, 1350 cm^{-1} and 1600 cm^{-1} . No clear higher order peaks are observed in our PECVD samples. The information obtained from the peaks (ratio's and widths) can be used to investigate the graphite quality of the sample. For more information about Raman spectroscopy on CNTs the reader is referred to appendix C.3.

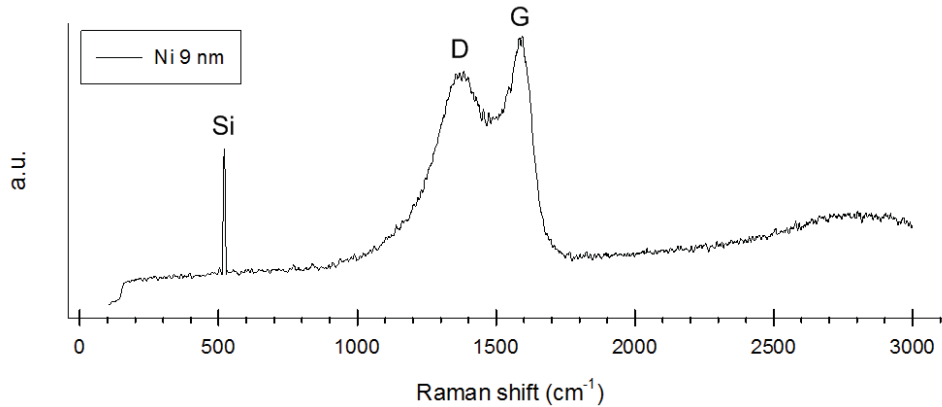


Figure 6.4: Raman spectrum of 9 nm Ni at 500 °C with peaks indicated

If we look at the I_D/I_G ratio (see table C.1) at 500 °C we see that the 9 nm of Ni sample has the lowest value, indicating it has the best graphite quality. This matches the findings from the SEM images. At 450 °C the Pd spectrum also showed a strong baseline, which made it impossible to extract any information. However, the I_D/I_G from the 9 nm of Ni sample could be obtained, which was higher than at 500 °C. This was to be expected as generally quality decreases for lower temperature [169].

Using curve fitting the width of the D peak was obtained. A wide D peak indicates a more defective graphite crystal structure. Antunes et al. [170] suggested that the product between I_D/I_G and FWHM(D) is a more accurate measure of quality than the ratio alone. This product indicates that both the patterned Ni sample and Pd sample are highly defective. The product of the width and ratio again indicates the 9 nm of Ni sample to have the best graphite quality. The product of the 9 nm Ni sample at 450 °C

lies too close to the value at 500 °C to draw a conclusion on how the quality changes vs. temperature.

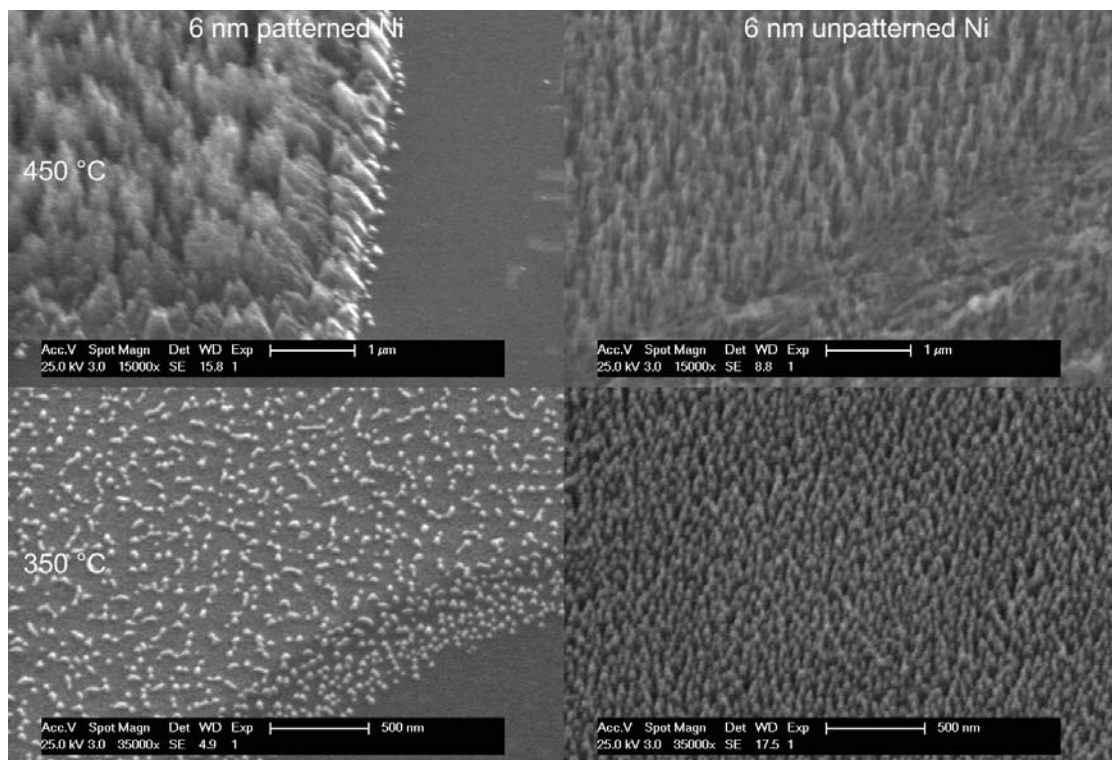


Figure 6.5: Results for 6 nm patterned and non-patterned Ni

The diameter depends on the catalyst thickness, thus no direct comparison between the diameters of these samples can be made. What is odd, however, is the fact that the 6 nm patterned Ni samples have a much larger diameter than the 9 nm samples, which is the inverse of what normally can be expected [31]. When the growth on 450 and 350 °C was performed there was also a 6 nm non-patterned sputtered Ni sample in the chamber. Figure 6.5 shows a comparison of the patterned and non-patterned Ni samples on those temperatures.

As can be seen from figure 6.5 and the 6 and 9 nm of Ni samples from figure 6.3 the CNT growth from the sample which has been patterned using photo-resist and cleaned with EKC505 shows growth of lower quality than the non-patterned sample. Clearly the tube diameter is much bigger, growth is highly non-uniform and only activation occurs at 350 °C. This was true even for relative big (50-100 μm) Ni islands. The conclusion we drew from this comparison and the comparison with 9 nm of Ni is that the patterning step has a negative influence on the growth, probably due to catalyst poisoning by the photo-resist and/or the cleaning method.

TEM was performed on the the samples discussed before (6 nm patterned Ni, 9 nm Ni and 1 nm Pd), the images can be found in figure 6.6. Figure 6.6a confirms our suspicion that the patterned Ni sample is highly defective nanofibre. No hollow core or crystalline planes can be found, indicating only short range order. The catalyst particle seems distributed over the filament length. Although only a small size nanostructure has been displayed in the figure, longer structures show the exact same behaviour.

The 9 nm of Ni sample in figure 6.6b indicates better crystallinity, as was to be expected from both the SEM and Raman results. It is interesting that still no hollow

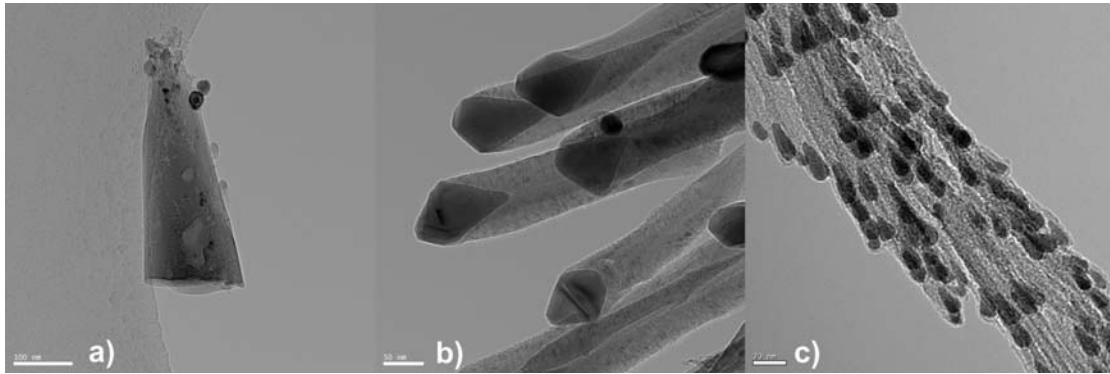


Figure 6.6: TEM image of growth using DC-PECVD at 500 °C, a) 6 nm of patterned Ni, b) 9 nm Ni, c) 1 nm Pd

core can be observed. Instead, tip growth, nanofibres with stacked graphite planes crossing the entire tube diameter are found. In some CNFs the onset of a hollow core can be observed.

Finally the Pd sample (figure 6.6c) displays an interesting behaviour. The big tube-like structures observed using SEM appear to be bundles of much smaller 10 nm tip growth tubes. When higher magnification images of the tubes were investigated quite defective bamboo CNTs could be observed, explaining the low quality of the sample.

6.2.2 Atmospheric pressure CVD

In case of atmospheric pressure CVD the temperature was varied between 450-640 °C. On the highest temperature of 640 °C all four catalyst were inside the chamber. However, no growth could be detected on the Ni samples. According to AIXTRON the recipe was not compatible with Ni, the focus will thus be on the remaining three catalysts.

Figure 6.7 shows the SEM images of the different catalyst after APCVD growth. Only the pictures with growth are displayed, which means that 1 nm Co and 10 nm of Fe didn't show any growth at 450 or 500 °C, while the thinner 1 and 5 nm of Fe didn't show any growth at 450 °C. Pd was the only catalyst which remained active for the three different temperatures. As can be seen the growth is random for all samples, except for the ones using Pd as catalyst which are vertically aligned. As there is no electric field present in the system the alignment is due to Van der Waals forces.

From the SEM images at 640 °C no diameter difference can be found between the 1, 5 and 10 nm Fe samples. However the SEM resolution is too limited to accurately determine the diameter. The density seems to be higher in case of the 5 and 10 nm Fe samples, when compared to the 1 nm of Fe and Co. As the Pd samples are aligned the tubes per square cm can be estimated, which is approximately 10^{12} cm⁻². The thickness of the Fe and Pd CNT layers is approximately 1 μm, while the Co layer appears to be thinner.

At lower temperature the thickness of the random CNT layer grown using Fe as catalyst reduces rapidly. Again it is difficult to determine the average diameter. In case of the Pd samples, however, the thickness of the layer doesn't decrease at 500 °C and also the density is still high ($10^{11} - 10^{12}$ cm⁻²). When we look at the sample grown at 450 °C the length (0.5 μm) and density (10^{10} cm⁻²) are reduced.

It is surprising that growth is still observed with Pd at 450 °C. The exact cause behind the lower allowed growth temperature when using Pd compared to Co and Fe

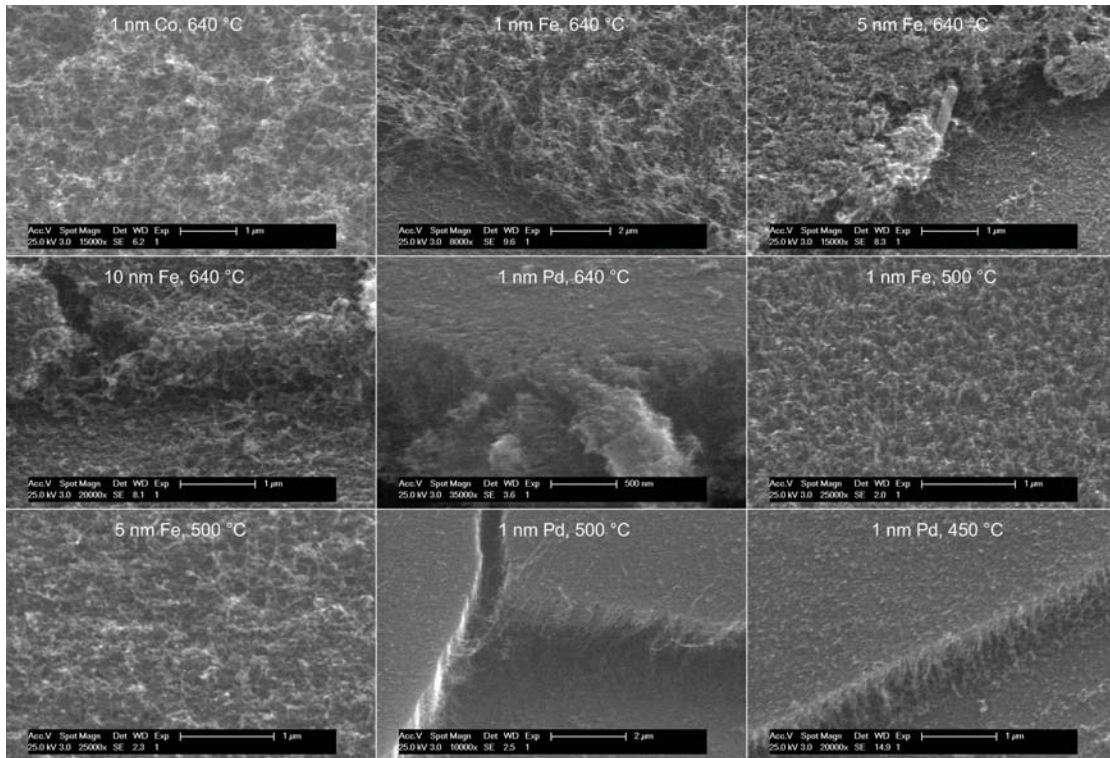


Figure 6.7: APCVD results for Co, Fe and Pd between 450-640 °C

is not known. As said before not much research has been done on Pd as catalyst, and similar results to ours have not been published. Unfortunately, no information about the surface diffusion of C on Pd is available. However, a publication was found where the C bulk diffusion between Pd, Ni, Co and Fe are compared [187]. The results of that research indicate that the bulk diffusion of C in Pd is 3-6 times higher than the other three metals. If the same is true for the surface diffusion this could explain the lower allowed growth temperature of Pd.

Next we look at the Raman spectra of the APCVD samples, which can be found in appendix C.4.1.2 and the data in table C.1. No baseline was observed for any of the APCVD samples. All spectra, except the ones using Pd as catalyst, show clear D, G and G' peaks, as is illustrated in figure 6.8 which is a typical CVD Raman spectrum. The absence of second order peaks in the Pd spectra indicate that the graphite quality is low in those samples.

In the left graph of figure 6.9 the I_D/I_G ratio has been plotted against temperature for the different samples. At a temperature of 640 °C the ratio suggest that 1 nm of Fe has the worst graphite quality, followed by 1 nm of Co, 10 nm of Fe, 1 nm of Pd and finally 5 nm of Fe. Although it is hard to judge quality from the SEM images, one would expect from them that 1 nm of Fe has a better quality than the thicker Fe samples [170].

If we look at the temperature dependence the I_D/I_G ratio of the 5 nm Fe sample follow the expected trend becoming more defective at lower temperature. However, the 1 nm of Fe and Pd samples show the exact opposite behaviour. The cause for this is unclear. TEM imaging on the Pd samples has been performed to investigate this behaviour, the results will be discussed further in this section.

We now look at the product of FWHM(D) and I_D/I_G , as suggested by Antunes et al. [170], which can be found in table C.1 of appendix C and in the right graph of figure

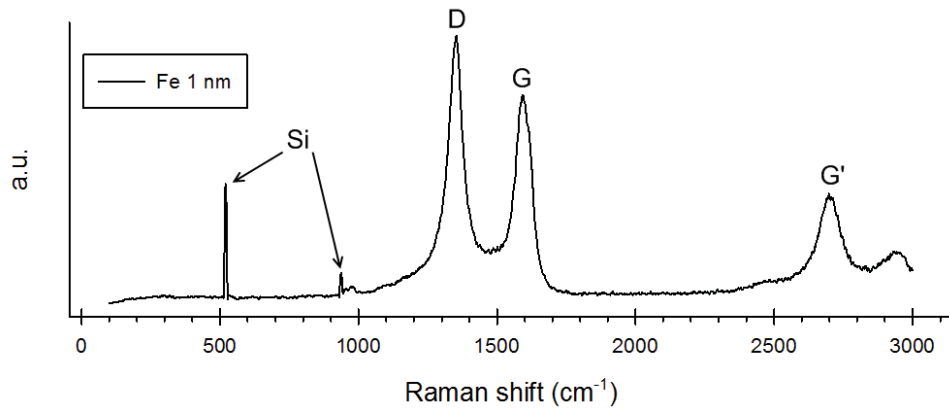


Figure 6.8: Raman spectrum of 1 nm of Fe at 640 °C with peaks indicated

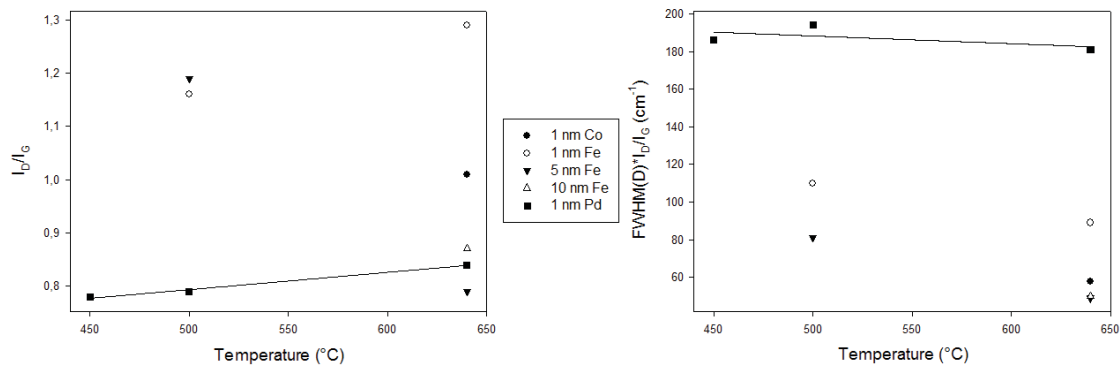


Figure 6.9: Different quality indicators against temperature for the APCVD samples, left: I_D/I_G , right: $\text{FWHM}(D) \cdot I_D/I_G$

6.9. The same order of quality can be found at 640 °C as was suggested by the ratio only. The 5 and 10 nm Fe samples are now almost equal, however. At 500 °C for both the 1 and 5 nm Fe sample the product increased, which implies a lower quality. For Pd an increase is seen at 500 °C, while at 450 °C a slight decrease is observed. However, this decrease is too small to indicate a real change in graphite quality compared to 500 °C. The product of $\text{FWHM}(D)$ and I_D/I_G thus seems a better indication for graphite quality, as it follows expectations from theory.

Musso et al. [188] suggested to use the $I_D/I_{G'}$ ratio to indicate quality. This ratio shows again roughly the same order as the previous indicators. However, this time the 10 nm of Fe sample is of best quality, although the difference with the 5 nm Fe sample is again very small. When the temperature is lowered to 500 °C the ratio increases (doubles in the case of 5 nm of Fe), which is in agreement with theory.

In figure 6.10 TEM figures obtained for the 1 nm of Co and 1 and 5 nm of Fe samples after 640 °C APCVD growth are displayed. All samples demonstrate tip growth with clear MWNT with some defects (bending, incomplete walls and bamboo growth). In all cases some break up of the catalyst particle of the CNT length could be found.

The Co sample had a rather uniform diameter around 25 nm. On the other hand the 1 nm Fe sample diameters were much less uniform, ranging from 20 to 50 nm. The larger tubes are more defective than the smaller ones. Finally the 5 nm of Fe sample has a diameter between 10-25 nm, which is surprising as the catalyst layer was relative thick. The 1 nm Fe sample displayed only growth in a circle half of the 1x1 cm piece, though.

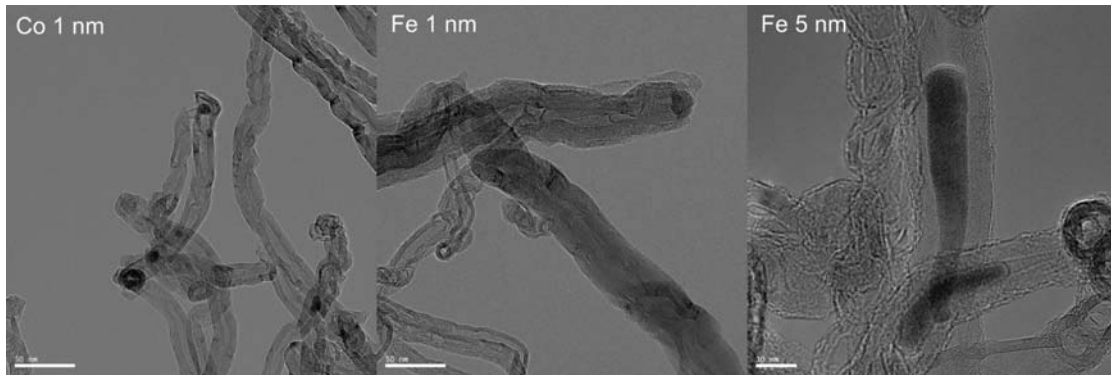


Figure 6.10: TEM images of Co and Fe samples after APCVD growth at 640 °C

It appeared as if the layer melted and was redistributed, which might have resulted in a local increase of catalyst thickness. Again the larger tubes appeared more defective for the 5 nm Fe sample. Large elongated catalyst particles could be observed, which are crystalline as fringes can be observed at high magnification.

Figure 6.11 shows the TEM images taken of the 1 nm Pd samples at the three different temperatures. As can be seen the tubes are highly defective bamboo MWNT at 640 °C, but change into carbon nanofibres without any hollow core at lower temperature. This corresponds well with the FWHM(D), which shows an increase between 640 and 500 °C and is about the same between 450 and 500 °C. Diameters are between 5-10 nm at all temperatures. As no catalyst can be observed at the tip a base growth mechanism is assumed.

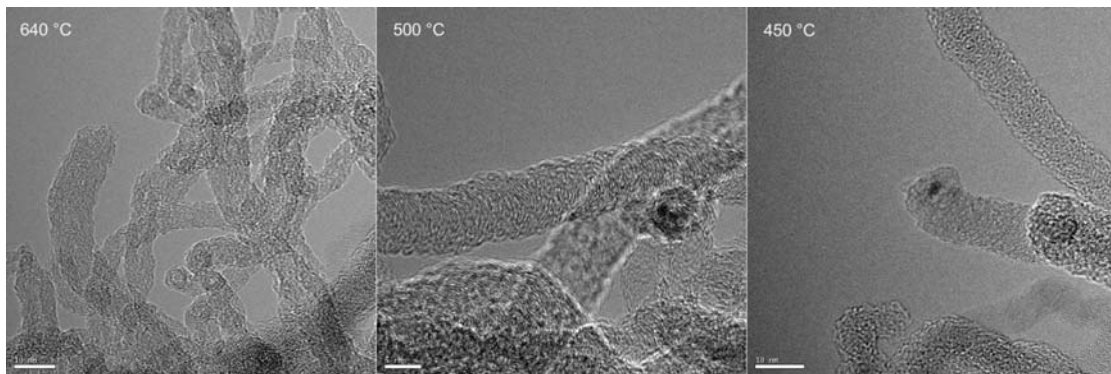


Figure 6.11: TEM images of the APCVD samples using 1 nm Pd as catalyst, the scale bar equals 5 nm for the centre image and 10 nm for the others

6.2.3 Hot filament PECVD

The hot-filament PECVD was the final experiment performed on the BlackMagic system and used rather similar settings as the DC-PECVD experiments. Instead of a substrate heater a hot-filament heater was used, though. The temperature of the filament was controlled by a thermocouple placed on the samples, which means that the actual temperature of the HF was higher as it was positioned a couple of cm away from the samples. Due to time constraints only growth at 500 °C was performed. Again hardly any growth was observed on samples with either Co or Fe as catalyst.

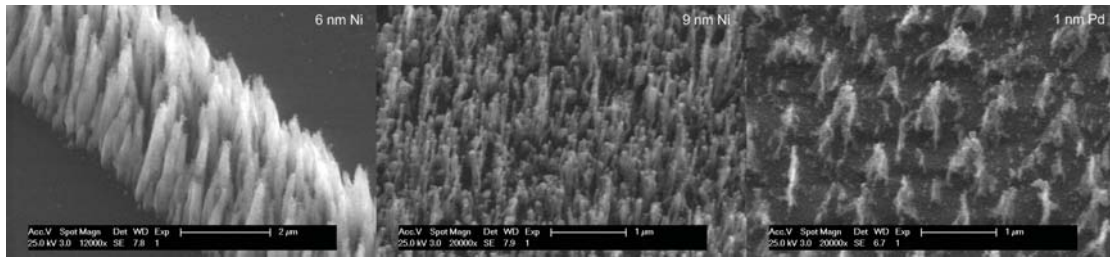


Figure 6.12: HF-PECVD results for 6 and 9 nm of Ni and 1 nm of Pd at 500 °C

In figure 6.12 the SEM images taken from the growth results can be found. The 6 nm of patterned Ni growth has a large diameter (100-150 nm) just as was the case with the DC-PECVD samples. However, the diameters are slightly smaller for the HF-PECVD samples, and the average length is with 2 μm longer. The density is again approximately 10^9 cm^{-2} .

The 9 nm of Ni samples are almost identical to the ones obtained by DC-PECVD, with the same diameter (50-100 nm) and density (10^{10} cm^{-2}). The length (1 μm) seems slight shorter. The Pd samples, however, appear rather different. The nano structures appear highly defective, no clear tube-like structures can be observed. The density has been reduced to $5 \cdot 10^8 \text{ cm}^{-2}$. The length of the structures is almost 1 μm .

If we look at the results of the Raman spectroscopy on the HF-PECVD samples and compare these with the DC-PECVD samples we again see a large baseline for the 6 nm of patterned Ni sample. The Pd sample had a huge Si peak, which has been cut out of the spectrum, but resulted in a noisy spectrum. The peak at 300 cm^{-1} is probably due to Si [189]. The 9 nm of Ni spectra appear to be practically the same.

If we compare the I_D/I_G ratios and FWHM(D) of the 9 nm of Ni sample they are, just like the spectrum, almost identical. This agrees well with the SEM results. The FWHM(D) of the patterned Ni sample increased dramatically compared to the DC-PECVD growth. However, in both spectra the large baseline made it very difficult to extract parameters. These differences can just as well be caused by poor baseline fitting. The Pd sample shows both a decrease in the I_D/I_G ratio and the FWHM(D), suggesting the graphite quality improved. The SEM pictures seem to indicate a decrease in quality, though. TEM should be performed to investigate what is actually happening.

If the observed differences were caused by the use of a hot-filament or due to the slightly different process conditions is unclear. It is advised to repeat the experiments with the exact same process conditions to determine what the cause of the observed changes. However, so far no advantage has been found for the use of the hot-filament over normal substrate heating.

6.3 Experiments performed at NanoLab

This section discusses the results obtained on different custom made CVD machines available at NanoLab. NanoLab is a small R&D firm in Newton, MA (USA) specialized in the fabrication of bulk volumes of CNTs and custom vertically aligned arrays for research institutes and industry. Experiments were performed in a horizontal hot-wall CVD furnace, HF-PECVD system and novel RF assisted cold wall CVD. Samples used in the experiments were created in the cleanroom of the DIMES technology centre. Investigating the results by SEM (JEOL JSM-7001F) was done in the Boston College

University cleanroom. As the samples are possible contaminated they cannot be investigated by any class 100 equipment in our cleanroom. However, we could perform Raman microscopy (Renishaw inVia) and TEM (FEI Tecnai G²).

6.3.1 RF assisted CVD

Obtaining growth results on this system was the main goal of the research at NanoLab as it was expected that growth could be achieved at lower substrate temperature by assisting the growth with local RF heating. The idea behind it was that when a high frequency (17 GHz) RF signal was put into the CVD chamber near the sample it would inductively heat the catalyst layer adding enough heat beside substrate heating to enable CNT growth. Before this could be tested, though, final system assembly and testing had to be performed.

The final configuration consisted of a cold-wall CVD chamber with Al canister to shield the user from RF radiation inside. A mechanical pump and turbopump were available with manual gate valve to set the system pressure and obtain base vacuum. Substrate heating was done by a ceramic heater covered by a graphite substrate holder and controlled by a thermocouple placed inside the holder. The gases NH₃ and C₂H₂ were available through MFC (Mass Flow Controllers). The RF signal was inserted at the top of the substrate with a dipole antenna and Cu reflector. To generate the RF signal a HP 8620C sweep oscillator with a 86260A RF plug-in set to 17 GHz combined with a Varian VZM 8-18 GHz 20 W amplifier were used. Figure 6.13 displays an overview of the system.

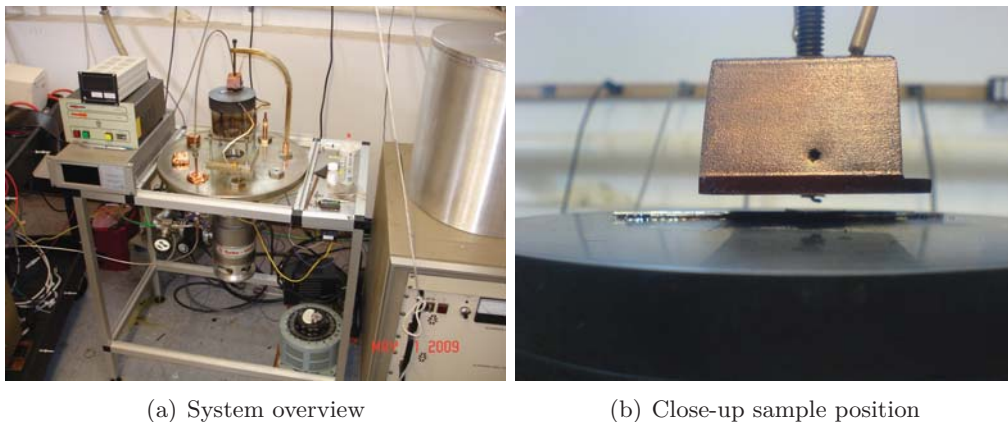


Figure 6.13: Pictures of RF assisted CVD system

After system assembly an experiment was performed to obtain pure thermal growth at 600 °C. First the samples were heated to the growth temperature in an NH₃ atmosphere of 1.33 mbar and held at that temperature for 10 minutes. After this the pressure was set to either 133 mbar, 1.7 mbar or 0.03 mbar and 150 sccm (50 sccm for the 0.03 mbar experiment) C₂H₂ was switched on while the NH₃ was turned off. Growth was performed for 10 minutes. The samples inside the chamber were 5 nm of Fe on 10 nm of Ti on p-type Si and 6 nm of Fe or Ni on 10 nm of Ti on 100 nm SiO₂ on a p-type wafer.

The sample with 5 nm of Fe gave growth for all pressures, whereas the 6 nm of Fe or Ni samples only showed growth at 133 and 1.7 mbar. In all cases the CNTs were random 30-50 nm tubes. Visually the samples appeared black/grey as was to be expected.

These experiments proved that the system was able to grow CNTs at 600 °C with the used recipe. The next step was to reduce the substrate temperature and apply RF heating to try to obtain similar results. As the RF signal could only be applied to a small 1x1 cm sample the best performing sample from the thermal run, 5 nm of Fe on 10 nm of Ti, was selected as the initial test sample.

A total of 21 test runs were performed in the system under various conditions in order to try and achieve CNT growth. As both the sample surface and the graphite substrate holder were flat keeping the sample under the antenna turned out to be a challenge (as the canister was made of Al it was impossible to tell if the sample moved until the experiment was finished). When more slowly pumping down and venting the system didn't resolve the problem it was decided to use dispersing fluid (NanoSpere AC, containing tetrahydrofuran, polyvinyl butyral and acetone) to adhere the sample to the substrate holder.

The next problem observed was that actually not the catalyst was locally heated, but instead the entire sample was heated by the RF signal. The frequency NanoLab selected for the system was too low to heat only a several nm thin layer (the skin depth of a 17 GHz signal is in the orders of hundreds of nm for good conductors). As the substrate made direct contact with the graphite, and later quartz substrate holder (the quartz holder was used to attempt to reduce this problem) the heat energy was quickly absorbed by this large thermal mass. These findings were confirmed when heating the substrate with a small thermocouple on top, with only the RF signal applied, in vacuum gave a limited temperature increase of 27 °C above ambient.

To solve this problem the substrate was put on top of two 1.5 mm hollow quartz tubes (see figure 6.13(b)). The entire construction was held together with the dispersing fluid. Experiments performed in vacuum without additional heating, with again a small thermocouple on the substrate, confirmed that with this setup it was possible to increase the temperature with more than 150 °C in vacuum in just one minute.

Unfortunately it was still not possible to obtain growth using this quartz stand-off when using the previous mentioned recipe. Another recipe with 70 sccm NH₃ and 30 sccm C₂H₂ was also attempted, but again gave no growth. In both cases a pressure of 1.33 mbar was used for both the annealing and the growth (low pressure was needed to make sure the heat loss to the ambient was minimal).

The before mentioned 6 nm of Fe or Ni samples were also tested instead of the 5 nm of Fe sample. In the case of the 6 nm of Ni sample we observed a partial film peel off at the spot the antenna was positioned, possibly due to the thermal stress of the rapid heating (still an activated layer of Ni particles was observed around the created gap). For the 5 and 6 nm of Fe sample only some a-C could be observed at the spot under the antenna.

Beside a substrate temperature of 400 °C also experiments were performed using 450 and 500 °C. However, at 500 °C the antenna isolation was damaged due to the radiant heating of the Cu RF reflector. Pre-annealing was tested both with and without RF assistance, again without any difference.

It was concluded that the power of the RF amplifier of the system was not sufficient to effectively heat the sample to a high enough temperature. Another cause could be the formation of a small GHz plasma in the system which etched away any CNT formation, however no signs were found for such a plasma on the RF reflector. Due to the lack of growth in this system the attention had to be shifted towards the other, high temperature, systems in order to grow CNTs for our measurement structures discussed in chapter 5.

6.3.2 HF-PECVD

The custom made HF-PECVD system consisted of a quartz bell jar with a 3" substrate holder. Above the substrate holder two tungsten hot-filaments were placed, above which the second electrode of the PECVD system was positioned. There was no temperature control present, but the average temperature was estimated to be 800 °C by the system operator. The plasma was generated by a DC power supply. A mechanical and turbopump combined with a gate valve controlled the pressure, before every experiment the system was pumped down to at least $3 \cdot 10^{-6}$ mbar. The system was used for production most of the time, limiting the experimental time for our purposes. It was operated by the system engineer of NanoLab.

Table 6.2: Process conditions for the NanoLab PECVD system. The 'x' stands for annealing during the entire heating cycle (only final HF power given) which took about an hour

Run	Step	Time (min)	HF power (W)	Plasma (W)	Gases	Flowrate (sccm)	Pressure (mbar)
1	Annealing	x	475		NH ₃	59	62.5
	Growth	3	490	400	NH ₃ /C ₂ H ₂	59/23	66.5
2	Annealing	x	440		NH ₃	59	64
	Activation	0.5	440	140	NH ₃	59	64
	Growth	3	500	400	NH ₃ /C ₂ H ₂	59/23	64
3	Annealing	x	500		N ₂	300	64
	Growth	3	500	420	NH ₃ /C ₂ H ₂	59/23	64
4	Annealing	x	440		NH ₃	59	64
	Activation	2	440	147	NH ₃	59	64
	Growth	3	500	408	NH ₃ /C ₂ H ₂	59/23	65

A total of four experimental runs were performed in the system, the process parameters can be found in table 6.2. As can be seen there were some slight variations in the plasma and HF power between the different runs, which are due to the complete manual operation of the system. The process engineer advised not to change the recipe, so instead different annealing steps were investigated in order to find the optimal activation method for our samples.

The first run consisted of the default recipe used by NanoLab. For the second and fourth run an activation step with low power NH₃ plasma was added (30 s. and 2 min. respectively), which (as discussed in section 3.2.4) can aid in the activation of the catalyst film. In run three a different annealing gas was used. As discussed by Pisana et al. [161] the precursor gas influences the activation. They achieved good results with Ar, which is an inert gas. As only N₂ was available as inert gas in this system we used it instead of Ar.

In all runs samples with 6 nm of patterned Ni on 10 nm of Ti and 6 or 9 nm of Ni on 10 nm of Ti and 100 nm SiO₂ were present. In run 2 and upwards also samples with 6 nm of Fe on 10 nm of Ti and 100 nm of SiO₂ and 10 nm of Fe on 10 nm of Ti were added. The 100 nm of oxide wafers are commercially oxidized wafers available in our cleanroom. In the first run also a sample with 1 nm of Pd on 10 nm Ti was inserted, however Pd gave hardly any growth in the PECVD system. All deposition except the patterned one were performed using the LH 560 e-beam evaporator in the class 10,000 cleanroom. The patterned samples were prepared using the P2700 process (appendix B.1).

The samples were analysed by SEM. However, it has to be noted that due to limited SEM time not all the samples could be imaged for every run. Figure 6.14 shows a

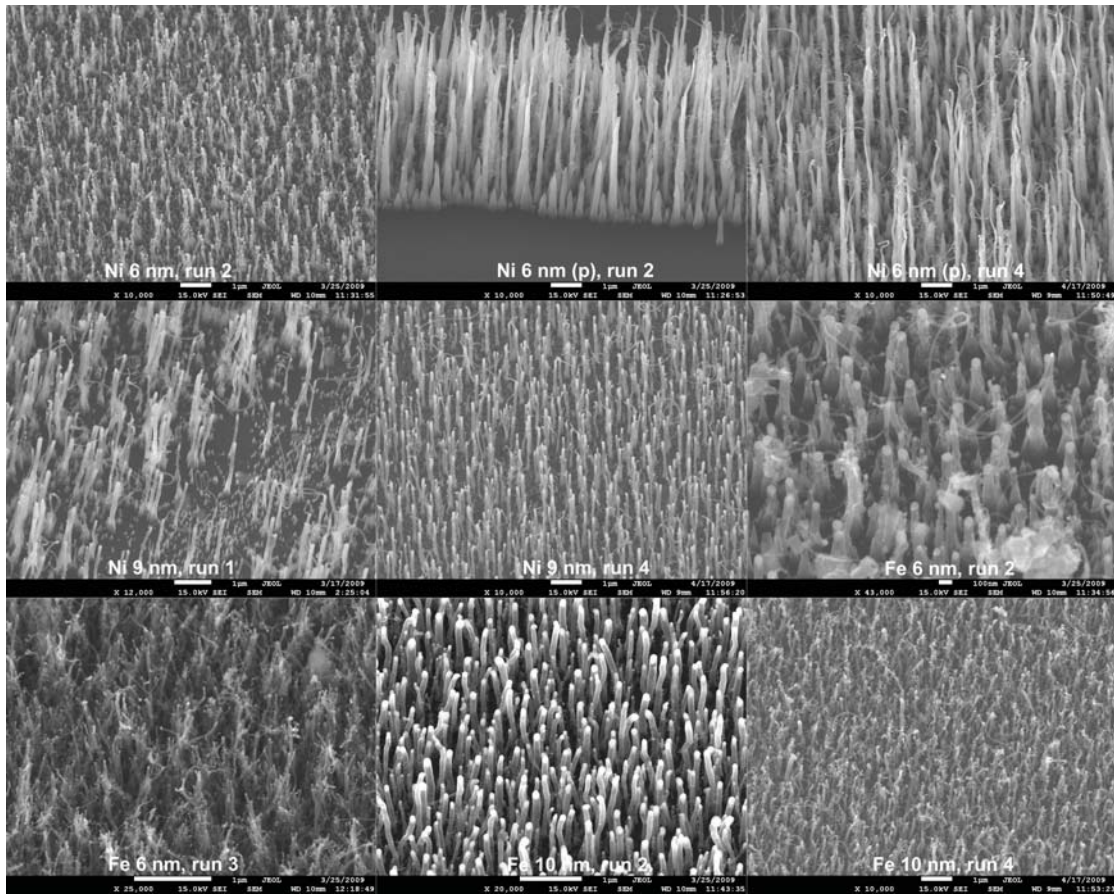


Figure 6.14: Selected SEM pictures of PECVD growth results

selection of SEM pictures from the PECVD growth, for the same catalyst only images with a difference compared to the other runs were selected.

No difference could be observed in the SEM images of the samples using 6 nm of non-patterned Ni between runs 1, 2 and 3 (run 4 was not imaged by SEM). In all cases density was low (10^9 cm^{-2}), length was about $1 \mu\text{m}$ and diameter between 50-80 nm. In-between the tubes small cone-like structures could be observed, which point to a non-uniform film break-up.

The slightly thicker 9 nm of Ni samples showed similar growth in run 1, however uniformity slightly improved when a long activation step with NH_3 plasma was employed. Density and length are the same compared to the 6 nm of Ni sample, however the diameter is slightly larger (80-100 nm) as was to be expected for a thicker catalyst film. The longer activation step clearly helps the film to break up more uniformly.

Just as with the results from the AIXTRON PECVD (section 6.2.1) the patterned Ni samples show a different behaviour (although in the experiments performed at NanoLab the non-patterned Ni samples have a layer of 100 nm of SiO_2 beneath the Ti). Between run 1 and 2 no difference was found between the patterned samples, while run 4 showed a slight decrease in density. For those three runs the CNT length differed between 1-5 μm , with a diameter around 100 nm. Density was in the same order of magnitude as the non-patterned samples. In case N_2 was used to anneal the patterned Ni sample only minor growth around the edge of the pattern was observed. This might be due to remaining photo-resist or EKC505 fluid which were removed by the NH_3 at high temperature.

When we look at the 6 nm of Fe sample a big difference is observed between the second and third run. The second run only showed short (500 nm) and thick (100 nm) CNT growth, with a comparable density as the Ni samples. When a N₂ anneal is used, however, much longer (1 μm) and thinner (40 nm) tubes are observed (not shown here). Density is now in the order of 10¹⁰ cm⁻². The vertical alignment decreased though, and tubes seem to form bundles. Apparently the Fe film breaks up more evenly when annealed in an inert gas, similar to the findings of Pisana et al. [161].

Finally the 10 nm of Fe samples showed uniform growth when only a short NH₃ etch was employed in run 2, with diameters around 100 nm, lengths up to a micron and a density of 10⁹ cm⁻². When the activation time is quadrupled the length and diameter became non-uniform. The density stayed the same, while the diameter was between 50-100 nm. Clearly a too long activation step decreases the quality of the growth.

What can be observed for all samples is that the growth mechanism of the aligned tubes appears to be tip growth, which is common for PECVD samples. However, in many samples small non-aligned tubes were observed in-between the bigger aligned tubes. It is believed that these tubes employ a base growth mechanism, as no clear metal particle could be observed at the tip. This would also explain the non-alignment, as tip growth seems to be required for aligned growth due to an electric field as proposed by Merkulov et al. [157].

Next we look at the Raman spectra of the samples. As contamination is not an issue in the Raman measurement device we were able to investigate all samples. The spectra can be found in appendix C.4.2.1 and the extracted parameters in table C.2.

When we look to the spectra of the 6 nm of Ni sample, which didn't show a notable variation in the SEM images, we do see some variation of parameters. The I_D/I_G ratio appears to be optimum for either the default recipe (run 1) or the N₂ annealing (run 3). However, the product of the I_D/I_G and FWHM(D) indicates that the graphite quality in run 3 is actually worse. According to Antunes et al. this indicates a spreading of defect domain size for the sample from run 3 [170]. In case of the NH₃ plasma activation step both the ratio and the product increase, clearly indicating a reduction of graphite quality. A longer activation step seems to be a bit more advantageous judging from the narrower D band in run 4.

The spectra of the thicker Ni sample (9 nm) show a different behaviour. For both the short and long activation step (run 2 and 4, respectively) the I_D/I_G ratio decreases. A short activation step seems to perform better than the default recipe. A longer activation step appears disadvantageous and gives a rapid D band broadening, however the ratio is still lower than run 1 (indeed the tubes seem to be of better quality judging from the SEM images in figure 6.14). Again the N₂ annealing increases the D band width, while the ratio remains relative similar, just as with the thinner 6 nm sample.

For the patterned 6 nm of Ni sample (which has no thick layer of oxide beneath the Ti) again a slight decrease can be seen in the I_D/I_G ratio for the short activation run. However, for both the short and long activation run the D band widens. As mentioned before hardly any growth could be observed in run 3. Thus for this sample the default recipe is optimum, just as with the non-patterned 6 nm Ni sample.

For the Ni samples a N₂ pre-anneal seems thus to be disadvantageous resulting in D band widening. A short activation step seems to improve the graphite quality when the Ni layer is thicker, while for 6 nm of Ni no special activation step gives the best result. As no clear G' peak could be observed only the I_D/I_G ratio and FWHM(D) could be used to judge graphite quality.

Unfortunately no Fe samples were present in the first PECVD run. What can directly

be seen from the spectra of the Fe samples is that they have a almost no baseline and show much sharper bands, especially for the 10 nm Fe sample. As in most sample a G' peak is present we can also use the $I_D/I_{G'}$ ratio to judge graphite quality. This also indicates graphite quality is generally higher than the Ni samples.

First we investigate the 6 nm of Fe samples. Both the I_D/I_G ratio and product of the ratio with the FWHM(D) indicate that best quality is obtained when a short activation step is used (run 2 vs. run 4). The $I_D/I_{G'}$ ratio seems to indicate that a N₂ anneal is advantageous, while the differences between the other measures of quality are in favour of the short pre-anneal (although the differences are not big). From the SEM images it can be concluded that the $I_D/I_{G'}$ ratio is likely to be correct.

Second we look at the 10 nm of Fe samples, which has no thick oxide layer underneath the Ti as with the 6 nm of Fe sample. Again a N₂ pre-anneal demonstrates the best graphite quality (with an I_D/I_G ratio and FWHM(D) product almost equal to run 2 and the $I_D/I_{G'}$ ratio clearly lower). As was to be expected from the SEM images, and is confirmed by the three quality measures, a long activation step drastically reduces the graphite quality.

We can thus conclude that for the Fe samples a N₂ pre-anneal gives good graphite quality for the grown CNTs/CNFs. A long pre-anneal is clearly disadvantageous for the graphite quality. Unfortunately it was not possible to compare the Fe samples to the default recipe with no special activation step.

Finally, TEM was performed to investigate the structure of the grown nanostructures. The images can be found in figure 6.15. In all cases bamboo (or herringbone) CNTs could be observed with clear tip growth. Often some catalyst particles can be found along the length of the tube, which were broken off from the central particle. This explains the decrease in diameter over length observed using SEM, for instance with the patterned 6 nm of Ni sample in figure 6.14.

In all samples some tubes showed so-called hybrid tip growth, which was also observed by Ngo et al. [115] using Pd as catalyst. These tubes appear to have an additional smaller diameter base growth on the tip of the CNT. This is likely the cause of the smaller random tubes observed using SEM. Tip growth indeed appears to be required for aligned growth, as was discussed before. However, apparently the base growth CNTs originate from the tip, instead of the substrate.

When the 6 nm of Ni samples from run 1 are compared, non-patterned (6.15a) and patterned (6.15b), some differences can be observed. While the diameters are comparable (40-70 nm), a clear difference in structure can be found. While for the non-patterned samples the distance between the hollow tube crossings are around 40 nm this distance for the patterned samples is reduced to 20 nm. The structure also appears more defective for the patterned sample (as can be seen from the irregularities in the vertical walls).

Figure 6.15c displays the growth obtained from 10 nm of Fe using run 2. The tubes are generally much wider compared to the Ni samples, approaching a diameter of 100 nm. What is interesting is that the big tubes have less outer walls than the smaller ones, and thus a larger hollow core. It could be that the particle receives insufficient carbon to generate additional walls. The 6 nm Fe samples from run 3 (figure 6.15d), on the other hand, are much smaller (20-30 nm) and have almost no hollow core. High resolution images revealed that the central core is regularly filled with a-C.

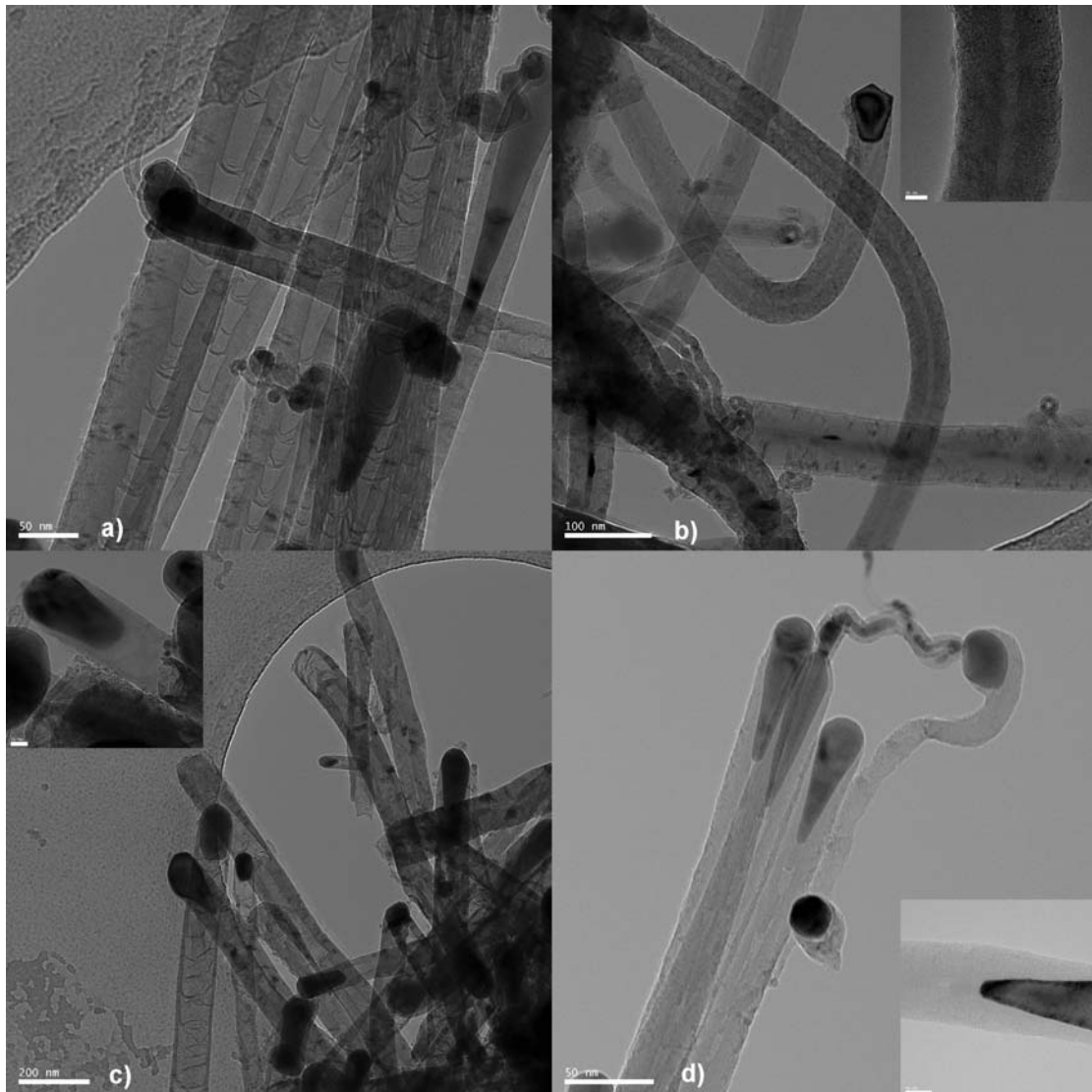


Figure 6.15: TEM images of several HF-PECVD samples: a) 6 nm Ni run 1; b) 6 nm patterned Ni, run 1 (inset scale 10 nm); c) 10 nm Fe, run 2 (inset scale 20 nm); d) 6 nm Fe, run 3 (inset scale 10 nm)

6.3.3 Thermal CVD

The thermal CVD system which could be used for experiments consisted of a horizontal Lindberg 3-zone furnace with a 2" or 3" quartz tube in it. A mechanical pump and gate valve were used to control pressure. It was possible to operate the furnace in atmospheric pressure mode through a gas bubbler. Temperature control was automatically done by the furnace, while pressure control was manual. Read-out of temperature and pressure was done by LabView 7. Gas control was performed with a MFC controller with four channels available and several MFC. The available gases were Ar, He, O₂, N₂, H₂, NH₃ and C₂H₂.

A recipe used by NanoLab for vertical aligned growth using a Al₂O₃ tri-layer structure with Fe in-between gave poor growth results with our samples and will not be further discussed. Some attempts to reconstruct the thermal CVD recipe used in the BlackMagic machine were not successful, no growth could be observed with SEM. Again

these results will not be discussed.

It was decided to develop a recipe from different publications found using a similar system and gases. A recipe from publications by Xu et al. [24, 25] using Ar, H₂ and C₂H₂ in combination with Fe seemed to perform best in the system at NanoLab and was thus selected. It was found that due to high contamination the 3" tube was unfit to grow good CNTs, which made us use a clean 2" tube (cleaning the 3" tube proved to be impossible).

The recipe started with a 20 min. anneal time after reaching the growth temperature while 400 sccm Ar and 100 sccm H₂ were flowing. The total pressure was regulated to 8 mbar. After this anneal 100 sccm of C₂H₂ was added and the pressure was again set to 8 mbar. Growth time was 30 minutes. After growth the C₂H₂ flow was stopped and the furnace was shut down. The Ar and H₂ remained flowing till the temperature reached 250 °C and the chamber was not vented before the temperature became lower than 200 °C.

The samples tested were the same as in the previous section. On the commercial wafers with 100 nm of oxide was, after 10 nm of Ti, a catalyst layer of either 6 or 9 nm of Ni or 6 nm of Fe deposited. On the p-type test wafers was, after 10 nm of Ti, either 1 nm of Pd, 1, 5 or 10 nm of Fe or 6 nm of patterned Ni (by the P2700 process, see appendix B.1) deposited. All deposition except the patterned Ni were performed in the LH 560 e-beam evaporator in the class 10,000 cleanroom.

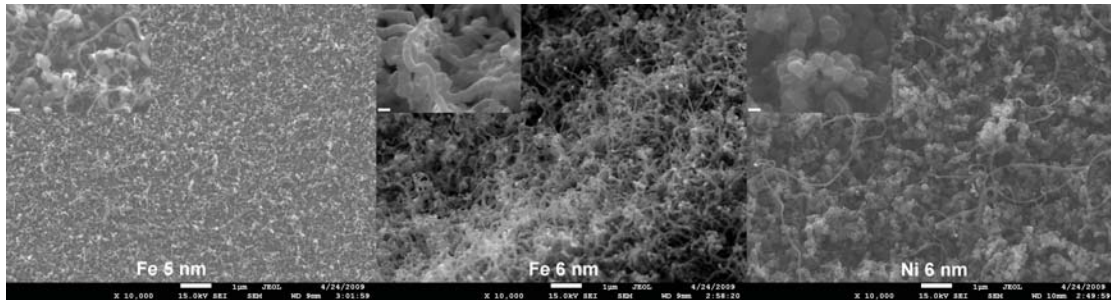


Figure 6.16: Growth results at 600 °C in the 3" tube using a Mo boat, the inset shows a 100,000x magnification (scale bar equals 100 nm)

Figure 6.16 displays the growth results obtained in the 3" tube furnace. Only growth was observed at the samples with 5 nm of Fe, 6 nm of Fe and 6 nm of Ni (the latter two having a oxide layer underneath the Ti). No growth could be observed on 1 nm of Pd or Fe and the patterned 6 nm of Ni.

The observed growth appeared highly defective for the three samples, indicating nanofibres instead of tubes. The 5 nm of Fe sample displayed only minor growth, mainly consisting of big (100 nm) fibres, with some smaller (10 nm) but longer tubes in-between. The 6 nm of Fe gave some surprising results. A thick foil of defective fibres with a diameter around 80 nm could be observed. This foil seemed to be peeled off from the surface and rippled at low magnification (which causes the black and bright areas due to height difference at the shown magnification). Probably the adhesion between the Ti and the oxide layer was poor, which enabled the film to come off. Although the 6 nm of Ni sample displayed similar growth as the 6 nm of Fe (albeit of even lower quality) in this sample the film seemed to be better adhered to the surface.

After switching to a clean 2" tube with the same recipe the growth greatly improved. Growth was now observed with samples of 1 nm of Pd or Fe and 6 nm of Fe or Ni (either patterned or non-patterned). On a sample with 10 nm of Fe only minor growth was

observed, possibly the catalyst film was too thick to effectively break-up. No 5 nm Fe sample was present (these were mostly used for experiments in the RF assisted CVD system, see also section 6.3.1). The SEM images can be found in figure 6.17.

The flow per area is higher in the 2" tube as the cross sectional area decreased. To rule out that the higher flow per area, or the quartz instead of Mo boat, were not the cause of the improved growth the experiment was repeated in the 3" tube with a quartz boat and doubled flow rates (the cross-sectional area of a 3" tube is roughly twice that of a 2" tube). Again similar results as with a lower flow rate and Mo boat were obtained, indicating that contamination and dirt build-up in the quartz tube are the cause of the poor growth results.

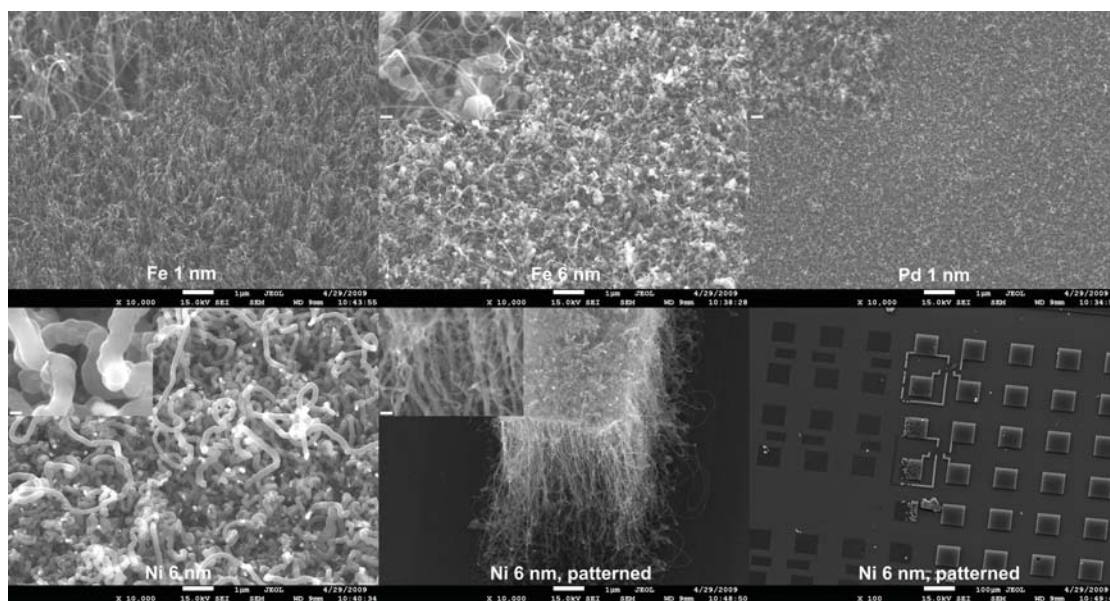


Figure 6.17: Growth results at 600 °C in the 2" tube using a quartz boat, the inset shows a 100,000x magnification (scale bar equals 100 nm)

As can be seen from the SEM images in figure 6.17 the sample with 1 nm of Fe displayed self-aligned growth. The tube diameter is 10-20 nm and density is in the order of $10^{10} - 10^{11} \text{ cm}^{-2}$ but is difficult to accurately determine as the tubes are not completely aligned. Length appears to be well over one micron. These results are quite promising and indicate that vertical aligned growth is possible in this reactor on our substrates.

TEM was performed on the 1 nm Fe sample grown at 600 °C, a low and high magnification image can be found in figure 6.18. The low magnification image (figure 6.18a) shows that the alignment is lost when the TEM grid is scraped across the surface. Some tubes display very few defects over a long length, clearly these tubes are much less bamboo than the previous PECVD samples. The high magnification image (figure 6.18b) displays a MWNT which consist of about 15 walls. The outer, and especially the inner walls display some defects. No clear catalyst particles could be observed at the tip, implying a base growth mechanism.

The thicker 6 nm Fe sample (with oxide underneath the Ti) shows a quite different growth pattern, when we look at figure 6.17. A combination of random big (100 nm) fibres, which appear to be very defective, combined with much longer and thinner (10-20 nm) tubes can be observed. No film peel off could be observed after this experiment as was the case in the 3" tube. The combination of big and small structures indicate

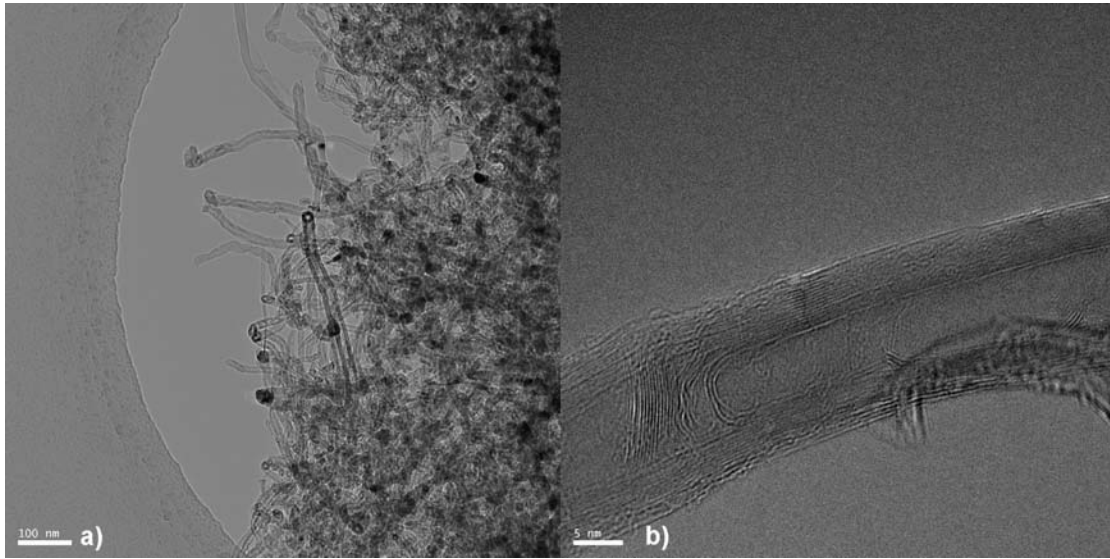


Figure 6.18: Low (a) and high (b) magnification TEM image of 1 nm Fe sample

non-uniform catalyst activation and appears to be similar to the bimodal film break-up reported by Nerushev et al. [166].

This recipe also allowed the growth of a very thin layer of small (below 10 nm) tubes using Pd as catalyst, proving again that Pd is a viable catalyst. Unfortunately although the growth appears quite dense no self-alignment is observed, possibly due to the short length of the tubes.

The non-patterned Ni (again with oxide underneath the Ti) demonstrates a thick film of big tubes (100 nm) which under high magnification appear to be rather defective (fibres). Growth is again random, with some fibres appearing to be quite long (over 10 μm). Only very few small tubes can be observed, indicating that film break-up is more uniform than with the 6 nm of Fe sample.

The patterned Ni gave the most surprising results. Vertically aligned growth up to 5 μm was observed with tubes diameters between 10-50 nm with a density around 10^{11} cm^{-2} . It appears as if the top layer is being lifted by the tubes, which is similar to the ‘sandwich’ growth reported by Chen et al. [114].

What is even more surprising is that the growth only occurred in an area of roughly 1/5 the total die area (which was 1 cm^2). In the region outside the growth area hardly any nanotubes could be observed. Repeated experiments under the same condition with other patterned 6 nm of Ni dies were not successful in repeating the observed growth. The cause of this is still unclear, but it is likely to be some non-uniformity in wafer processing.

Again Raman spectroscopy was performed to evaluate the quality of the samples, the spectra can be found in appendix C.4.2.2 and the obtained band information in table C.3. If we first compare the 6 nm of Fe and Ni samples between the 2” and 3” tube we see that all quality indicators (I_D/I_G and $I_D/I_{G'}$ the widths of the D and G’ peak and the product between I_D/I_G and FWHM(D)) show a clear improvement in quality for the 2” tube (as indicated by a decrease in all of them). This is consistent with the SEM observations.

If we compare the results at 600 $^\circ\text{C}$ in the 2” tube the sample with 1 nm of Fe as catalyst clearly has the highest quality (although the I_D/I_G ratio is not the lowest).

The samples with 100 nm of oxide underneath the Ti layer (Fe and Ni 6 nm) have a comparable quality, with the Ni sample being somewhat better. It is reasonable to assume that the small tubes in the 6 nm Fe sample are of high quality as they look similar to the 1 nm of Fe sample when observing the SEM images. However, the big defective CNFs appear to dominate the Raman spectrum of the 6 nm Fe sample.

The patterned Ni sample has a low I_D/I_G ratio, but a relative wide D and G' band which indicate that the graphite quality is not high. It must be noted however that the Raman spectrum was obtained by illuminating the sample from the top. If indeed the top catalyst layer has been lifted as was concluded from the SEM images the Raman spectrum will not be accurate as the actual tubes are covered by the lifted layer. Finally the Pd sample shows a very low I_D/I_G ratio, but an extremely broad D band and no higher order bands. This indicates the graphite quality of this sample is low.

The 6 nm of Fe and Ni samples also displayed CNF growth at lower temperatures and with a reduced flow rate (25 sccm of H_2 and C_2H_2 and 100 sccm of Ar). Presumably this is caused by a better activation due to the oxide layer underneath the Ti layer, which increases surface roughness. Although not imaged by SEM the Raman spectra allow us to investigate the temperature and flow rate dependency of the graphite quality. We expect that a lower temperature will result in a decrease of quality (although at lower temperature the pyrolysis of C_2H_2 also becomes lower, which can result in less a-C formation) [169].

But first we look how the reduced flow rate influences the Raman spectra. Only the samples with oxide underneath showed large area growth at lower flow rate. It is possible that the carbon supply was insufficient for large area growth on, for instance, the 1 nm of Fe sample. Another possibility as that catalyst activation suffered from the lower flow rate, as only growth was observed around the edges and some local spots on the other samples. This can indicate non-uniform catalyst activation.

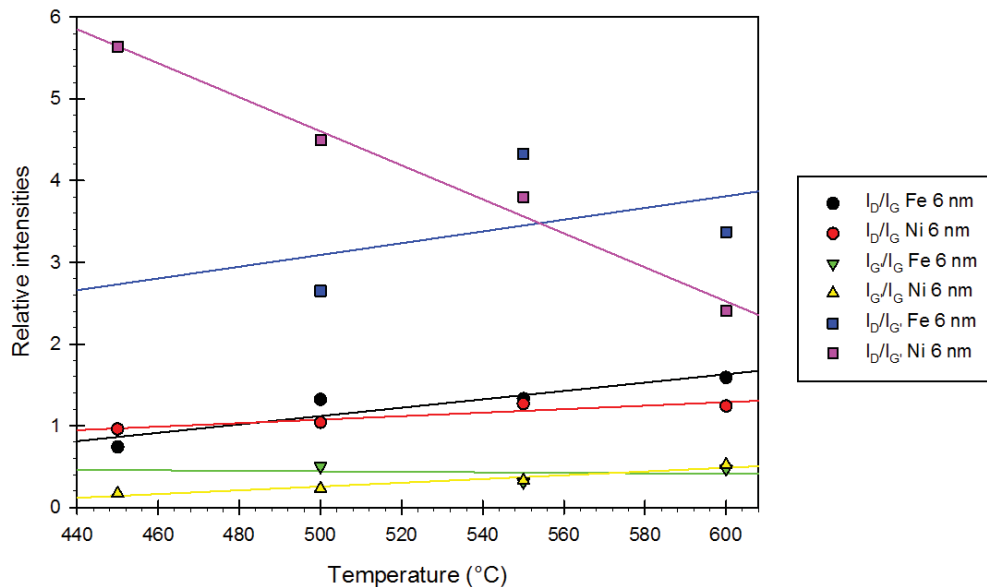


Figure 6.19: Relative intensities of the different Raman active bands against temperature

The Raman spectra of the samples with oxide underneath the Ti layer are roughly the same as with the higher flow rate, as can be seen from table C.3. Judging from the trend in the different quality indicators the sample with Fe as catalyst seems to have a

slightly better graphite quality, while Ni performs a bit worse. The differences are too small to draw any definite conclusions, though, and can just as well be caused by normal process variations of inaccuracy in curve fitting. We can thus conclude that the flowrate has no notable influence on the graphite quality of the 6 nm of Fe and Ni samples.

Next we investigate the temperature dependency of the information obtained from the Raman spectra. In figure 6.19 the different intensity ratio's have been plotted against temperature and a linear regression has been applied. The I_D/I_G ratio increases for both samples for increasing temperature, although the difference for the Ni sample is quite small. This actually suggest an improvement in graphite quality for decreasing temperature, which is counter intuitive but might be caused due to a reduction in a-C.

The $I_{G'}/I_G$ ratio seems to be insensitive to temperature for the Fe sample, while it increases slightly for higher temperature for the Ni sample. Antunes et al. [170] suggested this ratio to be quality dependent, however they didn't specify in what way. From our data it appears that this ratio is not a good measure of quality, as there is no distinct behaviour between the two samples.

The $I_D/I_{G'}$ ratio, finally shows a sharp decrease when increasing the temperature for the Ni sample. Musso et al. [188] found this ratio to be highly dependent to graphite quality (lower equals better), which is confirmed by the data from our Ni sample. The Fe sample shows a large drop for this ratio at 500 °C, while at 450 °C the G' and D+G peak fused together in such a way that both are indistinguishable from each other. This suggest that quality is very low at 450 °C [190]. It is possible that due to process variations the Fe sample at 500 °C somehow improved. From the data at higher temperature and the absence of a clear G' peak at 450 °C it is very likely that normally the $I_D/I_{G'}$ ratio would've shown a similar behaviour to that of the Ni sample.

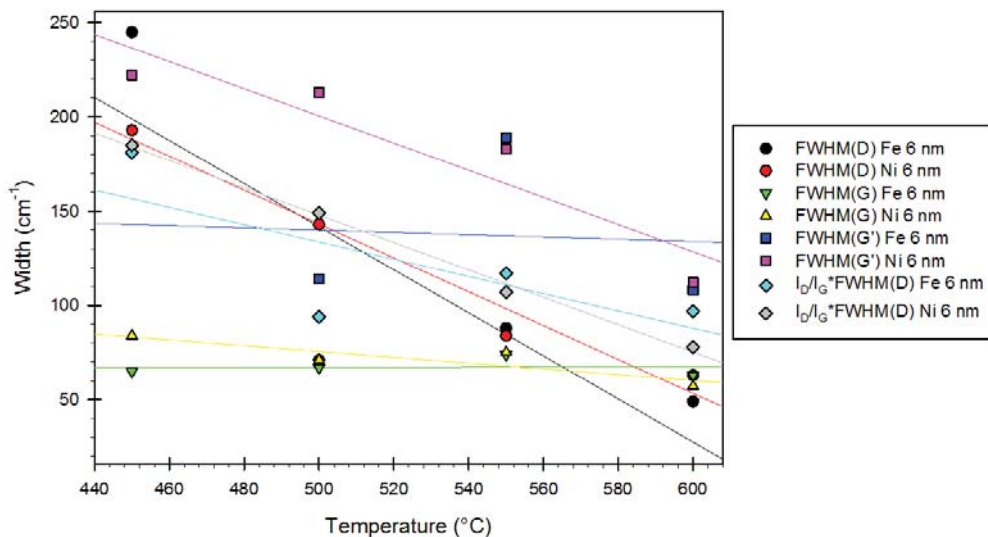


Figure 6.20: Raman band widths and $I_D/I_G \cdot \text{FWHM(D)}$ against temperature

In figure 6.20 the width of the D, G and G' band and the product of FWHM(D) and I_D/I_G have been plotted, again with a linear regression between the points. Both the D and G' band demonstrate a sharp decrease for higher temperature for all the samples (if we again ignore the result of Fe at 500 °C). This demonstrates a clear increase of graphite quality for increasing temperature [164, 170, 190]. The G band width seems relative insensitive to a change in temperature.

Antunes et al. suggested that the product of the FWHM(D) and I_D/I_G ratio would be a good measure of quality [170]. Indeed the behaviour of this product against temperature is in agreement with our expectations, even for the Fe sample. From their work we can conclude that in our samples both the number of defects as the size of the defects increases when temperature is decreased.

From our data we can thus conclude that the I_D/I_G ratio, the width of the D and G' peak (and the presence of second order bands in general) are a good indication for graphite quality. If no second order peaks are present the product of I_D/I_G and the FWHM(D) should be used, as the I_D/I_G ratio alone appears to be a poor indicator of quality. The recipe developed seems to give aligned growth on samples with a thin layer of Fe at temperatures at 600 °C. Fe or Ni on 10 nm Ti and 100 nm oxide are able to grow, albeit defective, CNTs/CNFs even at temperatures as low as 450 °C. Pd did show some growth at 600 °C, but only very minor and highly defective.

6.3.4 Experiments with lift-off wafers

In the end the goal was to create vertical interconnect measurement structures using the equipment and recipes which were found to give the best growth. As seen from the previous two sections both the default PECVD and the thermal CVD in the 2" tube furnace performed quite well and have the potential to grow aligned CNTs (although in case of the latter presumably only on thin catalyst layers).

As from experiments performed on a BlackMagic II (PE)CVD growth on samples patterned by photo-resist are of bad quality, and the fact that some difficulties in the wet etching of the catalyst and the Al layer were found in the P2748 process, only the P2752 process and lift-off remained. The P2752 process would result in substrates rather different from the ones tested (catalyst in an etched cavity instead of flat surface) and also required covering the catalyst with photo-resist. Thus, the lift-off process was chosen for the electrical measurement wafers.

As Al can't survive the high temperature processes in the NanoLab equipment it was decided to use Ti instead, as it was readily available in the sputter coater and could be etched with the ICP dry etcher. First 1 μm of Ti was deposited and afterwards patterned by lithography and dry etching. After this the lift-off process was performed. As lift-off of only a thin catalyst layer proved to be difficult first an additional 10 nm of Ti was deposited after which the catalyst was evaporated without breaking the vacuum. The batch sent to NanoLab used an exposure time of 8 s. and lift-off using a sonic acetone bath, both 3, 6 and 12 nm of Ni and Fe were deposited using the class 10000 e-beam evaporator (LH 560). Growth in the PECVD as well as in the CVD furnace was performed.

6.3.4.1 PECVD

Both Ni and Fe samples were tested in the PECVD. As the wafer holder was only big enough for a quarter wafer only one catalyst could be tested each time. As the default recipe used by NanoLab performed best for Ni it was used again as a starting point. Growth time was extended to 4 minutes in order to obtain longer tubes.

Surprising enough no growth at all could be observed on a 1/4 wafer piece of 6 nm of Ni when SEM was used to investigate the sample. Instead a film which looked like a-C was observed. It was possible that some contamination from the lift-off and subsequent cleaning in EKC505 remained. In order to test this hypothesis part of the wafer was cut

up and cleaned. One piece was cleaned by putting it 3 min. in acetone followed by 3 min. of methanol (piece nr. 1) followed by rinsing with distilled water. A second piece was treated the same way, but with an additional 5 min. cleaning step in $\text{NH}_4\text{OH}:\text{H}_2\text{O}:\text{H}_2\text{O}_2$ (1:5:1) to remove any organic contamination before rinsing with distilled water (nr. 2). A third untreated sample (nr. 3) was also put in the PECVD system, after which the same recipe was used to grow CNTs.

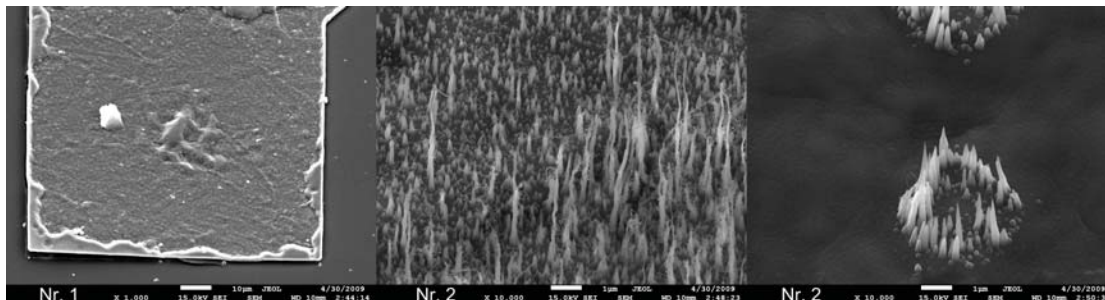


Figure 6.21: Comparison between different cleaning methods to enable growth on 6 nm of Ni pieces

Figure 6.21 displays the results obtained when cleaning the samples. Both the uncleaned and partly cleaned (nr. 1) sample showed no growth and were visually indistinguishable in the SEM. On the left the partly cleaned sample is shown, which appears to have an increased surface roughness at the spot where normally the catalyst would be. The Ti layer is peeled off from the substrate, very likely due to thermal stress (although Ti has a good adhesion to Si and the thermal expansion coefficient is ‘only’ 3 times higher). The samples were removed from the substrate while they were approximately 150 °C, further cooling before removing the sample should prevent the deformation of the Ti layer.

The 6 nm of Ni sample which was cleaned with the more aggressive solution (nr. 2) displayed very non-uniform growth. Fibres lengths were between a couple of hundred to several μm . The diameter was about 100 nm, while the density was low ($10^8 - 10^9 \text{ cm}^{-2}$). Some smaller tubes were observed alongside the longer fibres, similar to the results obtained before in section 6.3.2. Growth was observed on the patterned areas, indicating that features of at least 4 μm were successfully created using lift-off. The fact that cleaning the wafer enabled growth indicate that very likely some contamination existed on the wafers.

The samples with Fe instead of Ni did give growth without cleaning when PECVD was used. Figure 6.22 shows the SEM images obtained from 1/4 wafer samples with either 6 or 12 nm of Fe. As can be seen in both cases the growth is rather short (0.5 μm) and consists of thick 100 nm aligned CNFs together with random smaller CNTs (10-20 nm for 6 nm of Fe, 40 nm for the 12 nm of Fe sample). Density is about 10^9 cm^{-2} . Clearly the growth is much more defective than the Fe samples from section 6.3.2.

To investigate if the samples with Fe as catalyst would also benefit from cleaning the same experiment as done with Ni was performed with a partly cleaned (1), fully cleaned (2) and uncleaned (3) sample in the PECVD reactor. No change in structure could be observed by SEM, however the Raman spectra obtained from the three samples did show differences. The spectra can be found in figure C.13 and the data in table C.2.

As can be seen from both the general spectra as the quality indicators the sample which was cleaned with the ammonium hydroxide and hydrogen peroxide has the highest graphite quality. Although the I_D/I_G ratio slightly increased the width of the D band

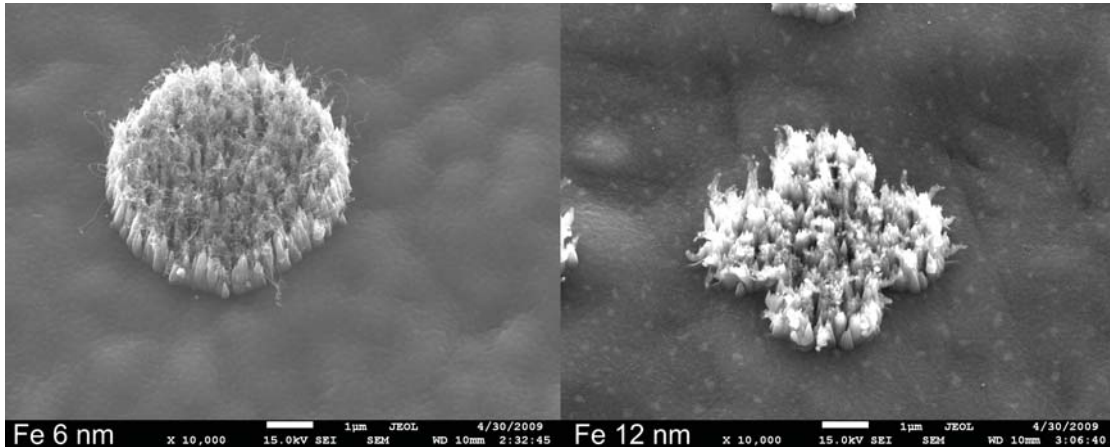


Figure 6.22: SEM images of 6 and 12 nm of Fe growth using HF-PECVD

decreased, the G' peak became more clear (the G' peak in sample 3 is deformed due to the strong baseline) and the product of the FWHM(D) and I_D/I_G is the lowest. The strange peak around 320 cm^{-2} is probably due to distortion. It is inside the RBM band, but corresponds to a SWNT with diameter between $0.7 - 0.8\text{ nm}$, which is unlikely to be grown in a DC-PECVD system. It can be concluded that cleaning is also beneficial for the Fe samples.

An attempt was made to create interconnect structures from the growth obtained at the 6 and 12 nm of Fe samples which were shown before. Unfortunately the CNT length was rather small, which limited the oxide thickness between the metal layers to 300 nm . A short (1 min.) CMP step was used to try to remove the oxide from the CNT tips. However, after the structures were completed the resistance measured was in the order of $\text{G}\Omega$, which indicates that very likely still an oxide layer is remaining. A longer CMP step should be used in the future.

Currently NanoLab is processing additional pieces of the Ni and Fe wafers which are cleaned by the cleaning procedure mentioned before, but now with a longer (10 min.) cleaning in ammonium hydroxide and hydrogen peroxide to, hopefully, improve the growth even further. Unfortunately, to date no results are available on the growth.

6.3.4.2 Thermal CVD

The recipe developed in section 6.3.3 was also used to attempt to grow aligned CNTs on the samples created by lift-off. As the 2" tube is too small to fit a quarter piece wafer some additional Si has to be removed to fit them. However, to save the limited amount of samples, growth was attempted with smaller 1 by 1 cm pieces first. Again, only a-C was observed on the samples with 6 nm of Ni as catalyst. The Fe samples performed much better and displayed random CNT growth at both $500\text{ }^\circ\text{C}$ and $600\text{ }^\circ\text{C}$, the SEM images are displayed in figure 6.23.

As can be seen from figure 6.23 a thick and dense random layer of CNTs was grown at $600\text{ }^\circ\text{C}$, with a tube diameter of $10\text{-}30\text{ nm}$. As the tubes are random orientated measuring the tube height and density is not possible, however the total layer of CNT is at least $1\text{ }\mu\text{m}$ thick. At $500\text{ }^\circ\text{C}$ the layer is little thinner and less dense, the diameter again is $10\text{-}30\text{ nm}$.

Again Raman spectroscopy was performed on the samples, the spectra can be found in figure C.20 and C.21, table C.3 contains the extracted data. It is interesting to see

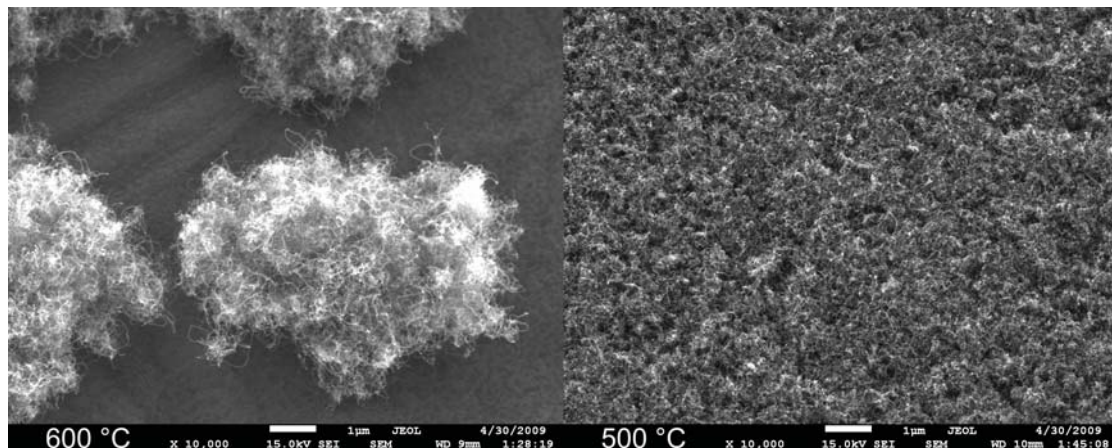


Figure 6.23: CVD growth results at different temperature of 6 nm of Fe samples created by lift-off

that the a-C of the Ni sample shows both a D and G peak. The I_D/I_G ratio is lower than the Fe sample, again indicating that this measure of graphite quality is unreliable. The absence of higher order peaks and the broad D band indicate a low graphite quality.

The Fe sample at 600 °C shows a sharp D and G' band, indicating relative good graphite quality. This is confirmed by the very low product of I_D/I_G and FWHM(D) and $I_D/I_{G'}$ ratio, both near the values obtained from 1 nm of Fe earlier in section 6.3.3. When the temperature is lowered to 500 °C the FWHM(D) increases and the G' band becomes less clear, indicating a decrease in graphite quality.

Beside Raman also TEM was performed on the 6 nm Fe samples at 500 and 600 °C, of which the results are shown in figure 6.24. The samples appeared to have relative good graphite quality, with only few 'bamboo' like defects. No clear catalyst could be observed at the tip, implying that the growth mechanism is most likely base growth. Not much visual difference could be observed between the two samples, indicating that graphite quality remains relative good when temperature is decreased.

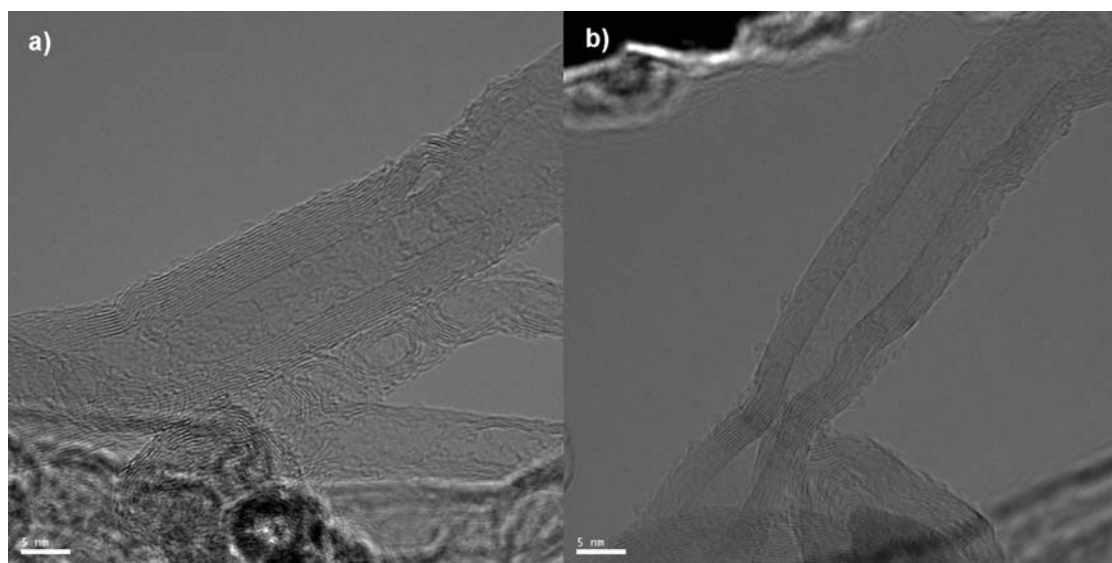


Figure 6.24: TEM images of 6 nm Fe after growth at a) 600 °C, and b) 500 °C

It was attempted to improve the growth of both the Ni and Fe sample by cleaning the samples in the solution mentioned in the previous section (with the longer 10 min. ammonium hydroxide step). Figure 6.25 shows the SEM results sent by NanoLab. The Fe growth appears to degrade significantly, showing large (100 nm) CNFs beside some smaller 10-20 nm, longer, CNTs. It is likely that the cleaning treatment reacted with the Fe layer (hydrogen peroxide can oxidise Fe) which caused the poor results.

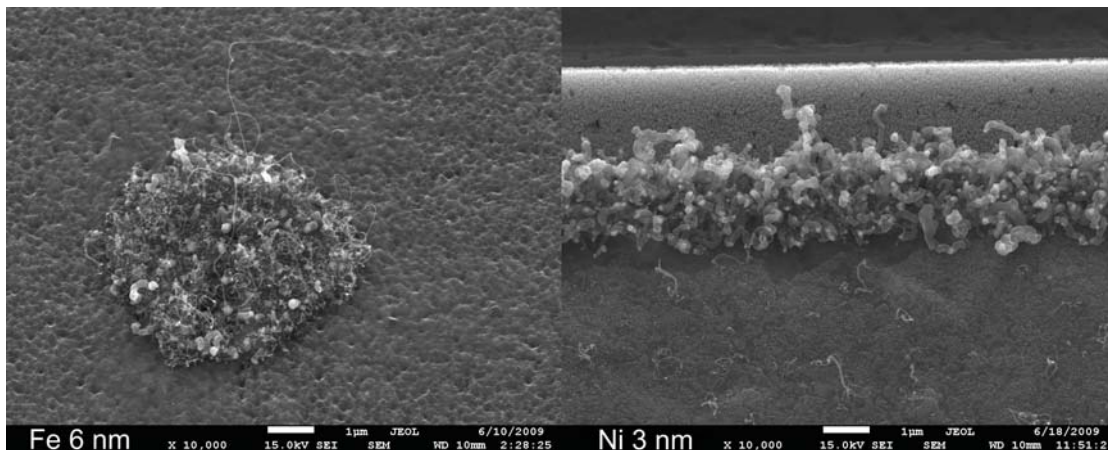


Figure 6.25: Growth results on Fe and Ni lift-off samples after cleaning

The 3 nm Ni sample did show some highly defective CNF growth at the edges of the big catalyst bars in the center of the dies. No growth was observed on the 6 nm Ni sample. If the growth on the 3 nm sample was due to the treatment is unknown, as no experiments have been done to date without cleaning for this catalyst thickness.

The cleaning should not be used in case of thermal CVD, as it degrades the growth for the Fe sample and doesn't enable good growth on the Ni samples. What is exactly withholding the Ni samples from growing CNTs is unclear at the moment. The next section discusses a possible cause found in literature and EDX experiments performed to investigate this possibility.

6.3.4.3 Possible cause for the absence of growth on Ni

As mentioned in the two previous sections no growth was observed when using Ni, which otherwise worked well in previous experiments. In section 6.3.4.1 it was found that cleaning the Ni samples with 3 min. acetone, 3 min. methanol and 5 min. $\text{NH}_4\text{OH}:\text{H}_2\text{O}:\text{H}_2\text{O}_2$ (1:5:1) enabled growth on the samples. This made us conclude that contamination was the likely candidate of preventing growth.

However, in section 6.3.4.2 hardly any growth was observed after cleaning. There might be other causes than just contamination preventing the growth. Of course it could be possible that the recipe used isn't compatible with Ni as a catalyst. We did, however, observe growth on a patterned Ni sample and samples with oxide underneath the Ti layer. It is thus not likely that this is the case.

Chuang et al. [191] recently reported that Ni can diffuse through a 40-100 nm Ti layer and into the Si substrate at relative low temperature (590 °C). As our Ti layer is rather thick compared to the Ni, the majority of Ni might diffuse deep into this layer, which prevents the carbon from reaching the catalyst. Indeed diffusion tables show that there exist a low temperature diffusion path (573 °C) for Ni into Ti [192].

More results indicating that the combination between Ni and Ti might negatively affect the growth come from Peng et al. [193]. They found that if a Ti layer on top of Si is pre-annealed before the deposition of the Ni catalyst it greatly improves both the length and the alignment of the as-grown CNTs. They reason that a high Ti percentage in the Ni would inhibit growth and annealing the Ti before prevents diffusion of the Ni in the obtained TiSi layer.

To investigate if Ni was indeed diffusing into the Ti layer a cross-section using ion milling (along the large bar in the centre of the die) was made from the Ni sample only cleaned by acetone and ethanol and used in the PECVD experiment discussed earlier (section 6.3.4.1). Next TEM and EDX analysis were performed to investigate if any Ni was present in the sample and how it was distributed among the layers.

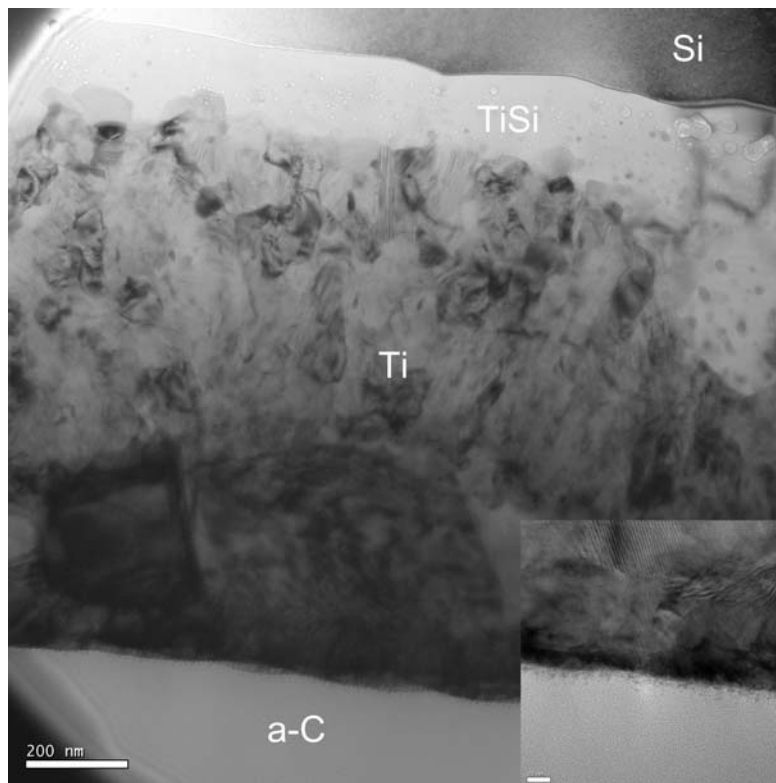


Figure 6.26: TEM image of cross-section of Ni sample, the inset shows a higher magnification of the bottom layer (scale bar equals 20 nm)

In figure 6.26 part of the cross-section can be found, while the EDX spectrum can be found in appendix C.2. The upper most layer is the Si wafer. The bright layer underneath is believed to be a TiSi alloy judging from the Si and Ti peak at that spot. Further towards the surface the Ti peak becomes stronger. The observed Si can be both due to contamination from the ion milling or actual present atoms. As the Si peak reduces further towards the surface the peak is most likely caused by a large amount of Si atoms diffusing into the Ti. It can be seen that the TiSi layer is present in both the original Si and Ti layer (remember that the Ti layer was originally 1 μm), indicating diffusion in both directions.

The following layer observed in figure 6.26 is the remaining Ti layer, which only shows a weak Si peak. Also a carbon and Cu peak are observed. Carbon is an easy contamination to pick up, which is most likely causing the peak. The Cu is due to the

TEM grid. The final layer which can be observed completely at the bottom is a thick a-C layer.

Surprisingly no Ni could be found at the surface, not even when the TEM bundle was elongated over the boundary layer. This makes us conclude that the Ni indeed diffused into the Ti, to such an extent it became undetectable with EDX. It is very unlikely for the plasma to have etched away the Ni layer, as no special etching step has been performed. Also, growth with a similar Ni thickness has been observed before in the plasma system (section 6.3.2).

These results found, together with the literature examples, make us conclude that Ni and a thick Ti layer are a combination to be avoided when growing CNTs. In case of the thin, 10 nm, Ti layers used before the Ni is unlikely to diffuse far into the Ti. However, a thick Ti layer can consume all the catalyst, preventing any growth.

6.4 Conclusion

When attempting to produce CNTs using the Novellus Concept One PECVD in the DIMES class 100 cleanroom, or the novel RF assisted CVD at NanoLab no growth could be obtained. In both cases likely due to a too low substrate temperature. However, when using the Blackmagic II 2" (PE)CVD and a custom made HF-PECVD and horizontal tube furnace CVD at Nanolab we were able to grow CNTs using different settings and catalysts. Underneath the catalyst 10 nm of Ti was present, except for the lift-off samples which used 1 μm of Ti.

The BlackMagic system proved to be able to grow aligned CNFs using PECVD at temperature of 500 °C using either Ni or Pd as a catalyst. When temperature was decreased to 450 °C only Pd displayed reasonable growth. The patterned Ni samples performed much worse than non-patterned catalyst layers, which is likely due to catalyst poisoning by either the photo-resist or cleaning methods.

The samples were examined by TEM and displayed bamboo tip grown CNTs when Pd was used. The non-patterned Ni displayed tip grown CNFs, and the patterned Ni samples nanofilament like structures. When a hot-filament was used instead of a substrate heater the differences were minimal for the Ni samples, however Pd appeared to perform much worse while Raman spectroscopy suggested an improvement. Generally, growth was very defective when using PECVD, judging from the Raman spectra and TEM images. When a hot-filament was used instead of substrate heating no notable difference could be observed.

At 640 °C using APCVD CNT growth was possible using either Co, Fe or Pd. The thin Fe samples (1 or 5 nm) and 1 nm Pd samples were able to grow at 500 °C, only Pd showed any growth at 450 °C. The Pd samples were also the only ones displaying self-alignment at all temperatures. The graphite quality of these samples was, however, very low judging from both Raman and TEM analysis. This in contrary to the MWNT grown with Co and Fe, which are of relative good quality (bamboo CNTs). High density self-aligned growth was never demonstrated before using Pd, which is an interesting catalyst as it also has been used as an excellent electrical contact material to CNTs.

Using the PECVD of NanoLab at ~ 800 °C defective bamboo CNT growth was observed using both Fe and Ni as catalyst, where Fe performed generally better than Ni. When lift-off wafers were used no growth was observed using Ni, while the quality of the Fe grown samples decreased compared to previous experiments. It was found that

cleaning the wafers for 5 min. with a solution of ammonium hydroxide and hydrogen peroxide enabled growth on the Ni samples and increased quality of the Fe samples.

A recipe developed for the horizontal furnace was found to allow self-aligned MWNT growth on 1 nm Fe samples at 600 °C in the 2" quartz tube thermal CVD of NanoLab. When observed with Raman and TEM the quality appeared high. Samples with a 100 nm oxide layer underneath the Ti and catalyst (either 6 nm Ni or Fe) layer were able to grow CNFs at temperatures as low as 450 °C.

Raman spectroscopy was performed on the 6 nm of Fe and Ni samples with oxide underneath the Ti. It was found that the I_D/I_G ratio is unreliable to assess graphite quality. Better measures are the product between I_D/I_G and the FWHM(D) or the $I_D/I_{G'}$ ratio, both indicating quality increased with temperature.

The same recipe was used on lift-off wafers which had 6 nm of Fe as catalyst. A thick layer of random MWNT could be observed at both 500 and 600 °C. Judging from Raman analysis and TEM the quality only decreased slightly when the temperature was decreased from 600 to 500 °C.

No good growth was found on the Ni samples placed in the thermal CVD, not even after cleaning. EDX analysis showed no traces of Ni on a lift-off sample used in the PECVD. This indicates that the Ni might have diffused across the Ti layer (as is possible according to literature) to such an extent it couldn't be detected by EDX. Deep diffusion of Ni into a thick Ti layer will cut-off the catalyst from the carbon feedstock, preventing growth.

For our purposes either the (PE)CVD growth in the BlackMagic machine or growth using the recipe developed in the thermal CVD at NanoLab seem most promising. All recipes were able to grow aligned CNTs or CNFs. Raman spectra and TEM demonstrated that growth from a PECVD systems or with Pd as catalyst is more defective compared to growth using Fe or Co in a thermal CVD. The density was generally the highest when using thermal CVD, judging from the SEM images obtained.

Conclusion

The goal of this work was to investigate if carbon nanotubes (CNT) can indeed be an alternative to traditional metals for 3D integrated circuits (IC). Interconnect issues, like their high power dissipation, increased sensitivity to electro-migration, and the increased resistance and delay caused by the downsizing of interconnects, are a problem in the realisation of current and future ICs. To decrease the interconnect delay 3D integration, the stacking of layers of transistors, has been proposed. Several challenges have to be solved in order to mature 3D integration, one of these being the creation of reliable vertical interconnects with high aspect ratio and low resistance. We argued that carbon nanotubes could be an excellent candidate for these vertical interconnects (vias).

The thesis consists of two parts. The first is a review of theory and the derivation of a circuit model for CNTs followed by electrical simulations. The second part consists of the development of fabrication methods and experiments performed to grow CNTs for vertical interconnects. Followed by the analysis of the obtained CNTs with different characterisation techniques.

After deriving the electrical model for the CNT it was found that the quantum capacitance and kinetic inductance, which exist in single tubes, disappear when a bundle of sufficient (i.e. many thousands) tubes is formed. The remaining electrostatic capacitance of a CNT bundle will be close to that of a metal line with the same dimensions. Only the resistance of the bundle, a combination between the quantum and contact resistance, will vary from a traditional metal via.

From the simulations performed we can conclude that only single-walled nanotubes (SWNT) have the ability to outperform bulk Al and Cu in terms of electrical resistance. For this the CNT density should be above $5 \cdot 10^{13} \text{ cm}^{-2}$; such very high densities have yet to be reported. For realistic high densities ($10^{12} - 10^{13} \text{ cm}^{-2}$) the resistance using SWNT will be at least one order of magnitude higher than bulk Al or Cu. When multi-walled nanotubes (MWNT) are used the resistance will always be higher than that of bulk Al and Cu, but the resistance hardly increases when density decreases.

Thus, in terms of electrical resistance carbon nanotubes will not likely outperform bulk metals. However, other properties of carbon nanotubes, the extremely high aspect ratio, potential very high thermal conductivity ($> 1000 \text{ W/m}\cdot\text{K}$) and high electrical and thermal stability can still make CNTs an interesting candidate for vertical interconnects in 3D integrated circuits.

Experimentally, several recipes were tested to grow low temperature CNTs and the results were investigated by SEM, TEM and Raman spectroscopy. No growth was obtained when using the Novellus Concept One PECVD in our cleanroom or a novel RF assisted CVD at NanoLab. It is likely the substrate temperature is too low for successful growth.

It was found that the DC-PECVD recipe from AIXTRON can be used to grow aligned CNTs of sufficient length using Ni and Pd as a catalyst, but with low density

and quality. When a hot-filament was used instead of substrate heating no notable difference was observed. Photo-resist patterning was found to have a negative influence on the CNT growth quality. A lift-off process was created to circumvent this problem.

When using an APCVD recipe from AIXTRON high density (10^{12} cm $^{-2}$) aligned growth could be obtained using Pd. However the quality was very low, resulting in carbon nanofilaments instead of tubes. High density self-aligned growth was never demonstrated before using Pd, which is an interesting catalyst as it has been used as an excellent electrical contact material to CNTs. High quality random growth was possible when using Fe or Co as catalyst.

The DC-PECVD process at NanoLab was high temperature (~ 800 °C) and therefore less interesting for us. However, aligned growth could be obtained in combination with Fe and Ni. A recipe developed for the use in a thermal CVD furnace was found to be able to grow aligned CNTs when a thin (1 nm) layer of Fe was used as catalyst at 600 °C. The quality was found to be high.

The same recipe was able to grow good quality random CNTs at both 500 and 600 °C when lift-off was used to pattern the 6 nm Fe catalyst on 1 μ m Ti. Ni patterned by lift-off was found to have difficulties when growing CNTs on top of a thick (1 μ m) Ti layer. From EDX measurements and literature it was concluded that Ni diffuses into the Ti, preventing growth.

We investigated if Raman spectroscopy could be used to determine the graphite quality of the grown CNTs. It was found that the I_D/I_G ratio often used in literature is an insufficient parameter to investigate quality. Better methods are the use of the product between FWHM(D) and I_D/I_G , or the $I_D/I_{G'}$ ratio if second order peaks can be observed. On it's own Raman spectroscopy is not sufficient to give a accurate overview of structural quality. But combined with additional SEM or TEM imaging on some samples it can be used to quickly check changes between samples, in order to investigate the dependency of graphite quality on different process settings.

Recommendations and future work

To obtain high quality growth with the APCVD recipe using Pd as catalyst changing the gas ratio's and flow rates is the only option, as temperature is already at the maximum and activation is excellent. With the same recipe in combination with Co and Fe the catalyst and contact layer should be optimized, as quality is good but density too low. The recipe developed for thermal CVD at NanoLab already gives good quality. Reducing the thickness of the Fe layer used on the lift-off samples is likely to increase density and enable self-alignment.

In case of DC-PECVD both quality and density are low. Quality can be increased by optimizing the ratio between the acetylene and ammonia, and plasma intensity. To increase the density the activation of the catalyst layer should be optimized by adjusting the layer thickness, activation time and plasma intensity. For recipe optimization the combination of Raman and SEM should be sufficient to do a quick investigation on morphology and quality. Atomic force microscopy could be used to investigate the activation of the catalyst layer.

The lift-off process can be further optimized now it is possible to deposit thinner layers of negative photo resist (1.4 μ m instead of 3 μ m). This should improve the transfer of smaller features. It is recommended to first start with the 'oxide before growth' flowcharts combined with lift-off, as CMP can be skipped. After this it would

be possible to perform electrical, and later on thermal, characterization of the grown CNTs using the same four-point electric resistance measurement structure

In summary it should be interesting to perform the following experiments and measurements:

- Optimize recipes for our catalyst by changing pressure, gas flows, plasma power and catalyst thickness. SEM and Raman can be used to investigate the results
- Optimize lift-off with 1.4 μm of negative photo resist. Order targets for Pd, Ti, Fe and Ni if not already available in the class 100 e-beam evaporator
- First use ‘oxide before growth’ process and perform resistance measurement vs. catalyst thickness (diameter), length, contact layer thickness and metal, and via configuration
- Develop a CMP recipe for ‘oxide after growth’ process
- Investigate electrical and thermal reliability
- Attempt to perform thermal conductivity measurements using the 3ω -method
- Investigate EXCIMER laser activation of catalyst layer
- Investigate if sputtering of TiN on top of Al can be used to prevent native oxide between tubes and metal

In the end the final goal is to use the obtained recipes and processes for the growth of carbon nanotubes, and incorporate them into an existing or new lay-out for a 3D integrated circuit replacing the traditional metal vias. For this a four year project will start in October, in which the author will participate as a PhD candidate.

Publications

Conference presentations

- S. Vollebregt, J. Derakhshandeh, R. Ishihara and C.I.M. Beenakker, “Growth of high density aligned carbon nanotubes using palladium as catalyst”, *51st Electronic Materials Conference (EMC’09)*, State College (PA), USA, June 2009

Submitted

- S. Vollebregt, J. Derakhshandeh, R. Ishihara, M.-Y. Wue, C.I.M. Beenakker, “Growth of high density self-aligned carbon nanotubes and nanofibres using palladium as catalyst”, *Journal of Electronic Materials*
- S. Vollebregt, J. Derakhshandeh, M.-Y. Wue, R. Ishihara, C.I.M. Beenakker, “Investigating low temperature high density aligned carbon nanotube and nanofilament growth using Palladium as catalyst”, *Workshop on Semiconductor Advances for Future Electronics (SAFE’09)*

Appendices

Appendix A

Phonons

Phonons are quantized particle-like vibrations in the lattice of a solid crystal. The origin of the vibration of lattice atoms is the thermal energy they have which makes them vibrate at their place (the atoms are normally not able to move through the lattice as they're bonded with each other). The lattice vibrates in response to this thermal energy, creating mechanical waves that can carry heat (and also sound) through the crystal. A packet of these waves is called a phonon in quantum mechanics and has both particle and wave properties (just like photons). In short a phonon is a basic energy quantum of a lattice wave (just like a photon is the basic energy quantum of an electromagnetic wave).

In section 2.2.1 so called acoustic phonons (AP) and optical phonons (OP) were mentioned. Acoustic phonons are phonons with frequencies that become small for larger wavelength and correspond to sound waves in the lattice. Optical phonons however always have a minimal frequency of vibration even for large wavelengths (they are called optical because they're easily excited by light). Phonons have influence on the electrical (and thermal) conduction as they distort the perfect lattice and thus induce scattering between electrons and lattice atoms (electron-phonon scattering).

Beside phonon-electron scattering also phonon-phonon scattering is possible. If we have two incoming phonons with wave vectors and they scatter their vectors will combine into a new one. If this resulting vector is within the first Brillouin zone (which is the primitive cell in the reciprocal lattice) the momentum will be conserved. However when the resulting vector is larger than the first Brillouin zone it becomes physically equivalent to a vector inside the first Brillouin zone pointing in another direction. This is called Umklapp scattering, after the German word for flip-over. It is a very important scattering mechanism limiting thermal conductivity in many materials. Beside Umklapp scattering a phonon can also scatter with crystal defects, junctions and impurities.

Appendix B

Process flowcharts

B.1 P2700

B.1.1 Starting material

Single side polished test wafers, 100 ± 0.2 mm diameter, 525 ± 15 μm thickness, p-type (boron), 100 orientation, 2-5 Ωcm .

B.1.2 Process steps

1. PECVD oxide deposition (1000 nm, backside) @ Class 100
Use the Novellus PECVD reactor to deposit a 1000 nm thick dielectric SiO_2 layer. Special recipe: 1.0 μSiO_2 at 400 °C in group ‘mix’.
2. Ti and Ni deposition by sputtering @ Class 100
Use the Trikon Sigma sputter coater for the deposition of the Ti and Ni layer on the test wafers. Deposition must be done at 200 °C with an Ar flow of 100 sccm. Do not break vacuum between depositions. Use recipe ‘10nmTi’ for the 10 nm thick Ti layer followed by recipe ‘3nmNi’ for a 3 nm thick Ni layer.
3. Coating and baking @ MEMS lab
Processing will be performed on the manual spinner with manual edge bead removal. Use resist AZ4562, with coating at 2000 rpm resulting in a thickness of 1 μm .
4. Ni wet etching from backside and edge of wafer @ MEMS lab
Use $\text{HNO}_3(65\%):\text{CH}_3\text{COOH}(100%):\text{H}_2\text{SO}_4(98%):\text{H}_2\text{O}=5:5:2:28$ at room temperature for 10 s to remove 3 nm of Ni from the backside and edge of the wafer. Rinse thoroughly.
5. Silicon dioxide wet etching @ MEMS lab
Use BHF(1:7) at room temperature to remove the 1000 nm layer of silicon dioxide on the backside of the wafer. Etch until the backside is hydrophobic, plus an additional 30 s. Rinse thoroughly.
6. Photoresist removal @ MEMS lab
Dissolve the photoresist in acetone. Manually rinse for a couple of minutes and then dry the wafers using the single wafer dryer.
7. Cleaning @ SA lab
Use EKC505 at 85 °C for 10 minutes to clean the wafers. Rinse in the water bath till the water resistance becomes 5 M Ω . Dry the wafers with the single wafer dryer.

8. Coating and baking @ Class 100
Use the EVG-120 automatic wafertrack to coat the wafers with 1.4 μm resist. The process includes a treatment with HMDS (hexamethyldisilazane) vapour with nitrogen as a carrier gas, spin coating for 30 s with Shipley SPR 3012 and pre baking for 1 minute at 95 $^{\circ}\text{C}$. Use recipe: Co - SPR3012 - 1400nm (resist thickness: 1.400 μm at 48% RV).
9. Alignment and exposure @ Class 100
Processing will be performed on the ASM PAS5500/80 automatic wafer stepper. Use mask PDM18, Number V1-in, job N10a-1 with exposure energy $E = 150$.
10. Development @ Class 100
After exposure a post-exposure bake at 115 $^{\circ}\text{C}$ for 1 minute is performed on the EVG-120 wafer track, followed by a development step using Shipley MF322 developer (single puddle process), and a post bake at 100 $^{\circ}\text{C}$ for 1 minute. Use recipe: Dev - Single Puddle
11. Inspection of linewidth and overlay @ Class 100
Visually inspect the wafers through a microscope and check linewidth and overlay.
12. Wet etching of Ni @ MEMS lab
Use $\text{HNO}_3(65\%):\text{CH}_3\text{COOH}(100%):\text{H}_2\text{SO}_4(98%):\text{H}_2\text{O}=5:5:2:28$ at room temperature to remove the uncovered Ni. Etch rate: 3 nm in 10 s. Rinse thoroughly.
13. Photoresist removal @ MEMS lab
Dissolve the photoresist in acetone. Manually rinse for a couple of minutes and then dry the wafers using the single wafer dryer.
14. Cleaning @ SA lab
Use EKC505 at 85 $^{\circ}\text{C}$ for 10 minutes to clean the wafers. Rinse in the water bath till the water resistance becomes 5 $\text{M}\Omega$. Dry the wafers with the single wafer dryer.
15. CNT growth @ Class 100
Use the Novellus PECVD to activate the Ni layer and grow CNTs. Use recipe CNTx-JD ($x = 1, 2$ or 3) in uniformity mode. Put the wafer in position 4.

B.1.3 Growth conditions

The next pages show the growth conditions used in the Novellus Concept One for the two batches of wafers produced with the above flowchart. Batch one has wafers with 3 nm Ni and the Ti was not completely removed (table B.1), while batch two has 6 nm of Ni (recipe '6nmNi' and all the uncovered Ti has been etched away by using 65 % $\text{HNO}_3:\text{BHF}$ (1:1) as an etchant (table B.2).

Table B.1: Novellus batch 1: 3 nm Ni, Ti not etched

Run	Temp (°C)	T _{act}	T _{ent}	Gas _{act}	Gas _{ent}	Flow (SCCM)	Pressure (mbar)	RF power (W)	LF power (W)	Comments
1	400	1		NH ₃	CH ₄ + H ₂	3000	2.67	1800		Only activation
2	400	1	19	NH ₃	CH ₄ + H ₂	3000	2.67	1800		
3	400	1	~2.5	NH ₃	CH ₄ + H ₂	3000	2.67	2200		Failed
4	400	1	19	NH ₃	CH ₄ + H ₂	3000	2.67	2000		
5	400	1		NH ₃	CH ₄ + H ₂	3000	2.67		500	Failed
6	400		10	NH ₃	CH ₄ + H ₂	3000	0.80	2000		Only growth
7	400	1	9	NH ₃	CH ₄ + H ₂	3000	2.67	2000		
8	400	1	39	NH ₃	CH ₄ + H ₂	3000	2.67	2000		

Table B.2: Novellus batch 2: 6 nm Ni, Ti etched

Run	Temp (°C)	T _{act}	T _{ent}	Gas _{act}	Gas _{ent}	Flow (SCCM)	Pressure (mbar)	RF power (W)	LF power (W)	Comments
1	400	1	39	NH ₃	CH ₄ + H ₂	3000	2.67	2000		
2	400	1	39	NH ₃	CH ₄ + H ₂	1000	2.67	2000		
3	400	1	39	NH ₃	CH ₄ + H ₂	500	2.67	2000		
4	400	5	35	NH ₃	CH ₄ + H ₂	500	2.67	2000		
5	400	~1		NH ₃	CH ₄ + H ₂	500	2.67	2000		Failed
5.2	400	3	27	NH ₃	CH ₄ + H ₂	500	0.80	1000		
6	400	2	8	NH ₃	CH ₄ + H ₂	500	2.67	1000		
6.2	400	3	57	NH ₃	CH ₄ + H ₂	500	2.67	1000		
7	400	3	27	NH ₃ /N ₂	CH ₄ + H ₂ /N ₂	250/750	1.60	1000		
8	400	3	57	NH ₃	CH ₄ + H ₂	500	2.67	1000	250	
9	400			NH ₃		250	1.33	2000		Failed

B.2 P2748

B.2.1 Starting material

Single side polished test wafers, 100 ± 0.2 mm diameter, 525 ± 15 μm thickness, p-type (boron), 100 orientation, 2-5 Ωcm .

B.2.2 Process steps

1. Thermal oxidation @ Class 100
Grow 30 nm of thermal oxide. Use furnace B2 with recipe 300Å
2. PECVD oxide deposition (1000nm, backside) @ Class 100
Use the Novellus PECVD reactor to deposit a 1000 nm thick dielectric SiO_2 layer. Special recipe: 1.0 μSiO_2 at 400 °C in group 'mix'.
3. Al, Ti and Ni deposition by sputtering @ Class 100
Use the Trikon Sigma sputter coater for the deposition of the second aluminium metal layer on the process wafers. The target must exist of 99% Al and 1% Si, and deposition must be done at 350 °C with an Ar flow of 100 sccm. Follow the operating instructions from the manual when using this machine. Use recipe 1475nm Al no RF @ 350C to sputter a 1.475 ± 0.1 μm thick layer.

Without breaking vacuum use the Trikon Sigma sputter coater for the deposition of the Ti and Ni layer on the test wafers. Deposition must be done at 200 °C with an Ar flow of 100 sccm. Do not break vacuum between depositions. Use recipe '10nmTi' for the 10 nm thick Ti layer followed by recipe 'XnmNi' for a 'X' nm thick Ni layer.

4. Number the wafers
5. Coating and baking @ MEMS lab
Processing will be performed on the manual spinner with manual edge bead removal. Use resist AZ4562, with coating at 2000 rpm resulting in a thickness of 1 μm .
6. Ni wet etching from backside and edge of wafer @ MEMS lab
Use $\text{HNO}_3(65\%):\text{CH}_3\text{COOH}(100%):\text{H}_2\text{SO}_4(98%):\text{H}_2\text{O}=5:5:2:28$ at room temperature for 10 s to remove 3 nm of Ni from the backside and edge of the wafer. Rinse thoroughly.
7. Silicon dioxide wet etching @ MEMS lab
Use BHF(1:7) at room temperature to remove the 1000 nm layer of silicon dioxide on the backside of the wafer. Etch until the backside is hydrophobic, plus an additional 30 s. Rinse thoroughly.
8. Photoresist removal @ MEMS lab
Dissolve the photoresist in acetone. Manually rinse for a couple of minutes and then dry the wafers using the single wafer dryer.
9. Cleaning @ SA lab
Use EKC505 at 85 °C for 10 minutes to clean the wafers. Rinse in the water bath till the water resistance becomes 5 M Ω . Dry the wafers with the single wafer dryer.
10. Coating and baking @ Class 100
Use the EVG-120 automatic wafertrack to coat the wafers with 1.4 μm resist. The process includes a treatment with HMDS (hexamethyldisilazane) vapour with nitrogen as a carrier gas, spin coating for 30 s with Shipley SPR 3012 and pre baking

for 1 minute at 95 °C. Use recipe: Co - SPR3012 - 1400nm (resist thickness: 1.400 µm at 48% RV).

11. Alignment and exposure @ Class 100
Use the EVG 420 contact aligner using soft contact and the default exposure time for Al underlayer for 1.4 µm resist (see manual). Use catalyst mask.
12. Development @ Class 100
After exposure a post-exposure bake at 115 °C for 1 minute is performed on the EVG-120 wafer track, followed by a development step using Shipley MF322 developer (single puddle process), and a post bake at 100 °C for 1 minute. Use recipe: Dev - Single Puddle
13. Inspection of linewidth and overlay @ Class 100
Visually inspect the wafers through a microscope and check linewidth and overlay.
14. Wet etching of Ni & Ti @ MEMS lab
Use Ni and Ti wet etching (BHF:HNO₃(%65):H₂O=1:1:50) in room temperature, to remove Ni and Ti. Rinse thoroughly.
15. Photoresist removal @ MEMS lab
Dissolve the photoresist in acetone. Manually rinse for a couple of minutes and then dry the wafers using the single wafer dryer.
16. Cleaning @ SA lab
Use EKC505 at 85 °C for 10 minutes to clean the wafers. Rinse in the water bath till the water resistance becomes 5 MΩ. Dry the wafers with the single wafer dryer.
17. Coating and baking @ Class 100
Use the EVG-120 automatic wafertrack to coat the wafers with 1.4 µm resist. The process includes a treatment with HMDS (hexamethyldisilazane) vapour with nitrogen as a carrier gas, spin coating for 30 s with Shipley SPR 3012 and pre baking for 1 minute at 95 °C. Use recipe: Co - SPR3012 - 1400nm (resist thickness: 1.400 µm at 48% RV).
18. Alignment and exposure @ Class 100
Use the EVG 420 contact aligner using soft contact and the default exposure time for Al underlayer for 1.4 µm resist (see manual). Use metal mask.
19. Development @ Class 100
After exposure a post-exposure bake at 115 °C for 1 minute is performed on the EVG-120 wafer track, followed by a development step using Shipley MF322 developer (single puddle process), and a post bake at 100 °C for 1 minute. Use recipe: Dev - Single Puddle
20. Aluminium etching @ MEMS lab
Use H₃PO₄:HNO₃:CH₃COOH:H₂O (4:1:4:1) to etch the Al till the Si is visible. Remake solution once it gets dirty.
21. Photoresist removal @ MEMS lab
Dissolve the photoresist in acetone. Manually rinse for a couple of minutes and then dry the wafers using the single wafer dryer.
22. Cleaning @ SA lab
Use EKC505 at 85 °C for 10 minutes to clean the wafers. Rinse in the water bath till the water resistance becomes 5 MΩ. Dry the wafers with the single wafer dryer.
23. CNT growth at external facility
24. Oxide deposition @ MEMS lab
Deposit a layer of oxide (thickness may vary depending on growth length). Use the

- STS PECVD with recipe SIO_STD4 (change deposition time). Put a test wafer first to see if time is correct for required thickness.
25. Optional: Chemical mechanical polishing
Use the MECAPOL E460 to remove part of the oxide to open up the CNT tips.
 26. Optional: Oxygen plasma etching of CNT tips @ MEMS lab
Use the EuroPlasma to perform etching on the CNTs to open the tips.
 27. Al deposition @ Solar Cell lab
Deposit 10 nm of Ti followed by 1.4 μm Al using LH 560 e-beam evaporator
 28. Coating and baking @ MEMS lab
Pretreat the wafers with HMDS with N_2 as carrier gas for 10 minutes. Deposit 2 μm of SPR3017 resist using the manual coater, bake for 1 min at 95 $^\circ\text{C}$.
 29. Alignment and exposure @ MEMS lab
Use the Karl Süss in soft contact mode to expose the wafers. Use metal2 mask.
 30. Development @ MEMS lab
Do a post exposure bake for 1 min at 120 $^\circ\text{C}$. Manually develop the wafers using Shipley MF332 developer for 20 s. and check if structures are ok. When required develop more to remove residual resist. End with a 1 min postbake at 120 $^\circ\text{C}$.
 31. Al dry etching @ MEMS lab
Use the Alcatel GIR300 to dry etch the Al using the standard recipe. First do a 15 min etch followed by a 10 minutes. If needed perform more (smaller) etching steps. After etching perform passivation.
 32. Photoresist removal @ MEMS lab
Use the Europlasma to strip the photoresist.
 33. Optional: thermal annealing @ MEMS lab Use the Carbolite ceramic oven to perform a 30 minutes anneal at 400 $^\circ\text{C}$.
 34. Clean the wafers Rinse thoroughly in water and dry with single wafer dryer.
 35. Coating and baking @ MEMS lab
Pretreat the wafers with HMDS with N_2 as carrier gas for 10 minutes. Deposit 2 μm of SPR3017 resist using the manual coater, bake for 1 min at 95 $^\circ\text{C}$.
 36. Alignment and exposure @ MEMS lab
Use the Karl Süss in soft contact mode to expose the wafers. Use contact hole mask.
 37. Development @ MEMS lab
Do a post exposure bake for 1 min at 120 $^\circ\text{C}$. Manually develop the wafers using Shipley MF332 developer for 20 s. and check if structures are ok. When required develop more to remove residual resist. End with a 1 min postbake at 120 $^\circ\text{C}$.
 38. Dry oxide etching @ MEMS lab
Use the Alcatel GIR300 to dry etch the SiO_2 and stop at metal 1 using standard etching recipe.
 39. Photoresist removal @ MEMS lab
Use the Europlasma to strip the photoresist. Clean the wafers in water and dry using single wafer dryer.

B.3 P2752

B.3.1 Starting material

Single side polished test wafers, 100 ± 0.2 mm diameter, 525 ± 15 μm thickness, p-type (boron), 100 orientation, 2-5 Ωcm .

B.3.2 Process steps

1. Thermal oxidation @ Class 100
Grow 30 nm of thermal oxide. Use furnace B2 with recipe 300Å
2. PECVD oxide deposition (1000nm, backside) @ Class 100
Use the Novellus PECVD reactor to deposit a 1000 nm thick dielectric SiO_2 layer. Special recipe: 1.0 μSiO_2 at 400 °C in group 'mix'.
3. First metallisation @ Class 100
Use the Trikon Sigma sputter coater for the deposition of the second aluminium metal layer on the process wafers. The target must exist of 99% Al and 1% Si, and deposition must be done at 350 °C with an Ar flow of 100 sccm. Follow the operating instructions from the manual when using this machine. Use recipe 1475nm Al no RF @ 350C to sputter a 1.475 ± 0.1 μm thick layer.
4. Number the wafers
5. Coating and baking @ Class 100
Use the EVG-120 automatic wafertrack to coat the wafers with 1.4 μm resist. The process includes a treatment with HMDS (hexamethyldisilazane) vapour with nitrogen as a carrier gas, spin coating for 30 s with Shipley SPR 3017M and pre baking for 1 minute at 95 °C. Use recipe: Co - SPR3017 - 2000nm (resist thickness: 2.00 μm at 48% RV).
6. Alignment and exposure @ Class 100
Use the EVG 420 contact aligner using soft contact and the default exposure time for Al underlayer for 2.0 μm resist (see manual). Use metall mask.
7. Development @ Class 100
After exposure a post-exposure bake at 115 °C for 1 minute is performed on the EVG-120 wafer track, followed by a development step using Shipley MF322 developer (single puddle process), and a post bake at 100 °C for 1 minute. Use recipe: Dev - Single Puddle
8. Dry etch aluminium @ Class 100
Use the Trikon Omega 201 plasma etcher to etch 1.4 μm Al. Follow the operating instructions from the manual when using this machine. The process conditions of the etch and passivation program may not be changed! Check both 'Cooling' and 'Main' switches of chiller are on. Use sequence AL14_350 at a platen temperature of 25 °C. Always check the wafer: no aluminum residues or under etching are allowed.
9. Remove photoresist @ Class 100
Use the Tepla plasma system to remove the photo resist in oxygen plasma. Follow the instructions specified for the Tepla stripper, and use the quartz carrier. Use program 1:1000W
10. Aluminium fence removal @ Class 100
Rinse: Use the special container filled with demi-water, to which Triton X-100 is added. Rinse for 1 minute.

Etchant: Use wetbench 'Aluminium-ets' (35 ± 1 °C); use the carrier with the yellow dot. 1 liter buffered etch fluid (Merck selectipur) contains: 770 ml concentrated phosphorus acid (H_3PO_4 , 85%), 14 ml concentrated nitric acid (HNO_3 , 65%), 140 ml concentrated acetic acid (CH_3COOH , 100%) and 76 ml deionized water

Etch time: 30 seconds.

QDR: Rinse in the Quick Dump Rinser with the standard program until the resistivity is 5 M Ω .

Drying: Use the Semitool "Rinser/dryer" with the standard program. Always use the special orange carrier with the black dot.

11. Cleaning procedure HNO_3 100% metal @ Class 100

Cleaning: 10 minutes in fuming nitric acid (Merck: HNO_3 100% selectipur) at ambient temperature. Use wet bench 'HNO₃ (100%) metal' and the carrier with the yellow and red dots.

QDR: Rinse in the Quick Dump Rinser with the standard program until the resistivity is 5 M Ω .

Drying: Use the Semitool "Rinser/dryer" with the standard program, and the white carrier with a black dot.

NOTE: No 65% HNO₃ cleaning step!

12. PECVD TEOS oxide deposition @ Class 100

Use the Novellus PECVD reactor to deposit a TEOS based silicon oxide with various thickness. Follow the operating instructions from the manual when using this machine. Use xxxnmTEOS Temp. 350 °C, change time (check log) to deposit oxide with required thickness.

13. Measure oxide thickness @ Class 100

Use the Leitz MPV-SP measurement system to measure the TEOS thickness. Program: TEOS, auto5pts

14. Coating and baking @ Class 100

Use the EVG 120 coater/developer to treat the wafers with HMDS, program only HMDS. Use the manual spin coater in red room to deposit AZ5214E image reverse resist. Program: N (thickness ~ 2.7 μm). Bake at 95 °C on hot plate spray coater.

15. Alignment and exposure @ Class 100

Processing will be performed on the EVG 420 contact aligner. Follow the operating instructions from the manual when using this machine. Use test wafer coated with Al to determine optimal exposure time, start with 0.9 s. Use catalyst mask.

16. Post exposure bake @ Class 100

Bake at 115 °C for 1 minute in red room.

17. Flood exposure @ Class 100

Perform a flood exposure for 10 s. with UV light in red room to make unexposed area soluble.

18. Development @ Class 100

Develop using the EVG-120 wafer track using Shipley MF322 developer. Follow the instructions specified for this equipment, and always check the temperature of the hotplates first. Recipe: Dev- Single Puddle No PEB No HB.

19. Windows etching in oxide @ Class 100

Use Drytek 384T plasma etcher with program Plasmax to etch the oxide and stop

at the aluminium, set t1 and t2 to correct values for the oxide thickness. Use test wafer to check. Follow the instructions when using this machine.

20. Remove photoresist @ Class 100
Use the Tepla plasma system to remove the photo resist in oxygen plasma. Follow the instructions specified for the Tepla stripper, and use the quartz carrier. Use program 1:1000W
21. Cleaning procedure HNO₃ 100% metal @ Class 100
Cleaning: 10 minutes in fuming nitric acid (Merck: HNO₃ 100% selectipur) at ambient temperature. Use wet bench 'HNO₃ (100%) metal' and the carrier with the yellow and red dots.

QDR: Rinse in the Quick Dump Rinser with the standard program until the resistivity is 5 MΩ.

Drying: Use the Semitool "Rinser/dryer" with the standard program, and the white carrier with a black dot.

NOTE: No 65% HNO₃ cleaning step!
22. Ti and Ni deposition @ Class 100
Perform RF in HSE before Ti deposition. Use the TRIKON SIGMA sputter coater for the deposition of the Ti layer on the wafers Deposition must be done at 200°C with variable thickness (10nm). Follow the operating instructions from the manual when using this machine. Use the TRIKON SIGMA sputter coater for the deposition of the Ni layer on the test wafers. Deposition must be done at 200°C with an Ar flow of 100 sccm. (various thickness: 3, 6 and 10nm). Follow the operating instructions from the manual when using this machine. Perform subsequent steps without breaking vacuum to prevent oxidation!
23. Coating and baking @ MEMS lab
Processing will be performed on the manual spinner with manual edge bead removal. Use resist AZ4562, with coating at 2000 rpm resulting in a thickness of 1 μm.
24. Ni wet etching from backside and edge of wafer @ MEMS lab
Use HNO₃(65%):CH₃COOH (100%):H₂SO₄(98%):H₂O=5:5:2:28 at room temperature for 10 s to remove 3 nm of Ni from the backside and edge of the wafer. Rinse thoroughly.
25. Silicon dioxide wet etching @ MEMS lab
Use BHF(1:7) at room temperature to remove the 1000 nm layer of silicon dioxide on the backside of the wafer. Etch until the backside is hydrophobic, plus an additional 30 s. Rinse thoroughly.
26. Photoresist removal @ MEMS lab
Dissolve the photoresist in acetone. Manually rinse for a couple of minutes and then dry the wafers using the single wafer dryer.
27. Cleaning @ SA lab
Use EKC505 at 85 °C for 10 minutes to clean the wafers. Rinse in the water bath till the water resistance becomes 5 MΩ. Dry the wafers with the single wafer dryer.
28. Coating and baking @ Class 100
Use the EVG-120 automatic wafertrack to coat the wafers with 1.4 μm resist. The process includes a treatment with HMDS (hexamethyldisilazane) vapour with nitrogen as a carrier gas, spin coating for 30 s with Shipley SPR 3012 and pre baking

- for 1 minute at 95 °C. Use recipe: Co - SPR3012 - 1400nm (resist thickness: 1.400 µm at 48% RV).
29. Alignment and exposure @ Class 100
Use the EVG 420 contact aligner using soft contact and the default exposure time for Al underlayer for 1.4 µm resist (see manual). Use catalyst mask.
 30. Development @ Class 100
After exposure a post-exposure bake at 115 °C for 1 minute is performed on the EVG-120 wafer track, followed by a development step using Shipley MF322 developer (single puddle process), and a post bake at 100 °C for 1 minute. Use recipe: Dev - Single Puddle
 31. Inspection: linewidth and overlay
Visually inspect the wafers through a microscope, and check linewidth and overlay.
 32. Wet etching of Ni and Ti @ MEMS lab
Use Ni wet etching (BHF:HNO₃(%65):H₂O=1:1:50) in room temperature, to remove Ni and Ti. Use t=10 seconds for 3nm Ni. Make sure to use fresh solution in your own small container with single wafer holder. Rinse Manually for a few minutes.
 33. Photoresist removal @ MEMS lab
Dissolve the photoresist in acetone. Manually rinse for a couple of minutes and then dry the wafers using the single wafer dryer.
 34. Cleaning @ SA lab
Use EKC505 at 85 °C for 10 minutes to clean the wafers. Rinse in the water bath till the water resistance becomes 5 MΩ. Dry the wafers with the single wafer dryer.
 35. CNT growth at external facility
 36. Oxide deposition @ MEMS lab
Deposit a layer of oxide to fill the via holes. Use the STS PECVD with recipe SIO_STD4 (change deposition time).
 37. Optional: Chemical mechanical polishing
Use the MECAPOL E460 to remove part of the oxide to open up the CNT tips.
 38. Optional: Oxygen plasma etching of CNT tips @ MEMS lab
Use the EuroPlasma to perform etching on the CNTs to open the tips.
 39. Al deposition @ Solar Cell lab
Deposit 10 nm of Ti followed by 1.4 µm Al using LH 560 e-beam evaporator
 40. Coating and baking @ MEMS lab
Pretreat the wafers with HMDS with N₂ as carrier gas for 10 minutes. Deposit 2 µm of SPR3017 resist using the manual coater, bake for 1 min at 95 °C.
 41. Alignment and exposure @ MEMS lab
Use the Karl Süss in soft contact mode to expose the wafers. Use metal2 mask.
 42. Development @ MEMS lab
Do a post exposure bake for 1 min at 120 °C. Manually develop the wafers using Shipley MF332 developer for 20 s. and check if structures are ok. When required develop more to remove residual resist. End with a 1 min postbake at 120 °C.
 43. Al dry etching @ MEMS lab
Use the Alcatel GIR300 to dry etch the Al using the standard recipe. First do a 15 min etch followed by a 10 minutes. If needed perform more (smaller) etching steps. After etching perform passivation.

44. Photoresist removal @ MEMS lab
Use the Europlasma to strip the photoresist.
45. Optional: thermal annealing @ MEMS lab Use the Carbolite ceramic oven to perform a 30 minutes anneal at 400 °C.
46. Clean the wafers Rinse thoroughly in water and dry with single wafer dryer.
47. Coating and baking @ MEMS lab
Pretreat the wafers with HMDS with N₂ as carrier gas for 10 minutes. Deposit 2 μm of SPR3017 resist using the manual coater, bake for 1 min at 95 °C.
48. Alignment and exposure @ MEMS lab
Use the Karl Süss in soft contact mode to expose the wafers. Use contact hole mask.
49. Development @ MEMS lab
Do a post exposure bake for 1 min at 120 °C. Manually develop the wafers using Shipley MF332 developer for 20 s. and check if structures are ok. When required develop more to remove residual resist. End with a 1 min postbake at 120 °C.
50. Dry oxide etching @ MEMS lab
Use the Alcatel GIR300 to dry etch the SiO₂ and stop at metal 1 using standard etching recipe.
51. Photoresist removal @ MEMS lab
Use the Europlasma to strip the photoresist. Clean the wafers in water and dry using single wafer dryer.

B.4 Lift-off

1. Coating and baking @ Class 100
Add one or two test wafers and make sure they are the first to be coated as resist might be dirty for the first wafer. Use the EVG-120 automatic wafertrack to coat the wafers with 3.0 μm resist. The process includes a treatment with HMDS (hexamethyldisilazane) vapour with nitrogen as a carrier gas, spin coating for 30 s with AZnLOF 2070 negative resist and pre baking for 1 minute at 95 °C. Use recipe: Co - AZNLOF2070 - 3000nm (resist thickness: 3.0 μm at 48% RV).
2. Alignment and exposure @ Class 100
Use the EVG 420 contact aligner using soft contact and an exposure time of 3.8 sec. Use catalyst mask.
3. Development @ Class 100
After exposure a post-exposure bake at 115 °C for 1 minute is performed on the EVG-120 wafer track, followed by a development step using Shipley MF322 developer (double puddle process), and a post bake at 100 °C for 1 minute. Use recipe: Dev - Double Puddle 2
4. Inspection: linewidth and overlay
Visually inspect the wafers through a microscope, and check linewidth and overlay and if the resist is removed from the unexposed area.
5. Ti and Ni deposition @ Class 100/10000
Perform subsequent Ti and Ni deposition using the class 100 or class 10000 e-beam evaporator.
6. Resist removal @ SA lab
Fill a single wafer beaker with acetone, but one or two wafers in each beaker

and let stand overnight. Slightly shake the wafers after half an hour and before taking them out to remove the resist. Rinse and dry using N_2 . Do not use single wafer dryer if no backside contamination step has been performed after the e-beam evaporation!

7. Inspection @ SA lab

Use the microscope to check if all photo resist is removed and the wanted pattern is still on the wafer. Put a tissue on the microscope stage to prevent contamination!

Appendix C

Experimental methods & Raman spectra

C.1 SEM and TEM

Scanning electron microscopy (SEM) and transmission electron microscopy (TEM) are both characterisation techniques using a high power electron beam to view samples on the micro- and nanometre scale. Although they both use electron beam, the working principle and sample requirements are quite different.

In case of SEM the surface of a sample (which can be a full scale wafer) is scanned with an electron beam typically with an energy ranging from several keV to 30 keV. As the electrons interact with the sample they generate secondary electrons (electrons generated as ionization products) which are detected and used to form an image of the surface topography. No sample preparation is typically needed when imaging semiconductor industry samples. However, non conductive parts will be charged due to the electron beam and thus become brighter after prolonged exposure.

SEM is an ideal method to quickly investigate growth results of CNTs, although due to the sometimes limited resolution it might be difficult to obtain an accurate diameter estimation or quality assessment. For our experiments the samples were tilted 45° to get a better view of the growth and estimate length. Generally a high acceleration voltage (15-25 keV) was used to improve resolution. For imaging the Novellus samples the Philips FEI XL50 in the class 100 was used, while for the BlackMagic II the Philips FEI XL30, which used to be in the class 10000, was employed due to contamination regulations. The NanoLab samples were imaged using a high resolution JEOL JSM-7001F in the Boston College University nanofabrication cleanroom.

In case of TEM a beam of electrons is transmitted through a very thin sample, just like a typical optical microscope but with much larger magnification. The microscope was used in bright field mode, in which the image is formed due to occlusion and absorption of electrons by the sample. As electrons have to pass through the sample it should be thinned to just a few nm. This requires a lot of sample processing. For imaging CNTs a TEM grid can be used to scrape of some tubes, which makes sample preparation relative fast.

As the resolution of TEM is much higher the individual walls of CNTs can be observed and it is possible to accurately determine diameter and quality. The images in this report were obtained using a FEI Tecnai G² of the Applied Physics Kavli Institute of Nanoscience.

This microscope was also used to perform EDX (Energy-dispersive X-ray spectroscopy). This technique can be used for analysing which elements are present in the sample by investigating the x-rays emitted when the sample is bombarded by electrons from the TEM beam.

C.2 EDX spectrum of lift-off Ni sample

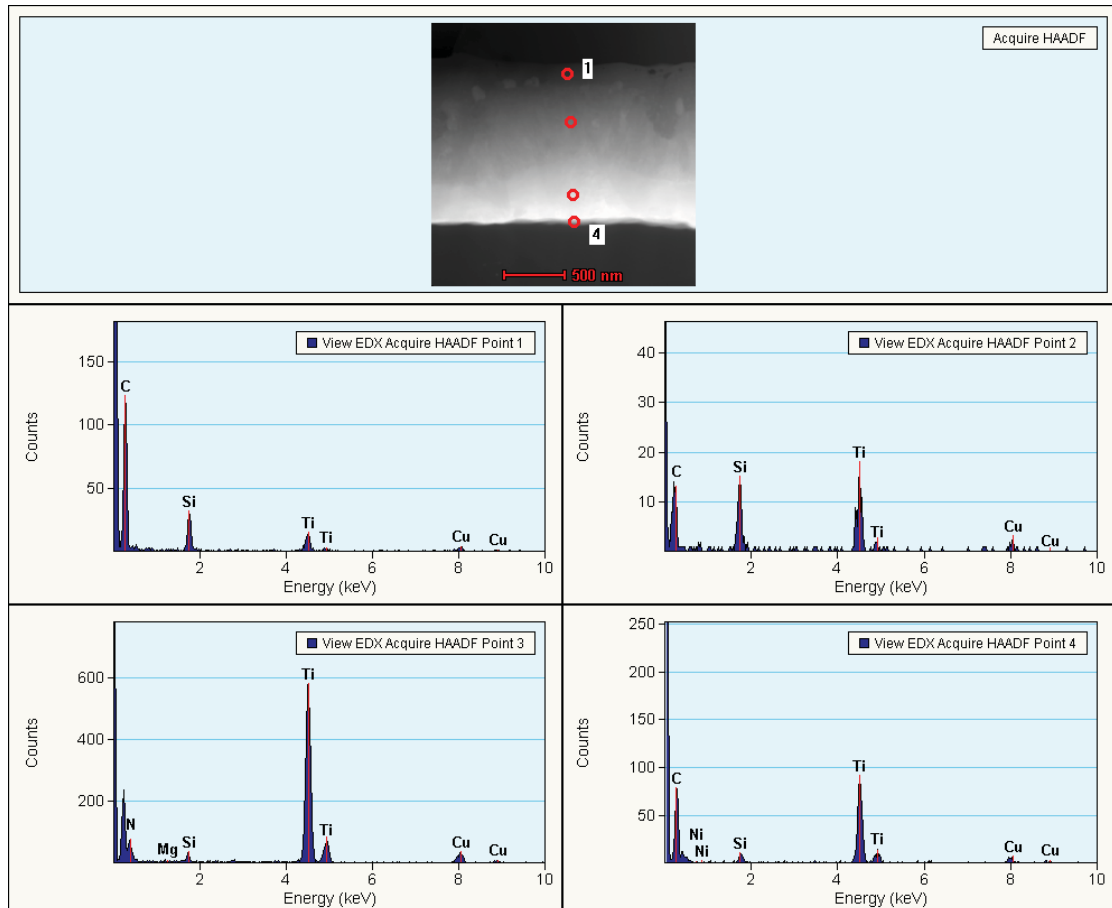


Figure C.1: EDX spectrum obtained at different points in the Ni cross-section

C.3 Introduction to Raman spectroscopy on CNTs

Raman spectroscopy is a method to study low frequency (i.e. vibrational) modes of a system. The mechanism behind it is the inelastic, or Raman, scattering of photons from a monochromatic light source (usually a laser in or around the visible range). The photons interact with the phonons of the system resulting in the photon energy being shifted up or down. This shift supplies information on the phonon modes of the system.

As the Raman scattering is generally weak compared to the elastic Rayleigh scattering, this component has to be filtered from the return signal in order to observe the Raman spectrum. The advantage of Raman spectroscopy is that it is a fast and non-destructive method to investigate all kinds of samples without preparation.

Micro Raman spectroscopy was performed using a Renishaw inVia Raman microscope with an 514 nm Argon laser. From all samples the baseline (when present) was subtracted, unwanted (cosmic rays or large Si peaks) were removed or reduced and finally the spectrum was smoothed using the WiRE 2.0 SP9 software available on the Raman microscope. The parameters of the spectrum were extracted by a small self-written Matlab script, which can be found in appendix D.3. It was found that extracting the peak widths using Lorentzian curve fitting with the WiRE software was more accurate than with the Matlab FWHM() function. Thus the values found in this report are obtained using Lorentzian curve fitting [189].

As the laser intensity differs from sample to sample peak intensities cannot be compared directly (hence the arbitrary units for the y-axis). However, it is possible to compare ratio's of peaks determined from a spectrum and their widths between different samples.

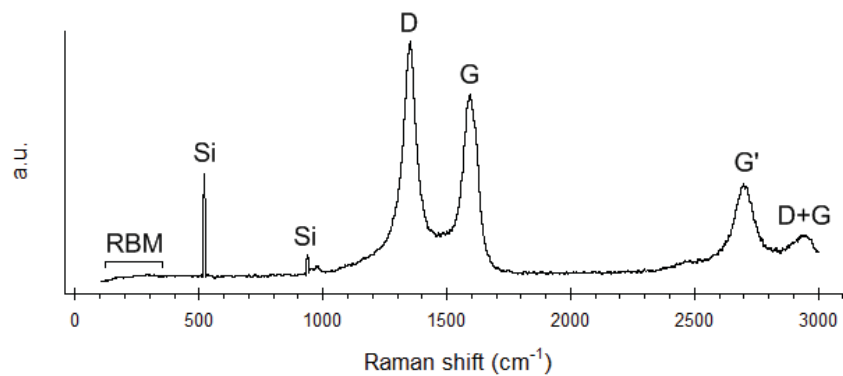


Figure C.2: Peak assignment in Raman spectra of carbon nanotubes (MWNT sample)

In the Raman spectrum made from a CNT (bundle) multiple peaks can be observed, as displayed in figure C.2. Beside the CNT/graphite related peaks often a Si related peak around 500 and 1000 cm^{-1} can be observed, especially for low density samples. For the samples where this peak had a magnitude much larger than either the D or G peak the magnitude has been reduced, as this peak is not of much interest to us.

In the range of 120-350 cm^{-1} the so-called Radial Breathing Mode (RBM) can be found when SWNT samples are excited. These first order modes are unique to CNTs and are caused by the vibration of the carbon atoms in the radial direction (often described as if the tube was breathing, hence the name). The frequency at which the RBM occur is diameter dependent by $\omega_{rbm} = A/d + B$ (A typical being 248 cm^{-1}nm and $B = 10 \text{ cm}^{-1}$) [189]. Beside for determining the diameter the RBM can be used to extract the (n, m) parameters of the tube from a clear spectrum [194]. For tubes above 2 nm the RBM becomes very weak, which is the reason they're not observed in MWNT samples.

The next band is the so-called D-peak (or D-band) around 1350 cm^{-1} , which is also present in graphite-like materials. It is a second order phonon mode band related to disorder in the system [170,195]. All kinds of disorder has been related with the D band, such as defects, end caps, bending and a-C [196]. The position of the D band depends on the diameter and chirality of the CNT and the laser energy [170,189].

Around 1600 cm^{-1} the G-peak is found. Again this peak is not unique to CNTs and appears in all graphite materials. It is associated with the graphite in-plane unit cell and is a first order mode (the only for graphite) [189]. For small diameter CNT the G-band can split into two separate peaks (G^- and G^+). The G^- lineshape tells

something about the electric type (a Lorentzian shape can be found for semiconducting tubes). The positions of the two separated tubes depends on the diameter [195]. For large diameter tubes only a single G-peak can be observed. The G-peak is not sensitive to laser energy [189].

The following peak is the G' or 2D peak, which is the overtone of the D-peak and can be found around the double of its frequency (2700 cm^{-1}). While the D band can be almost absent in high quality samples the G' band doesn't need defects to exist [170,189]. For an individual SWNT the place and shape of the G' band can be used to check if the estimated (n, m) parameters are correct [194]. The frequency of the band depends again on the laser energy.

The last peak is the combination of the D and G peak [170]. To the authors knowledge not much research has been done on the properties of this band (Raman spectroscopy on CNT is still a rather new field, especially for the case of MWNT [189]). Therefore we will only name it.

As our samples consist of MWNT bundles we're mainly interested to use Raman spectroscopy to investigate the graphite quality of the samples. The ratio between the density of the D and G peak (I_D/I_G) has been used to tell something about the sample graphite quality for quite some time [170,189,196]. Besides the ratio also the peak widths (full width at half maximum, FWHM to be precise) have been used. A very broad FWHM of the D-peak has been associated with a-C [195] and an increase in defect size [170]. Generally, the appearance of clear and sharp higher order peaks has been associated with high crystallinity [164,190].

Antunes et al. investigated the properties of the intensity ratios and the FWHM of the D, G and G' peaks against diameter. They found that an increasing I_D/I_G with constant FWHM(D) indicates an increase of the number of defects with the same spreading in domain size. The opposite, however, indicates an increase of defects with a further spreading of the domain size. They state that the product of I_D/I_G and FWHM(D) is a better parameter to investigate the defect density. They also found the the FWHM(G') shows about the same sensitivity to the defect density as the before mentioned product. Finally they state that the width of the G and G' bands and their ratio $I_{G'}/I_G$ are also sensitive to the defect density, but to what extend is not mentioned.

More information about the relation between quality and second order peaks can be found in the work of Lee [197] on graphite. For graphite both the G' and D+G peak intensity increase when the quality increases, while the width decreases. There results were verified with XRD (X-ray Diffraction), the second order peaks were found to be more accurate than the first order peaks when the data was compared with XRD.

In case of MWNT Musso et al. [188] found an decrease in I_D/I_G' ratio when annealing MWNT at a higher temperature. The I_D/I_G' appeared to be more sensitive to defects than the I_D/I_G ratio. In their results the $I_{G'}/I_G$ ratio showed only minor change over annealing temperature range. Again the results were compared with XRD.

C.4 Raman spectra of growth experiments

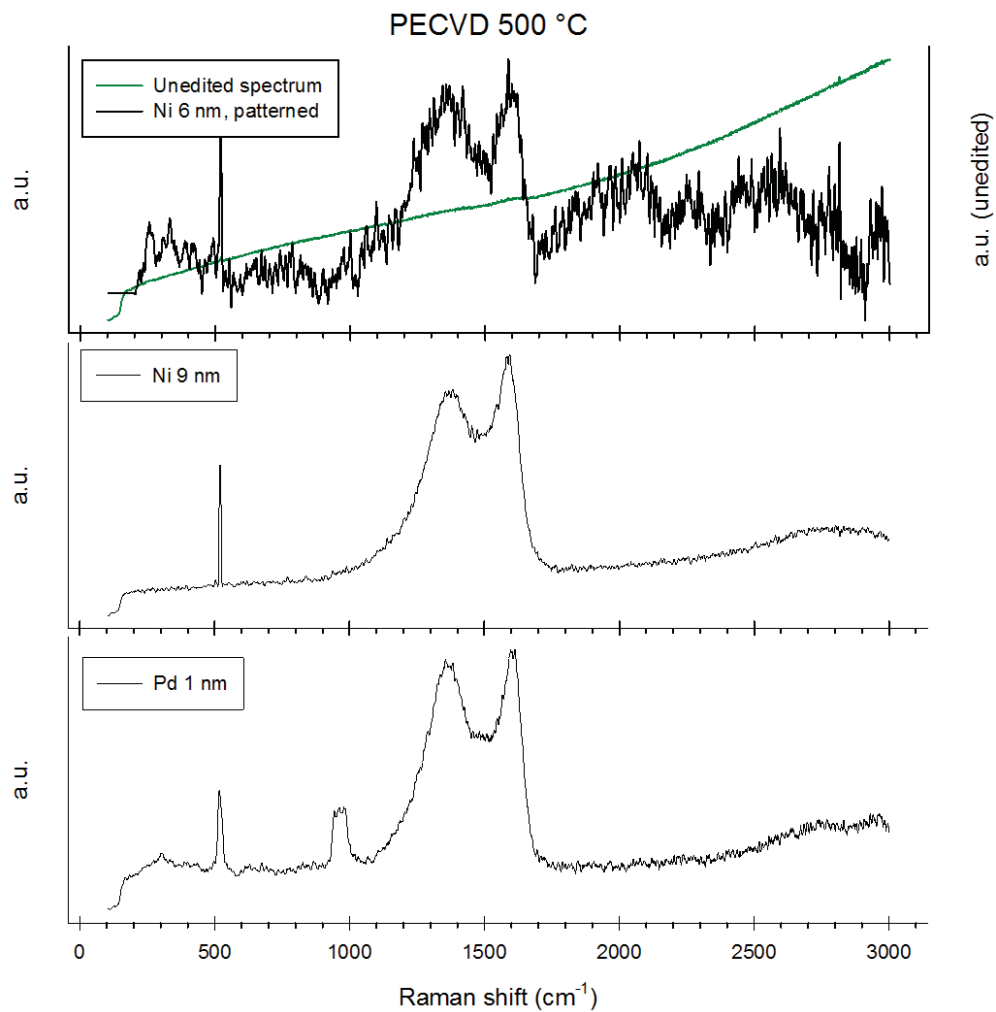
In this section all the Raman spectra taken from the samples can be found. The baseline has been subtracted when present, unwanted peaks have been removed or reduced and the final result has been smoothed. For samples with a strong baseline the original spectrum has been plotted in green on the right axis. Lorentzian curve fitting was performed with the WiRE software in order to determine the width of the peaks [189].

C.4.1 BlackMagic II

Table C.1: Extracted parameters from the Raman spectra of the AIXTRON samples. The 'p' stands for patterned

CVD type	Temp. (°C)	Sample	D freq. (cm^{-1})	G freq. (cm^{-1})	G' freq. (cm^{-1})	I_D/I_G	$I_{G'}/I_G$	$I_D/I_{G'}$	FWHM(D) (cm^{-1})	FWHM(G) (cm^{-1})	FWHM(G') (cm^{-1})	FWHM(D) · I_D/I_G (cm^{-1})
DC-PECVD	500	Ni 6 nm(p)	1356	1587		0.89			266	80		237
		Ni 9 nm	1385	1594		0.87			231	76		201
		Pd 1 nm	1357	1597		0.95			242	68		230
	450	Ni 9 nm	1371	1602		0.92			222	77		204
		Pd 1 nm										
APCVD	640	Co 1 nm	1352	1584	2707	1.01	0.78	1.29	57	60	87	58
		Fe 1 nm	1352	1594	2698	1.29	0.52	2.45	69	67	105	89
		Fe 5 nm	1351	1585	2704	0.79	0.75	1.05	62	56	87	49
		Fe 10 nm	1354	1585	2706	0.87	0.90	0.97	57	54	82	50
			Pd 1 nm	1347	1599		0.84		216	72		181
			Fe 1 nm	1349	1599	2695	1.16	0.30	3.85	95	70	146
	500	Fe 5 nm	1357	1591	2713	1.19	0.50	2.39	68	67	100	81
		Pd 1 nm	1351	1596		0.79			246	74		194
HF-PECVD	500	Pd 1 nm	1343	1594		0.78			239	75		186
		Ni 6 nm(p)	1380	1603		0.88			384	74		338
		Ni 9 nm	1366	1588		0.88			230	77		202
		Pd 1 nm	1354	1617		0.83		198	79		164	

C.4.1.1 DC-PECVD

**Figure C.3:** Raman spectra of 500 °C DC-PECVD

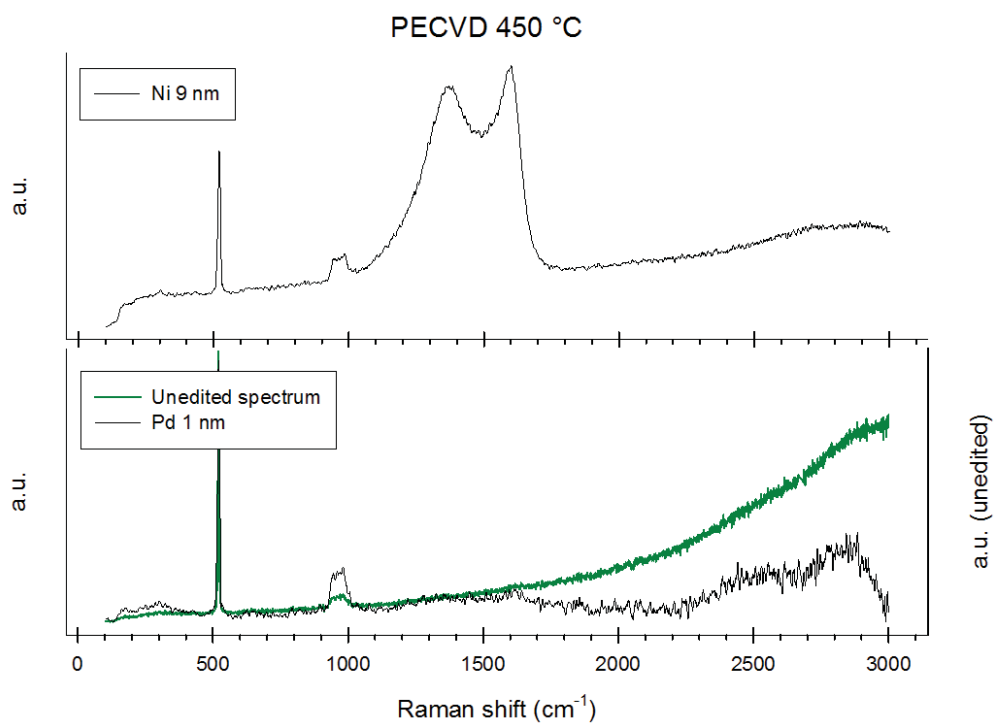


Figure C.4: Raman spectra of 450 °C DC-PECVD

C.4.1.2 APCVD

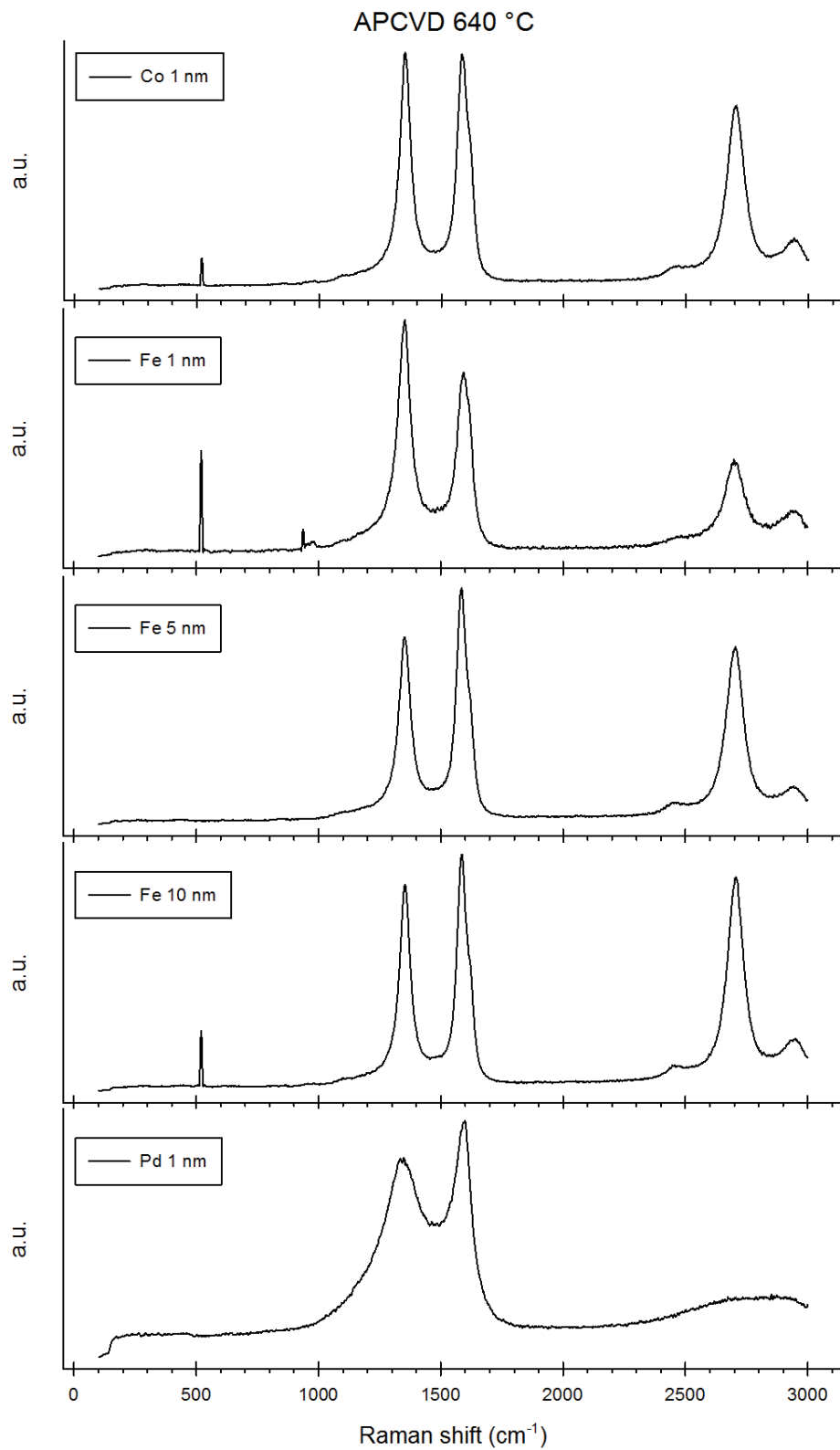
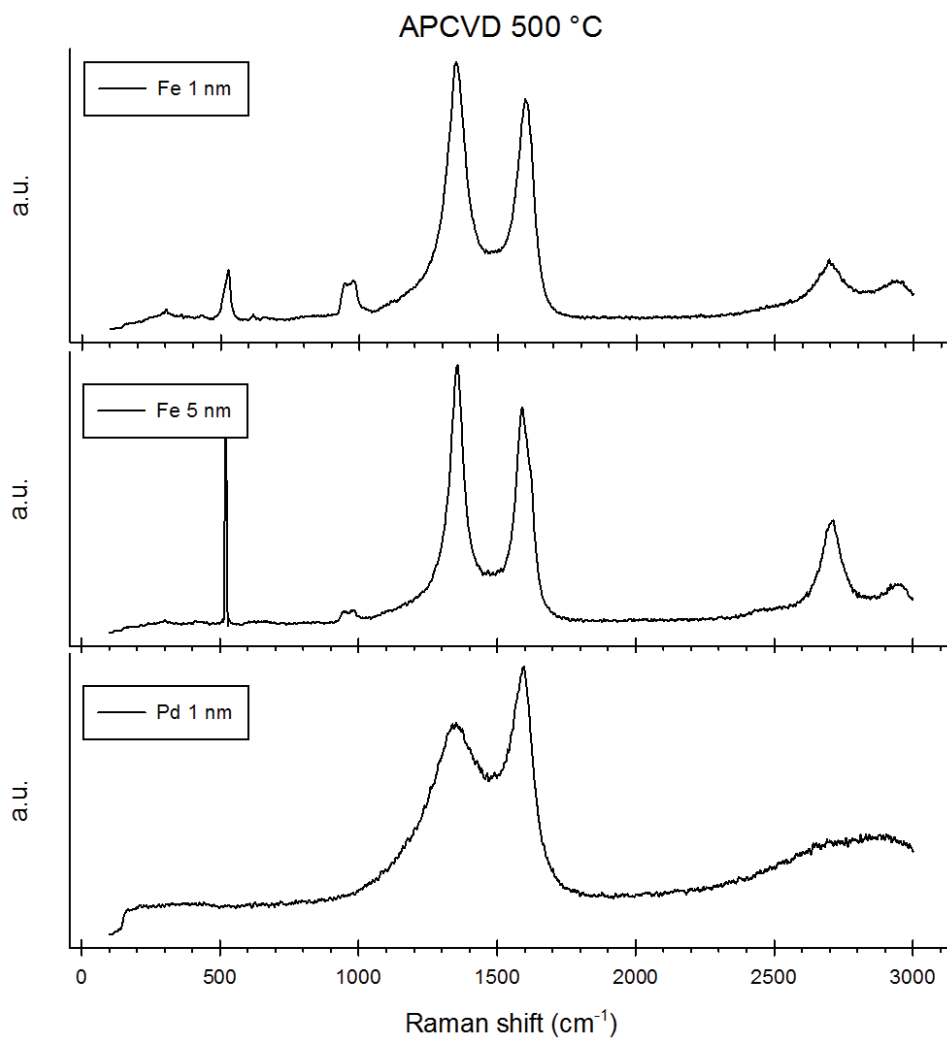
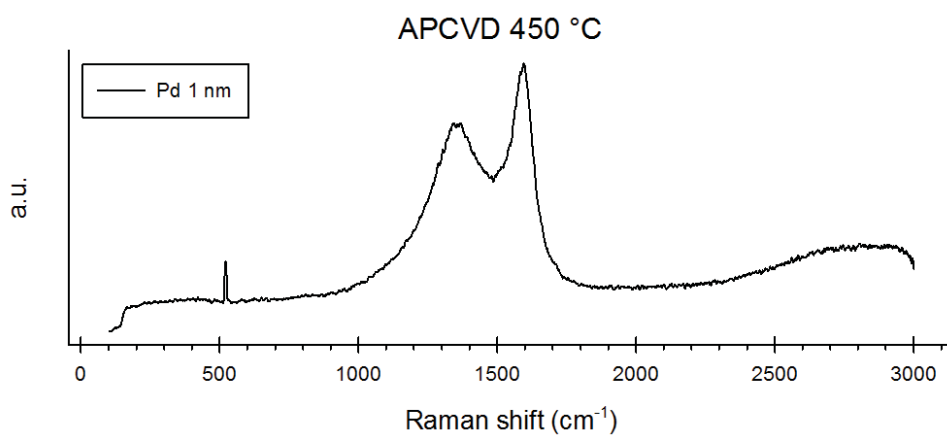
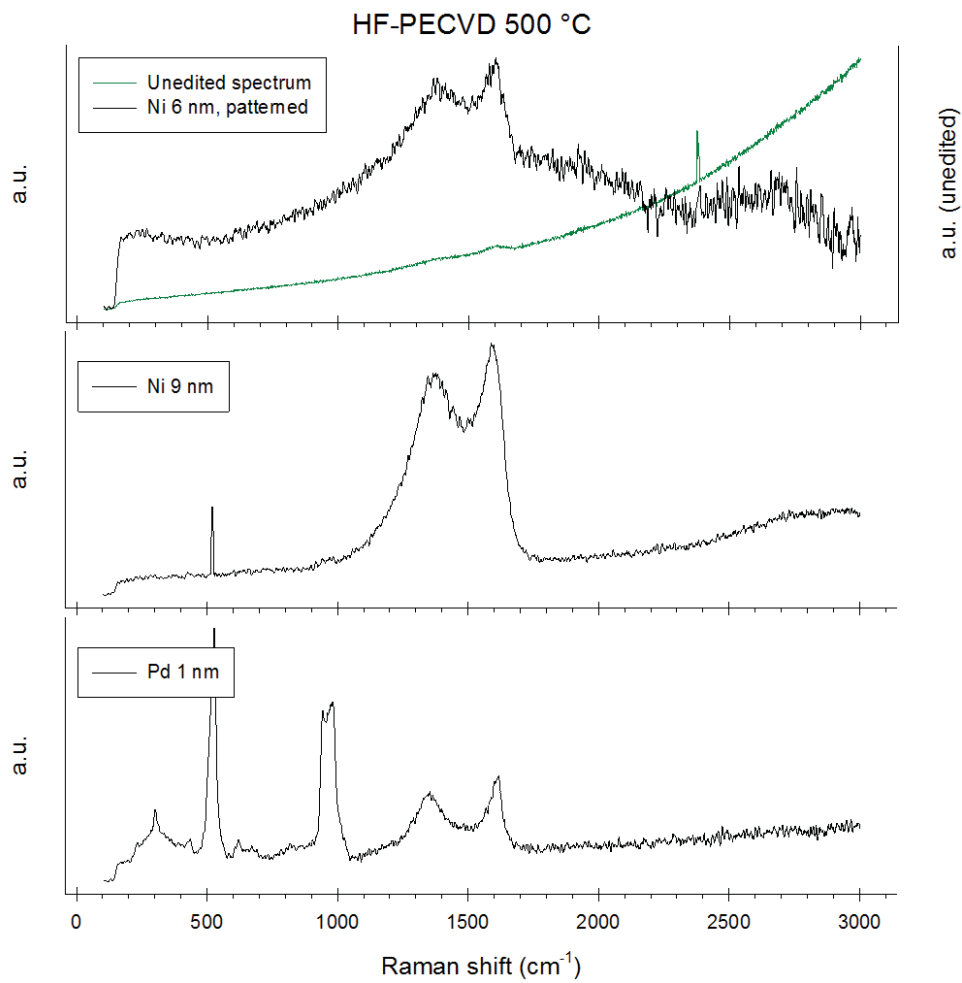


Figure C.5: Raman spectra of 640 °C APCVD

**Figure C.6:** Raman spectra of 500 °C APCVD**Figure C.7:** Raman spectra of 450 °C APCVD

C.4.1.3 HF-PECVD

**Figure C.8:** Raman spectra of 500 °C HF-PECVD

C.4.2 NanoLab

Table C.2: Extracted parameters from the Raman spectra of the NanoLab HF-PECVD samples. A 'p' stands for patterned

Run	Sample	D freq. (cm^{-1})	G freq. (cm^{-1})	G' freq. (cm^{-1})	I_D/I_G	$I_{G'}/I_G$	$I_D/I_{G'}$	FWHM(D) (cm^{-1})	FWHM(G) (cm^{-1})	FWHM(G') (cm^{-1})	FWHM(D) · I_D/I_G (cm^{-1})
1	Ni 6 nm	1365	1593		0.88			172	82		152
	Ni 6 nm (p)	1356	1581		0.98			155	77		152
	Ni 9 nm	1356	1591		0.92			162	80		149
2	Fe 6 nm	1351	1594	2690	0.95	0.22	4.26	106	88	289	101
	Fe 10 nm	1362	1591	2717	0.71	0.28	2.59	99	73	155	70
	Ni 6 nm	1365	1588		0.95			236	58		225
	Ni 6 nm (p)	1365	1585		0.91			193	87		175
	Ni 9 nm	1380	1591		0.71			105	84		74
3	Fe 6 nm	1359	1594	2713	1.01	0.27	3.73	126	77	239	128
	Fe 10 nm	1356	1582	2700	0.69	0.48	1.44	104	75	200	72
	Ni 6 nm	1359	1590		0.87			215	86		187
	Ni 9 nm	1372	1596		0.94			182	87		171
	Fe 6 nm	1374	1594		1.00			201	113		201
4	Fe 10 nm	1356	1591	2729	0.93	0.29	3.21	91	76	160	85
	Ni 6 nm	1377	1591		0.95			204	76		194
	Ni 6 nm (p)	1357	1578		1.02			215	59		219
	Ni 9 nm	1366	1593		0.83			224	75		186
	Fe 6 nm, 1	1356	1588		1.00			141	129		141
Lift-off	Fe 6 nm, 2	1352	1590	2713	1.05			129	82	143	136
	Fe 6 nm, 3	1357	1593	2694	0.90	0.74	1.21	177	72	229	159

Table C.3: Extracted parameters from the Raman spectra of the NanoLab CVD samples. A 'p' stands for patterned, 'lo' for lift-off and 'lf' indicates reduced flow rate

Temp. (°C)	Sample	D freq. (cm^{-1})	G freq. (cm^{-1})	G' freq. (cm^{-1})	I_D/I_G	$I_{G'}/I_G$	$I_D/I_{G'}$	FWHM(D) (cm^{-1})	FWHM(G) (cm^{-1})	FWHM(G') (cm^{-1})	FWHM(D) · I_D/I_G (cm^{-1})
600 (3'')	Fe 5 nm	1356	1593	2702	1.48	0.32	4.58	70	66	131	104
	Fe 6 nm	1349	1584	2700	1.60	0.44	3.65	64	65	131	102
	Ni 6 nm	1349	1590	2704	1.26	0.42	2.97	87	74	179	110
600 (2'')	Fe 1 nm	1354	1584	2708	1.31	0.68	1.93	49	57	84	64
	Fe 6 nm	1354	1588	2699	1.59	0.47	3.37	61	63	108	97
	Ni 6 nm	1352	1587	2711	1.24	0.52	2.40	63	57	112	78
	Ni 6 nm (p)	1356	1594	2710	1.14	0.40	2.89	93	72	145	106
	Pd 1 nm	1363	1600		0.82			272	82		223
600 (2'', lf)	Fe 6 nm	1351	1584	2703	1.47	0.51	2.91	59	61	103	87
	Ni 6 nm	1351	1588	2706	1.44	0.47	3.07	54	56	115	78
550 (2'')	Fe 6 nm	1348	1587	2686	1.33	0.31	4.33	88	74	189	117
	Ni 6 nm	1349	1588	2707	1.27	0.33	3.80	84	75	183	107
500 (2'')	Fe 6 nm	1354	1587	2706	1.32	0.50	2.65	71	67	114	94
	Ni 6 nm	1342	1593	2704	1.04	0.23	4.49	143	71	213	149
450 (2'')	Fe 6 nm	1348	1606		0.74			245	65		181
	Ni 6 nm	1349	1593	2678	0.96	0.17	5.64	193	84	222	185
600 (2'')	Fe 6 nm (lo)	1352	1584	2704	1.11	0.66	1.70	58	60	88	64
	Ni 6 nm (lo)	1363	1605		0.81			217	87		176
500 (2'')	Fe 6 nm (lo)	1354	1593	2702	1.10	0.59	1.85	85	73	138	94

C.4.2.1 HF-PECVD

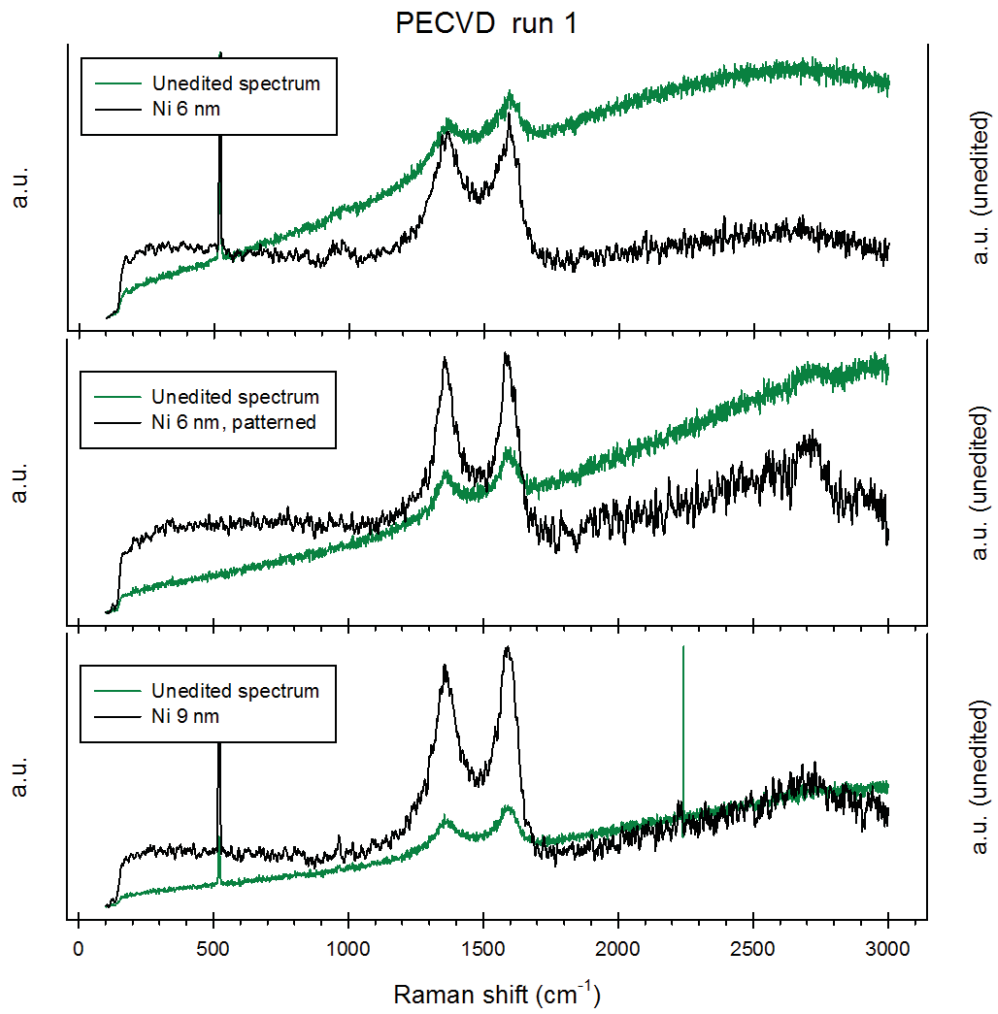


Figure C.9: Raman spectra of HF-PECVD run 1

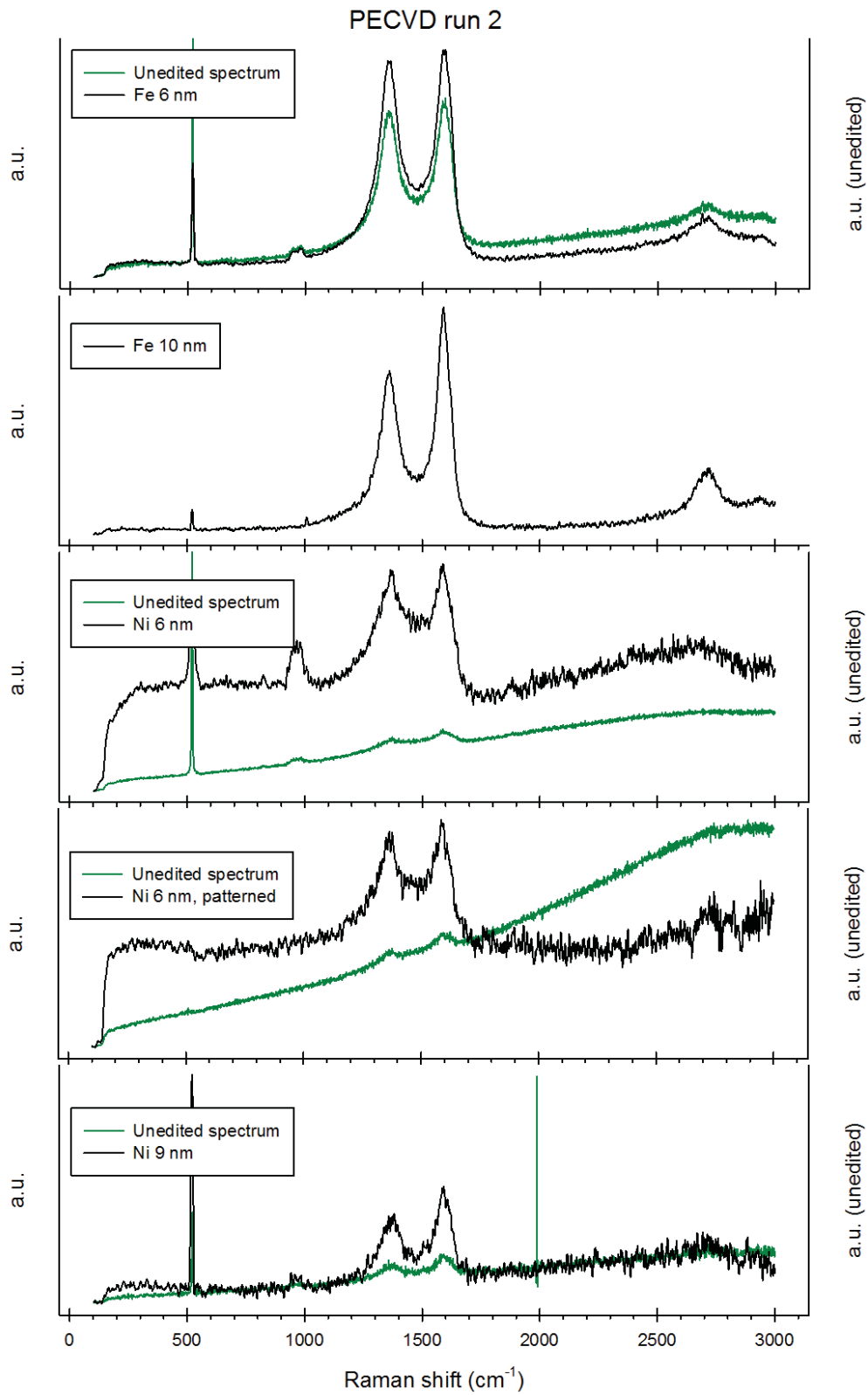


Figure C.10: Raman spectra of HF-PECVD run 2

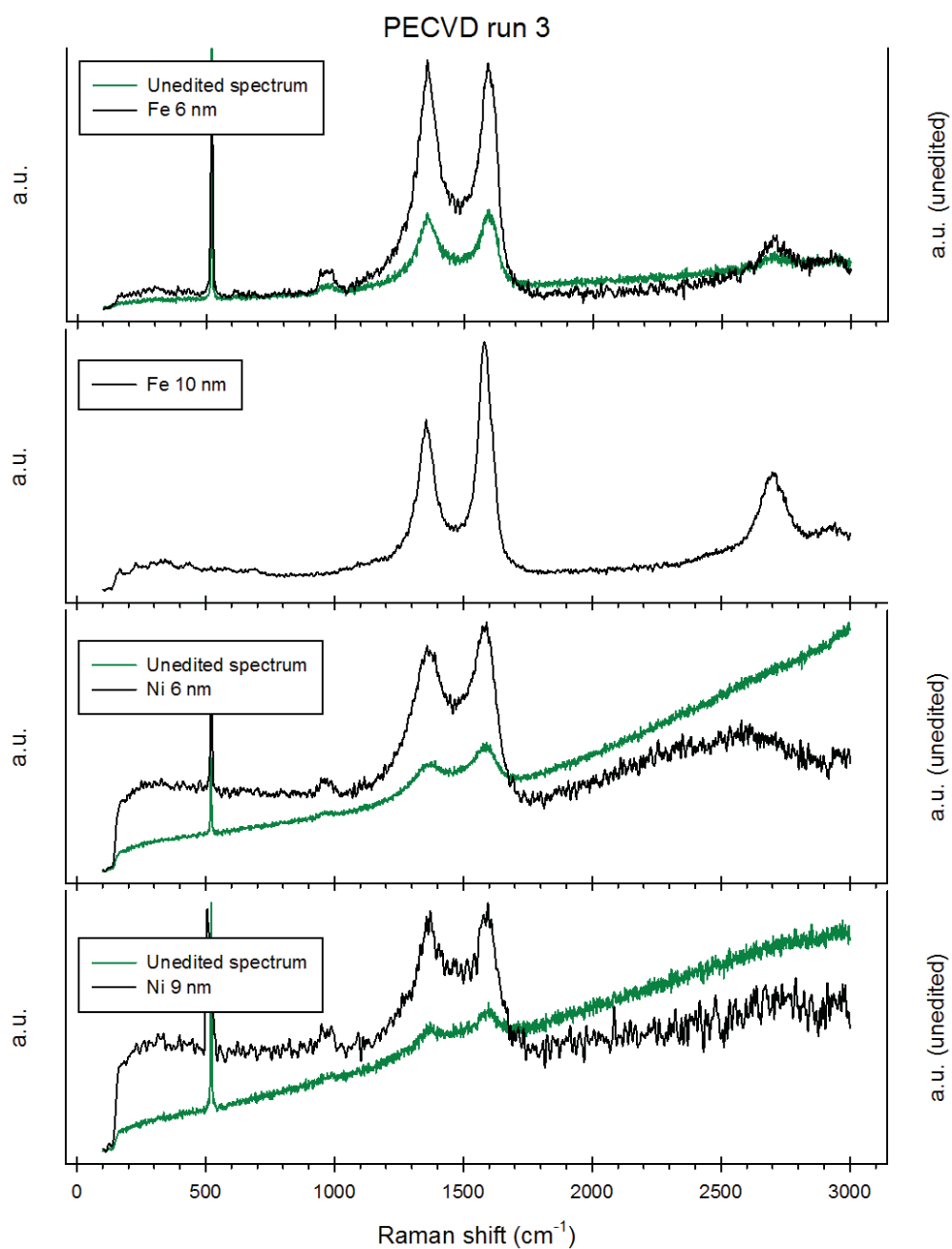


Figure C.11: Raman spectra of HF-PECVD run 3

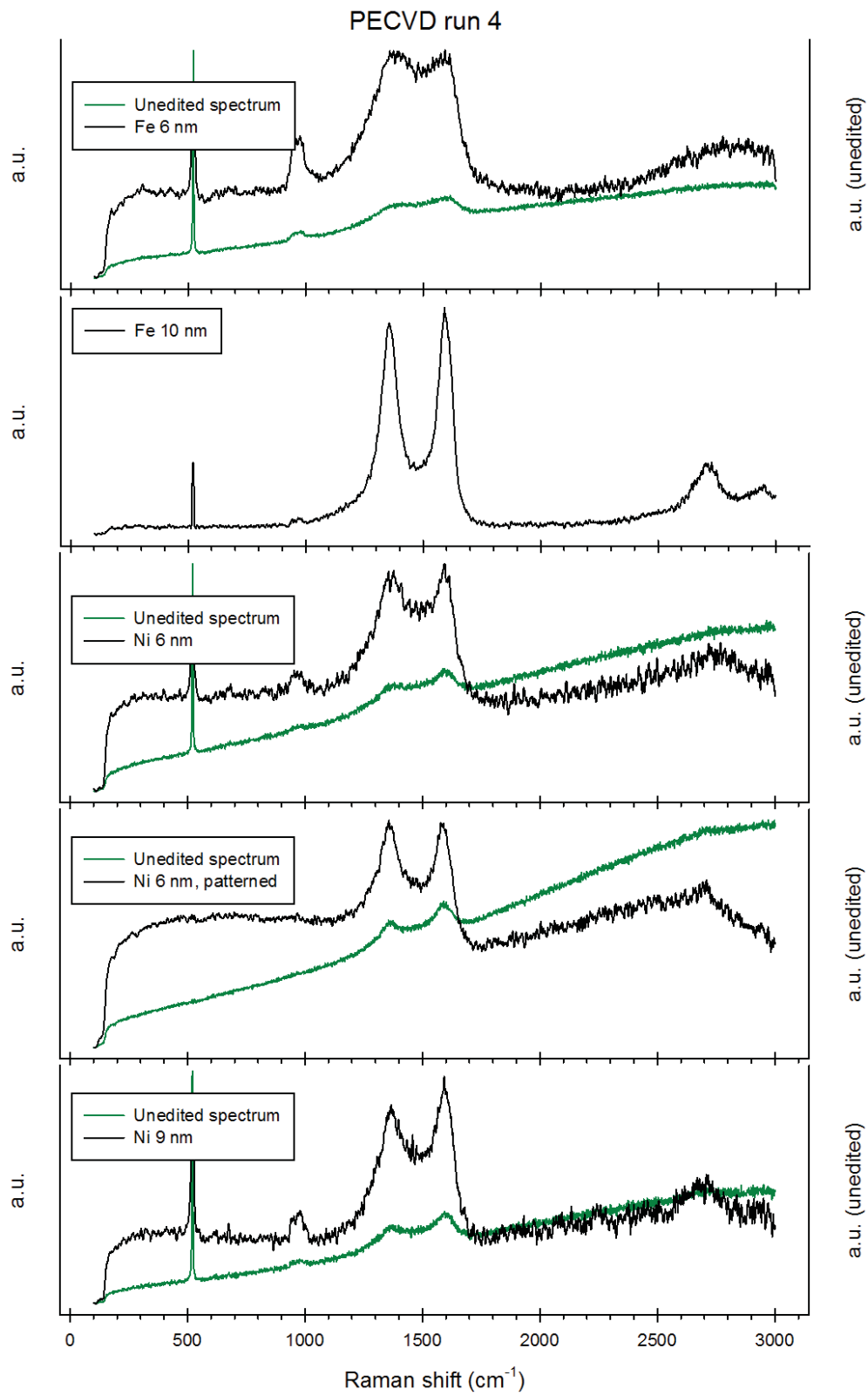


Figure C.12: Raman spectra of HF-PECVD run 4

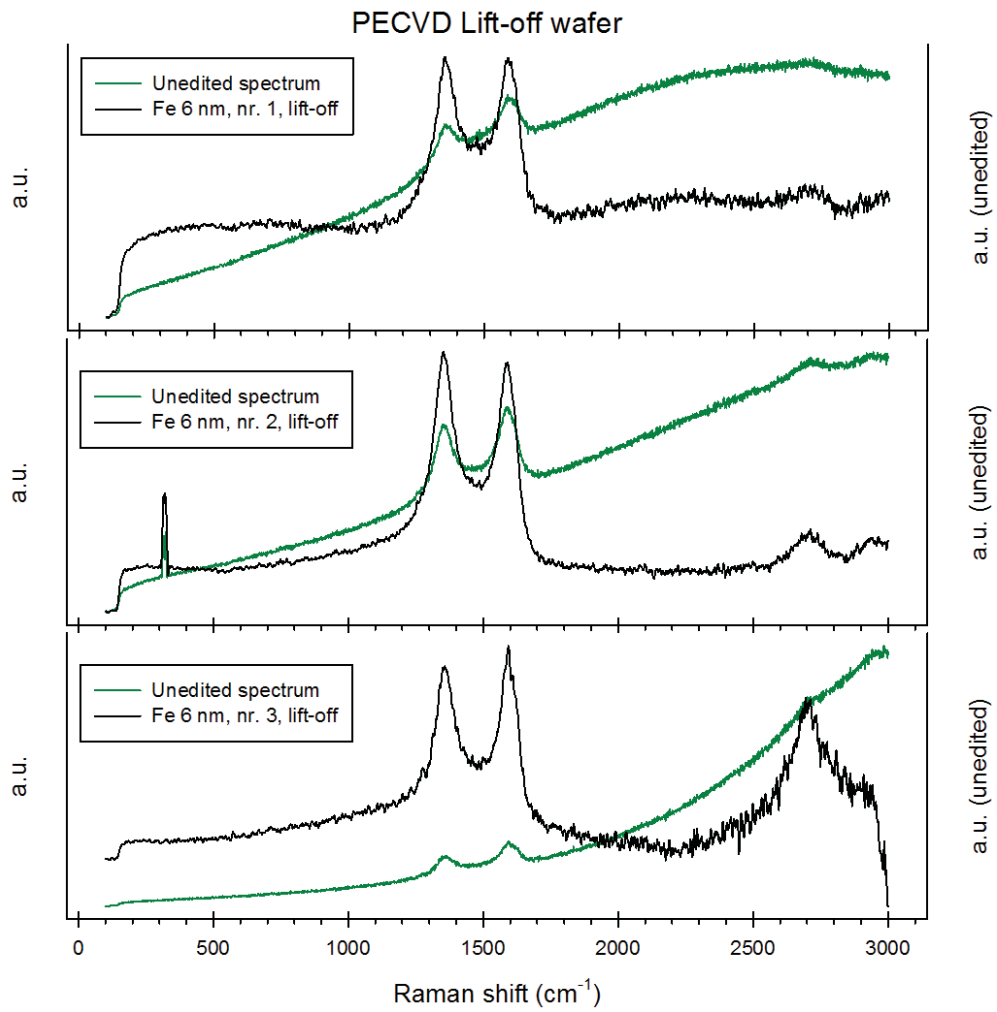


Figure C.13: Raman spectra of HF-PECVD differently cleaned Fe 6 nm lift-off

C.4.2.2 Thermal CVD

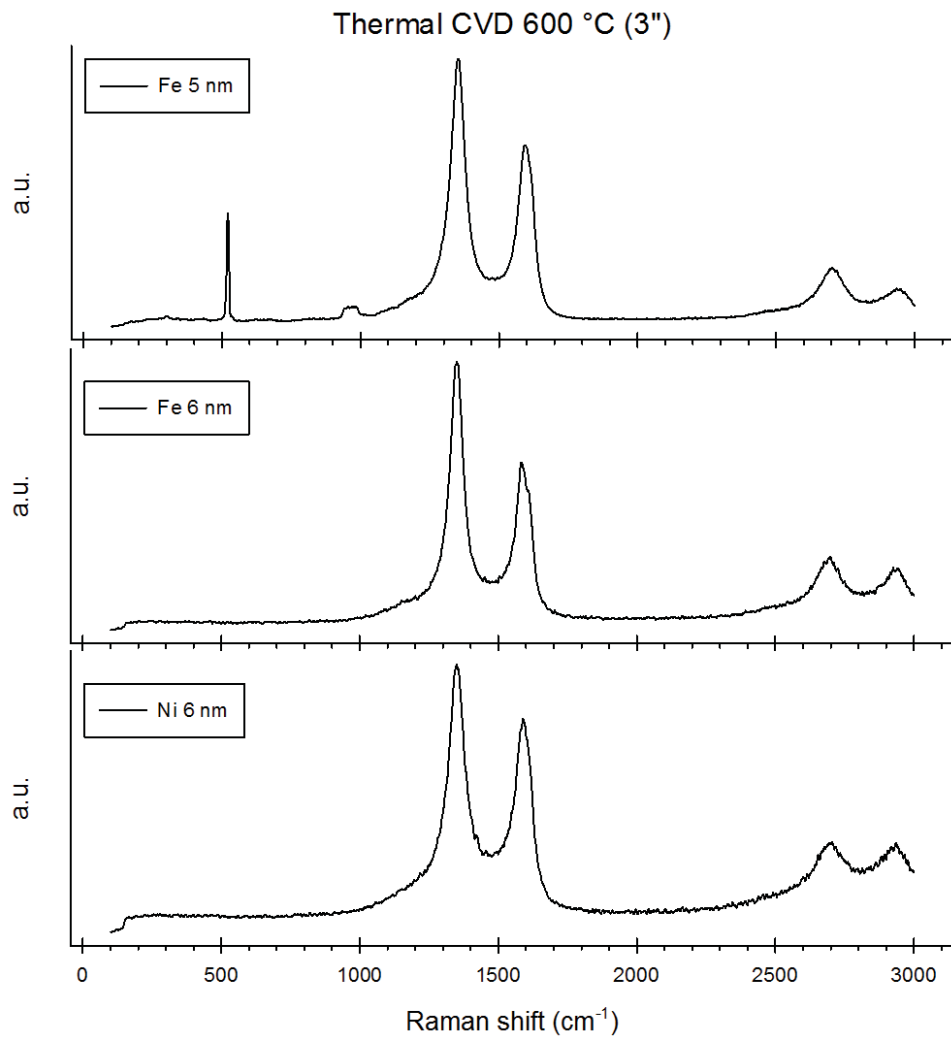


Figure C.14: Raman spectra of 3" furnace CVD at 600 °C

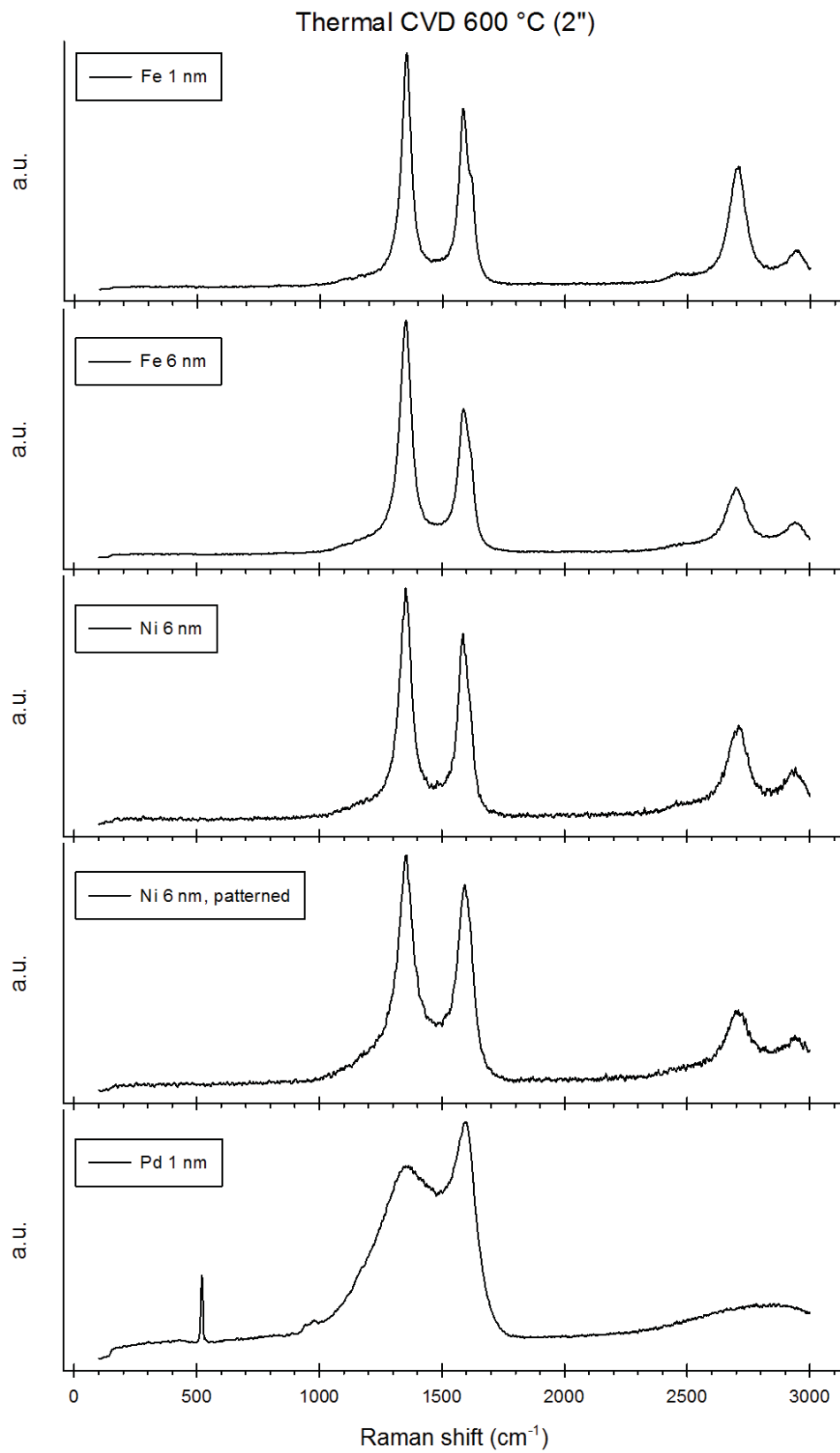


Figure C.15: Raman spectra of 2" furnace CVD at 600 °C

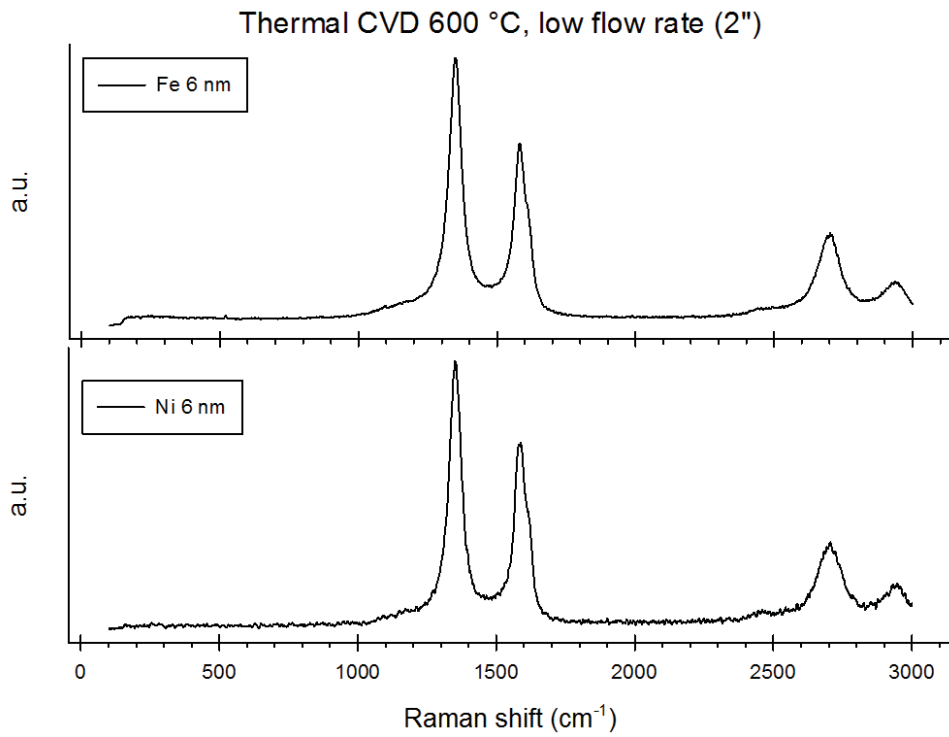


Figure C.16: Raman spectra of 2" furnace CVD at 600 °C with reduced flow-rate

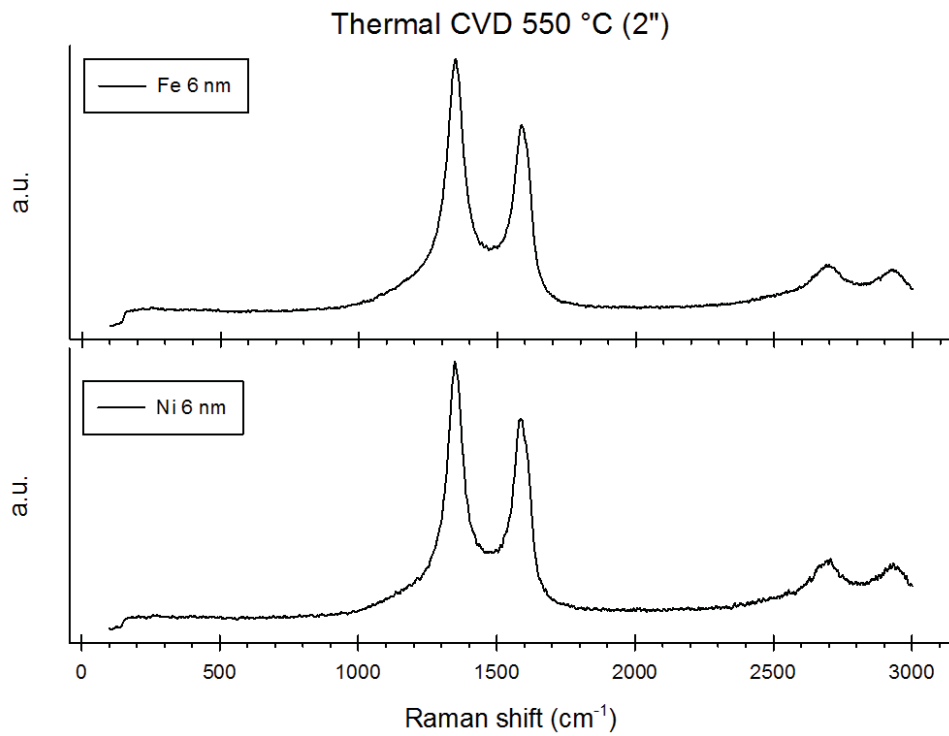


Figure C.17: Raman spectra of 2" furnace CVD at 550 °C

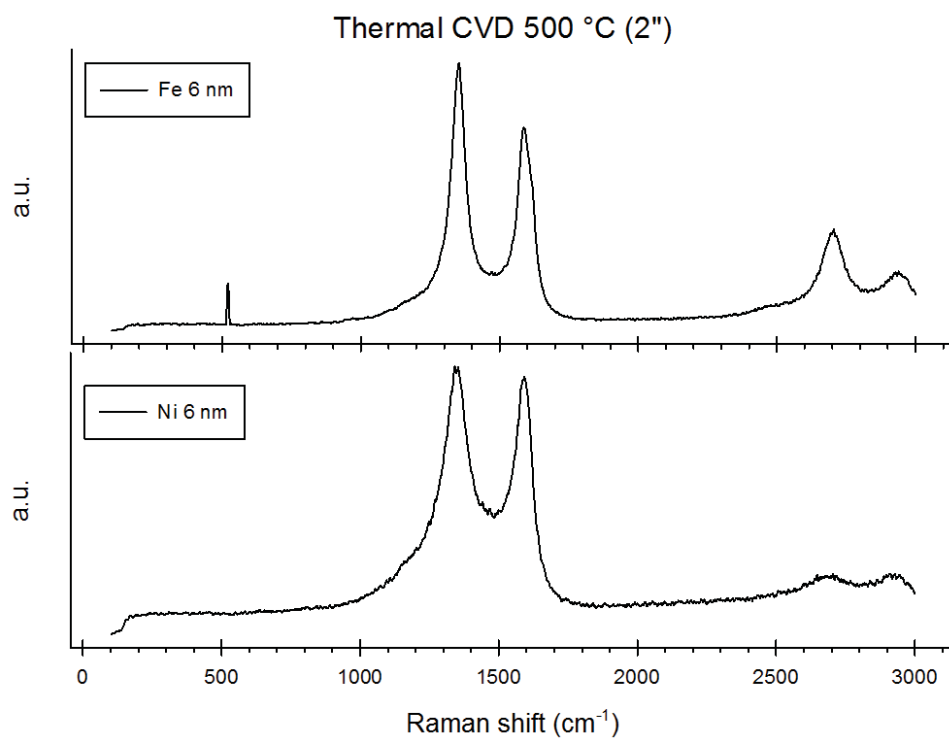


Figure C.18: Raman spectra of 2" furnace CVD at 500 °C

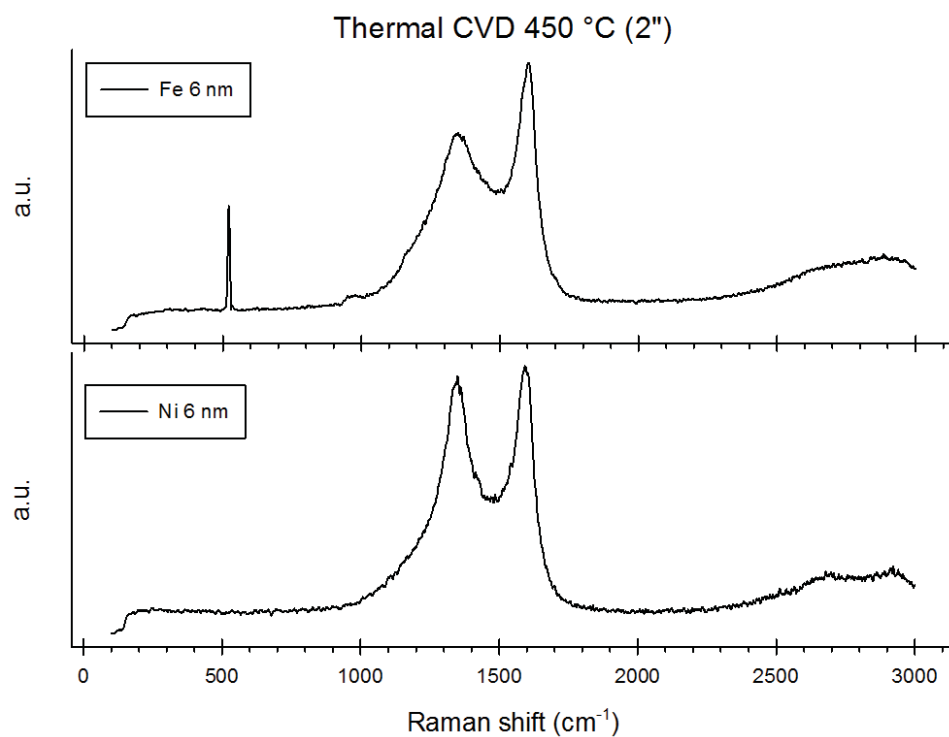


Figure C.19: Raman spectra of 2" furnace CVD at 450 °C

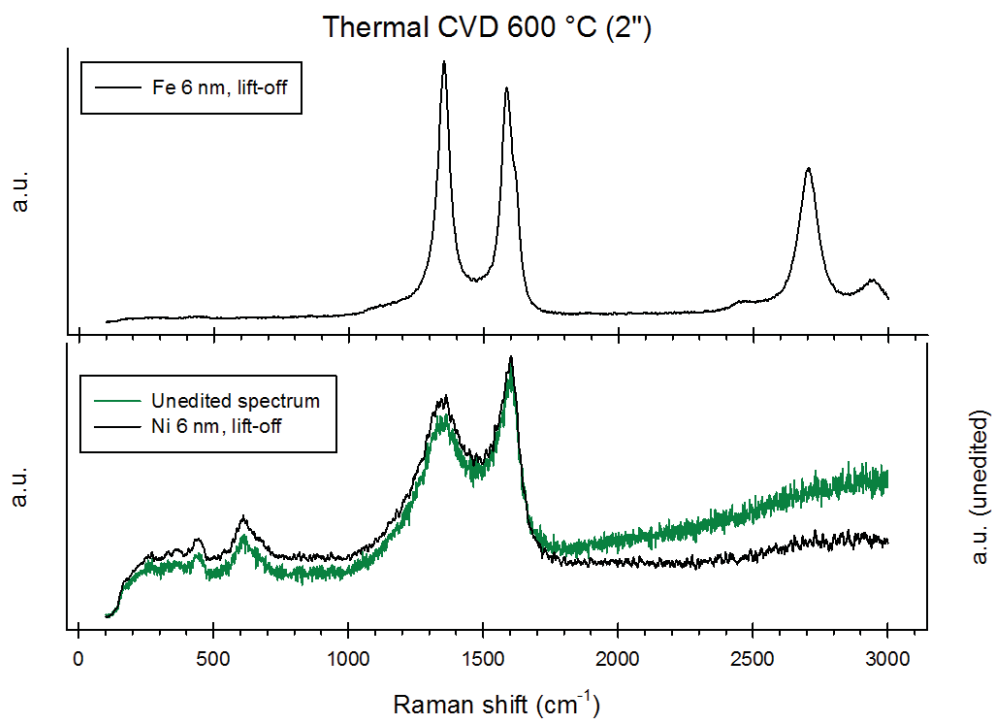


Figure C.20: Raman spectra of lift-off samples at 600 °C

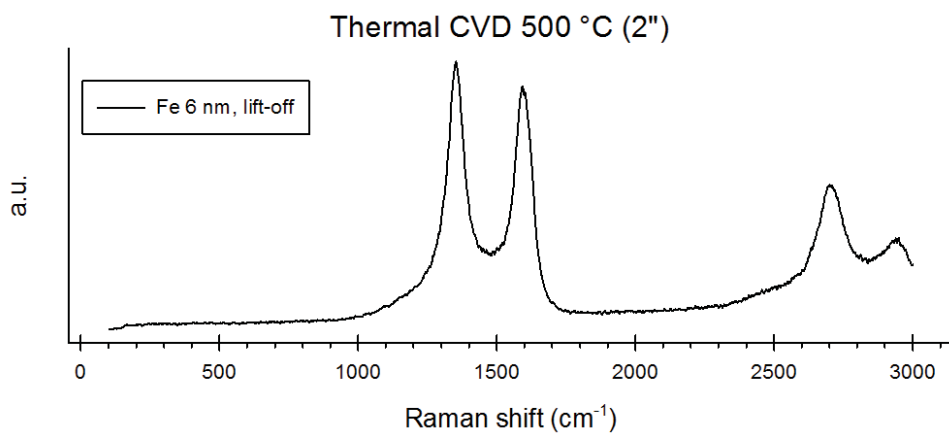


Figure C.21: Raman spectra of lift-off samples at 500 °C

Appendix D

Matlab files

D.1 SWNT simulations

```
clear all;

%Parameters
W = 10000000; %Bundle width
H =10000000; %Bundle heigth
s_min = 0; %Minumum separation
s_max = 5.0; %Maximum separation
s_increment = 0.1; %Increment steps separation
d_start = 0.6; %Minumum diameter
d_end = 3; %Maximum diameter
d_increment = 0.1; %Increment steps diameter
Rq = 6450; %Quantum resistance
Rc = 0; %Contact resistance

%Calculations
j=1;
for(s=s_min:s_increment:s_max) %s-loop
    i=1;
    for(d=d_start:d_increment:d_end) %d-loop
        Nw = floor((W+s)/(d+s));
        Nh = floor((H-d)/((d+s)*sqrt(3)/2))+1;
        if((W+s-Nw*(d+s))>((d+s)/2))
            Ncnt = Nw*Nh;
        else
            Ncnt = Nw*Nh - floor(Nh/2);
        end
        Density(i,j) = Ncnt/((W/1e7)*(H/1e7)); %Matrix with densities
        Rcnt(i,j) = 3*Rq/Ncnt + 3*Rc/Ncnt; %Matrix with bundle resistances
        Rcntcm2(i,j) = (3*Rq/Ncnt + 3*Rc/Ncnt)*((W/1e7)*(H/1e7)); %Matrix with bundle resistance/cm2
        d_vec(i,1) = d;
        i = i + 1;
    end
    s_vec(j,1) = s;
    j = j + 1;
end
```

D.2 MWNT simulations

```
clear all;
```

```

%Parameters
W = 10000000; %Bundle width
H = 10000000; %Bundle height
s_min = 0; %Minimum separation
s_max = 10.0; %Maximum separation
s_increment = 0.1; %Increment steps separation
d_start = 3; %Minimum diameter
d_end = 100; %Maximum diameter
d_increment = 1; %Increment steps diameter
d_ratio = 0.5; %Dmin/Dmax
Rq = 6450; %Quantum resistance
Rc = 0; %Contact resistance

%Calculations
j=1;
for(s=s_min:s_increment:s_max) %s-loop
    i=1;
    for(d=d_start:d_increment:d_end) %d-loop
        Nw = floor((W+s)/(d+s));
        Nh = floor((H-d)/((d+s)*sqrt(3)/2))+1;
        if((W+s-Nw*(d+s))>((d+s)/2))
            Ncnt = Nw*Nh;
        else
            Ncnt = Nw*Nh - floor(Nh/2);
        end
        Density(i,j) = Ncnt/((W/1e7)*(H/1e7)); %Matrix with densities
        if(d<6)
            Nchan = 2/3*(1+floor((d-d_ratio*d)/(2*0.34)));
        else
            Nchan = (1+floor((d-d_ratio*d)/(2*0.34)))*(1/2*0.0612*(d+d_ratio*d)+0.425);
        end
        Nchan_vec(i,1) = Nchan; %Vector with channels vs diameter
        Rcnt(i,j) = 2*Rq/(Nchan*Ncnt); %Matrix with bundle resistances
        Rcntcm2(i,j) = 2*Rq/(Nchan*Ncnt)*((W/1e7)*(H/1e7)); %Matrix with bundle resistance/cm2
        d_vec(i,1) = d;
        i = i + 1;
    end
    s_vec(j,1) = s;
    j = j + 1;
end
end

```

D.3 Raman analysis

```

function [d_freq, d_mag, g_freq, g_mag, gprime_freq, gprime_mag, idoig, igoigp, idoigp] = cnt_raman(raw)

%Raw is the unprocessed data from the Raman spectra imported from e.g. a
%txt file
%No solid peak detection has yet been found and implemented (for clear
%spectras it is not difficult, but for noisy spectra it is hard to
%determine a clear peak). Thus the user has to specify which peaks FWHM he wants
%to be checked using the three check parameters. Final visual inspection of
%the values with the actual spectra is highly recommended, especially for
%the G' peak.
%ATTENTION: It is advised to use the WiRE software to obtain the peak widths instead
%of using this script

data = flipud(raw); %Start at low frequency
freq = data(:,1); %Frequency shift vector
spec = data(:,2); %Spectral vector

```

```

%Extract place and magnitude of D-peak
f_1100 = find(freq > 1099 & freq < 1101);
f_1500 = find(freq > 1499 & freq < 1501);
[d_mag,d_index] = max(spec(f_1100:f_1500));
d_freq = freq(f_1100+d_index-1);

%Extract place and magnitude of G-peak
f_1800 = find(freq > 1799 & freq < 1801);
[g_mag,g_index] = max(spec(f_1500:f_1800));
g_freq = freq(f_1500+g_index-1);

%Extract place and magnitude of G'-peak
f_2500 = find(freq > 2499 & freq < 2501);
f_2850 = find(freq > 2849 & freq < 2851);
[gprime_mag,gprime_index] = max(spec(f_2500:f_2850));
gprime_freq = freq(f_2500+gprime_index-1);

%Calculate ratios
idoig = d_mag./g_mag;
igoigp = g_mag./gprime_mag;
idoigp = d_mag./gprime_mag;

%Determine index minimum between D and G peak
[mag_mindg,f_mindg] = min(spec(f_1100+d_index-1:f_1500+g_index-1));
f_mindg = f_1100 + d_index + f_mindg - 2; %Correct to full scale data

%Determine FWHM D-peak
%if(check_d == 1)
%   d_width = fwhm(freq(f_1100:f_mindg),spec(f_1100:f_mindg));
%   if(isnan(d_width) == 1)
%       d_width = -1; %Return width of -1 if the function couldn't determine FWHM
%       disp('D peak not separated enough to determine FWHM') %due to lack of data
%   end
%else
%   d_width = -1;
%end

%Determine FWHM G-peak
%if(check_g == 1)
%   g_width = fwhm(freq(f_mindg:f_1800),spec(f_mindg:f_1800));
%   if(isnan(g_width) == 1)
%       g_width = -1; %Return width of -1 if the function couldn't determine FWHM
%       disp('G peak not separated enough to determine FWHM') %due to lack of data.
%   end
%else
%   g_width = -1;
%end

%Determine FWHM G'-peak
%if(check_gprime == 1)
%   gprime_width = fwhm(freq(f_2500:f_2850),spec(f_2500:f_2850));
%   if(isnan(gprime_width) == 1)
%       gprime_width = -1; %Return width of -1 if the function couldn't determine FWHM
%       disp('G prime peak not separated enough to determine FWHM') %due to lack of data.
%   end
%else
%   gprime_width = -1;
%end
plot(freq,spec);

```

References

- [1] C. Disco and B. V. D. Meulen, *Getting New Technologies Together*. New York: Walter de Gruyter, 1998.
- [2] “International technology roadmap for semiconductors,” 2008. <http://public.itrs.net/>.
- [3] S. List, M. Bamal, M. Stucchi, and K. Maex, “A global view of interconnects,” *Microelectronic Engineering*, vol. 83, pp. 2200–2207, 2006.
- [4] J. D. Meindl, “Beyond Moore’s Law: the interconnect era,” *Computing in Science & Engineering*, vol. 5, pp. 20–24, 2003.
- [5] N. Srivastava and K. Banerjee, “Interconnect challenges for nanoscale electronic circuits,” *JOM*, vol. 56, no. 10, pp. 30–31, 2004.
- [6] S. M. Rossnagel, R. Wisnieff, D. Edelstein, and T. S. Kuan, “Interconnect issues post 45nm,” in *Electron Devices Meeting, 2005. IEDM Technical Digest. IEEE International*, pp. 89–91, 2005.
- [7] A. Naeemi, R. Sarvari, and J. D. Meindl, “Performance modeling and optimization for single- and multi-wall carbon nanotube interconnects,” in *Design Automation Conference, 2007. DAC '07. 44th ACM/IEEE*, pp. 568–573, 2007.
- [8] M. Engelhardt, G. Schindler, W. Steinhögl, G. Steinlesberger, and M. Traving, *Materials for Information Technology*, ch. Interconnect Technology - Today, Recent Advances and a Look into the Future, pp. 213–224. Engineering Materials and Processes, Springer London, 2005.
- [9] J. Robertson, “Growth of nanotubes for electronics,” *Materials Today*, vol. 10, no. 1-2, pp. 36–43, 2007.
- [10] A. W. Topol, J. D.C. La Tulipe, L. Shi, D. J. Frank, K. Bernstein, S. E. Steen, A. . Kumar, G. U. Singco, A. M. Young, K. W. Guarini, and M. Jeong, “Three-dimensional integrated circuits,” *IBM Journal of Research and Development*, vol. 50, pp. 491–506, 2006.
- [11] V. W. C. Chan, P. C. H. Chan, and M. Chan, “Three dimensional CMOS integrated circuits on large grain polysilicon films,” in *Electron Devices Meeting, 2000. IEDM Technical Digest. International*, pp. 161–164, 2000.
- [12] M. Koyanagi, H. Kurino, K. W. Lee, K. Sakuma, N. Miyakawa, and H. Itani, “Future system-on-silicon LSI chips,” *Micro, IEEE*, vol. 18, no. 4, pp. 17–22, 1998.
- [13] L. Zhu, Y. Sun, J. Xu, Z. Zhang, D. W. Hess, and C. P. Wong, “Aligned carbon nanotubes for electrical interconnect and thermal management,” in *Electronic Components and Technology Conference, 2005. Proceedings. 55th*, pp. 44–50, 2005.
- [14] T. Yamamoto, K. Watanabe, and E. R. Hernández, *Carbon Nanotubes*, vol. 111 of *Topics in Applied Physics*, ch. Mechanical Properties, Thermal Stability and Heat Transport in Carbon Nanotubes, pp. 165–194. Springer Berlin/Heidelberg, 2008.
- [15] A. P. Graham, G. S. Duesberg, W. Hoenlein, F. Kreupl, M. Liebau, R. Martin, B. Rajasekharan, W. Palmer, R. Seidel, W. Steinhoegl, and E. Unger, “How do carbon nanotubes fit into the semiconductor roadmap?,” *Applied Physics A*, vol. 80, pp. 1141–1151, 2005.
- [16] D. Yokoyama, T. Iwasaki, K. Ishimaru, S. Sato, T. Hyakushima, M. Nihei, Y. Awano, and H. Kawarada, “Electrical properties of carbon nanotubes grown at a low temperature for use as interconnects,” *Japanese Journal of Applied Physics*, vol. 4, no. 4, pp. 1985–1990, 2008.
- [17] J. Wu, J. Walenza-Slabe, M. Mann, K. B. K. Teo, W. I. Milne, and J. Jiao, “Novel fabrication of carbon nanotube vias for VLSI interconnects,” *Microscopy and Microanalysis*, vol. 14 (Suppl. 2), pp. 298–299, 2008.
- [18] J. Li, Q. Ye, A. Cassell, H. T. Ng, R. Stevens, J. Han, and M. Meyyappan, “Bottom-up approach for carbon nanotube interconnects,” *Applied Physics Letters*, vol. 82, no. 15, pp. 2491–2493, 2003.
- [19] A. Naeemi and J. D. Meindl, “Monolayer metallic nanotube interconnects: Promising candidates for short local interconnects,” *IEEE Electron Device Letters*, vol. 26, no. 8, pp. 544–546, 2005.
- [20] G. F. Close, S. Yasuda, B. Paul, S. Fujita, and H.-S. P. Wong, “Sub-ns delay through multi-wall carbon nanotube local interconnects in a CMOS integrated circuit,” in *Interconnect*

- Technology Conference, 2008. IITC 2008. International*, pp. 234–236, 2008.
- [21] N. Srivastava and K. Banerjee, “A comparative scaling analysis of metallic and carbon nanotube interconnections for nanometer scale VLSI technologies,” in *Proceedings of the 21st International VLSI Multilevel Interconnect Conference (VMIC)*, pp. 393–398, 2004.
- [22] N. Srivastava and K. Banerjee, “Performance analysis of carbon nanotube interconnects for VLSI applications,” in *Computer-Aided Design, 2005. ICCAD-2005. IEEE/ACM International Conference on*, pp. 383–390, 2005.
- [23] M. Nihei, A. Kawabata, D. Kondo, M. Horibe, S. Sato, and Y. Awano, “Electrical properties of carbon nanotube bundles for future via interconnects,” *Japanese Journal of Applied Physics*, vol. 44, no. 4A, pp. 1626–1628, 2005.
- [24] T. Xu, Z. Wang, J. Miao, X. Chen, and C. M. Tan, “Aligned carbon nanotubes for through-wafer interconnects,” *Applied Physics Letters*, vol. 91, p. 042108, 2007.
- [25] T. Xu, Z. Wang, and J. Miao, “Through-wafer interconnects using carbon nanotubes synthesized by chemical vapor deposition,” in *Nano/Micro Engineered and Molecular Systems, 2008. NEMS 2008. 3rd IEEE International Conference on*, pp. 471–475, 2008.
- [26] S. Iijima, “Helical microtubules of graphitic carbon,” *Nature*, vol. 354, pp. 56–58, 1991.
- [27] M. Monthieux and V. L. Kuznetsov, “Who should be given the credit for the discovery of carbon nanotubes?,” *Carbon*, vol. 44, pp. 1621–1623, 2006.
- [28] J. Han, *Carbon Nanotubes: Science and Applications*, ch. Structures and Properties of Carbon Nanotubes, pp. 1–24. CRC Press, 2005.
- [29] L. Solymar and D. Walsh, *Electrical Properties of Materials, Seventh Edition*. Oxford University Press, 2004.
- [30] X. Zhao, Y. Liu, S. Inoue, T. Suzuki, R. Jones, and Y. Ando, “Smallest carbon nanotube is 3 Å in diameter,” *Physical Review Letters*, vol. 92, no. 12, p. 125502, 2004.
- [31] M. Chhowalla, K. B. K. Teo, C. Ducati, N. L. Rupesinghe, G. A. J. Amaratunga, A. C. Ferrari, D. Roy, J. Robertson, and W. I. Milne, “Growth process conditions of vertically aligned carbon nanotubes using plasma enhanced chemical vapor deposition,” *Journal of Applied Physics*, vol. 90, no. 10, pp. 5308–5317, 2001.
- [32] J.-C. Charlier and S. Iijima, *Carbon Nanotubes*, ch. Growth Mechanisms of Carbon Nanotubes, pp. 55–81. No. 80 in *Topics in Applied Physics*, Springer Berlin/Heidelberg, 2001.
- [33] H. Dai, *Carbon Nanotubes*, vol. 80 of *Topics in Applied Physics*, ch. Nanotube Growth and Characterization, pp. 29–53. Springer Berlin/Heidelberg, 2001.
- [34] F. Kreupl, A. P. Graham, M. Lieba, G. S. Duesber, R. Seide, and E. Unger, “Carbon nanotubes for interconnect applications,” in *Electron Devices Meeting, 2004. IEDM Technical Digest. IEEE International*, pp. 683–686, 2004.
- [35] M. Freitag, *Carbon Nanotubes: Properties and Applications*, ch. Carbon nanotube electronics and devices, pp. 83–117. Taylor and Francis, 2006.
- [36] C. Dekker, “Carbon nanotubes as molecular quantum wires,” *Physics Today*, vol. 52, no. 5, pp. 22–28, 1999.
- [37] R. Saito, G. Dresselhaus, and M. S. Dresselhaus, “Electronic structure of double-layer graphene tubules,” *Journal of Applied Physics*, vol. 73, no. 2, pp. 494–500, 1993.
- [38] Y. Tison, C. E. Giusca, V. Stolojan, Y. Hayashi, and S. R. P. Silva, “The inner shell influence on the electronic structure of double-walled carbon nanotubes,” *Advanced Materials*, vol. 20, pp. 189–194, 2008.
- [39] Z. Yao, C. Dekker, and P. Avouris, *Carbon Nanotubes*, vol. 80 of *Topics in Applied Physics*, ch. Electrical Transport Through Single-Wall Carbon Nanotubes, pp. 147–171. Springer Berlin/Heidelberg, 2001.
- [40] P. L. McEuen and J.-Y. Park, “Electron transport in single-walled carbon nanotubes,” *MRS Bulletin*, vol. 29, no. 4, pp. 272–275, 2004.
- [41] H. J. Li, W. G. Lu, J. J. Li, X. D. Bai, and C. Z. Gu, “Multichannel ballistic transport in multiwall carbon nanotubes,” *Physical Review Letters*, vol. 95, p. 086601, 2005.
- [42] S. Frank, P. Poncharal, Z. L. Wang, and W. A. de Heer, “Carbon nanotube quantum resistors,” *Science*, vol. 280, pp. 1744–1746, 1998.
- [43] A. Naeemi and J. D. Meindl, “Compact physical models for multiwall carbon-nanotube interconnects,” *IEEE Electron Device Letters*, vol. 27, no. 5, pp. 338–340, 2006.

- [44] E. Pop, D. Mann, J. Reifenberg, K. Goodson, and H. Dai, "Electro-thermal transport in metallic single-wall carbon nanotubes for interconnect applications," in *Electron Devices Meeting, 2005. IEDM Technical Digest. IEEE International*, p. 4, 2005.
- [45] A. Raychowdhury and K. Roy, "A circuit model for carbon nanotube interconnects: Comparative study with Cu interconnects for scaled technologies," in *Computer Aided Design, 2004. ICCAD-2004. IEEE/ACM International Conference on*, pp. 237–240, 2004.
- [46] A. Naeemi and J. D. Meindl, "Impact of electron-phonon scattering on the performance of carbon nanotube interconnects for GSI," *Electron Device Letters, IEEE*, vol. 26, no. 7, pp. 476–478, 2005.
- [47] D.-A. Borca-Tasciuc, L. Pietruszka, T. Borca-Tasciuc, R. Vajtai, and P. M. Ajayan, "Thermal transport measurements in multi-wall carbon nanotube strands using the 3ω method," in *Semiconductor Thermal Measurement and Management Symposium, 2005 IEEE Twenty First Annual IEEE*, pp. 247–252, 2005.
- [48] T.-Y. Choi, D. Poulidakos, J. Tharian, and U. Sennhauser, "Measurement of the thermal conductivity of individual carbon nanotubes by the four-point three- ω method," *Nano Letters*, vol. 6, no. 8, pp. 1589–1593, 2006.
- [49] Z. L. Wang, D. W. Tang, X. B. Li, X. H. Zheng, W. G. Zhang, L. X. Zheng, Y. T. Zhu, A. Z. Jin, H. F. Yang, and C. Z. Gu, "Length-dependent thermal conductivity of an individual single-wall carbon nanotube," *Applied Physics Letters*, vol. 91, p. 123119, 2007.
- [50] L. Chico, L. X. Benedict, S. G. Louie, and M. L. Cohen, "Quantum conductance of carbon nanotubes with defects," *Physical Review B*, vol. 54, no. 4, pp. 2600–2606, 1996.
- [51] S. G. Louie, *Carbon Nanotubes*, vol. 80 of *Topics in Applied Physics*, ch. Electronic Properties, Junctions, and Defects of Carbon Nanotubes, pp. 113–145. Springer Berlin/Heidelberg, 2001.
- [52] R. Tarkiainen, M. Ahlskog, J. Penttilä, L. Roschier, P. Hakonen, M. Paalanen, and E. Sonin, "Multiwalled carbon nanotube: Luttinger versus Fermi liquid," *Physical Review B*, vol. 64, p. 195412, 2001.
- [53] P. J. de Pablo, E. Graugnard, B. Walsh, R. P. Andres, S. Datta, and R. Reifengerger, "A simple, reliable technique for making electrical contact to multiwalled carbon nanotubes," *Applied Physics Letters*, vol. 74, no. 2, pp. 323–325, 1999.
- [54] B. Q. Wei, R. Vajtai, and P. M. Ajayan, "Reliability and current carrying capacity of carbon nanotubes," *Applied Physics Letters*, vol. 79, no. 8, pp. 1172–1174, 2001.
- [55] M. Nihei, D. Kondo, A. Kawabata, S. Sato, H. Shioya, M. Sakaue, T. Iwai, M. Ohfuti, and Y. Awano, "Low-resistance multi-walled carbon nanotube vias with parallel channel conduction of inner shells," in *Interconnect Technology Conference, 2005. Proceedings of the IEEE 2005 International*, pp. 234–236, 2005.
- [56] S. Sato, M. Nihei, A. Mimura, A. Kawabata, D. Kondo, H. Shioya, T. Iwai, M. Mishima, M. Ohfuti, and Y. Awano, "Novel approach to fabricating carbon nanotube via interconnects using size-controlled catalyst nanoparticles," in *Interconnect Technology Conference, 2006 International*, pp. 230–232, 2006.
- [57] D. Yokoyama, T. Iwasaki, T. Yoshida, H. Kawarada, S. Sato, T. Hyakushima, M. Nihei, and Y. Awano, "Low temperature grown carbon nanotube interconnects using inner shells by chemical mechanical polishing," *Applied Physics Letters*, vol. 91, p. 263101, 2007.
- [58] S. Sanvito, Y.-K. Kwon, D. Tománek, and C. J. Lambert, "Fractional quantum conductance in carbon nanotubes," *Physical Review Letters*, vol. 84, no. 9, pp. 1974–1977, 2000.
- [59] Q. Yan, J. Wu, G. Zhou, W. Duan, and B.-L. Gu, "Ab initio study of transport properties of multiwalled carbon nanotubes," *Physical Review B*, vol. 72, p. 155425, 2005.
- [60] Q. Ngo, D. Petranovic, S. Krishnan, A. M. Cassell, Q. Ye, J. Li, M. Meyyappan, and C. Y. Yang, "Electron transport through metal-multiwall carbon nanotube interfaces," *Nanotechnology, IEEE Transactions on*, vol. 3, no. 2, pp. 311–317, 2004.
- [61] L. Zhang, D. Austin, V. I. Merkulov, A. V. Meleshko, K. L. Klein, M. A. Guillorn, D. H. Lowndes, and M. L. Simpson, "Four-probe charge transport measurements on individual vertically aligned carbon nanofibers," *Applied Physics Letters*, vol. 84, no. 20, pp. 3972–3974, 2004.
- [62] M. Nihei, T. Hyakushima, S. Sato, T. Nozue, M. Norimatsu, M. Mishima, T. Murakami,

- D. Kondo, A. Kawabata, M. Ohfuti, and Y. Awano, "Electrical properties of carbon nanotube via interconnects fabricated by novel damascene process," in *International Interconnect Technology Conference, IEEE 2007*, pp. 204–206, 2007.
- [63] Y. Zhang, T. Ichihashi, E. Landree, F. Nihey, and S. Iijima, "Heterostructures of single-walled carbon nanotubes and carbide nanorods," *Science*, vol. 285, pp. 1719–1722, 1999.
- [64] J.-O. Lee, C. Park, J.-J. Kim, J. Kim, J. W. Park, and K.-H. Yoo, "Formation of low-resistance ohmic contacts between carbon nanotube and metal electrodes by a rapid thermal annealing method," *Journal of Physics D: Applied Physics*, vol. 33, pp. 1953–1956, 2000.
- [65] O. Hjortstam, P. Isberg, S. Söderholm, and H. Dai, "Can we achieve ultra-low resistivity in carbon nanotube-based metal composites?," *Applied Physics A*, vol. 78, pp. 1175–1179, 2004.
- [66] A. Javey, J. Guo, Q. Wang, M. Lundstrom, and H. Dai, "Ballistic carbon nanotube field-effect transistors," *Nature*, vol. 424, pp. 654–657, 2003.
- [67] P. Tarakeshwar, J. J. Palacios, and D. M. Kim, "Interface study of metal electrode and semiconducting carbon nanotubes: Effects of electrode atomic species," *Nanotechnology, IEEE Transactions on*, vol. 7, no. 2, pp. 124–127, 2008.
- [68] D. Mann, A. Javey, J. Kong, Q. Wang, and H. Dai, "Ballistic transport in metallic nanotubes with reliable Pd ohmic contacts," *Nano Letters*, vol. 3, no. 11, pp. 1541–1544, 2003.
- [69] G. F. Close and H.-S. P. Wong, "Fabrication and characterization of carbon nanotube interconnects," in *Electron Devices Meeting, 2007. IEDM 2007. IEEE International*, pp. 203–206, 2007.
- [70] P. J. Burke, "Luttinger liquid theory as a model of the gigahertz electrical properties of carbon nanotubes," *Nanotechnology, IEEE Transactions on*, vol. 1, no. 3, pp. 129–144, 2002.
- [71] P. J. Burke, "An RF circuit model for carbon nanotubes," *Nanotechnology, IEEE Transactions on*, vol. 2, no. 1, pp. 55–58, 2003.
- [72] M. D'Amore, M. S. Sarto, and A. Tamburrano, "Modelling of multiwall carbon nanotube transmission lines," in *Electromagnetics in Advanced Applications, 2007. ICEAA 2007. International Conference on*, pp. 629–632, 2007.
- [73] D. Rossi, J. M. Cazeaux, C. Metra, and F. Lombardi, "Modeling crosstalk effects in CNT bus architectures," *Nanotechnology, IEEE Transactions on*, vol. 6, no. 2, pp. 133–145, 2007.
- [74] Q. Ngo, S. Krishnan, A. M. Cassell, Y. Ominami, J. Li, M. Meyyappan, and C. Y. Yang, "Electrical characterization of carbon nanofibers for on-chip interconnect applications," in *Nanotechnology, 2005. 5th IEEE Conference on*, vol. 1, pp. 431–434, 2005.
- [75] H. Kitsuki, M. Suzuki, Q. Ngo, K. Gleasson, A. M. Cassell, Y. Ominami, C. R. Moylan, J. Li, and C. Y. Yang, "High-current reliability of carbon nanofibers for interconnect applications," in *Mater. Res. Soc. Symp. Proc.*, vol. 1018, 2007.
- [76] M. Suzuki, Y. Ominami, Q. Ngo, C. Y. Yang, A. M. Cassell, and J. Li, "Current-induced breakdown of carbon nanofibers," *Journal of Applied Physics*, vol. 101, p. 114307, 2007.
- [77] J. Hone, *Carbon Nanotubes*, vol. 80 of *Topics in Applied Physics*, ch. Phonons and Thermal Properties of Carbon Nanotubes, pp. 273–286. Springer Berlin/Heidelberg, 2001.
- [78] C. Masarapu, L. L. Henry, and B. Wei, "Specific heat of aligned multiwalled carbon nanotubes," *Nanotechnology*, vol. 16, pp. 1490–1494, 2005.
- [79] J. X. Cao, X. H. Yan, and Y. Xiao, "Specific heat of single-walled carbon nanotubes: A lattice dynamics study," *Journal of the Physical Society of Japan*, vol. 72, no. 9, pp. 2256–2259, 2003.
- [80] S. Berber, Y.-K. Kwon, and D. Tománek, "Unusually high thermal conductivity of carbon nanotubes," *Physical Review Letters*, vol. 84, no. 20, pp. 4613–4616, 2000.
- [81] J. Che, T. Çağın, and W. A. G. III, "Thermal conductivity of carbon nanotubes," *Nanotechnology*, vol. 11, pp. 65–69, 2000.
- [82] X.-S. Yang, "Modelling heat transfer of carbon nanotubes," *Modelling and Simulation in Materials Science and Engineering*, vol. 13, pp. 893–902, 2005.
- [83] J. Hone, M. Whitney, and A. Zettl, "Thermal conductivity of single-walled carbon nano-

- tubes,” *Synthetic Materials*, vol. 103, pp. 2498–2499, 1999.
- [84] P. Kim, L. Shi, A. Majumdar, and P. L. McEuen, “Thermal transport measurements of individual multiwalled nanotubes,” *Physical Review Letters*, vol. 87, no. 21, p. 215502, 2001.
- [85] M. Grujicic, G. Cao, and W. N. Roy, “Computational analysis of the lattice contribution to thermal conductivity of single-walled carbon nanotubes,” *Journal of Materials Science*, vol. 40, pp. 1943–1952, 2005.
- [86] N. Mingo and D. A. Broido, “Carbon nanotube ballistic thermal conductance and its limits,” *Physical Review Letters*, vol. 95, p. 096105, 2005.
- [87] E. Pop, D. Mann, Q. Wang, K. Goodson, and H. Dai, “Thermal conductance of an individual single-wall carbon nanotube above room temperature,” *Nano Letters*, vol. 6, no. 1, pp. 96–100, 2006.
- [88] C. Yu, S. Saha, J. Zhou, L. Shi, A. M. Cassell, B. A. Cruden, Q. Ngo, and J. Li, “Thermal contact resistance and thermal conductivity of a carbon nanofiber,” *Journal of Heat Transfer*, vol. 128, pp. 234–239, 2006.
- [89] Y. Zhang, Y. Xu, and E. Suhir, “Effect of rapid thermal annealing (RTA) on thermal properties of carbon nanofibre (CNF) arrays,” *Journal Of Physics D: Applied Physics*, vol. 39, pp. 4878–4885, 2006.
- [90] H. Xie, A. Cai, and X. Wang, “Thermal diffusivity and conductivity of multiwalled carbon nanotube arrays,” *Physics Letters A*, vol. 369, pp. 120–123, 2007.
- [91] G. E. Begtrup, K. G. Ray, B. M. Kessler, T. D. Yuzvinsky, H. Garcia, and A. Zettl, “Extreme thermal stability of carbon nanotubes,” *Physica Status Solidi (b)*, vol. 244, no. 11, pp. 3960–3963, 2007.
- [92] Q. Liu, W. Ren, F. Li, H. Cong, and H.-M. Cheng, “Synthesis and high thermal stability of double-walled carbon nanotubes using nickel formate dihydrate as catalyst precursor,” *Journal of Physical Chemistry C*, vol. 111, pp. 5006–5013, 2007.
- [93] K. Hata, D. N. Futaba, K. Mizuno, T. Namai, M. Yumura, and S. Iijima, “Water-assisted highly efficient synthesis of impurity-free single-walled carbon nanotubes,” *Science*, vol. 306, pp. 1362–1364, 2004.
- [94] M. J. López, A. Rubio, and J. A. Alonso, “Deformations and thermal stability of carbon nanotube ropes,” *IEEE Transactions on Nanotechnology*, vol. 3, no. 2, pp. 230–236, 2004.
- [95] Y. Kim, H. Muramatsu, T. Hayashi, M. Endo, M. Terrones, and M. Dresselhaus, “Thermal stability and structural changes of double-walled carbon nanotubes by heat treatment,” *Chemical Physics Letters*, vol. 398, pp. 87–92, 2004.
- [96] G. Dereli, B. Süngü, and C. Özdoğan, “Thermal stability of metallic single-walled carbon nanotubes: an $O(N)$ tight-binding molecular dynamics simulation study,” *Nanotechnology*, vol. 18, p. 245704, 2007.
- [97] K. M. Liew, C. H. Wong, X. Q. He, and M. J. Tan, “Thermal stability of single and multi-walled carbon nanotubes,” *Physical Review B*, vol. 71, p. 075424, 2005.
- [98] E. Joselevich, H. Dai, J. Liu, K. Hata, and A. H. Windle, *Carbon Nanotubes*, vol. 111 of *Topics in Applied Physics*, ch. Carbon Nanotube Synthesis and Organization, pp. 101–165. Springer Berlin/Heidelberg, 2008.
- [99] C. Kocabas, S.-H. Hur, A. Gaur, M. A. Meitl, M. Shim, and J. A. Rogers, “Guided growth of large-scale, horizontally aligned arrays of single-walled carbon nanotubes and their use in thin-film transistors,” *Small*, vol. 1, no. 11, pp. 1110–1116, 2005.
- [100] H. Ago, K. Nakamura, K. ichi Ikeda, N. Uehara, N. Ishigami, and M. Tsuji, “Aligned growth of isolated single-walled carbon nanotubes programmed by atomic arrangement of substrate surface,” *Chemical Physics Letters*, vol. 408, pp. 433–438, 2005.
- [101] Ç. Öncel and Y. Yürüm, “Carbon nanotube synthesis via the catalytic cvd method: A review on the effect of reaction parameters,” *Fullerenes, Nanotubes, and Carbon Nanostructures*, vol. 14, pp. 17–37, 2006.
- [102] S. Hofmann, B. Kleinsorge, C. Ducati, A. C. Ferrari, and J. Robertson, “Low-temperature plasma enhanced chemical vapour deposition of carbon nanotubes,” *Diamond and Related Materials*, vol. 13, pp. 1171–1176, 2004.
- [103] S. Hofmann, C. Ducati, and J. Robertson, “Low-temperature growth of carbon nanotubes

- by plasma-enhanced chemical vapor deposition,” *Applied Physics Letters*, vol. 81, no. 1, pp. 135–137, 2003.
- [104] Y. Yamazaki, N. Sakuma, M. Katagiri, M. Suzuki, T. Sakai, S. Sato, M. Nihei, and Y. Awano, “High-quality carbon nanotube growth at low temperature by pulse-excited remote plasma chemical vapor deposition,” *Applied Physics Express*, vol. 1, p. 034004, 2008.
- [105] S. B. Sinnott, R. Andrews, D. Qian, A. M. Rao, Z. Mao, E. C. Dickey, and F. Derbyshire, “Model of carbon nanotube growth through chemical vapor deposition,” *Chemical Physics Letters*, vol. 315, pp. 25–30, 1999.
- [106] R. T. Baker, P. S. Harris, R. B. Thomas, and R. J. Waite, “Formation of filamentous carbon from iron, cobalt and chromium catalyzed decomposition of acetylene,” *Journal of Catalysis*, vol. 30, pp. 86–95, 1973.
- [107] S. Helveg, C. López-Cartes, J. Sehested, P. L. Hansen, B. S. Clausen, J. R. Rostrup-Nielsen, F. Abild-Pedersen, and J. K. Nørskov, “Atomic-scale imaging of carbon nanofibre growth,” *Nature*, vol. 427, pp. 426–429, 2004.
- [108] H. Zhu, K. Suenaga, A. Hashimoto, K. Urita, K. Hata, and S. Iijima, “Atomic-resolution imaging of the nucleation points of single-walled carbon nanotubes,” *Small*, vol. 1, no. 12, pp. 1180–1183, 2005.
- [109] R. Sharma, P. Rez, M. M. J. Treacy, and S. J. Stuart, “In situ observation of the growth mechanisms of carbon nanotubes under diverse reaction conditions,” *Journal of Electron Microscopy*, vol. 54, pp. 231–237, 2005.
- [110] S. Hofmann, R. Sharma, C. Ducati, G. Du, C. Mattevi, C. Cepek, M. Cantoro, S. Pisana, A. Parvez, F. Cervantes-Sodi, A. C. Ferrari, R. Dunin-Borkowski, S. Lizzit, L. Petaccia, A. Goldoni, and J. Robertson, “In situ observations of catalyst dynamics during surface-bound carbon nanotube nucleation,” *Nano Letters*, vol. 7, no. 3, pp. 602–608, 2007.
- [111] V. Vinciguerra, F. Buonocore, G. Panzera, and L. Occhipinti, “Growth mechanisms in chemical vapour deposited carbon nanotubes,” *Nanotechnology*, vol. 14, pp. 655–660, 2004.
- [112] J.-Y. Raty, F. Gygi, and G. Galli, “Growth of carbon nanotubes on metal nanoparticles: A microscopic mechanism from ab initio molecular dynamics simulations,” *Physical Review Letters*, vol. 95, p. 096103, 2005.
- [113] S. Hofmann, G. Csányi, A. C. Ferrari, M. C. Payne, and J. Robertson, “Surface diffusion: The low activation energy path for nanotube growth,” *Physical Review Letters*, vol. 95, p. 036101, 2005.
- [114] Z. Chen, J. Merikhi, I. Koehler, and P. K. Bachmann, “Sandwich growth of carbon nanotubes,” *Diamond and Related Materials*, vol. 15, pp. 104–108, 2006.
- [115] Q. Ngo, A. M. Cassell, V. Radmilovic, J. Li, S. Krishnan, M. Meyyappan, and C. Y. Yang, “Palladium catalyzed formation of carbon nanofibers by plasma enhanced chemical vapor deposition,” *Carbon*, vol. 45, pp. 424–428, 2007.
- [116] Y. Abdi, J. Koohsorkhi, J. Derakhshandeh, S. Mohajezadeh, H. Hoseinzadegan, M. Robertson, J. Bennett, X. Wu, and H. Radamson, “PECVD-grown carbon nanotubes on silicon substrates with a nickel-seeded tip-growth structure,” *Materials Science and Engineering C*, vol. 26, pp. 1219–1223, 2006.
- [117] H. Amara, C. Bichara, and F. Ducastelle, “Understanding the nucleation mechanisms of carbon nanotubes in catalytic chemical vapor deposition,” *Physical Review Letters*, vol. 100, p. 056105, 2008.
- [118] L. Delzeit, B. Chen, A. Cassell, R. Stevens, C. Nguyen, and M. Meyyappan, “Multilayered metal catalysts for controlling the density of single-walled carbon nanotube growth,” *Chemical Physical Letters*, vol. 348, pp. 368–374, 2001.
- [119] G. S. Duesberg, A. P. Graham, F. Kreupl, M. Liebau, R. Seidel, E. Unger, and W. Hoenlein, “Ways towards the scaleable integration of carbon nanotubes into silicon based technology,” *Diamond and Related Materials*, vol. 13, pp. 354–361, 2004.
- [120] Y.-M. Choi, S. Lee, H. S. Yoon, M.-S. Lee, H. Kim, I. Han, Y. Son, I.-S. Yeo, U.-I. Chung, and J.-T. Moon, “Integration and electrical properties of carbon nanotube array for interconnect applications,” in *Nanotechnology, 2006. IEEE-NANO 2006. Sixth IEEE Conference on*, pp. 262–265, 2006.

- [121] M. Cantoro, S. Hofmann, S. Pisana, V. Scardaci, A. Parvez, C. Ducati, A. C. Ferrari, A. M. Blackburn, K.-Y. Wang, and J. Robertson, "Catalytic chemical vapor deposition of single-wall carbon nanotubes at low temperatures," *Nano Letters*, vol. 6, no. 6, pp. 1107–1112, 2006.
- [122] Y. Nakayama, L. Pan, and G. Takeda, "Low-temperature growth of vertically aligned carbon nanotubes using binary catalysts," *Japanese Journal of Applied Physics*, vol. 45, pp. 369–371, 2006.
- [123] S. Sato, A. Kawabata, M. Nihei, and Y. Awano, "Growth of diameter-controlled carbon nanotubes using monodisperse nickel nanoparticles obtained with a differential mobility analyzer," *Chemical Physics Letters*, vol. 382, pp. 361–366, 2003.
- [124] M. Horibe, M. Nihei, D. Kondo, A. Kawabata, and Y. Awano, "Carbon nanotube growth technologies using tantalum barrier layer for future ulsis with Cu/Low-k interconnect processes," *Japanese Journal of Applied Physics*, vol. 44, no. 7A, pp. 5309–5312, 2005.
- [125] Y. Awano, "Carbon nanotube technologies for LSI via interconnects," *IEICE Transactions on Electronics*, vol. 89, no. 11, pp. 1499–1503, 2006.
- [126] Z. F. Ren, Z. P. Huang, J. W. Xu, J. H. Wang, P. Bush, M. P. Siegal, and P. N. Provencio, "Synthesis of large arrays of well-aligned carbon nanotubes on glass," *Science*, vol. 282, pp. 1105–1107, 1998.
- [127] S. Fan, M. G. Chapline, N. R. Franklin, T. W. Tombler, A. M. Cassell, and H. Dai, "Self-oriented regular arrays of carbon nanotubes and their field emission properties," *Science*, vol. 283, pp. 512–514, 1999.
- [128] A. Kawabata, S. Sato, T. Nozue, T. Hyakushima, M. Norimatsu, M. Mishima, T. Murakami, D. Kondo, K. Asano, M. Ohfuti, H. Kawarada, T. Sakai, M. Nihei, and Y. Awano, "Robustness of CNT via interconnect fabricated by low temperature process over a high-density current," in *Interconnect Technology Conference, 2008. IITC 2008. International*, pp. 237–239, 2008.
- [129] G. Takeda, L. P. S. Akita, and Y. Nakayama, "Vertically aligned carbon nanotubes grown at low temperatures for use in displays," *Japanese Journal of Applied Physics*, vol. 44, no. 7B, pp. 5642–5645, 2005.
- [130] M. J. Bronikowski, "CVD growth of carbon nanotube bundle arrays," *Carbon*, vol. 44, pp. 2822–2832, 2006.
- [131] T. Y. Lee, J.-H. Han, S. H. Choi, J.-B. Yoo, C.-Y. Park, T. Jung, S. Yu, J. Lee, W. Yi, and J. M. Kim, "Comparison of source gases and catalyst metals for growth of carbon nanotube," *Surface and Coatings Technology*, vol. 169-170, pp. 348–352, 2003.
- [132] M. Meyyappan, *Carbon Nanotubes: Science and Applications*, ch. Growth: CVD and PECVD, pp. 99–116. CRC Press, 2005.
- [133] Y. Yabe, Y. Ohtake, T. Ishitobi, Y. Show, T. Izumi, and H. Yamauchi, "Synthesis of well-aligned carbon nanotubes by radio frequency plasma enhanced CVD method," *Diamond and Related Materials*, vol. 13, pp. 1292–1295, 2004.
- [134] T. Hirao, K. Ito, H. Furuta, Y. K. Yap, T. Ikuno, S. ichi Honda, Y. Mori, T. Sasaki, and K. Oura, "Formation of vertically aligned carbon nanotubes by dual-RF-plasma chemical vapor deposition," *Japanese Journal of Applied Physics*, vol. 40, pp. 631–634, 2001.
- [135] G.-H. Jeong, N. Satake, T. Kato, T. Hirata, R. Hatakeyama, and K. Tohji, "Simple methods for site-controlled carbon nanotube growth using radio-frequency plasma-enhanced chemical vapor deposition," *Applied Physics A*, vol. 79, p. 85–87, 2004.
- [136] A. Okita, A. Ozeki, Y. Suda, J. Nakamura, A. Oda, K. Bhattacharyya, H. Sugawara, and Y. Sakai, "Analysis of oxidation state of multilayered catalyst thin films for carbon nanotube growth using plasma-enhanced chemical vapor deposition," *Japanese Journal of Applied Physics*, vol. 45, no. 10B, pp. 8323–8329, 2006.
- [137] Z. Luo, S. Lim, Y. You, J. Miao, H. Gong, J. Zhang, S. Wang, J. Lin, and Z. Shen, "Effect of ion bombardment on the synthesis of vertically aligned single-walled carbon nanotubes by plasma-enhanced chemical vapor deposition," *Nanotechnology*, vol. 19, p. 255607, 2008.
- [138] A. Suzuki, H. Sato, T. Sakai, H. Takegawa, K. Hata, K. Kajiwara, and Y. Saito, "Growth control of carbon nanotubes by RF plasma enhanced chemical vapor deposition," in *Vacuum Nanoelectronics Conference, 2007. IVNC. IEEE 20th International*, pp. 193–194,

- 2007.
- [139] Y. Show, Y. Yabe, T. Izumi, and H. Yamauchi, "Development of triode type RF plasma enhanced CVD equipment for low temperature growth of carbon nanotube," *Diamond and Related Materials*, vol. 14, pp. 1848–1851, 2005.
- [140] T. Kato, G.-H. Jeong, T. Hirata, and R. Hatakeyama, "Structure control of carbon nanotubes using radio-frequency plasma enhanced chemical vapor deposition," *Thin Solid Films*, vol. 457, pp. 2–6, 2004.
- [141] T. Yuji and Y.-M. Sung, "RF PECVD characteristics for the growth of carbon nanotubes in a $\text{CH}_4\text{-N}_2$ mixed gas," *Plasma Science, IEEE Transactions on*, vol. 35, no. 4, pp. 1027–10323, 2007.
- [142] S. Xu, Z. Tskadze, J. Long, K. Ostrikov, and N. Jiang, "Low temperature growth of vertically aligned carbon nanofibres in a low frequency inductively coupled plasma reactor," in *Optoelectronic and Microelectronic Materials and Devices, 2002 Conference on*, pp. 177–180, 2002.
- [143] S. ichi Honda, M. Katayama, K.-Y. Lee, T. Ikuno, S. Ohkura, K. Oura, H. Furuta, and T. Hirao, "Low temperature synthesis of aligned carbon nanotubes by inductively coupled plasma chemical vapor deposition using pure methane," *Japanese Journal of Applied Physics*, vol. 42, pp. 441–443, 2003.
- [144] K.-Y. Lee, M. Katayama, S. ichi Honda, T. Kuzuoka, T. Miyake, Y. Terao, J.-G. Lee, H. Mori, T. Hirao, and K. Oura, "Synthesis of aligned carbon nanofibers at 200°C," *Japanese Journal of Applied Physics*, vol. 42, pp. 804–806, 2003.
- [145] Y. Li, D. Mann, M. Rolandi, W. Kim, A. Ural, S. Hung, A. Javey, J. Cao, D. Wang, E. Yenilmez, Q. Wang, J. F. Gibbons, Y. Nishi, and H. Dai, "Preferential growth of semi-conducting single-walled carbon nanotubes by a plasma enhanced CVD method," *Nano Letters*, vol. 4, no. 2, pp. 317–321, 2004.
- [146] V. I. Merkulov, D. H. Lowndes, Y. Y. Wei, G. Eres, and E. Voelkl, "Patterned growth of individual and multiple vertically aligned carbon nanofibers," *Applied Physics Letters*, vol. 76, no. 24, pp. 3555–3557, 2000.
- [147] S. Hofmann, M. Cantoro, B. Kleinsorge, C. Casiraghi, A. Parvez, and J. Robertson, "Effects of catalyst film thickness on plasma-enhanced carbon nanotube growth," *Journal of Applied Physics*, vol. 98, p. 034308, 2005.
- [148] M. Cantoro, S. Hofmann, S. Pisana, C. Ducati, A. Parvez, A. Ferrari, and J. Robertson, "Effects of pre-treatment and plasma enhancement on chemical vapor deposition of carbon nanotubes from ultra-thin catalyst films," *Diamond and Related Materials*, vol. 15, pp. 1029–1035, 2006.
- [149] K. B. K. Teo, D. B. Hash, R. G. Lacerda, N. L. Rupesinghe, M. S. Bell, S. H. Dalal, D. Bose, T. R. Govindan, B. A. Cruden, M. Chhowalla, G. A. J. Amaratunga, M. Meyyappan, and W. I. Milne, "The significance of plasma heating in carbon nanotube and nanofiber growth," *Nano Letters*, vol. 4, no. 5, pp. 921–926, 2004.
- [150] M. Katagiri, N. Sakuma, M. Suzuki, T. Sakai, S. Sato, T. Hyakushima, M. Nihei, and Y. Awano, "Carbon nanotube vias fabricated by remote plasma-enhanced chemical vapor deposition," *Japanese Journal of Applied Physics*, vol. 47, no. 4, pp. 2024–2027, 2008.
- [151] Y. Y. Wang, S. Gupta, and R. J. Nemanich, "Role of thin Fe catalyst in the synthesis of double- and single-wall carbon nanotubes via microwave chemical vapor deposition," *Applied Physics Letters*, vol. 85, no. 13, pp. 2601–2603, 2004.
- [152] G. Zhong, T. Iwasaki, K. Honda, Y. Furukawa, I. Ohdomari, and H. Kawarada, "Low temperature synthesis of extremely dense and vertically aligned single-walled carbon nanotubes," *Japanese Journal of Applied Physics*, vol. 44, no. 4A, pp. 1558–1561, 2005.
- [153] M. S. Bell, K. B. K. Teo, R. G. Lacerda, W. I. Milne, D. B. Hash, and M. Meyyappan, "Carbon nanotubes by plasma-enhanced chemical vapor deposition," *Pure and Applied Chemistry*, vol. 778, no. 6, pp. 1117–1125, 2006.
- [154] C. Bower, W. Zhu, S. Jin, and O. Zhou, "Plasma-induced alignment of carbon nanotubes," *Applied Physics Letters*, vol. 77, no. 6, pp. 830–832, 2000.
- [155] E. Mendoza, S. J. Henley, C. H. P. Poa, G. Y. Chen, C. E. Giusca, A. A. D. T. Adikaari, J. D. Carey, and S. R. P. Silva, "Large area growth of carbon nanotube arrays for sensing

- platforms,” *Sensors and Actuators B*, vol. 109, pp. 75–80, 2005.
- [156] B. O. Boskovic, V. B. Golovko, M. Cantoro, B. Kleinsorge, A. T. H. Chuang, C. Ducati, S. Hofmann, J. Robertson, and B. F. G. Johnson, “Low temperature synthesis of carbon nanofibres on carbon fibre matrices,” *Carbon*, vol. 43, pp. 2643–2648, 2005.
- [157] V. I. Merkulov, A. V. Melechko, M. A. Guillorn, D. H. Lowndes, and M. L. Simpson, “Alignment mechanism of carbon nanofibers produced by plasma-enhanced chemical-vapor deposition,” *Applied Physics Letters*, vol. 79, no. 18, pp. 2970–2972, 2001.
- [158] K. B. K. Teo, M. Chhowalla, G. A. J. Amaratunga, and W. I. Milne, “Uniform patterned growth of carbon nanotubes without surface carbon,” *Applied Physics Letters*, vol. 79, no. 10, pp. 1534–1536, 2001.
- [159] G. F. Zhong, T. Iwasaki, and H. Kawarada, “Semi-quantitative study on the fabrication of densely packed and vertically aligned single-walled carbon nanotubes,” *Carbon*, vol. 44, pp. 2009–2014, 2006.
- [160] M. L. Terranova, V. Sessa, and M. Rossi, “The world of carbon nanotubes: An overview of CVD growth methodologies,” *Chemical Vapor Deposition*, vol. 12, pp. 315–325, 2006.
- [161] S. Pisana, M. Cantoro, A. Parvez, S. Hofmann, A. Ferrari, and J. Robertson, “The role of precursor gases on the surface restructuring of catalyst films during carbon nanotube growth,” *Physica E*, vol. 37, pp. 1–5, 2007.
- [162] M. Meyyappan, L. Delzeit, A. Cassell, and D. Hash, “Carbon nanotube growth by PECVD: a review,” *Plasma Sources Science and Technology*, vol. 12, pp. 205–216, 2003.
- [163] M. Jónsson, O. Nerushev, and E. Campbell, “Dc plasma-enhanced chemical vapour deposition growth of carbon nanotubes and nanofibres: in situ spectroscopy and plasma current dependence,” *Applied Physics A*, vol. 88, pp. 261–267, 2007.
- [164] S. Wei, W. Kang, J. Davidson, and J. Huang, “Aligned carbon nanotubes fabricated by thermal CVD at atmospheric pressure using Co as catalyst with NH_3 as reactive gas,” *Diamond and Related Materials*, vol. 15, pp. 1828–1833, 2006.
- [165] H. Cui, G. Eres, J. Howe, A. Ppuretkzy, M. Varela, D. Geohegan, and D. Lowndes, “Growth behavior of carbon nanotubes on multilayered metal catalyst film in chemical vapor deposition,” *Chemical Physics Letters*, vol. 374, pp. 222–228, 2003.
- [166] O. Nerushev, R.-E. Morjan, D. Ostrovskii, M. Sveningsson, M. Jónsson, F. Rohmund, and E. Campbell, “The temperature dependence of Fe-catalysed growth of carbon nanotubes on silicon substrates,” *Physica B*, vol. 323, pp. 51–59, 2002.
- [167] J. hee Han, B.-S. Moon, W. S. Yang, J.-B. Yoo, and C.-Y. Park, “Growth characteristics of carbon nanotubes by plasma enhanced hot filament chemical vapor deposition,” *Surface and Coatings Technology*, vol. 131, pp. 93–97, 2000.
- [168] T. Iwasaki, G. Zhong, T. Aikawa, T. Yoshida, and H. Kawarada, “Direct evidence for root growth of vertically aligned single-walled carbon nanotubes by microwave plasma chemical vapor deposition,” *Journal of Physical Chemistry B*, vol. 109, pp. 19556–19559, 2005.
- [169] Y. T. Lee, J. Park, Y. S. Choi, H. Ryu, and H. J. Lee, “Temperature-dependent growth of vertically aligned carbon nanotubes in the range 800–1100 °C,” *Journal of Physical Chemistry B*, vol. 106, pp. 7614–7618, 2002.
- [170] E. F. Antunes, A. O. Lobo, E. J. Corat, and V. J. Trava-Airoldi, “Influence of diameter in the Raman spectra of aligned multi-walled carbon nanotubes,” *Carbon*, vol. 45, pp. 913–921, 2007.
- [171] S. Reich, L. Li, and J. Robertson, “Control the chirality of carbon nanotubes by epitaxial growth,” *Chemical Physics Letters*, vol. 421, pp. 469–472, 2006.
- [172] Y. Li, S. Peng, D. Mann, J. Cao, R. Tu, K. J. Cho, and H. Dai, “On the origin of preferential growth of semiconducting single-walled carbon nanotubes,” *Journal of Physical Chemistry B*, vol. 109, pp. 6968–6971, 2005.
- [173] A. Naeemi and J. D. Meindl, *Carbon Nanotube Electronics*, ch. Performance Modeling for Carbon Nanotube Interconnects, pp. 163–190. Series on Integrated Circuits and Systems, Springer US, 2009.
- [174] C. T. White and T. N. Todorov, “Carbon nanotubes as long ballistic conductors,” *Nature*, vol. 393, pp. 240–242, 1998.
- [175] J. Jiang, J. Dong, H. T. Yang, and D. Y. Xing, “Universal expression for localization length

- in metallic carbon nanotubes,” *Physical Review B*, vol. 64, p. 045409, 2001.
- [176] H.-S. P. Wong, A. Lin, J. Deng, A. Hazegehi, T. Krishnamohan, and G. Wan, *Carbon Nanotube Electronics*, ch. Carbon Nanotube Device Modeling and Circuit Simulation, pp. 133–162. Series on Integrated Circuits and Systems, Springer US, 2009.
- [177] D. K. Schroder, *Semiconductor Material and Device Characterisation*. Wiley-Interscience, third ed., 2005.
- [178] R. Vajtai, K. K. b, B. Wei, J. Békési, S. Leppävuori, T. George, and P. Ajayan, “Carbon nanotube network growth on palladium seeds,” *Materials Science and Engineering C*, vol. 19, pp. 271–274, 2002.
- [179] S.-H. Tsai, C.-T. Shiu, S.-H. Lai, and H.-C. Shih, “Tubes on tube - a novel form of aligned carbon nanotubes,” *Carbon*, vol. 40, p. 1597, 2002.
- [180] Y. Wong, S. Wei, W. Kang, J. Davidson, W. Hofmeister, J. Huang, and Y. Cui, “Carbon nanotubes field emission devices grown by thermal CVD with palladium as catalysts,” *Diamond & Related Materials*, vol. 13, pp. 2105–2112, 2004.
- [181] Y. Breton, M. Verstraete, R. Fleurier, T. Cacciaguerra, J.-C. Charlier, A.-L. Thomann, and J.-P. Salvetat, “Anomalous ESR behavior of carbon nanofilaments grown from palladium seeds,” *Carbon*, vol. 42, pp. 1049–1052, 2004.
- [182] Y. Ominami, Q. Ngo, A. J. Austin, H. Yoong, C. Y. Yang, A. M. Cassell, B. A. Cruden, J. Li, and M. Meyyappan, “Structural characteristics of carbon nanofibers for on-chip interconnect applications,” *Applied Physics Letters*, vol. 87, p. 233105, 2005.
- [183] S.-Y. Lee, M. Yamada, and M. Miyake, “Synthesis of carbon nanotubes and carbon nanofilaments over palladium supported catalysts,” *Science and Technology of Advanced Materials*, vol. 6, pp. 420–426, 2005.
- [184] X. Tao, X. Zhang, J. Wang, J. Cheng, F. Liu, J. Luo, and Z. Luo, “Controllable synthesis of CNTs using Pd catalyst,” in *Nano/Micro Engineered and Molecular Systems, 2006. NEMS '06. 1st IEEE International Conference on*, pp. 559–562, 2006.
- [185] D. Beke, ed., *Diffusion in Semiconductors*. Springer-Verlag, 1998.
- [186] L. So, J. S. Whiteley, S. K. Ghandhi, and B. J. Baliga, “Lifetime control by palladium diffusion in silicon,” *Solid-State Electronics*, vol. 21, no. 6, pp. 887–890, 1978.
- [187] H. Yokoyama, H. Numakura, and M. Koiwa, “The solubility and diffusion of carbon in palladium,” *Acta Materialia*, vol. 46, no. 8, pp. 2823–2830, 1998.
- [188] S. Musso, M. Giorcelli, M. Pavese, S. Bianco, M. Rovere, and A. Tagliaferro, “Improving macroscopic physical and mechanical properties of thick layers of aligned multiwall carbon nanotubes by annealing treatment,” *Diamond and Related Materials*, vol. 17, pp. 542–547, 2008.
- [189] M. S. Dresselhaus, G. Dresselhaus, R. Saito, and A. Jorio, “Raman spectroscopy of carbon nanotubes,” *Physics Reports*, vol. 409, pp. 47–99, 2005.
- [190] W. Li, H. Zhang, C. Wang, Y. Zhang, L. Xu, K. Zhu, and S. Xie, “Raman characterization of aligned carbon nanotubes produced by thermal decomposition of hydrocarbon vapor,” *Applied Physics Letters*, vol. 70, no. 20, pp. 2684–2686, 1997.
- [191] C.-C. Chuang, W.-L. Liu, W.-J. Chen, and J.-H. Huang, “The role of ti interlayer in carbon nanotube growth,” *Surface & Coatings Technology*, vol. 202, pp. 2121–2125, 2008.
- [192] O. Madelung, ed., *Diffusion in Solid Metals and Alloys*, vol. 26 of *Landolt-Börnstein - Group III Condensed Matter*. Springer-Verlag, 1990.
- [193] H. C. Peng, C. C. Chieng, C. H. Tsai, and F. G. Tseng, “Manipulation of carbon nanotubes (CNTs) profile by pre-annealed Ni/Ti/Si substrate,” in *Nano/Micro Engineered and Molecular Systems, 2008. NEMS 2008. 3rd IEEE International Conference on*, pp. 812–815, 2008.
- [194] R. Saito, A. Jorio, A. G. S. Filho, G. Dresselhaus, M. S. Dresselhaus, A. Gr^uneis, L. G. Cançado, and M. A. Pimenta, “First and second-order resonance raman process in graphite and singlewall carbon nanotubes,” *Japanese Journal of Applied Physics*, vol. 41, pp. 4878–4882, 2002.
- [195] T. Belin and F. Epron, “Characterization methods of carbon nanotubes: a review,” *Materials Science and Engineering B*, vol. 119, pp. 105–118, 2005.
- [196] Y. Ouyang, L. Cong, L. Chen, Q. Liu, and Y. Fang, “Raman study on single-walled carbon

- nanotubes and multi-walled carbon nanotubes with different laser excitation energies,” *Physica E*, vol. 40, pp. 2386–2389, 2008.
- [197] Y.-J. Lee, “The second order raman spectroscopy in carbon crystallinity,” *Journal of Nuclear Materials*, vol. 325, pp. 174–179, 2004.

List of Figures

1.1	Moore's Law	1
1.2	Interconnect RC delay vs. clock cycle (logic delay)	2
1.3	Trends in chip design	4
2.1	Graphene sheet, SWNT and MWNT	8
2.2	Chiral vector and chiral type naming	9
2.3	The definition of carbon nanotubes and nanofibres	10
2.4	Band structure of a metallic CNT and semiconducting CNT	11
2.5	Number of conductive channels per wall vs. diameter ($T = 300$ K)	13
2.6	Different MFP vs. temperature for low bias	14
2.7	Conductivity of various diameter MWNT compared with SWNT and copper with different dimensions	15
2.8	Temperature dependency of the specific heat for various systems	19
2.9	Thermal conductivity at high temperature	21
3.1	CNT growth models	27
3.2	Typical hot-wall thermal CVD lay-out	29
3.3	Typical RF or DC PECVD lay-out	30
3.4	Close-up of nickel nano-particles on titanium buffer layer	33
4.1	Simplified circuit model for a single metallic SWNT	40
4.2	Ideal tight packed and sparse packed bundle	40
4.3	CNT density as predicted by the model against diameter and separation	41
4.4	SWNT bundle resistance per unit area vs. length for different l_0	43
4.5	SWNT bundle resistance per unit area vs. tube diameter and separation	44
4.6	N_{channels} , density and product of channels and density vs. diameter	46
4.7	MWNT bundle resistance per unit area vs. tube diameter and separation	47
4.8	MWNT bundle resistance per unit area against tube diameter for different $D_{\text{min}}/D_{\text{max}}$ ratio's	48
5.1	3D image of 4-point probe structure	52
5.2	3D image of 2-point probe structure	52
5.3	Overview of the P2748 process	54
5.4	Overview of the P2752 process	55
5.5	Overview of the lift-off process to obtain 'oxide after growth' wafer	57
5.6	Overview of the die lay-out	58
5.7	Overview of measurement structures	59
5.8	Lay-out of the contact aligner masks	60
5.9	Cross-section along diagonal of 4-point structure including zeroth order thermal model	62
6.1	SEM images of batch 2	67
6.2	SEM images of DC-PECVD growth at 500 °C	68
6.3	PECVD results for 6 and 9 nm Ni and 1 nm Pd between 350 - 500 °C	69
6.4	Raman spectrum of 9 nm Ni at 500 °C with peaks indicated	70
6.5	Results for 6 nm patterned and non-patterned Ni	71

6.6	TEM image of growth using DC-PECVD at 500 °C	72
6.7	APCVD results for Co, Fe and Pd between 450-640 °C	73
6.8	Raman spectrum of 1 nm of Fe at 640 °C with peaks indicated	74
6.9	Different quality indicators against temperature for the APCVD samples .	74
6.10	TEM images of Co and Fe samples after APCVD growth at 640 °C	75
6.11	TEM images of the APCVD samples using 1 nm Pd as catalyst	75
6.12	HF-PECVD results for 6 and 9 nm of Ni and 1 nm of Pd at 500 °C	76
6.13	Pictures of RF assisted CVD system	77
6.14	Selected SEM pictures of PECVD growth results	80
6.15	TEM images of several HF-PECVD samples	83
6.16	Growth results at 600 °C in the 3" tube using a Mo boat	84
6.17	Growth results at 600 °C in the 2" tube using a quartz boat	85
6.18	Low and high magnification TEM image of 1 nm Fe sample	86
6.19	Relative intensities of the different Raman active bands against temperature	87
6.20	Raman band widths and $I_D/I_G \cdot \text{FWHM}(D)$ against temperature	88
6.21	Comparison between different cleaning methods to enable growth on 6 nm of Ni pieces	90
6.22	SEM images of 6 and 12 nm of Fe growth using HF-PECVD	91
6.23	CVD growth results at different temperature of 6 nm of Fe samples created by lift-off	92
6.24	TEM images of 6 nm Fe after growth at 600 °C and 500 °C	92
6.25	Growth results on Fe and Ni lift-off samples after cleaning	93
6.26	TEM image of cross-section of Ni sample	94
C.1	EDX spectrum obtained at different points in the Ni cross-section	122
C.2	Peak assignment in Raman spectra of carbon nanotubes (MWNT sample)	123
C.3	Raman spectra of 500 °C DC-PECVD	126
C.4	Raman spectra of 450 °C DC-PECVD	127
C.5	Raman spectra of 640 °C APCVD	128
C.6	Raman spectra of 500 °C APCVD	129
C.7	Raman spectra of 450 °C APCVD	129
C.8	Raman spectra of 500 °C HF-PECVD	130
C.9	Raman spectra of HF-PECVD run 1	133
C.10	Raman spectra of HF-PECVD run 2	134
C.11	Raman spectra of HF-PECVD run 3	135
C.12	Raman spectra of HF-PECVD run 4	136
C.13	Raman spectra of HF-PECVD differently cleaned Fe 6 nm lift-off	137
C.14	Raman spectra of 3" furnace CVD at 600 °C	138
C.15	Raman spectra of 2" furnace CVD at 600 °C	139
C.16	Raman spectra of 2" furnace CVD at 600 °C with reduced flow-rate . . .	140
C.17	Raman spectra of 2" furnace CVD at 550 °C	140
C.18	Raman spectra of 2" furnace CVD at 500 °C	141
C.19	Raman spectra of 2" furnace CVD at 450 °C	141
C.20	Raman spectra of lift-off samples at 600 °C	142
C.21	Raman spectra of lift-off samples at 500 °C	142

List of Tables

3.1	Qualitative overview of growth properties vs. parameters	35
5.1	Via configurations	59
6.1	Process conditions BlackMagic II	68
6.2	Process conditions for the NanoLab PECVD system	79
B.1	Novellus batch 1: 3 nm Ni, Ti not etched	109
B.2	Novellus batch 2: 6 nm Ni, Ti etched	110
C.1	Extracted parameters from the Raman spectra of the AIXTRON samples	125
C.2	Extracted parameters from the Raman spectra of the NanoLab HF-PECVD samples	131
C.3	Extracted parameters from the Raman spectra of the NanoLab CVD sam- ples	132

List of Abbreviations

a-C	Amorphous Carbon
AP	Acoustic Phonons
CCP	Capacitively Coupled Plasma
CMP	Chemical Mechanical Polishing
CNF	Carbon Nanofibres
CNT	Carbon Nanotube
CVD	Chemical Vapour Deposition
DC	Direct Current
DWNT	Double-Walled Nanotube
EDX	Energy-dispersive X-ray spectroscopy
FWHM	Full Width at Half Maximum
HAR	High Aspect Ratio
HF	Hot-Filament
HRTEM	High Resolution Transmission Electron Microscopy
IC	Integrated Circuit
ICP	Inductively Coupled Plasma
MFC	Mass Flow Controllers
MFP	Mean Free Path
MW	Microwave
MWNT	Multi-Walled Nanotube
OP	Optical Phonons
PECVD	Plasma Enhanced Chemical Vapour Deposition
RBM	Radial Breathing Mode
RF	Radio Frequency
RTA	Rapid Thermal Annealing
SB	Schottky Barrier
sccm	Standard Cubic Centimetres per Minute
SEM	Scanning Electron Microscopy
SiP	System in Package
SoC	System on Chip
SWNT	Single-Walled Nanotube
TEM	Transmission Electron Microscopy
VA	Vertically Aligned
XRD	X-ray Diffraction